Stefan P. Hau-Riege
High-Intensity X-Rays –
Interaction with Matter

Related Titles

Vollath, D.

Nanomaterials
An Introduction to Synthesis, Properties and Applications

2008
ISBN 978-3-527-31531-4

Meschede, D.

Optics, Light and Lasers
The Practical Approach to Modern Aspects of Photonics and Laser Physics

2007
ISBN 978-3-527-40628-9

Talman, R.

Accelerator X-Ray Sources

2006
ISBN 978-3-527-40590-9

Stefan P. Hau-Riege

High-Intensity X-Rays – Interaction with Matter

Processes in Plasmas, Clusters, Molecules, and Solids

WILEY-VCH Verlag GmbH & Co. KGaA

The Author

Dr. Stefan P. Hau-Riege
Lawrence Livermore
National Laboratory
Livermore, CA, USA
hauriege1@llnl.gov

Cover figure

Stefan P. Hau-Riege, Livermore

Using of programm Automatic PSF Generation Plugin, Version 1.0

Library of Congress Card No.: applied for

British Library Cataloguing-in-Publication Data:
A catalogue record for this book is available from the British Library.

Bibliographic information published by the Deutsche Nationalbibliothek
The Deutsche Nationalbibliothek lists this publication in the Deutsche Nationalbibliografie; detailed bibliographic data are available on the Internet at http://dnb.d-nb.de.

Typesetting le-tex publishing services GmbH, Leipzig
Printing and Binding Fabulous Printers Pte Ltd, Singapore

Cover Design Grafik-Design Schulz, Fußgönheim

Printed in Singapore
Printed on acid-free paper

ISBN Print 978-3-527-40947-1

ISBN ePDF 978-3-527-63638-9
ISBN ePub 978-3-527-63637-2
ISBN oBook 978-3-527-63636-5
ISBN Mobi 978-3-527-63639-6

for Christine, Jamie, and Justin

Contents

Preface

This monograph provides a coherent and current overview of the interaction of x rays with matter, specifically focussing on high-intensity short-pulse radiation. We discuss the relevant physical processes, including the interaction of the x-ray field with electrons, the coupling of electrons and ions, the microscopic and macroscopic changes in materials, and the feedback of these processes. We conclude by providing several examples taken from the recent scientific literature.

There are many books available that treat the interaction of x-ray radiation with matter at intensities that are sufficiently low so that the materials do not change. On the other end of the spectrum are plasma-physics books that discuss the interaction of high-intensity photon beams with plasmas. This book bridges these two extremes by providing a comprehensive coverage of the full spectrum of interactions of low- to high-intensity x-ray radiation with materials. It discusses how x rays affect the state of matter, and, in turn, how these changes affect x-ray–matter interaction.

Similar books have been published for the optical wavelength regime. In contrast, x-ray wavelengths are on the order of interatomic distances, and x-ray energies are comparable to the transition and ionization energies of atoms and ions. Therefore, the relevant physical processes are very different.

X-ray–matter interaction draws from various disciplines, ranging from atomic physics, laser physics, plasma physics, astrophysics, computational physics, materials science, to chemistry. Most elements of this book are scattered throughout the scientific literature and have been published in scientific journals and the more introductory materials in book form. We aim at enabling the reader to gain an understanding of the fundamentals and to get an idea of the current state of research efficiently without being bogged down by either the scientific jargon specific to each discipline or by the sheer volume of publications. This will be especially useful for young researchers and occasional practitioners of this field who need to learn about the most relevant aspects of the various fields quickly.

The recent advent of new powerful x-ray sources such as x-ray free-electron lasers make the release of this book very timely. Within the context of large-scale facilities, the scientific community at large is currently shifting its focus away from particle physics toward photon science. The recent shutdown of the particle physics facility Barbar and the construction of the LCLS x-ray free-electron laser (FEL) in its

place at the SLAC National Accelerator Laboratory in the USA is a testimony to this change. Numerous large-scale photon-science facilities producing EUV (extreme ultraviolet) and x-ray radiation are being built all over the world: The first EUV FEL at DESY in Germany became operational in 2005, Japan demonstrated an EUV FEL in 2006, and others are planned, for example in Italy, Switzerland, and the USA. To access the shorter wavelength regime, an x-ray free-electron laser has been built in the USA (LCLS), and others are in progress, including in Germany (XFEL) and in Japan (SCSS). In addition to these facilities, new x-ray synchrotron sources such as PETRA III at DESY will also be available soon.

In light of these developments, this book has several target audiences: (i) Young scientists, postdoctoral researchers, graduate students, and senior undergraduate students who recognize the exciting field of x-ray–matter interaction science, and want to participate in it, (ii) more experienced scientists who want to change their research focus toward photon science, and (iii) scientists from various disciplines, such as life sciences, biology, materials science, physics, and chemistry, that plan on applying these new facilities in their respective fields. The interdisciplinary nature of the field of x-ray–matter interaction may make this book even interesting for the more casual reader.

The prerequisite for this book is a basic understanding of mechanics, electrodynamics, and quantum mechanics, even though most basic concepts are briefly explained whenever they are introduced, and relevant and introductory literature is cited. In that sense, the readership level is advanced. We hope that the book still has appeal to the more experienced research worker (specialist).

We have tried to make this monograph self-contained by including reviews of the basic aspects of atomic physics, electrodynamic wave propagation, and electron dynamics, with a specific focus on aspects relevant to high-intensity x-ray–matter interaction. An introduction to the field of x-ray–matter interaction is given in Chapter 1, in which we give an overview of available x-ray sources, summarize the processes relevant to x-ray–matter interaction, and point out the key aspects relevant to high-intensity pulses. In Chapter 2, we discuss the atomic physics relevant to x-ray-irradiated matter. This subject is essential in order to understand x-ray absorption processes and the subsequent electron dynamics. In Chapter 3, scattering of x-ray radiation from atoms, molecules, and other aggregates of atoms and different media is discussed. In Chapter 4, we discuss the propagation of electromagnetic waves in different media, and especially focus on the intensity distribution of the electromagnetic field since this determines the interaction of x rays with materials. In Chapter 5, we discuss the dynamics of the electrons in x-ray-irradiated materials.

The following chapters focus on high-intensity, short x-ray pulses, motivated by the recent advent of x-ray free-electron lasers. In Chapter 6, we discuss the characteristics of short x-ray pulses and describe instrumentation to create and diagnose such pulses. We also include the effects of the pulse duration on x-ray–matter interaction processes. In the related Chapter 7, we discuss aspects of the interaction of high-intensity x-ray pulses with matter. Since x rays modify matter, their interaction with the material changes with time. This aspect is discussed in Chapter 8. In Chapter 9, we present modeling approaches for x-ray–matter interaction. Finally,

in Chapter 10, we give some recent examples of high-intensity x-ray–matter interaction. This chapter is strongly biased by the research interests of the author.

I am deeply grateful to innumerable discussions with a large number of long-term colleagues, who over many years participated in carrying out calculations and experiments, and in interpreting the obtained results. It is a great pleasure to specifically mention valuable advice, help, and support from Elden Ables, Jennifer Alameda, John Arthur, Eduard Arzt, Sasa Bajt, Sherry Baker, Anton Barty, Brian Bennion, Karl Van Bibber, Richard Bionta, Michael Bogan, Sebastien Boutet, Carl Caleman, Jaromir Chalupksy, Henry Chapman, Rip Collins, Tilo Döppner, Paul Emma, James Evans, Gyula Faigel, Roger Falcone, Carsten Fortmann, Matthias Frank, Jerome Gaudin, Siegfried Glenzer, Jim Glosli, Bill Goldstein, Alexander Graf, Frank Graziani, Janos Hajdu, Rick Iverson, Verne Jacobs, Jacek Krzywinski, Jaroslav Kuba, Steve Lane, Dick Lee, Richard London, Stefano Marchesini, Marty Marinak, Dennis Matthews, Marc Messerschmidt, Paul Mirkarimi, Stefan Moeller, Michael Murillo, Michael Pivovaroff, Dave Richards, Dmitri Ryutov, Howard Scott, Marvin Seibert, Ryszard Sobierajski, Klaus Sokolowski-Tinten, Regina Soufli, John Spence, Eberhard Spiller, Fred Streitz, Hannah and Abraham Szöke, Michael Thomas, Nicusor Timneanu, Thomas Tschentscher, Jim Turner, and Chris Walton.

I would like to acknowledge my teachers and mentors over the years, who introduced me to the science and the scientific methods. I am especially appreciative to Detlef Heitmann from the Universität Hamburg, Judith Prybyla and Walter Brown from (formerly) AT&T Bell Laboratories, Carl Thompson from the Massachusetts Institute of Technology, and Harold Frost from Dartmouth College. I owe a debt of gratitude to the *Studienstiftung des deutschen Volkes* for supporting me early on in my career.

I thank the team at Wiley-VCH Verlag who have been a great help in publishing the manuscript, all the way from the initial planning stage to final production. I would explicitly like to recognize the Commissioning Editor Ulrike Fuchs, the Project Editor Ulrike Werner, and the copy editing of le-tex publishing services. I would like to thank the people who encouraged me to pursue and finish this project, in particular Jamie. Finally, I deeply acknowledge my friends and colleagues from the x-ray–matter interaction community for proofreading the manuscript and providing valuable comments and suggestions. Specifically, I thank Tilo Döppner, Carsten Fortmann, Richard London, Nina Rohringer, Eberhard Spiller, Jon Weisheit, and Beata Ziaja.

Fremont, January 2011 *Stefan P. Hau-Riege*

1
Introduction

Wilhelm Conrad Röntgen discovered x rays at the University of Würzburg in 1895, and published his results in a groundbreaking report entitled *Über eine neue Art von Strahlen* (*On a new kind of rays*) [1]. In the twentieth century, x rays have played an important role in gaining an understanding of matter on the atomic scale and quantum mechanics in general. Table 1.1 shows some of the key events in this fast-paced journey of discoveries. The discovery of x rays sparked a new era of science. One of the major accomplishments, has been the exploration of the microscopic structural details of molecules, liquids and solids at length scales of interatomic distances.

X rays can penetrate thick objects that are opaque to visible light. On the basis of this property, atomic-resolution three-dimensional real-space imaging methods are used to obtain the at-first invisible interior structure of objects. Several x-ray imaging techniques have been developed for this purpose. For example, real-space x-ray microscopy is similar to visible light microscopy, except that traditional refractive lenses are replaced by x-ray lenses such as zone plates. Lensless imaging does away with lenses altogether [2], and instead reciprocal-space coherent diffraction patterns are recorded. They are subsequently inverted using computational algorithms to obtain a real-space image. These techniques allow the recording of high-resolution images that can be sensitive to elemental composition, chemical state, and state of magnetism.

With the advent of high-intensity short-pulse x-ray sources, ultrafast processes have become accessible for investigations. These sources will allow the study of materials on time scales comparable to the motion of electrons circling around atoms, on spatial scales of interatomic bonds, and on energy scales that hold electrons in correlated motion with their neighbors. Ultrashort electromagnetic radiation sources are a critical tool for studying material properties, with the ultimate outlook of recording femtosecond movies of atomic and chemical processes.

The earliest x-ray sources were x-ray tubes. Even though their light output is of relatively low brightness, x-ray tubes have enabled numerous important discoveries, as laid out in Table 1.1. The laser was invented about 50 years ago and has led to steep progress in the optical sciences. Similarly, the advent of dedicated synchrotron sources around 1970 has enabled enormous advances in the x-ray sciences. We are now witnessing the emergence of short-pulse high-intensity x-ray

High-Intensity X-rays – Interaction with Matter, First Edition. Stefan P. Hau-Riege.

Table 1.1 An abbreviated history of x-ray physics.

Year	Event
1895	Wilhelm Röntgen takes first medical x ray of his wife's hand
1901	Wilhelm Röntgen receives Nobel prize for producing and detecting x rays
1909	Charles Barkla and Charles Sadler observe characteristic x rays by electron bombardment of pure elements
around 1910	Discovery that x rays are electromagnetic waves of shorter wavelength and higher energy than normal light
1912	Discovery of x-ray diffraction by Max von Laue, Walter Friedrich, and E. Paul Knipping
1913	William H. and William L. Bragg build an x-ray spectrometer
1913	William L. Bragg observes the first x-ray spectrum
1913	Henry Moseley establishes the relation between atomic number and the specific x-ray wavelength of the elements
1914	Max von Laue receives Nobel prize for the discovery of diffraction of x rays by crystals
1915	William H. and William L. Bragg receive the Nobel prize for determining crystal structures with x rays
1916	Karl Siegbahn and W. Stenstroem observe x-ray emission satellites
1917	Charles Barkla receives the Nobel prize for the discovery of the characteristic x-ray radiation of the elements
around 1920	Wave–particle duality generally accepted
1922	Lise Meitner discovers Auger electrons
1924	Karl Siegbahn receives Nobel prize for his discoveries and research in the field of x-ray spectroscopy
1927	Arthur Compton receives the Nobel prize for demonstrating the particle concept of electromagnetic radiation
1936	Peter Debye receives the Nobel prize for his contributions to the study of molecular structure (by x-ray diffraction)
1962	Max Perutz and John Kendrew receive the Nobel prize for determining the structure of hemoglobin and myoglobin
1964	Dorothy Crowfoot Hodgkin receives the Nobel prize for determining the structure of penicillin and other important biochemical substances
1964	Synchrotron radiation available down to 0.1 Å
1976	William Lipscomb receives the Nobel prize for his studies on the structure of boranes illuminating problems of chemical bonding
1979	Allan Cormack and Godfrey Hounsfield receive the Nobel prize for the development of computerized tomography
1981	Kai Siegbahn receives the Nobel prize for his contributions to the development of high-resolution electron spectroscopy
1985	Herbert Hauptman and Jerome Karle receive the Nobel prize for developing direct methods for x-ray structure determination
1988	Johann Deisenhofer, Robert Huber, and Hartmut Michal receive the Nobel prize for the determination of the protein structures crucial to photosynthesis
1994	First soft x-ray scanning transmission microscope (STXM)
1999	Chandra x-ray observatory in use
2009	First hard-x-ray free-electron laser in use

sources such as x-ray free-electron lasers (XFELs), high-harmonic generators, x-ray lasers, and laser-plasma sources. With these new sources we are at the dawn of a very exciting time in x-ray science. One can expect progress of similar grandeur as resulted from the introduction of lasers and synchrotrons.

Reversible interaction mechanisms of x rays with matter, such as elastic x-ray scattering, are often used to probe materials. Since these interactions are usually relatively weak, large photon fluxes are required to obtain sufficiently intense probe signals. Since the absorption of x rays is typically much stronger than the elastic scattering strength, high-intensity x-ray radiation also modifies the structure of materials, and this is the main topic of this book: How x rays can be used to probe *and modify* matter.

We will now provide examples for the application of x-ray–matter interaction and discuss methods to produce x-ray radiation. We will then summarize fundamental models to describe x-ray–matter interaction, such as the Maxwell equations, semiclassical methods, and quantum electrodynamics. Subsequently, we will discuss x-ray–matter interaction processes in materials. Finally, we will point to some databases with information relevant to x-ray–matter interaction.

1.1 Examples for the Application of X-Ray–Matter Interaction

X rays find their application in diverse disciplines, including the life sciences, crystallography, atomic physics, plasma physics, materials science, chemistry, and astronomy. We will now discuss some of the key applications of x rays that highlight their versatility and that draw on their various unique properties, including their high penetrating power in materials and their short wavelengths that are comparable to interatomic distances. In addition, x-ray radiation can be prepared to have a high spectral purity, which is useful for x-ray spectroscopy, a very short pulse duration, which enables time-resolved studies, and high intensity, which can lead to nonlinear x-ray–matter interaction phenomena.

X-ray astronomy has enabled detailed studies of supernovae, pulsars, and black holes. Since the Earth's atmosphere is opaque to x-ray radiation, x rays can only be observed from outer space. The first rocket launch carrying a scientific payload that detected a cosmic x-ray source was performed in 1962 by American Science and Engineering (AS&E) and led to the detection of Scorpius X-1, the brightest x-ray source in the sky [3]. By today, numerous satellite missions have been carried out to study high-energy astrophysics with x rays.

In the laboratory, we can build x-ray sources and study the interaction of x rays with materials systematically. Since the first man-made x-ray sources were relatively weak, x rays were initially used primarily as a probe, and the modification of materials by x-ray beams was less common. One notable exception is medical x-ray imaging, which is the earliest application of laboratory x-ray sources, and which had a phenomenal commercial success. Medical x-ray imaging takes advantage of the high penetrating power of x rays, as we will discuss in the next section. In or-

der to minimize damage to the human tissue, the x-ray dose has to be kept low and the exposure time long, but medical x-ray imaging still increases the cancer risk through modification of biological molecules by x-ray radiation.

Another way to probe materials with x rays is scattering. In x-ray crystallography, x rays are scattered from atoms that are arranged in repeating unit cells, leading to strong interference peaks called Bragg spots. Since the wavelength of x-ray light is on the order of interatomic distances, x-ray crystallography allows structure determination at atomic resolution. This technique has led to major advances in structural biology. When x-ray crystallography is performed using short-duration x-ray pulses, time-resolved x-ray studies become possible, allowing us to probe the evolution of materials at atomic resolution. Whereas x-ray crystallography is used primarily to determine the spatial arrangement of the ions, x-ray spectroscopy provides information about the electronic structure and chemical state of the materials. X-ray spectroscopy requires x-ray beams with high spectral purity. Finally, high-intensity x rays can be used to modify matter so strongly that the interaction becomes nonlinear. This has become a very active area of research since x-ray lasers have become available. We will now discuss some of these applications in more detail.

1.1.1 Medical Imaging with X Rays

Shortly after the discovery of x rays, Röntgen imaged the interior of his wife's hand on photographic plates, which was the very first picture obtained using x rays. This experiment was the first example of radiography, the most commonly used medical imaging technique to date. In radiography, an x-ray shadow graph is recorded, which is a two-dimensional projection of the imaged object. X-ray tomography is an extension of this technique and is used to generate three-dimensional medical images by measuring multiple one- or two-dimensional projections.

Both these imaging techniques are based on the variation of x-ray absorption in different types of body tissues. Figure 1.1 shows the linear attenuation coefficient μ of biological materials as a function of x-ray energy. The quantity μ is defined through

$$I = I_0 \exp(-\mu t), \tag{1.1}$$

where I_0 is the intensity of a monoenergetic incoming beam, I the intensity of the emerging radiation, and t is the material thickness. Relevant biological tissues, listed in order of decreasing linear absorption coefficient, are bones, muscles, and fat. X-ray absorption in water is similar to muscle tissue. Typically, x-ray energies in the range of 15–30 keV are used for imaging soft tissue, such as in mammography, and larger energies are used to image bones. Sometimes, opaque contrast materials are used, such as barium compounds, to visualize certain structures of the human body.

X rays are ionizing radiation since they ionize and dissociate molecules. These kinds of modifications can cause biological damage, including mutation and genet-

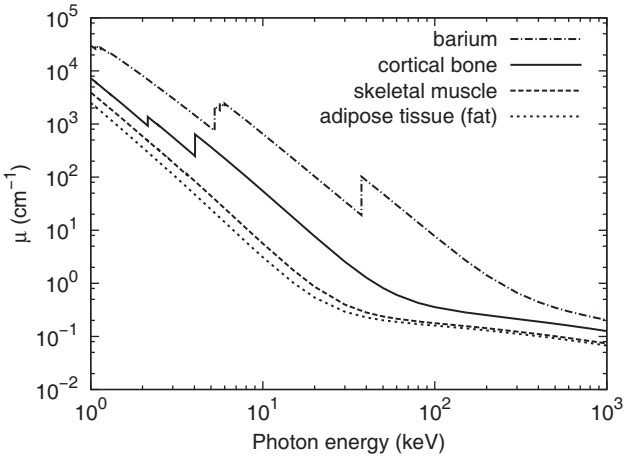

Figure 1.1 Linear absorption coefficient μ of human body tissue as a function of x-ray energy. For comparison, the data for barium, a common constituent of contrast enhancers, is also shown. The linear absorption coefficients of water and muscle tissue are very similar. Data were taken from [4].

ic modifications due to changes in the genetic sequence, radiation sickness caused by a too large x-ray dose over a short period of time, and an increase in the probability of cancer occurrence. The radiation exposure a patient receives from a full-body computer-tomography scan, often referred to as a CT or CAT scan, is often 500 times larger than for a conventional x-ray radiograph.

1.1.2
X-Ray Scattering and Spectroscopy

Most x-ray photons that interact with materials are absorbed through photoionization or are inelastically or elastically scattered. Figure 1.2 shows the interaction cross sections of 10-keV x rays as a function of the atomic charge number Z. The scattered x-ray photons are valuable in material diagnostics to obtain information about the crystal structure, chemical composition, and physical properties. For applications of structure determination, a short wavelength is required in order to resolve interatomic distances, whereas for spectroscopy applications, a narrow bandwidth and a tunable x-ray source, preferably near an absorption resonance, are desirable.

For elastic scattering, the phase relationship and the energy of the incoming and outgoing photons are preserved. In crystallography, the periodic arrangement of atoms or molecules leads to sharp Bragg peaks in the scattering pattern, from which the structure of crystals can be determined. For example, protein crystallography can be used to investigate complex biological macromolecules. Typically, x rays in the 3.5–20-keV energy range are used for atomic-resolution structure determination of matter. Currently, about 80% of new macromolecular structures

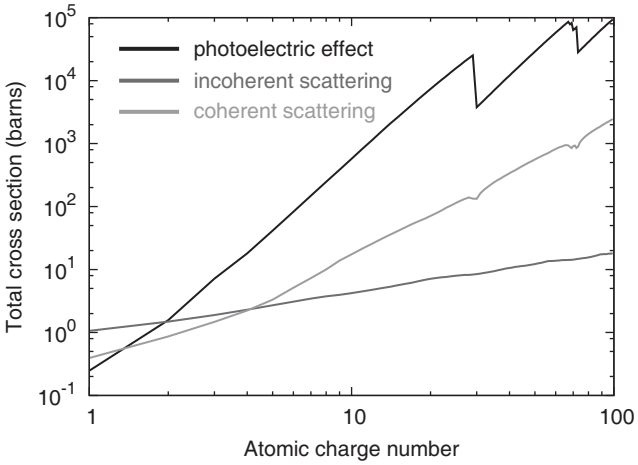

Figure 1.2 Atomic photoionization, incoherent scattering, and elastic scattering cross sections of 10-keV x rays as a function of the atomic charge number Z [5].

are determined through x-ray crystallography at synchrotron facilities. For higher-Z materials, x rays in the energy range from 20 to 100 keV are used to increase penetration and to reduce absorption and damage. X-ray scattering also allows the measurement of the grain size in materials, the thickness and roughness of layers and films, and the mechanical state. Now that high-intensity x-ray sources have become available, x-ray diffractive imaging of single nanoparticles has become possible. In the small-angle-x-ray scattering (SAXS) technique, the structure of matter is probed with a resolution down to a μm or nm. In wide-angle-x-ray scattering (WAXS), the diffracted light is measured at higher (sub-nm) resolution.

For inelastic scattering events, the energy of the photon changes due to interaction with the electron system. By measuring the spectrum of the scattered photons, we can obtain information about the electronic structure. Multiple techniques have been developed for this purpose, including x-ray Thomson scattering as a plasma diagnostic. By measuring the spectrum of the scattered photons, we obtain fundamental information about the plasma, such as density, temperature, and collective properties [6]. Resonant inelastic scattering (RIXS) is an x-ray spectroscopy technique to obtain information about the electronic structure by measuring the momentum transfer near intrinsic excitations. By operating near the resonance of the system, the x-ray interaction cross sections are relatively large. Another important class of x-ray analysis techniques are x-ray absorption spectroscopy (XAS) methods. By tuning the x-ray radiation, the absorption edges of materials can be mapped out. Similar to the optical regime, the most intense features in the spectrum are related to electric-dipole transitions. When specific absorption edges are studied in detail, the technique is called x-ray absorption fine-structure spectroscopy (XAFS), which encompasses two techniques: (i) Studying the rising edge of the absorption spectrum is called extended x-ray absorption near-

edge structure (XANES) or near-edge x-ray absorption fine structure (NEXAFS). (ii) When the region above the edge is studied, the ejected photoelectron scatters off neighboring ions, so that the absorption spectrum is sensitive to the chemical environment. This technique is called extended x-ray absorption fine structure (EXAFS).

1.1.3 Short-Pulse X-Ray Probing of Matter

Short x-ray pulses can be used to obtain snapshots of material properties, thereby enabling the study of the dynamics of material processes. X-ray pulses with femtosecond duration potentially allow probing the evolution of chemical reactions through x-ray spectroscopy, which holds the promise of detecting the formation and breaking of molecular bonds, and the identification of intermediate transition states. X rays can also be used to generate and probe the evolution of excited states. Short-pulse optical lasers have enabled time-resolved studies of chemical reaction. Short-pulse x-ray radiation additionally promises to provide spatial resolution of the chemical reaction process.

In the field of time-resolved macromolecular x-ray crystallography, short optical and x-ray pulses are used to obtain information about the function of molecules, specifically transient structures and reaction mechanism. Reactions are typically initiated with short pulses from an optical laser with a duration ranging from a few femtoseconds to 100 ns, and then the crystal is probed with short x-ray pulses from a synchrotron light source with pulse length as short as 10 ps. A major concern is x-ray radiation damage to the crystals, since when short-duration x-ray pulses are used to probe materials, the photon flux is often increased in order to maintain required signal levels.[1)] A larger photon flux may lead to modification of materials through x-ray-induced ionization and subsequent atomic motion which, in turn, can lead to changes in the optical properties and the x-ray–matter interaction mechanism. In recent experiments using free-electron lasers it has been demonstrated that atomic motion can be delayed on the time scale of tens of femtoseconds due to the inertia of the atomic nuclei [7], whereas the optical properties are determined by the evolution of the electron system which occurs much faster. For example, materials may become transparent due to the depletion of electrons from resonance states [8].

1.2 Electromagnetic Spectrum

X rays can be described as electromagnetic waves, just like optical and ultraviolet radiation. A portion of the spectrum of electromagnetic waves is shown in Figure 1.3,

1) The photon flux is defined as the number of photons per unit area per unit time, and the photon fluence of an x-ray pulse is defined as the number of photons per unit area.

along with the names of the energy regimes. The boundaries of these regimes are not very well defined.

For x rays, it is often convenient to express the wavelength λ in units of Ångströms, abbreviated by the symbol Å. One Ångström equals 0.1 nm, 10^{-8} cm, or 10^{-10} m. X rays lie approximately in the wavelength regime between 200 and 0.1 Å. Wavelengths are also often given in energy units, hc/λ, where h is the Planck constant, and c is the speed of light. In convenient units,

$$\lambda\,[\mathrm{eV}] \approx \frac{12\,398.417}{\lambda\,[\text{Å}]}\ . \tag{1.2}$$

In this book, we consider photons in the soft and hard x-ray regime, ranging from 250 eV to 100 keV.

Also shown in Figure 1.3 are liner absorption coefficients for different kinds of materials. Whereas for energies below 100 eV the linear absorption coefficient

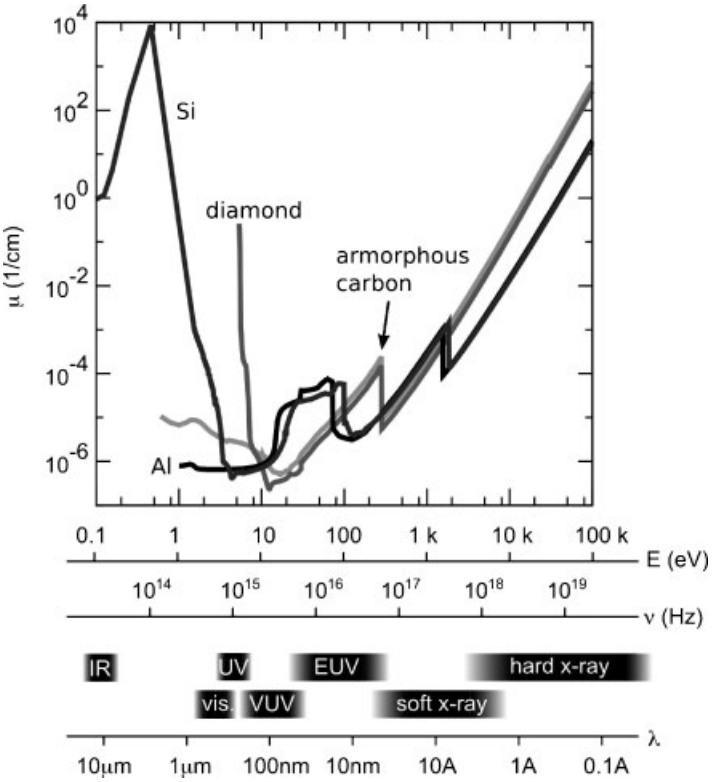

Figure 1.3 Overview of the electromagnetic spectrum. IR = infrared, vis. = visible, UV = ultraviolet, VUV = vacuum ultraviolet, and EUV = extreme ultraviolet. The top graph shows the linear absorption coefficient μ for different material types [9].

shows a complex dependence on the photon energy since it is determined by the valence and bonding environment of the atoms, in the x-ray regime this dependence is much more straight-forward since inner-shell isolated-atom response is dominant.

1.3 X-Ray Light Sources

Progress in x-ray physics has been tightly coupled to the advancement of light sources. Since the discovery of x rays in 1895, the average brightness of x-ray sources has been increasing steadily over three orders of magnitude every ten years. The brightness B is defined as the number of photons N divided by the product of the beam area A, the divergence ϵ, the pulse length τ, and the fractional bandwidth of energy $\Delta E/E$,

$$B = \frac{N}{A\epsilon\tau\frac{\Delta E}{E}} \,. \tag{1.3}$$

The divergence is the opening solid angle of the radiation beam. A typical unit for the brightness is number of photons/(s mm^2 mrad^2 0.1% bandwidth).

We will now give an overview of the various x-ray sources and their output characteristics. Specifically, *short*-pulse x-ray sources that are required for time-resolved studies are described in more detail in Section 6.2.1.

1.3.1 X-Ray Tubes

X-ray tubes are the oldest kind of laboratory x-ray source. In an x-ray tube, electrons are extracted from a cathode and then accelerated toward an anode in vacuum by applying a voltage ranging from a few to 100 kV. Typical cathode and anode materials are aluminum and platinum, respectively. When the electrons hit the anode, x rays are generated. A special kind of x-ray tube is the Crookes tube, in which the number of x rays is increased by replacing the vacuum environment with a dilute gas. In the gas, additional secondary electrons are generated through electron impact ionization and accelerated toward the anode, leading to the emission of a larger number of x rays. The anode is angled to make it easier for the x rays to escape. It is often desirable to make the electron beam as small as possible to create an x-ray point source, but then heating is a concern and the anode needs to be cooled since the x-ray power is limited by heat dissipation from the focal spot on the anode. This limit can be substantially improved by rotating the anode, and letting the electron beam sweep over it. A schematic of this rotating-anode x-ray source is shown in Figure 1.4. This setup requires an anode made out of high-temperature materials, and cooling of the anode in vacuum, which is a challenging task.

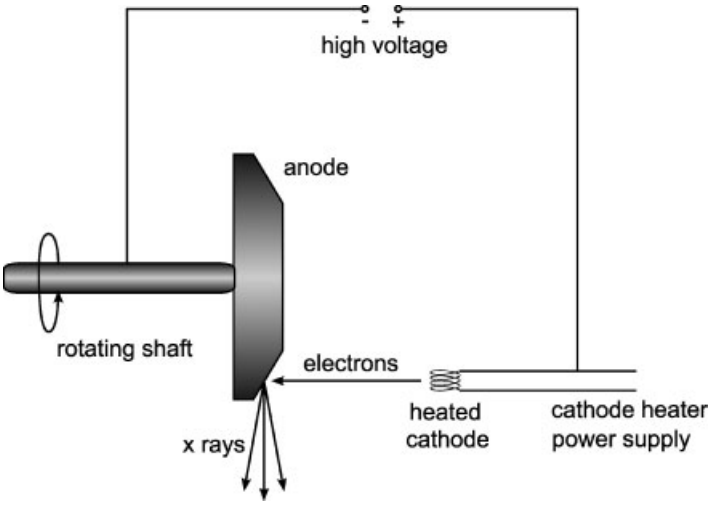

Figure 1.4 Schematic of a rotating-anode x-ray source.

1.3.2
Laser-Produced X-Ray Sources

By irradiating solid and gas targets with high-power optical lasers, high-energy density plasmas are generated that emit photon radiation in the x-ray regime. As shown in Table 1.2, various methods have been proposed to use this radiation as x-ray sources, which we will summarize now. For more details, the reader is referred to [10].

Two very large laser facilities are currently being constructed, the National Ignition Facility (NIF) at Lawrence Livermore National Laboratory (LLNL) in the USA, and the Laser Megajoule (LMJ) at the Commissariat a l'Energy Atomique (CEA) in France. These lasers produce visible-light pulses with energies of more than 1 MJ. Focusing them onto a high-Z target leads to the creation of a hot plasma with electron temperatures of several keV. These electrons emit x rays as line radiation (characteristic x rays) and in the continuum through bremsstrahlung.

More readily accessible are table-top solid-state lasers with TW (10^{12} W) pulse powers, which can reach PW (10^{15} W) power in larger-scale facilities. Ti-doped sapphire lasers with a wavelength around 806 nm are commonly used. These lasers can produce visible-light pulses with a pulse energy of up to 1 J that are only a few wave cycles in duration. Large pulse intensities of 10^{17}–10^{21} W/cm^2 can be achieved using the technique of chirped-pulse amplification (CPA), where short optical pulses are dispersively stretched, amplified, and then compressed again [11], coupled with techniques for diffraction-limited focusing. When matter is irradiated with such laser light, electrons in the material quiver (oscillate) with quiver energies of up to 1 MeV, which is comparable to the rest mass of an electron. When these electrons hit a target, line emission by inner-shell ionization and continuous hard-

Table 1.2 Some laser-produced x-ray sources.

Name	Photon regime	Pulse length	Coherence
High-harmonic-generation (HHG) x-ray sources	up to 1 keV	ultrafast	coherent
MJ-class laser-produced plasmas	up to tens of keV	ns	incoherent
PW-class laser-produced plasmas	up to MeV	ns	incoherent
X-ray lasers	hard x rays	ultrafast	coherent
Laser-wake acceleration techniques	up to GeV		incoherent
Inverse-Compton sources	hard x rays	ultrafast	incoherent

bremsstrahlung occur. The source size of this radiation is relatively large due to the large interaction volume of the relativistic electrons with matter.

In laser-wake acceleration techniques, a visible light pulse shorter than 1 ps and with intensities larger than 10^{18} W/cm^2 propagates through a plasma. Since electrons tend to leave volume with a high electromagnetic field (this is called the ponderomotive effect), electrons are ejected from the wake of the laser pulse, thereby exciting a plasma wave that is transverse to the laser pulse direction. For plasma waves with a sufficiently large amplitude, electrons can be accelerated to very high energies. Upon further interaction with matter, these electrons induce the emission of x rays.

Inverse-Compton sources are compact x-ray sources that emit relatively monochromatic x-ray pulses. In these sources, electron and laser beams intersect. Utilizing the effect of linear inverse Compton scattering, in which photons are scattered from electrons with a kinetic energy that is larger than the photon energy, energy is transferred from the electron to the photon, leading to tunable, short x-ray pulses.

Various other methods for producing x rays with high-intensity lasers exist, including the technique of high-harmonic generation that is described in more detail in Section 6.2.1.1 on short-pulse x-ray sources.

1.3.3 X-Ray Lasers

In a laser, light is amplified through stimulated emission [12]. Typically, a laser requires a medium that is inverted, which means that the population of the excited state exceeds the ground-state population [13], so that light propagating through the medium gains intensity. It becomes increasingly difficult to build lasers at larger photon energies since the lifetime τ of the excited states decreases roughly with the square of the wavelength λ [14],

$$\tau\,[\mathrm{fs}] \approx \lambda^2\,[\mathrm{Å}^2]\,. \tag{1.4}$$

Therefore, at shorter wavelengths, significantly more pump energy is needed in order to establish a population inversion. Since traditional solid and gaseous gain media are often inadequate, it has been proposed to use a very high-energy electron beam in an undulator, leading to the free-electron laser described in Section 6.2.1.7, or to use a plasma instead. The plasma state can be obtained with optical lasers or optical discharges. In these kinds of lasers, a transient population inversion is created by collisional excitation of the pumped plasma of carefully selected atomic systems, which may lead to the amplification of spontaneous emission. Soft x-ray lasers were demonstrated first in 1985 [15, 16]. Transitions in x-ray plasma lasers are typically between excited states of highly charged ions to achieve short wavelengths, such as Ta^{45+} for 4.5-nm light. The first hard x-ray lasers with a plasma medium were pumped using nuclear explosions, see below.

Since low-loss laser resonator cavities are difficult to build due to the lack of efficient normal-incidence x-ray mirrors, it has been suggested to operate x-ray lasers as single-pass devices in an amplified spontaneous emission mode (ASE) without mirrors, assuming that the gain of the medium is sufficiently large. In this scheme, the x-ray pulse is simply amplified by stimulated emission when propagating through the population-inverted material once [17]. The worse spatial and temporal coherence associated with this approach can be offset by using injection seeding with a suitable narrow-band seed source.[2)]

As an extreme measure for creating materials with a population inversion suitable for x-ray lasing, it has been proposed to use the extremely intense x-ray flashes produced by nuclear explosions [14, 19, 20]. A nuclear explosion is an exothermic, self-sustaining chain reaction based on nuclear fission, that is the splitting of atomic nuclei. Nuclear fission leads to the isotropic emission of neutrons and x rays. Such a laser was a candidate component for the US Strategic Defense Initiative (SDI), and details remain classified. Robinson wrote that LLNL had demonstrated a laser device pumped by x rays from a small nuclear detonation [21].

1.3.4 Z-Pinch

We now consider a plasma in the shape of a cylinder and an electric current running parallel to the cylinder axis. The electric current generates a magnetic field that squeezes or pinches the plasma due to the Lorentz force, leading to its collapse. This effect is called a Z-pinch, named after the propagation direction of the current in the z direction. In general, Z-pinches are unstable dynamical systems since the plasma tends to twist and wriggle before breaking up. One of the most

2) The *coherence* is a measure for the correlation of the electric field at different points in space and time. A sinusoidal wave that exists everywhere in space is perfectly coherent since if the electric field is known at a certain location and time, it is known everywhere for all times. In practice, waves are only partially coherent, i.e., coherence exists only over a limited distance or for a limited time duration. Typically, coherence is divided into temporal or longitudinal coherence, which means coherence in the direction of the wavefront propagation, and spatial or lateral coherence, which means coherence in the plane of the wavefront [18].

important applications of Z-pinches is providing a source of x rays and neutrons. The emitted photon spectrum typically consists of 100 to 1000-eV continuum radiation, and in addition some characteristic K-α line radiation of several keV. The actual power output and spectral intensity distribution depend on the current in the plasma and its rise time, and is difficult to estimate since the dynamics of Z-pinches is not perfectly understood. The broad spectral range is often useful for x-ray lithography, spectroscopy, and microscopy.

Z-pinches are commonly implemented as metallic wire arrays, called a liner, driven by high-power current pulses. One of the largest implementations is the Z machine at Sandia National Laboratory. At that facility, a very powerful discharge with a current of tens of MA and a duration of less than 100 ns is fired into an array of metallic wires. The large current transforms the wires into a high-temperature plasma and induces the powerful magnetic field that leads to the Z-pinch. Using steel wires, a temperature of 3.7 GK has been achieved [22]. The emitted powerful x-ray pulse has an integrated pulse energy of 2.7 MJ and a duration of 5 ns.

1.3.5 Novel X-Ray Source Capabilities

Nowadays, a variety of other x-ray sources exist. For many applications, a large *peak* instead of *average* brightness is desirable. Figure 1.5 shows the evolution of the peak brightness of x-ray sources. Most large-scale x-ray sources require an electron accelerator and an undulator, and the performance is determined primarily by the accelerator technology. Such large-scale x-ray sources include storage rings, energy-recovery linear accelerators, and free-electron lasers and are described in more detail in Section 6.2.1.

Even though x-ray free-electron lasers are just starting to become available, plans are already being made to improve on these sources. Of particular interest is the

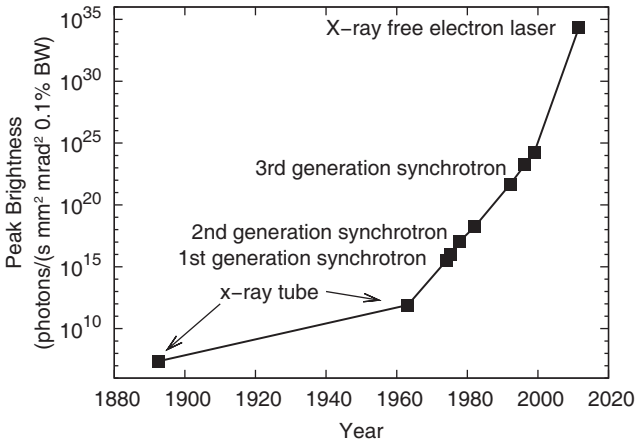

Figure 1.5 Typical peak brightness for some x-ray light sources (BW = band width).

control of the time structure of the x-ray pulses, which includes the creation of attosecond pulses for improved temporal resolution, Fourier-transform-limited pulses of a few fs to sub-fs (see Section 6.1.3), the control of the temporal pulse shape in amplitude and phase, and the improved synchronization with conventional lasers [23]. Short pulses are needed for various applications, including studies of chemical reactions, nonthermal melting, the dynamics of phase transitions, and flash imaging.

There is also a need for full transverse coherence for real-space imaging, diffraction imaging, and photon-correlation spectroscopy. Some of the x-ray sources, such as free-electron lasers, already provide lateral coherence, and there is a need to develop optical systems that preserve the coherence. Nowadays, a large peak brightness can be achieved, and the next improvement will be a large *average* brightness, as well. This will probably be made possible by increasing the repetition rate of the photon pulses. In addition, tunability, polarization control, and a larger range of photon energies will be required.

1.4 Fundamental Models to Describe X-Ray–Matter Interaction

Multiple basic theories are available to describe x-ray radiation and its interaction with matter, including classical electromagnetic theory, semiclassical theory, and quantum electrodynamics (QED). We will first discuss the classical treatment, in which both the particles and the electromagnetic field are treated classically. We will then discuss how this classical treatment relates to the more exact but also more complex quantum treatments. In the semiclassical theory, the particles are treated quantum mechanically, while the electromagnetic field is still treated classically. Finally, quantum electrodynamics is the most exact treatment in which both particles and electromagnetic field are treated quantum mechanically.

1.4.1 Maxwell Equations

In the classical picture, the equations governing electromagnetic phenomena in vacuum in the presence of charges and electric currents are the Maxwell equations, which in differential form are given by

$$\nabla \cdot \boldsymbol{E} = \frac{\rho}{\epsilon_0} \,, \tag{1.5}$$

$$\nabla \cdot \boldsymbol{B} = 0 \,, \tag{1.6}$$

$$\nabla \times \boldsymbol{E} = -\frac{\partial \boldsymbol{B}}{\partial t} \,, \tag{1.7}$$

$$\nabla \times \boldsymbol{B} = \mu_0 \boldsymbol{J} + \mu_0 \epsilon_0 \frac{\partial \boldsymbol{E}}{\partial t} \,. \tag{1.8}$$

$\boldsymbol{E}$ is the electric field vector, $\boldsymbol{B}$ is the magnetic field vector, ρ is the electric charge density, t is the time, $\mu_0 = 4\pi \times 10^{-7}\,\mathrm{N\,A^{-2}}$ is the permeability of free space, $\epsilon_0 \approx 8.854\,187\,817 \times 10^{-12}\,\mathrm{A^2\,s^4\,kg^{-1}\,m^{-3}}$ is the permittivity of free space, $\nabla\cdot$ is the divergence operator, and $\nabla\times$ is the curl operator. The force on a particle with charge q and velocity $\boldsymbol{v}$ is given by the Lorentz force equation,

$$\boldsymbol{F} = q\,(\boldsymbol{E} + \boldsymbol{v} \times \boldsymbol{B})\,. \tag{1.9}$$

We can derive a continuity equation for the electric charge from the Maxwell equations by inserting the time derivative of (1.5) into the divergence of (1.8),

$$\nabla \cdot \nabla \times \boldsymbol{B} = \mu_0 \nabla \cdot \boldsymbol{J} + \mu_0 \epsilon_0 \frac{\partial \nabla \cdot \boldsymbol{E}}{\partial t} \tag{1.10}$$

$$= \mu_0 \nabla \cdot \boldsymbol{J} + \mu_0 \frac{\partial \rho}{\partial t}\,. \tag{1.11}$$

Since the divergence of a curl is zero, we obtain the continuity equation

$$\nabla \cdot \boldsymbol{J} = -\frac{\partial \rho}{\partial t}\,. \tag{1.12}$$

It is often convenient to introduce the scalar potential Φ and the vector potential $\boldsymbol{A}$. Since $\nabla \cdot \boldsymbol{B} = 0$, we can always find a vector function $\boldsymbol{A}(\boldsymbol{r}, t)$ such that

$$\boldsymbol{B} = \nabla \times \boldsymbol{A}\,, \tag{1.13}$$

and then (1.7) can be rewritten as

$$\nabla \times \left(\boldsymbol{E} + \frac{\partial \boldsymbol{A}}{\partial t} \right) = 0\,. \tag{1.14}$$

Therefore, there exists a scalar function $\Phi(\boldsymbol{r}, t)$ such that

$$\boldsymbol{E} = -\nabla \Phi - \frac{\partial \boldsymbol{A}}{\partial t}\,. \tag{1.15}$$

The Maxwell equations then reduce to

$$\nabla^2 \Phi + \frac{\partial}{\partial t}\,(\nabla \cdot \boldsymbol{A}) = -\frac{\rho}{\epsilon_0}\,, \tag{1.16}$$

$$\nabla^2 \boldsymbol{A} - \frac{1}{c^2}\frac{\partial^2 \boldsymbol{A}}{\partial t^2} - \nabla \left(\nabla \cdot \boldsymbol{A} + \frac{1}{c^2}\frac{\partial \Phi}{\partial t} \right) = -\mu_0 \boldsymbol{J}\,, \tag{1.17}$$

with $c^2 = 1/\mu_0\epsilon_0$. The Lorentz force equation (1.9) can then be rewritten as

$$\boldsymbol{F} = q \left[-\nabla \Phi - \frac{\partial}{\partial t}\boldsymbol{A} + \boldsymbol{v} \times (\nabla \times \boldsymbol{A}) \right]. \tag{1.18}$$

The fields $\boldsymbol{E}$ and $\boldsymbol{B}$ remain unchanged under the gauge transformation

$$\boldsymbol{A} \to \boldsymbol{A} + \nabla \Lambda \quad \text{and} \tag{1.19}$$

$$\Phi \to \Phi - \frac{\partial \Lambda}{\partial t}\,, \tag{1.20}$$

where Λ is a scalar function of $\boldsymbol{r}$ and t. A useful gauge that we will use in this book is the radiation gauge for which

$$\nabla \cdot \boldsymbol{A} = 0 \quad \text{and} \tag{1.21}$$

$$\nabla^2 \Phi = -\frac{\rho}{\epsilon_0} \,. \tag{1.22}$$

In the absence of charges, $\rho = 0$. In that case we can choose $\Phi = 0$.

In macroscopic media, the Maxwell equations in differential form are given by

$$\nabla \cdot \boldsymbol{D} = \rho \,, \tag{1.23}$$

$$\nabla \cdot \boldsymbol{B} = 0 \,, \tag{1.24}$$

$$\nabla \times \boldsymbol{E} = -\frac{\partial \boldsymbol{B}}{\partial t} \,, \tag{1.25}$$

$$\nabla \times \boldsymbol{H} = \boldsymbol{J} + \frac{\partial \boldsymbol{D}}{\partial t} \,. \tag{1.26}$$

Here $\boldsymbol{D}$ is the electric displacement field, and $\boldsymbol{H}$ is the magnetizing field.

Using Stokes's and Gauss's theorem,[3] the Maxwell equations in differential form for macroscopic media, (1.23)–(1.26), can be rewritten in integral form as

$$\int_{S_1} \boldsymbol{D} \cdot d\boldsymbol{A}_1 = \int_{V_1} \rho \, dV_1 \,, \tag{1.29}$$

$$\int_{S_1} \boldsymbol{B} \cdot d\boldsymbol{A}_1 = 0 \,, \tag{1.30}$$

$$\oint_{C_2} \boldsymbol{E} \cdot d\boldsymbol{l}_2 = -\int_{S_2} \frac{\partial \boldsymbol{B}}{\partial t} \cdot d\boldsymbol{A}_2 \,, \tag{1.31}$$

$$\oint_{C_2} \boldsymbol{H} \cdot d\boldsymbol{l}_2 = \int_{S_2} \left(\boldsymbol{J} + \frac{\partial \boldsymbol{D}}{\partial t} \right) \cdot d\boldsymbol{A}_2 \,. \tag{1.32}$$

V_1 is a finite volume in space with the closed surface S_1, and $d\boldsymbol{A}_1 = \boldsymbol{n}_1 dA_1$. dA_1 is an area element on the surface and $\boldsymbol{n}_1$ a unit vector normal to the surface pointing outward from the enclosed volume, see Figure 1.6a. As shown in Figure 1.6b, S_2 is an open surface with the closed boundary C_2, $d\boldsymbol{l}_2$ is a line element on the contour, and $d\boldsymbol{A}_2 = \boldsymbol{n}_2 dA_2$ is an area element on the surface. $\boldsymbol{n}_2$ is a unit normal pointing in the direction given by the right-hand rule from the sense of integration around the contour.

3) Stokes's theorem, often also referred to as the curl theorem, relates the surface integral of a vector field $\boldsymbol{F}$ over a surface S to the line integral of the vector field over its boundary C,

$$\int_S \nabla \times \boldsymbol{F} \cdot d\boldsymbol{A} = \oint_C \boldsymbol{F} \cdot d\boldsymbol{l} \,. \tag{1.27}$$

Gauss's theorem, often also referred to as the divergence theorem, relates the volume integral of a divergence of a vector field $\boldsymbol{F}$ over a volume V to the surface integral of $\boldsymbol{F}$ over the surface S of V,

$$\int_V \nabla \cdot \boldsymbol{F} \, dV = \int_S \boldsymbol{F} \cdot d\boldsymbol{A}. \tag{1.28}$$

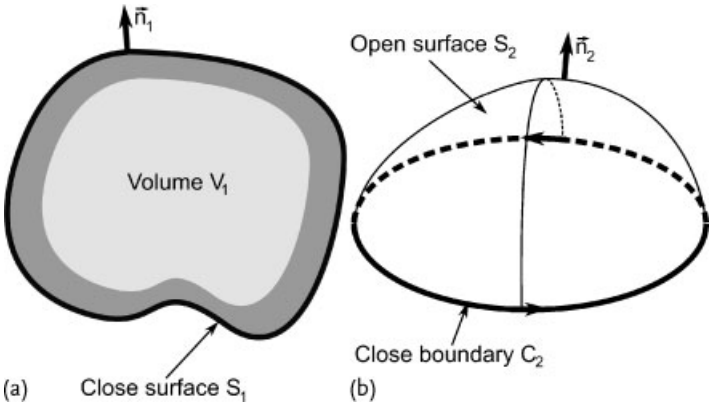

Figure 1.6 Geometry for (a) Stokes's and (b) Gauss's theorem.

The Maxwell equations together with the Lorentz force equation provide the foundation for classical electrodynamics and classical optics. There are, however, cases when this set of equations fails to describe observations, as we will discuss next.

1.4.2 Relation of Maxwell Equations to Quantum Electrodynamics and the Semiclassical Treatment

The *photoelectric effect* demonstrates that the electromagnetic field is quantized: When light falls onto a metal surface, electrons are only emitted if the frequency of the light is larger than a certain threshold value. The number of emitted electrons is proportional to the light intensity, whereas the average kinetic energy of the electrons is independent of it. Einstein invoked a simple quantum picture in 1905 to interpret these findings [24]. He proposed that electrons are bound in a quantum well with a minimum energy E_0, that light consists of discrete particles (*photons*) of energy $\hbar\omega$ and frequency ω, and that absorption only occurs when $\hbar\omega > E_0$. The intensity of the light in this picture is proportional to the photon flux.

A full description of this phenomenon requires quantum mechanics and quantum electrodynamics, which is also able to describe very high intensity effects such as multiphoton absorption. QED provides the ultimate description of light as single photons, which involves a quantization of the electromagnetic field [25]. In many cases, however, a semiclassical description is sufficient. In the semiclassical approach, particles are treated quantum mechanically, but the electromagnetic field is not quantized and is treated as an external perturbation instead.

Classical electromagnetic theory has had great success in describing a large variety of optical phenomena, including electromagnetic wave propagation and interference and diffraction phenomena [26]. Semiclassical treatments can explain phenomena such as photoelectric bunching, which means that photoelectric emis-

sion is more likely to occur close together than far apart in time, and photoelectric counting statistics [27]. In certain cases, internal contradictions of the semiclassical treatment are revealed, and the electromagnetic field needs to be quantized also. For example, the concept of an absolute phase of an oscillatory field becomes meaningless when only a few photons are involved [27]. Also the fluctuations of the electric field strength are infinite in vacuum, which means that the field strength is completely uncertain [28].

In Section 2.2.1.1 we describe the quantization of the electromagnetic field in free space by introducing a Fourier decomposition of the vector potential $\boldsymbol{A}$ in the radiation gauge. This is a Fourier expansion in terms of transversal plane wave modes, characterized by a wave vector $\boldsymbol{k}$ and angular frequency $\omega_{\boldsymbol{k}} = ck$. The energy of each mode can be written like a harmonic oscillator. In a quantum-mechanical treatment, this leads to a quantization, which means that the spectrum of eigenvalues is discrete, given by $\hbar\omega_{\boldsymbol{k}}(n_{\boldsymbol{k}} + 1/2)$ with $n_{\boldsymbol{k}} = 0, 1, \ldots$ Discrete quanta or excitations of the electromagnetic field are known as *photons*. $n_{\boldsymbol{k}}$ is the number of photons belonging to mode $\boldsymbol{k}$ (and polarization s). In classical electromagnetic theory, the linear momentum $\boldsymbol{P}$ of the field is proportional to the volume integral of the Poynting vector,

$$\boldsymbol{P}(t) = \epsilon_0 \int \boldsymbol{E}(\boldsymbol{r}, t) \times \boldsymbol{B}(\boldsymbol{r}, t) d^3\boldsymbol{r} \,, \tag{1.33}$$

whereas in QED the linear momentum of a photon in mode $\boldsymbol{k}$ of polarization s is $\hbar\boldsymbol{k}$. A photon is associated with a plane wave and is therefore not localized. A more localized wavepacket can be created through superposition, but then $\boldsymbol{k}$ is spread out. Note that the zero point energy of a quantum-mechanical harmonic oscillator causes problems: A major difficulty in QED that has never been resolved satisfactorily is that the zero field contribution $\hbar\omega/2$, summed over all modes, is infinite.

The question remains as to why classical electrodynamics works so well. In general, a classical description is only sufficient when noncommutivity of dynamical variables is not important, which is the case for large occupation numbers. In the case of the electromagnetic field, the number of photons per λ^3, sometimes called the degeneracy parameter, has to be much greater than 1. This is typically the case only for lasers [28, 29]. For example, the occupation operator of photon modes does not commute with $\boldsymbol{A}$, $\boldsymbol{E}$, and $\boldsymbol{B}$, so that any pair cannot be determined with arbitrary degree of accuracy. This explains why in vacuum, where the occupation operator is by definition exactly zero, the field fluctuations are arbitrarily large. It turns out, however, that classical optics is very often sufficient even for small photon numbers since we mainly deal with light intensities and phase *differences*, and not absolute phases [27].

1.5
Introduction to X-Ray–Matter Interaction Processes

Macroscopically, the propagation of x rays in matter can be treated using Maxwell's equations. In this approach, the x-ray absorption is described by the dielectric function. We will now consider the microscopic processes underlying the interaction of x rays with matter, and discuss the effects on the material properties. When x rays irradiate a material, the photons are either absorbed or scattered. Photoabsorption is often the most likely process to occur and involves the emission of a photoelectron. This high-energy electron then propagates in the material and interacts with other atoms, leading to the emission of secondary electrons. Eventually, the kinetic energy of the electrons becomes so small that they cannot excite atoms any further. On a similar time scale, electrons and ions begin to equilibrate, followed by various materials processes, including melting, ablation, and spallation. We will now give an overview of these processes. A much more thorough treatment is the subject of the remaining chapters in this monograph.

1.5.1
Atomic and Electronic X-Ray–Matter Interaction Processes

When x rays irradiate matter, they interact primarily with the electrons in the material. Photons can be absorbed and disappear from the system, or they can be scattered, which means that they change their direction and possibly their energy. For frequencies close to atomic resonances, atoms may also be excited. Absorption occurs mostly through photoionization, leading to the ejection of an electron from the ion. This process is sketched in the top left part of Figure 1.7. X-ray photons interact primarily with the firmly bound inner-shell electrons of the atoms. For moderate x-ray intensities, photoionization occurs only for photons above a certain threshold energy, independent of their intensity [24]. The released photoelectrons pick up the difference between the photon energy and the electron binding energy as kinetic energy to ensure energy conservation. Recently, nonlinearities have been observed in the photoionization process at very high intensities [30].

Photon scattering can be either an elastic or an inelastic process. Elastic scattering, for which the photon energy does not change, is also called Rayleigh scattering. Strictly speaking, elastic scattering is an idealized concept since energy and momentum can only be conserved when the scatterer has an infinitely large mass. This situation is most closely realized for atomically bound electrons since then the massive atomic nucleus can balance the change in momentum of the photon without requiring a large energy change. For free electrons, only lower-energy photons have a sufficiently small momentum for quasi-elastic scattering. In inelastic scattering, the energy of the photon changes. Inelastic scattering off free electrons is called Compton scattering. Considering the momentum and energy of the photon, a conservation balance shows that the scattered photon is downshifted in energy, see (3.10) and (10.11). As described in Section 3.1.2, the scattering cross section for

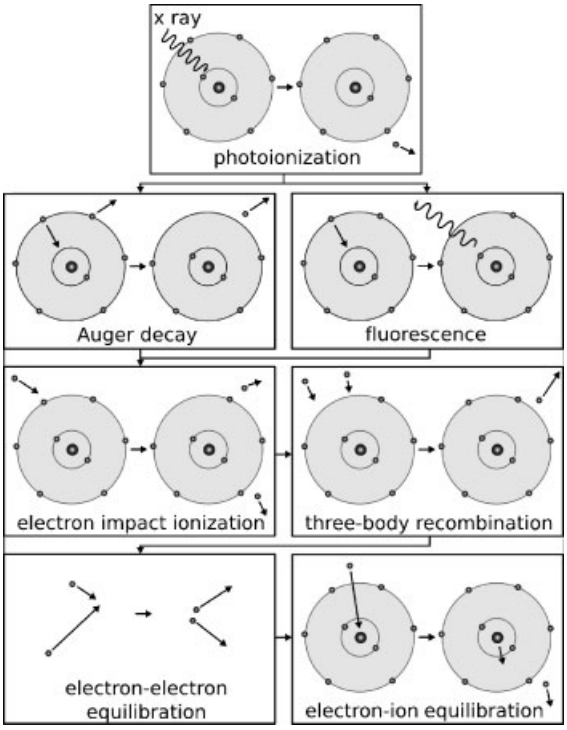

Figure 1.7 X-ray, electronic, and atomic processes when materials are exposed to x-ray radiation. Reprinted with permission from [31].

Compton scattering from free electrons is given by the Klein–Nishina formula. For photon energies beyond $2m_e c^2 \approx 1.02$ MeV, spontaneous electron–positron pair production can occur, where, m_e is the electron mass, and c is the velocity of light. This is discussed in Section 7.5.1.

Figure 1.8 shows the relative importance of the three dominant energy absorption processes: The photoeffect, inelastic (Compton) scattering, and the pair production process. At low photon energies, photoelectric absorption dominates, at intermediate energies, Compton scattering is prevalent, and at large energies of more than 1.02 MeV, primarily pair production occurs. Figure 1.7 shows the x-ray, electronic, and atomic processes that are relevant for x-ray–matter interaction at moderate x-ray energies. Most x rays are absorbed by inner-shell electrons, creating excited atoms. For example, 10-keV x-ray photons lead to the ejection of photoelectrons with a kinetic energy of several keV. The atom then relaxes through fluorescence or auto ionization, such as Auger decay, with the emission of another electron with an energy of several hundred eV. For lighter atoms, Auger decay dominates over fluorescence, as discussed in Section 2.2.2. Both Auger- and photoelectrons interact with other atoms in the material through electron impact ionization. The ejected secondary electrons have kinetic energies of typically a few to tens of eV. Each x-ray absorption step leads to a cascade of ionization events. When

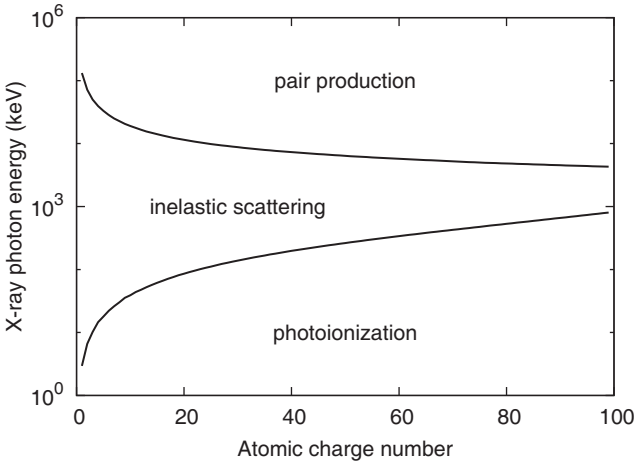

Figure 1.8 Dominant interaction processes of x rays with atoms as a function of atomic charge number and photon energy [5, 32].

the electron density becomes sufficiently high and the electron temperature is low, electrons start to recombine through three-body recombination. At the same time, electrons equilibrate among themselves. On a somewhat longer time scale, electron–ion equilibration occurs.

1.5.2 Energy and Time Scales

Figure 1.9 shows characteristic time scales and energies of the processes occurring in materials irradiated by short x-ray pulses. Within tens of fs, the relatively high photon energy is transferred to a photoelectron and then distributed over multiple secondary electrons in a cascade process [33]. The intensity and duration of the x-ray pulse determine the temperature and density of the quasi-free electron gas. The electron dynamics, characterized in large part by the electrons' inelastic mean free path, determine the evolution of the material.

For short pulses, such as generated by x-ray free-electron lasers, energy transport is usually insignificant during the pulse, and the absorbed x-ray dose roughly corresponds to the energy density in the material. For relatively large x-ray doses in excess of 1 eV/atom, the irradiated material turns into a plasma. Between approximately 1 and 50 eV/atom, the plasma is warm and dense, and beyond about 50 eV/atom, the plasma is hot. On a time scale of 1 ps $= 10^{-12}$ s, the hot electrons equilibrate with the cold ions. For high x-ray doses, this leads to a thermalized plasma, whereas for low x-ray doses around 1 eV/atom or less, the material can undergo thermal melting on a time scale of 1–10 ps. Then ablation can occur, which is the removal of material from the surface. Since ablation requires the motion of large amounts of masses, it proceeds on a significantly longer time scale. Even if the x-ray dose is too low for thermal melting, it can still generate large temperature

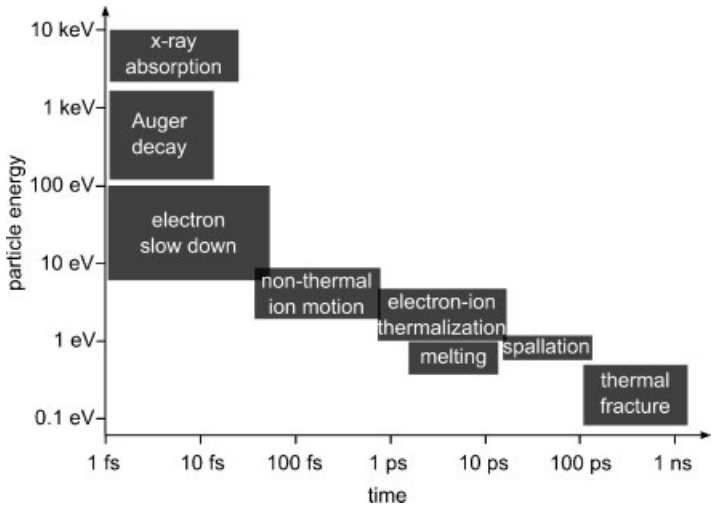

Figure 1.9 Characteristic time scales and energies in short-pulse x-ray–matter interaction for a low-*Z* material irradiated by a 10-keV x-ray pulse of 70-fs duration. Reprinted with permission from [31].

gradients, which will induce a pressure wave. When this pressure wave is reflected from the free surface of the material, large tensile stresses are generated, which, in turn, can lead to spallation (internal rupture followed by ejection). Spallation occurs on a time scale of 10–100 ps. If the x-ray dose induces tensile pressures that are too low for spallation, the material may still undergo thermal fracture on a time scale of 100 ps to 1 ns. Thermal melting, ablation, and spallation are discussed in more detail in Sections 8.3.1, 8.4, and 8.6, respectively.

At around 1 eV/atom, the number of dislodged electrons may be so large that the energy structure holding the atoms in place is significantly perturbed, leading to an ultrafast order–disorder transformation on the time scale of hundreds of fs. This process is also called nonthermal melting and is discussed in Section 8.5.1.

During the time the electrons interact with the material, heat conduction is taking place. Various channels exist for extracting heat from the x-ray interaction zone, ranging from quasi-ballistic fast-electron transport over thermal-electron heat conduction to atomic-(phonon)-heat conduction. Not all these processes may be operational, and the relevance of heat extraction from the interaction zone depends also on the size of the sample and the characteristics of the x-ray beam. Electron transport is treated in Chapter 5.

1.5.3 Length Scales

Multiple length scales are relevant for characterizing the energy deposition through x rays in matter. As a clarifying example, we will analyze the case of a 10-keV x-ray beam irradiating a semi-infinite solid. We denote the grazing angle of incidence

by θ, so that $\theta = 90°$ corresponds to normal incidence. This example is directly relevant for grazing-incidence x-ray optics. The penetration depth d_x of the x rays depends on the angle of incidence, the x-ray wavelength λ, and the optical properties of the material through (4.47). Figure 1.10 shows d_x as a function of the atomic charge number Z for different angles of incidence. Overlaid on these curves in gray is the range d_e of the photoelectrons that are created by the 10-keV x-rays. When an electron penetrates a solid, it gets scattered and deposits its energy in a plume-like volume. The electron range is the straight-line penetration distance in a solid and is approximately [34]

$$d_e \approx 0.07 \frac{E_e^{1.66}}{\rho} , \tag{1.34}$$

where d_e is given in μm, E_e is the initial electron energy in keV, and ρ is the mass density in g/cm^3. The electron straggle d_{str} is the width of the interaction volume of an electron in a solid perpendicular to the penetration distance. Typically, d_{str} is smaller than d_e.

The interaction volume of an x-ray beam in a material depends strongly on the angle of incidence and the polarization of the incidence x-ray beam due to two effects. First, the relative magnitude of the x-ray penetration depth d_x and the electron range d_e are dependent on the angle of incidence. For normal incidence, $d_x \gg d_e$, whereas for grazing incidence there are multiple materials for which $d_e > d_x$. Secondly, the emission direction of the photoelectrons is in the direction of the electric field vector, which is perpendicular to the direction of the x-ray beam. The different interaction modes are illustrated in Figure 1.11. In this analysis we assume that the pulses are sufficiently short so that we can neglect thermal transport. Since photoelectrons escape from the interaction region of the x rays with

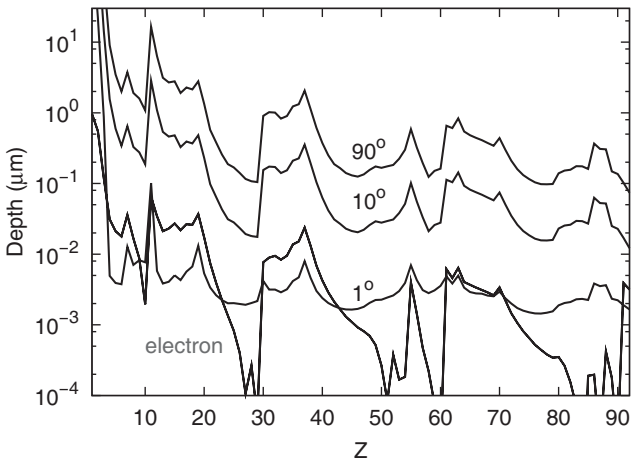

Figure 1.10 Penetration depth of 1-keV x-ray photons in materials of different atomic charge numbers Z for different off-normal angles of incidence. Also shown in gray is the range of the photo electrons.

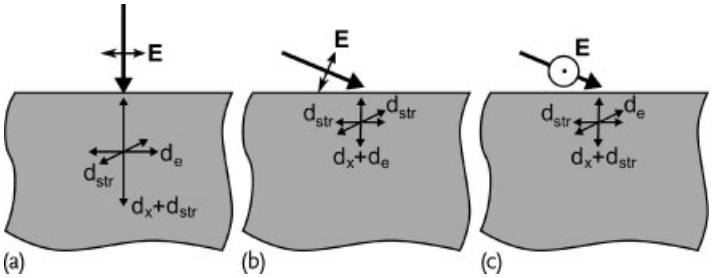

Figure 1.11 Interaction volume of a linearly polarized, small x-ray beam with a semi-infinite sample for normal incidence (a) and grazing incidence (b and c). The sum should be taken as the geometric sum, for example $(d_x^{-1} + d_{str}^{-1})^{-1}$.

the material, this volume will be positively charged. The full excitation volume depends on d_x, the electron range d_e, and the electron straggle d_{str}. To bring out the different effects, we neglect the effect of the beam size and assume that the x-ray beam has a relatively small diameter in comparison with d_e and d_x. For normal incidence, the lateral size of the interaction volume is determined by the electron range and straggle. This effect is washed out for larger-diameter x-ray beams. For grazing incidence radiation, the actual interaction volume is larger than the x-ray penetration depth due to the range or straggle of the photoelectrons, depending on the polarization of the x-ray beam. This effect occurs both for small and large beam diameters.

1.5.4 Size Effects

In structures that are small in comparison to the electron range d_e, a substantial fraction of the electrons escape the sample, leaving a positive charge behind. For high-intensity x-ray pulses, the accumulated charge becomes so large that the electron dynamics is affected by electrostatic forces. As a consequence, electrons with lower kinetic energy are electrostatically trapped. In increasing order of cumulated positive charge, secondary electrons, Auger electrons, and photoelectrons are confined to the sample. Electrostatic charge trapping is strongly dependent on the x-ray pulse characteristics, such as pulse energy and length, as well the detailed sample geometry. It is described in more detail in Section 5.8.

1.6 Databases Relevant to Photon–Matter Interaction

Numerous databases are available that list constants and materials data relevant to x-ray–matter interaction. Most of these databases can conveniently be accessed through the Internet.

The *x-ray data booklet* lists x-ray properties of the elements, describes properties of synchrotron radiation, x-ray optics, and detectors, and discusses x-ray and electron scattering processes. It can be accessed at http://xdb.lbl.gov (last access: 15 May 2011). The *x-ray data booklet* is published by the Center for X-Ray Optics at the Lawrence Berkeley National Laboratory. They also provide access to the *Henke tables* [35] for the atomic scattering factors and other x-ray properties of the elements at http://henke.lbl.gov/optical_constants (last access: 15 May 2011). On this website, one can also find online calculators for the index of refraction, attenuation length, transmission, and reflectivity of compound materials.

The Physics Laboratory of The National Institute of Standards and Technology (NIST) makes several x-ray databases available. The *X-Ray Attenuation and Absorption for Materials of Dosimetric Interest* (XAAMDI) database lists the photon attenuation coefficients for elements with Z from 1 to 92 and some compounds, between 1 keV and 20 MeV. The XAAMDI database is available at http://www.nist.gov/physlab/data/xraycoef/index.cfm. The *Photon Cross Section Database* XCOM provides the photon cross sections for scattering, photoelectric absorption, and pair production between 1 keV and 100 GeV for elements, compounds, and mixtures with $Z \leq 100$, accessible at http://www.nist.gov/physlab/data/xcom/index.cfm (last access: 15 May 2011). Finally, the *X-Ray Form Factor, Attenuation and Scattering Tables* (FFAST) lists atomic form factors, photoelectric attenuation coefficients for atoms and just the K shell for Z ranging from 1 to 92 between 1 eV and 1 MeV. The database [36, 37] can be accessed at http://www.nist.gov/physlab/data/ffast/index.cfm (last access: 15 May 2011).

Lawrence Livermore National Laboratory has assembled multiple databases of photon and electron data. Of particular interest are the *Evaluated Photon Data Library, '97 Version* (EPDL97) [5], the *Evaluated Electron Data Library* (EEDL) [38], and the *Evaluated Atomic Data Library* (EADL) [39]. The EPDL97 database describes the interaction of photons with matter and the production of secondary photons and electrons. It contains data on coherent and incoherent scattering, photoelectric reactions by atom and subshell, pair production reactions, and triplet production reactions for photon energies between 1 eV and 100 GeV. The EEDL database describes the interaction of electrons with matter for Z from 1 to 100 and for electron energies between 10 eV and 100 GeV. It contains information on elastic scattering processes, ionization reactions, Bremsstrahlung, and excitation. The EADL database describes the relaxation of ionized atoms through fluorescence and Auger and Coster–Kronig reactions, and it specifically contains information on transition probabilities. The documentation and the databases can be accessed at http://www-nds.iaea.org/epdl97.

References

1 Röntgen, W.C. (1896) On a new kind of rays. *Nature*, **53**, 274–276.

2 Sayre, D. (1952) Some implications of a theorem due to Shannon. *Acta Crystallogr.*, **5**, 843.

3 Giacconi, R., Gursky, H., Paolini, F.R., and Rossi, B.B. (1962) Evidence for x rays from sources outside the Solar System. *Phys. Rev. Lett.*, **9**, 439–443.

4 Hubbell, J.H. and Seltzer, S.M. (2004) Tables of x-ray mass attenuation coefficients and mass energy-absorption coefficients from 1 keV to 20 MeV for elements $Z = 1$ to 92 and 48 additional substances of dosimetric interest. *Tech. Rep. NISTIR 5632*.

5 Cullen, D.E., Hubbell, J.H., and Kissel, L. (1997) EPDL97: The evaluated photon data library '97 version. *EPDL Tech. Rep. UCRL-50400*.

6 Glenzer, S.H., Gregori, G., Lee, R.W., Rogers, F.J., Pollaine, S.W., and Landen, O.L. (2003) Demonstration of spectrally resolved x-ray scattering in dense plasmas. *Phys. Rev. Lett.*, **90**, 175002.

7 Hau-Riege, S.P., Chapman, H.N., Krzywinski, J., Sobierajski, R., Bajt, S., London, R.A., Bergh, M., Caleman, C., Nietubyc, R., Juha, L., Kuba, J., Spiller, E., Baker, S., Bionta, R., Sokolowski-Tinten, K., Stojanovic, N., Kjornrattanawanich, B., Gullikson, E., Plönjes, E., Toleikis, S., and Tschentscher, R. (2007) Subnanometer-scale measurements of the interaction of ultrafast soft x-ray free-electron-laser pulses with matter. *Phys. Rev. Lett.*, **98**, 145502.

8 Nagler, B., Zastrau, U., Fäustlin, R.R., Vinko, S.M., Whitcher, T., Nelson, A.J., Sobierajski, R., Krzywinski, J., Chalupsky, J., Abreu, E., Bajt, S., Bornath, T., Burian, T., Chapman, H., Cihelka, J., Döppner, T., Düsterer, S., Dzelzainis, T., Fajardo, M., Förster, E., Fortmann, C., Galtier, E., Glenzer, S.H., Göde, S., Gregori, G., Hajkova, V., Heimann, P., Juha, L., Jurek, M., Khattak, F.Y., Khorsand, A.R., Klinger, D., Kozlova, M., Laarmann, T., Lee, H.J., Lee, R.W., Meiwes-Broer, K.-H., Mercere, P., Murphy, W.J., Przystawik, A., Redmer, R., Reinholz, H., Riley, D., Röpke, G., Rosmej, F., Saksl, K., Schott, R., Thiele, R., Tiggesbäumker, J., Toleikis, S., Tschentscher, T., Uschmann, I., Vollmer, H.J., and Wark, J.S. (2009) Turning solid aluminium transparent by intense soft x-ray photoionization. *Nat. Phys.*, **5**, 693–696.

9 Palik, E.D. (1998) *Handbook of Optical Constants of Solids*, Vol. 1–3. Academic Press, San Diego, CA.

10 Hudson, L.T. and Seeley, J.F. (2010) Laser-produced x-ray sources. *Radiat. Phys. Chem.*, **79**, 132–138.

11 Strickland, D. and Mourou, G. (1985) Compression of amplified chirped optical pulses. *Opt. Commun.*, **56**, 219–221.

12 Schawlow, A.L. and Townes, C.H. (1958) Infrared and optical masers. *Phys. Rev.*, **112**, 1940–1949.

13 Svelto, O. (2010) *Principles of Lasers*, 4th edn, Springer.

14 Chapline, G. and Wood, L. (1975) X-ray lasers. *Phys. Today*, **40**, 8.

15 Matthews, D.L., Hagelstein, P.L., Rosen, M.D., Eckart, M.J., Ceglio, N.M., Hazi, A.U., Medecki, H., MacGowan, B.J., Trebes, J.E., Whitten, B.L., Campbell, E.M., Hatcher, C.W., Hawryluk, A.M., Kauffman, R.L., Pleasance, L.D., Rambach, G., Scofield, J.H., Stone, G., and Weaver, T.A. (1985) Demonstration of a soft x-ray amplifier. *Phys. Rev. Lett.*, **54**, 110–113.

16 Rosen, M.D., Hagelstein, P.L., Matthews, D.L., Campbell, E.M., Hazi, A.U., Whitten, B.L., MacGowan, B., Turner, R.E., Lee, R.W., Charatis, G., Busch, G.E., Shepard, C.L., and Rockett, P.D. (1985) Exploding foil-technique for achieving a soft-x-ray laser. *Phys. Rev. Lett.*, **54**, 106–109.

17 Hecht, J. (2008) The history of the x-ray laser. *Opt. Photonics News*, **19**, 26–33.

18 Goodman, J.W. (1996) *Introduction to Fourier Optics*, 2nd edn, McGraw-Hill, New York.

19 Bloembergen, N., Patel, C.K.N., Avizonis, P., Clem, R.G., Hertzberg, A., Johnson, T.H., Marshall, T., Miller, R.B., Morrow, W.E., Salpeter, E.E., Sessler, A.M., Sullivan, J.D., Wyant, J.C., Yariv, A., Zare, R.N., Glass, A.J., Hebel, L.C., Pake, G.E., May, M.M., Panofsky, W.K., Schawlow, A.L., Townes, C.H., and York, H. (1987) Report to The American Physical Society of the study group on science and technology of directed energy weapons. *Rev. Mod. Phys.*, **59**(3), S1–S201.

20 Nilsen, J. (2003) Reminiscing about the early years of the x-ray laser. *Quantum Electron.*, **33**, 1–2.

21 Robinson Jr., C.A. (1981) Advances made on high-energy laser. *Aviat. Week Space Technol.* (23 Feb. 1981), 25–27.

22 Haines, M.G., LePell, P.D., Coverdale, C.A., Jones, B., Deeney, C., and Apruzese, J.P. (2006) Ion viscous heating in a magnetohydrodynamically unstable Z pinch at over 2×10^9 K. *Phys. Rev. Lett.*, **96**, 075003.

23 Bergmann, U., Corlett, J., Dierker, S., Falcone, R., Galayda, J., Gibson, M., Hastings, J., Hettel, B., Hill, J., Hussain, Z., Kao, C.-C., Kirz, J., Long, G., McCurdy, B., Raubenheimer, T., Sannibale. F., Seeman. J., Shen, Z.-X., Shenoy, G., Schoenlein, B., Shen, Q., Stephenson, B., Stöhr, J., and Zholents, A. (2008) Science and technology of future light sources. *DOE Tech. Rep. ANL-08/39, BNL-81895-2008, LBNL-1090E-2009, SLAC-R-917*.

24 Einstein, A. (1905) On a heuristic viewpoint concerning the production and transformation of light. *Ann. Phys.*, **17**, 132–148.

25 Berestetskii, V.B., Pitaevskii, L.P., and Lifshitz, E.M. (1982) *Quantum Electrodynamics*, 2nd edn, Butterworth-Heinemann, Oxford.

26 Jackson, J.D. (1975) *Classical Electrodynamics*, 2nd edn, John Wiley & Sons, New York.

27 Mandel, L. and Wolf, E. (1995) *Optical Coherence and Quantum Optics*. Cambridge University Press, Cambridge.

28 Sakurai, J.J. (1967) *Advanced Quantum Mechanics*, Addison-Wesley, New York.

29 Lengeler, B. (2001) Coherence in x-ray physics. *Naturwissenschaften*, **88**, 249–260.

30 Sorokin, A.A., Bobashev, S.V., Feigl, T., Tiedtke, K., Wabnitz, H., and Richter, M. (2007) Photoelectric effect at ultrahigh intensities. *Phys. Rev. Lett.*, **99**, 213002.

31 London, R.A., Bionta, R.M., Tatchyn, R.O., and Roesler, S. (2001) Computational simulations of high-intensity x-ray matter interaction. *Proc. SPIE*, **4500**, 51–62.

32 Bergstrom Jr., P.M. and Pratt, R.H. (1997) An overview of the theories used in Compton scattering calculations. *Radiat. Phys. Chem.*, **50**, 3–29.

33 Ziaja, B., London, R.A., and Hajdu, J. (2005) Unified model of secondary electron cascades in diamond. *J. Appl. Phys.*, **97**, 064905.

34 Joy, D.C. (1995) *Monte Carlo Modeling for Electron Microscopy and Microanalysis*. Oxford Series in Optical and Imaging Sciences. Oxford University Press, New York.

35 Henke, B.L., Gullikson, E.M., and Davis, J.C. (1993) X-ray interactions: photoabsorption, scattering, transmission, and reflection at $E = 50{-}30\,000$ eV, $Z = 1{-}92$. *Atom. Data Nucl. Data Tables*, **54**, 181–342.

36 Chantler, C.T. (1995) Theoretical form factor, attenuation and scattering tabulation for $Z = 1 - 92$ from $E = 1{-}10$ eV to $E = 0.4{-}1.0$ MeV. *J. Phys. Chem. Ref. Data*, **24**, 71–643.

37 Chantler, C.T. (2000) Detailed tabulation of atomic form factors, photoelectric absorption and scattering cross section, and mass attenuation coefficients in the vicinity of absorption edges in the soft x-ray ($Z = 30{-}36$, $Z = 60{-}89$, $E = 0.1$ keV-10 keV), addressing convergence issues of earlier work. *J. Phys. Chem. Ref. Data*, **29**, 597–1048.

38 Cullen, D.E., Perkins, S.T., and Seltzer, S.M. (1991) Tables and graphs of electron-interaction cross sections from 10 eV to 100 GeV derived from the LLNL evaluated electron data library (EEDL), $Z = 1{-}100$. *LLNL Tech. Rep. UCRL-50400*.

39 Cullen, D.E., Perkins, S.T., and Seltzer, S.M. (1991) Tables and graphs of atomic subshell and relaxation data derived from the LLNL evaluated atomic data library (EADL), $Z = 1{-}100$. *LLNL Tech. Rep. UCRL-50400*.

2
Atomic Physics

X-ray–matter interaction is based on the interaction of radiation with individual atoms since x-ray energies allow access of the inner atomic shells and the wavelengths are on the order of the mean distance between nuclei and electrons. The detailed atomic configuration needs to be considered to understand these dynamics. The interaction may be modified by the environment of the atoms in plasmas, solids, or molecules. In Section 2.1 we summarize the physics describing the states in which atomic systems can be found, and in Section 2.2 we discuss the transitions between these states. Both topics require a quantum-mechanical description.

2.1
Atomic States

We now summarize how quantum mechanics can be used to obtain the detailed configuration of atoms with single and multiple electrons. This can be used to determine the electron density distribution around a nucleus and with that the x-ray scattering properties of atoms, as discussed in Section 3.2. We also outline the structure of the periodic system of the elements since we will consider the trends of x-ray–matter interaction processes as a function of the nuclear charge number throughout this book. In Section 2.1.3.3 we mention the Dirac equation which is needed to understand some high-intensity x-ray-induced processes (see Section 7.5.1). We then simplify the discussion by introducing the hydrogenic model in Section 2.1.6; it is sufficient for our purposes to limit the description of most atomic transition processes in Section 2.2 to this approximation.

We use the coordinate representation of the Schrödinger picture. We consider an atomic system consisting of a nucleus with charge Ze, mass M, coordinate vector $\boldsymbol{R}_n$, and spin coordinate Σ_n, and N electrons, each with charge $-e$, mass m_e, coordinate vector $\boldsymbol{r}_k$, and spin coordinate σ_k. The state of this system is described by a time-dependent wavefunction

$$\Phi\left(\boldsymbol{R}_n, \Sigma_n, \boldsymbol{r}_1, \sigma_1, \ldots, \boldsymbol{r}_N, \sigma_N, t\right) = \Phi\left(\boldsymbol{X}_n, \boldsymbol{x}_1, \ldots, \boldsymbol{x}_N, t\right) \tag{2.1}$$

$$= \Phi\left(\boldsymbol{X}_n, \boldsymbol{X}, t\right) , \tag{2.2}$$

High-Intensity X-rays – Interaction with Matter, First Edition. Stefan P. Hau-Riege.

with $\boldsymbol{X}_n = (\boldsymbol{R}_n, \Sigma_n)$, $\boldsymbol{x}_k = (\boldsymbol{r}_k, \sigma_k)$, and $\boldsymbol{X} = (\boldsymbol{x}_1, \ldots, \boldsymbol{x}_N)$. The time evolution of this state is described by the Schrödinger equation

$$H\Phi\left(\boldsymbol{X}_n, \boldsymbol{X}, t\right) = i\hbar \frac{\partial \Phi\left(\boldsymbol{X}_n, \boldsymbol{X}, t\right)}{\partial t} \,, \tag{2.3}$$

where H is the Hamiltonian of the system. If H does not explicitly depend on time and if $\Psi(\boldsymbol{X}_n, \boldsymbol{X}, t)$ is an eigenfunction of H with eigenvalue E, viz.,

$$H\Psi\left(\boldsymbol{X}_n, \boldsymbol{X}\right) = E\Psi\left(\boldsymbol{X}_n, \boldsymbol{X}\right) \,, \tag{2.4}$$

then the solution of the *time-independent Schrödinger equation* (2.4) is

$$\Phi\left(\boldsymbol{X}_n, \boldsymbol{X}, t\right) = e^{-i\frac{E}{\hbar}t}\Psi\left(\boldsymbol{X}_n, \boldsymbol{X}\right) \,. \tag{2.5}$$

Because H is a Hermitian operator,[1] E is a real number.

2.1.1 Center-of-Mass Motion

We first decouple the center-of-mass (CM) motion of the system. We will ignore the effect of the spin initially but will include it later in the framework of the relativistic Dirac equation. The nonrelativistic Hamiltonian is given by

$$\begin{aligned} H_{full} = & \frac{\boldsymbol{P}_n^2}{2M_n} + \sum_{i=1}^{N}\left(\frac{\boldsymbol{p}_{ei}^2}{2m_e} - \frac{Ze^2}{4\pi\epsilon_0|\boldsymbol{r}_i - \boldsymbol{R}_n|}\right) \\ & + \sum_{i=1}^{N}\sum_{j=i+1}^{N}\frac{e^2}{4\pi\epsilon_0|\boldsymbol{r}_i - \boldsymbol{r}_j|} \,, \end{aligned} \tag{2.6}$$

where $\boldsymbol{P}_n$ and $\boldsymbol{p}_e$ are the momentum operators for the nucleus and electrons, respectively. The CM coordinate is given by

$$\boldsymbol{R} = \frac{M_n\boldsymbol{R}_n + m_e\sum_{i=1}^{N}\boldsymbol{r}_i}{M_n + Nm_e} \,, \tag{2.7}$$

and the relative distance coordinates are given by

$$\tilde{\boldsymbol{r}}_i = \boldsymbol{r}_i - \boldsymbol{R}_n. \tag{2.8}$$

We can then rewrite the full Hamiltonian from (2.6) as

$$H_{full} = H_{CM} + H \,, \quad \text{with} \tag{2.9}$$

$$H_{CM} = \frac{\boldsymbol{P}^2}{2M} + \frac{1}{M_n}\sum_{i=1}^{N}\sum_{j=i+1}^{N}\boldsymbol{p}_i\cdot\boldsymbol{p}_j \,, \tag{2.10}$$

1) A Hermitian operator A is a special operator for which $\int \Psi_m^* A\Psi_n \, dV = (\int \Psi_n^* A\Psi_m \, dV)^*$. The eigenvalues of a Hermitian operator are real. Observable quantities in quantum mechanics are represented by Hermitian operators.

$$H = \sum_{i=1}^{N} \frac{\boldsymbol{p}_i^2}{2\mu} - \sum_{i=1}^{N} \frac{Ze^2}{4\pi\epsilon_0|\tilde{\boldsymbol{r}}_i|} + \sum_{i=1}^{N} \sum_{j=i+1}^{N} \frac{e^2}{4\pi\epsilon_0|\tilde{\boldsymbol{r}}_i - \tilde{\boldsymbol{r}}_j|} \,, \tag{2.11}$$

$$M = M_n + N m_e \,, \tag{2.12}$$

$$\mu = \frac{M_n m_e}{M_n + m_e} \,, \tag{2.13}$$

$$\boldsymbol{P} = \boldsymbol{P}_n + \sum_{i=1}^{N} \boldsymbol{p}_{ei} = -i\hbar\nabla_{\boldsymbol{R}} \,, \quad \text{and} \tag{2.14}$$

$$\boldsymbol{p}_i = \boldsymbol{p}_{ei} - \frac{m_e}{M}\boldsymbol{P} = -i\hbar\nabla_{\tilde{\boldsymbol{r}}_i} \,. \tag{2.15}$$

Assuming $M_n \gg m_e$, we neglect the $\boldsymbol{p}_i \cdot \boldsymbol{p}_j$ mass polarization term in (2.10), and the CM motion is decoupled from the internal motion of the electrons: The eigenfunctions of the CM motion are known, $\Phi_{CM}(\boldsymbol{R}, t) \propto \exp(-i\boldsymbol{K}\cdot\boldsymbol{R} - iE_{CM}t/\hbar)$ with eigenvalues $E_{CM} = \hbar K^2/M$, and we only need to solve an effective N-body Schrödinger equation for the relative motion of the electrons,

$$H\Psi(\tilde{\boldsymbol{r}}_1, \ldots, \tilde{\boldsymbol{r}}_N) = E\Psi(\tilde{\boldsymbol{r}}_1, \ldots, \tilde{\boldsymbol{r}}_N) \,. \tag{2.16}$$

The solution of the Schrödinger equation of the $N + 1$-body system is then given by the product $\Phi_{CM}(\boldsymbol{R}, t)\Phi(\boldsymbol{r})\exp(-iEt/\hbar)$.

2.1.2 Constants of Motion

The mean value of a Hermitian operator A representing an observable of a system in a state described by the wavefunction Φ is given by

$$\overline{A} = \int \Phi^* A \Phi \, dV \,. \tag{2.17}$$

Using the time-dependent Schrödinger equation (2.3), the temporal evolution of $\overline{A}$ is given by

$$\frac{d\overline{A}}{dt} = \int \Phi^* \frac{\partial A}{\partial t}\Phi \, dV + \int \left(\frac{\partial \Phi^*}{\partial t} A\Phi + \Phi^* A \frac{\partial \Phi}{\partial t} \right) dV \tag{2.18}$$

$$= \overline{\frac{\partial A}{\partial t}} + \frac{i}{\hbar}\overline{[H, A]} \,, \tag{2.19}$$

where the commutator is defined by $[H, A] = HA - AH$. If A does not explicitly depend on time, $\partial A/\partial t = 0$, and the expectation value of A is a constant of motion if A commutes with H. For example, the energy of a system that is described by a time-independent Hamiltonian is conserved.

2.1.3 Atoms with a Single Electron

We will now discuss the one-body (hydrogenic) Schrödinger equation and how it relates to the relativistic Dirac equation.

2.1.3.1 One-Body Schrödinger Equation

By separating out the CM motion, the nonrelativistic hydrogenic Hamiltonian can be simplified to

$$H = \frac{\boldsymbol{p}^2}{2\mu} + V(r) \,, \tag{2.20}$$

where $\mu = M_n m_e/(M_n + m_e)$, $\boldsymbol{p}$ is the momentum operator (2.15) for the relative nucleus-electron motion, and $\boldsymbol{r} = \boldsymbol{r}_e - \boldsymbol{R}_n$ is the relative distance coordinate. We then need to solve an effective one-body Schrödinger equation for the relative motion,

$$H\Psi(\boldsymbol{r}) = E\Psi(\boldsymbol{r}) \,. \tag{2.21}$$

2.1.3.2 The Radial Schrödinger Equation

We now consider a two-body system with a potential energy $V(r)$ that depends only on the separation $r = |\boldsymbol{r}|$. In this case, the components of the angular momentum,

$$\boldsymbol{L} = \boldsymbol{r} \times \boldsymbol{p} \tag{2.22}$$

as well as $\boldsymbol{L}^2 = L_x^2 + L_y^2 + L_z^2$ are constants of motion. In general, a physical system is fully described by a complete set of commuting observables, where complete means that there is no other independent observable that commutes with all members of the set. In this case, H, $\boldsymbol{L}^2$ and one component of $\boldsymbol{L}$, for example L_z, form a complete set of observables for the particle.

We can rewrite the Hamiltonian (2.20) as

$$H = \frac{\hbar^2}{2\mu}\left(\frac{\partial^2}{\partial r^2} + \frac{2}{r}\frac{\partial}{\partial r} - \frac{\boldsymbol{L}^2}{r^2\hbar^2}\right) + V(r) \,. \tag{2.23}$$

The eigenvectors of $\boldsymbol{L}^2$ and L_z are the spherical harmonics $Y_{l,m}(\theta, \phi)$,

$$\boldsymbol{L}^2 Y_{l,m}(\theta, \phi) = l(l+1)\hbar^2 Y_{l,m}(\theta, \phi) \,, \quad \text{and} \tag{2.24}$$

$$L_z Y_{l,m}(\theta, \phi) = m\hbar Y_{l,m}(\theta, \phi) \,, \tag{2.25}$$

with the angular momentum quantum number $l = 0, 1, \ldots$ and the azimuthal quantum number $m = -l, -l+1, \ldots, l-1, l$. The solution to the Schrödinger equation (2.21) can then be written as

$$\Psi(\boldsymbol{r}) = R_l(r) Y_{l,m}(\theta, \phi) \,. \tag{2.26}$$

It is convenient to set

$$R_l(r) \equiv \frac{1}{r} u_l(r) \,, \tag{2.27}$$

where $u_l(r)$ satisfies the radial Schrödinger equation

$$H_l u_l(r) \equiv \left[-\frac{\hbar^2}{2m} \frac{d}{dr^2} + V_{eff}(r) \right] u_l(r) = E u_l(r) \,, \quad \text{with} \tag{2.28}$$

$$V_{eff}(r) \equiv \frac{l(l+1)\hbar^2}{2mr^2} + V(r) \,. \tag{2.29}$$

Physically admissible solutions to (2.28) require that $u_l(r) \propto r^{l+1}$ as $r \to 0$, and that $u_l(r)$ be square integrable, that is $\int_0^\infty u_l^2(r) dr$ is finite.

For a general potential energy $V(r)$, the radial Schrödinger equation (2.28) can be solved numerically. For the specific case of a Coulomb potential,

$$V(r) = -\frac{1}{4\pi\epsilon_0} \frac{Ze^2}{r} \,, \tag{2.30}$$

the radial eigenfunctions of the bound states are

$$u_{n,l}(r) = \frac{1}{n} \left[\frac{(n-l-1)!}{a_Z (n+l)!} \right]^{1/2} \left(\frac{2r}{n a_Z} \right)^{l+1} e^{-\frac{r}{n a_Z}} L_{n-l-1}^{2l+1} \left(\frac{2r}{n a_Z} \right) , \tag{2.31}$$

where L_ν^α is the generalized Laguerre polynomial, and a_Z the radius,

$$a_Z \equiv \frac{4\pi\epsilon_0 \hbar^2}{mZe^2} \approx \frac{0.529\,\text{Å}}{Z} \,. \tag{2.32}$$

The radius a_1 for hydrogen is called the Bohr radius and is typically designated a_0. The principal quantum number n is limited to $n = 1, 2, \ldots$, the angular momentum quantum number l is limited to $l = 0, 1, \ldots, n-1$, and $|m| \leq l$. The energy eigenvalues, which are independent of the angular momentum quantum numbers, are

$$E_n = -\frac{\frac{\hbar^2}{2ma_Z^2}}{n^2} \,, \quad \text{with the Rydberg energy} \tag{2.33}$$

$$Ry_Z \equiv \frac{me^4}{8\epsilon_0^2 h^2} = \frac{\hbar^2}{2ma_Z^2} \approx 13.61 Z^2\,\text{eV} \,. \tag{2.34}$$

2.1.3.3 The Schrödinger Equation as the Nonrelativistic Limit of the Dirac Equation

The time-dependent Schrödinger equation is not form-invariant under Lorentz transformation since it is linear in time and quadratic in spatial derivatives. To describe a free electron in a relativistically covariant way, Dirac showed that it is necessary to replace the one-component wavefunction by a four-component spinor,

$$\Phi(\mathbf{r}, t) = \begin{bmatrix} \Phi_1(\mathbf{r}, t) \\ \Phi_2(\mathbf{r}, t) \\ \Phi_3(\mathbf{r}, t) \\ \Phi_4(\mathbf{r}, t) \end{bmatrix} \,. \tag{2.35}$$

The spinor $\Phi(\boldsymbol{r}, t)$ fulfills the covariant *Dirac equation*,

$$i\hbar \frac{\partial \Phi(\boldsymbol{r}, t)}{\partial t} = \left[\frac{\hbar c}{i} \left(\alpha_1 \frac{\partial}{\partial x^1} + \alpha_2 \frac{\partial}{\partial x^2} + \alpha_3 \frac{\partial}{\partial x^3} \right) + \beta m c^2 \right] \Phi(\boldsymbol{r}, t) \,, \tag{2.36}$$

where in standard representation

$$\alpha_i = \begin{pmatrix} 0 & 0 & & \\ 0 & 0 & & \sigma_i \\ & & 0 & 0 \\ & \sigma_i & 0 & 0 \end{pmatrix} \,, \quad \text{and} \tag{2.37}$$

$$\beta = \begin{pmatrix} 1 & 0 & 0 & 0 \\ 0 & 1 & 0 & 0 \\ 0 & 0 & -1 & 0 \\ 0 & 0 & 0 & -1 \end{pmatrix} \,. \tag{2.38}$$

The Pauli matrices are given by

$$\sigma_1 = \begin{pmatrix} 0 & 1 \\ 1 & 0 \end{pmatrix} \,, \quad \sigma_2 = \begin{pmatrix} 0 & -i \\ i & 0 \end{pmatrix} \,, \quad \text{and} \quad \sigma_3 = \begin{pmatrix} 1 & 0 \\ 0 & -1 \end{pmatrix} \,. \tag{2.39}$$

Setting $\Phi(\boldsymbol{r}, t) = \Psi(\boldsymbol{r}) \exp(-i E t/\hbar)$ and inserting in (2.36), we obtain the time-independent Dirac equation,

$$E \Psi(\boldsymbol{r}) = \left(c \boldsymbol{\alpha} \cdot \boldsymbol{p} + \beta m c^2 \right) \Psi(\boldsymbol{r}) \,. \tag{2.40}$$

To describe the motion of a particle in a central potential energy $V(\boldsymbol{r})$ instead of in free space, we add $V(\boldsymbol{r})$ to the Hamiltonian in (2.36) and (2.40). Using the notation

$$\Psi(\boldsymbol{r}) = \begin{bmatrix} \Psi_A(\boldsymbol{r}) \\ \Psi_B(\boldsymbol{r}) \end{bmatrix} \,, \tag{2.41}$$

$$\Psi_A(\boldsymbol{r}) = \begin{bmatrix} \Psi_1(\boldsymbol{r}) \\ \Psi_2(\boldsymbol{r}) \end{bmatrix} \,, \quad \text{and} \tag{2.42}$$

$$\Psi_B(\boldsymbol{r}) = \begin{bmatrix} \Psi_3(\boldsymbol{r}) \\ \Psi_4(\boldsymbol{r}) \end{bmatrix} \tag{2.43}$$

instead of (2.35), we can rewrite the time-independent Dirac equation (2.40) as two coupled equations,

$$\boldsymbol{\sigma} \cdot \boldsymbol{p} \, \Psi_B(\boldsymbol{r}) = \frac{1}{c} \left[E - V(\boldsymbol{r}) - m c^2 \right] \Psi_A(\boldsymbol{r}) \,, \quad \text{and} \tag{2.44}$$

$$\boldsymbol{\sigma} \cdot \boldsymbol{p} \, \Psi_A(\boldsymbol{r}) = \frac{1}{c} \left[E - V(\boldsymbol{r}) + m c^2 \right] \Psi_B(\boldsymbol{r}). \tag{2.45}$$

For a free electron at rest, the Dirac equations (2.44) and (2.45) reduce to $0 = (E - m c^2) \Psi_A(\boldsymbol{r}) = (E + m c^2) \Psi_B(\boldsymbol{r})$. There are two solutions with positive energy

$E = mc^2$ ($\Psi_B = 0$ and $\Psi_A = (1\,0)^T$ or $(0\,1)^T$), and two solutions with negative energy $E = -mc^2$ ($\Psi_A = 0$ and $\Psi_B = (1\,0)^T$ or $(0\,1)^T$). The solutions with positive energy describe an electron in its two spin states, and the solutions with negative energy can be interpreted as a positron, the antiparticle to the electron, also in its two spin states. For particles that are not at rest, the positive energy solutions show a component $\Psi_B(\boldsymbol{r}) \neq 0$ that is usually small unless $E \gg mc^2$.

We now consider the nonrelativistic limit of the time-independent Dirac equation (2.44) and (2.45). As described in more detail in [1], we solve (2.45) for $\Psi_B(\boldsymbol{r})$ and insert it in (2.44), and obtain

$$(\epsilon - V(\boldsymbol{r}))\,\Psi_A(\boldsymbol{r}) = \frac{1}{2m}\left\{\boldsymbol{\sigma}\cdot\boldsymbol{p}\left[1 + \frac{\epsilon - V(\boldsymbol{r})}{2mc^2}\right]^{-1}\boldsymbol{\sigma}\cdot\boldsymbol{p}\right\}\Psi_A(\boldsymbol{r})\,. \tag{2.46}$$

Here we set $\epsilon \equiv E - mc^2$. With $\{1 + [\epsilon - V(\boldsymbol{r})]/2mc^2\}^{-1} \approx 1 - [\epsilon - V(\boldsymbol{r})]/2mc^2$ and $(\boldsymbol{\sigma}\cdot\boldsymbol{p})(\boldsymbol{\sigma}\cdot\boldsymbol{p}) = \boldsymbol{p}^2$, we obtain the lowest order correction ($\propto v^2/c^2$) to the nonrelativistic Schrödinger equation,

$$\epsilon\,\Psi_A(\boldsymbol{r}) = \left\{\left[1 - \frac{\epsilon - V(\boldsymbol{r})}{2mc^2}\right]\frac{\boldsymbol{p}^2}{2m} + \frac{\hbar}{4mc^2}\frac{1}{r}\frac{dV(\boldsymbol{r})}{dr}(\boldsymbol{r}\cdot\boldsymbol{p}) \right. \tag{2.47}$$

$$\left. + \frac{\hbar}{4m^2c^2}\frac{1}{r}\frac{dV(\boldsymbol{r})}{dr}\boldsymbol{\sigma}\cdot(\boldsymbol{r}\times\boldsymbol{\sigma})\right\}\Psi_A(\boldsymbol{r}) \tag{2.48}$$

$$\approx \left[\frac{\boldsymbol{p}^2}{2m} - \frac{\boldsymbol{p}^4}{8m^3c^2} + V(\boldsymbol{r}) + H_{LS} + H_D\right]\Psi_A(\boldsymbol{r})\,, \tag{2.49}$$

where we have set $\boldsymbol{S} = \hbar\boldsymbol{\sigma}/2$ and $\boldsymbol{L} = \boldsymbol{r}\times\boldsymbol{p}$ for the electron spin and orbital momentum, respectively, and

$$H_{LS} = \frac{1}{2m^2c^2}\frac{1}{r}\frac{dV}{dr}\boldsymbol{L}\cdot\boldsymbol{S} \quad \text{and} \tag{2.50}$$

$$H_D = \frac{\hbar^2}{8m^2c^2}\nabla^2 V(\boldsymbol{r}) \tag{2.51}$$

for the so-called spin–orbit interaction and the symmetrized Darwin term, respectively. For the Coulomb potential energy $V(r) = -Ze^2/4\pi\epsilon_0 r$ we obtain

$$H_{LS} = \frac{1}{4\pi\epsilon_0}\frac{Ze^2}{2m^2c^2}\frac{1}{r^3}\boldsymbol{L}\cdot\boldsymbol{S} \quad \text{and} \tag{2.52}$$

$$H_D = \frac{1}{4\pi\epsilon_0}\frac{\pi\hbar^2 Ze^2}{2m^2c^2}\delta(\boldsymbol{r})\,. \tag{2.53}$$

Solving the (2.49) for this case, the energy eigenvalues can be written as

$$\epsilon_{n,j} \approx -R\gamma_Z\left[\frac{1}{n^2} - \frac{(Z\alpha)^2}{n^2}\left(\frac{n}{j+\frac{1}{2}} - \frac{3}{4}\right)\right], \tag{2.54}$$

with the total angular momentum quantum number $j = l + m_s$ and the spin quantum number $m_s = +1/2$ or $-1/2$. The fine structure constant is given by $\alpha \equiv e^2/(\hbar c) \approx 1/137$. The second term in (2.54) describes the fine structure lowering of all energy levels.

2.1.4 Atoms with Multiple Electrons

We now consider the N-electron problem. Even though the decoupling of the center-of-mass motion from the full Hamiltonian (2.9) is a significant simplification, the electron–electron interaction, represented by the third term in (2.11), makes accurate calculations difficult. If this third term were absent, the Hamiltonians in (2.11) would simply be the sum of N single-particle Hamiltonians, whose eigenfunctions $\Psi_j(\boldsymbol{x}_k)$ are given by the one-electron solutions (2.26). Even so, the indistinguishability of the electrons does not allow us to simply write $\Psi(\boldsymbol{x}_1, \ldots, \boldsymbol{x}_N) = \prod_{k=1}^{N} \Psi_k(\boldsymbol{x}_k)$: If the coordinates of any two particles j and k are exchanged, the value of the probability density $|\Psi(\boldsymbol{x}_1, \ldots, \boldsymbol{x}_N)|^2$ does not change. In nature, the exchange of any two coordinates in an electron system is equivalent to multiplying the wavefunction by a factor -1. Particles with this property are fermions, and their wavefunction has to be totally asymmetric. In this case, $\Psi(\boldsymbol{r}_1, \ldots, \boldsymbol{r}_N)$ can be constructed from the Slater determinant, which is the antisymmetrized product of single-particle eigenfunctions,

$$\Psi(\boldsymbol{x}_1, \ldots, \boldsymbol{x}_N) = \frac{1}{\sqrt{N!}} \begin{vmatrix} \Psi_1(\boldsymbol{x}_1) & \ldots & \Psi_1(\boldsymbol{x}_N) \\ \vdots & & \vdots \\ \Psi_N(\boldsymbol{x}_1) & \ldots & \Psi_N(\boldsymbol{x}_N) \end{vmatrix} . \tag{2.55}$$

Generally, the electron–electron interaction term in (2.11) is important and cannot be neglected. Various approximate schemes for solving (2.16) have been devised. A particularly successful class of schemes uses a mean single-particle potential, which is a modified (non-Coulombic) single-particle potential $V(\boldsymbol{r})$ that accounts for a large part of the electron–electron interaction. Such schemes formally retain the independence of the electrons, and states can still be classified by the principal quantum number n, the angular quantum number l, the azimuthal quantum number m, and the spin coordinate m_s. We designate states with the same principal quantum number n as shells, and states with the same value of n and l as subshells. It is customary to label the shells for $n = 1, 2, 3, 4, 5, 6, 7, \ldots$ with the capital letters $K, L, M, N, O, P, Q, \ldots$ According to the Pauli exclusion principle [2], the number of single-particle states in each subshell is $2(2l + 1)$, so that in the $l = 0, 1, 2, 3, \ldots$ subshells, denoted by s, p, d, f, …, there are 2, 6, 10, 14, … unique, one-electron states. As discussed in the next section, the ground-state wavefunction is built up by successively filling the subshells. For a pure Coulombic potential, all states within a shell are degenerate, see (2.33). In a more general central potential, this degeneracy with respect to l is lifted; a noncentral interaction lifts the degeneracy with respect to m.

One particular mean single-particle potential method is the Hartree–Fock method, which is based on a total wavefunction given by the Slater determinant (2.55). We assume that the single-particle eigenfunctions $\Psi_j(\boldsymbol{x})$ are orthonormalized. Using a variational approach it can be shown that the optimal wavefunction, that is the wavefunction with the lowest total energy among wavefunctions of

the form (2.55), can be constructed from single-particle states Ψ_i that fulfill the Hartree–Fock equations

$$\epsilon_i \Psi_i(\boldsymbol{x}) = h(\boldsymbol{x})\Psi_i(\boldsymbol{x}) + \sum_{j=1}^{N}\left[\int \frac{e^2|\Psi_j(\boldsymbol{x}')|^2}{4\pi\epsilon_0|\boldsymbol{r}'-\boldsymbol{r}|}d\boldsymbol{x}'\right]\Psi_i(\boldsymbol{x}) \tag{2.56}$$

$$-\sum_{j=1}^{N}\left[\int \frac{e^2\Psi_j^*(\boldsymbol{x}')\Psi_i(\boldsymbol{x}')}{4\pi\epsilon_0|\boldsymbol{r}'-\boldsymbol{r}|}\right]\Psi_j(\boldsymbol{x})\,, \quad \text{with} \tag{2.57}$$

$$h(\boldsymbol{x}) = -\frac{\hbar^2}{2m}\nabla^2 - \frac{Ne^2}{4\pi\epsilon_0 r}\,, \tag{2.58}$$

where Ψ_k are occupied *and* unoccupied single particle states. Note that the sum in (2.56) runs only over the occupied single particle states $\Psi_1, \ldots, \Psi_N$. Equations 2.56 are nonlinear eigenvalue equations in that the operator depends on the eigenfunction, so that this is a self-consistent-field approach. In practise, a self-consistent solution to the Hartree–Fock equations is obtained numerically by guessing an initial solution, calculating the mean potentials, and then solving the eigenvalue equations for an improved guess of the wavefunctions and so on. Electron–electron correlation effects are neglected in the Hartree–Fock approximation, and a number of approaches have been devised, called post-Hartree–Fock methods, to address this issue.

Other methods have been suggested to solve the N-electron problem (2.16), including the Thomas–Fermi model, based on the single-particle density of a degenerate free-electron gas, as well as more elaborate density-functional methods, based on Hohenberg–Kohn theorems. The reader is referred to the literature [3, 4] for details.

2.1.5
The Periodic System of the Elements

The atomic ground-state wavefunction can be built up by successively filling the subshells of single particle states. The subshells are filled in the order 1s, 2s, 2p, 3s, and 3p. The next subshells are 4s and 3d which are nearly degenerate. The outer electrons determine the chemical properties of the atoms. The complete set of quantum numbers n and l of the occupied shells define the configuration of an atom. Figure 2.1 shows the configuration of the atoms in their ground state. For example, the configuration of a carbon atom is [Be] $2p^2 = 1s^2 2s^2 2p^2$, which means that the 1s and 2s single-particle states are completely filled and that the 2p shell contains two electrons. As an abbreviation, we denote all the filled subshells of an element by brackets around the element symbol, for example [He] $= 1s^2$.

The electron configuration does not completely determine the state of an atom. For example for carbon, there are $2(2l+1) = 6$ possible states for the first 2p electron, and $2(2l+1) - 1 = 5$ possible states for the second 2p electron. Since the electron–electron interaction of these states is slightly different, their energies vary.

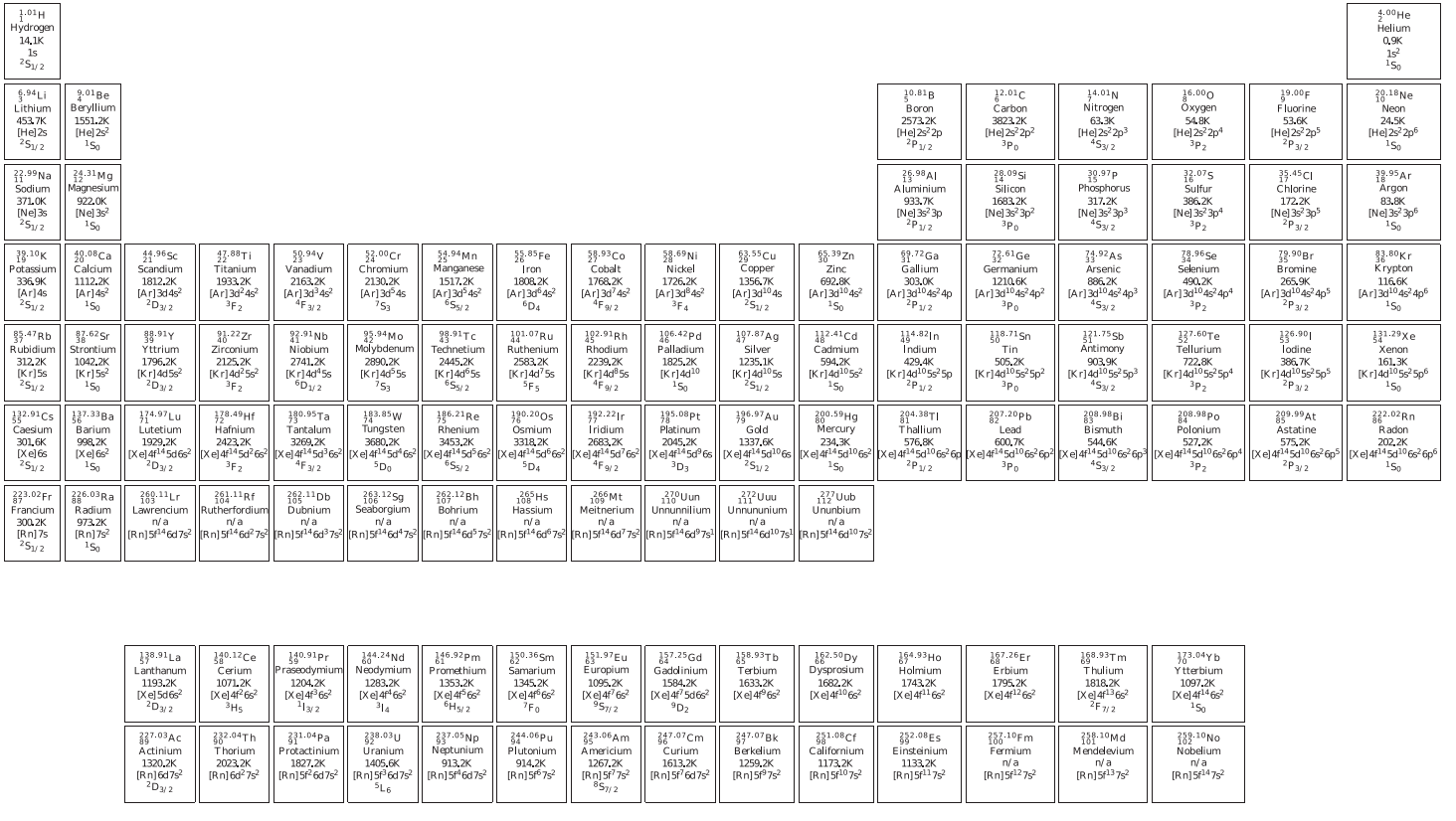

Figure 2.1 Periodic table of the elements.

In addition, spin–orbit interaction, see (2.50), further lifts the degeneracy. Whereas states with different configurations differ in energy by several eV, energy differences due to electron–electron interaction for the same configuration are on the order of 0.1 eV. For light elements, spin–orbit splitting is even weaker, on the order of 10^{-2} to 10^{-3} eV.

We now introduce the spectroscopic notation to characterize the state of the atoms. If the spin–orbit interaction is negligible, then $\boldsymbol{L} = \sum_{i=1}^{N} \boldsymbol{L}_i$ and $\boldsymbol{S} = \sum_{i=1}^{N} \boldsymbol{S}_i$ are constants of motion, so that their components and $\boldsymbol{L}^2$ and $\boldsymbol{S}^2$ commute with the Hamiltonian. The eigenvalues of $\boldsymbol{L}^2$ are $L(L+1)\hbar^2$, with $L = 0, 1, 2, \ldots$, labeled $S, P, D, \ldots$ The states are $(2L+1)$ times degenerate in L_z. The eigenvalues of $\boldsymbol{S}^2$ are $S(S+1)\hbar^2$, and are $(2S+1)$ degenerate in S_z, so that the total degeneracy is $(2L+1)(2S+1)$. The state is characterized by the term symbol ${}^{2S+1}L$. For example, ${}^3P$ corresponds to a state with $S = 1$ and $L = 1$. If spin–orbit coupling is not negligible, then $\boldsymbol{L}$ and $\boldsymbol{S}$ do not commute with the Hamiltonian anymore, but $\boldsymbol{J} = \boldsymbol{L} + \boldsymbol{S}$ is still a constant of motion. Possible values for J are $|L-S|, |L-S|+1, \ldots, |L+S|$. These states are $2J+1$ times degenerate in J_z. The term symbols for these states are ${}^{2S+1}L_J$. For example, ${}^4D_{5/2}$ means $S = 3/2$, $L = 2$, and $J = 5/2$. Note that only at the beginning of the periodic table can one clearly assign a value for L, S, and J, since $\boldsymbol{L}$ and $\boldsymbol{S}$ are approximately constants of motions. For heavier atoms, the spin–orbit coupling is so strong that for each electron $\boldsymbol{J}_i = \boldsymbol{L}_i + \boldsymbol{S}_i$ is approximately a constant of motion instead, and these angular momenta are strongly coupled.

The term symbol corresponding to the ground state can be determined using an empirical set of rules, Hund's rules, to yield the total $\boldsymbol{J} = \sum_i \boldsymbol{J}_i$ and its projection $J_z = \sum_i (J_z)_i$:

1. For a given configuration, the state with the largest value of S has the lowest energy.
2. For a given value of S, the state with the largest value of L is energetically lowest.
3. For given values of S and L, $J = |L-S|$ if the shell is filled less than half, and $J = L+S$ if the state is more than half filled.

The first two rules are due to the minimization of the effect of the short-range electron–electron repulsion. The periodic table in Figure 2.1 also shows the term symbols of the atoms in their ground states.

2.1.6
Screened Hydrogenic Model

The many-electron models discussed above are rather involved. If atomic ionization and emission profiles of systems with various ionization states are to be described (e.g., for plasma spectroscopy), the screened hydrogenic ionization model is much more practical and sufficient for our purposes. The screened hydrogenic ionization model can be justified in the framework of the WKB method [1, 5–7] that is a semiclassical approximation to quantum mechanics.

2.1.6.1 Semiclassical Approximation (WKB Method)

Similar to geometrical optics being the limiting case of wave optics for short wavelengths, a quantum-mechanical system tends toward classical behavior if the de-Broglie wavelengths of the particles are much smaller than characteristic dimensions of the system. Considering the case of a single particle, the wavefunction describing the system can generally be written as

$$\Phi(\boldsymbol{r}, t) = a(\boldsymbol{r}, t) e^{\frac{i}{\hbar} S(\boldsymbol{r}, t)} , \tag{2.59}$$

where S and a are real functions. To determine the time evolution of S and a (and therefore Φ), we insert (2.59) into the time-dependent Schrödinger equation (2.4). Separating into a real and imaginary part, we obtain

$$0 = \frac{\partial S}{\partial t} + \frac{1}{2m} (\nabla S)^2 + V - \frac{\hbar^2}{2ma} \nabla^2 a \tag{2.60}$$

$$= \frac{\partial S}{\partial t} + \frac{1}{2m} (\nabla S)^2 + V \quad \text{for } \hbar \to 0, \text{ and} \tag{2.61}$$

$$0 = \frac{\partial a^2}{\partial t} + \nabla \cdot \left(a^2 \frac{\nabla S}{m} \right) . \tag{2.62}$$

Notice that in the classical limit $\hbar \to 0$, (2.61) is the *classical* Hamilton–Jacobi equation for the evolution of the action S of a particle. Equation 2.62 is the continuity equation for the probability density as the particle evolves according to the laws of classical mechanics, (2.61).

In the WKB approximation, we consider the one-dimensional motion of a point particle, and we assume that the wavefunction $\Phi(r, t) = e^{ig(r)} e^{-iEt/\hbar}$ is a stationary solution of the time-dependent Schrödinger equation with eigenvalue E. Inserting $e^{ig(r)}$ into the time-independent Schrödinger equation (2.21), we obtain a differential equation for the complex-valued function $g(r)$,

$$g'(r) = \pm \frac{p(r)}{\hbar} \sqrt{1 + i \frac{\hbar^2}{p(r)^2} g''(r)} \tag{2.63}$$

$$\approx \pm \frac{p(r)}{\hbar} \pm i \frac{\hbar}{2p(r)} g''(r) \quad \text{for small } \hbar , \tag{2.64}$$

where $p(r) = \sqrt{2m[E - V(r)]}$ is the local momentum. Since $g'(r) \approx \pm p(r)/\hbar$, $g''(r) \approx \pm p'(r)/\hbar$. Inserting $g''(r)$ into (2.64) and integrating over r, we obtain the WKB approximation to the wavefunction,

$$\Psi_{WKB}(r) = e^{ig(r)} \propto \frac{1}{\sqrt{p(r)}} e^{\pm \frac{i}{\hbar} \int^r p(r') dr'} . \tag{2.65}$$

Note that Ψ_{WKB} can simply be obtained from an integral over $p(r)$ which often allows for analytical solutions. Ψ_{WKB} is an oscillating function in the classically allowed region $E > V(r)$, and is monotonically decreasing or increasing in the classically forbidden region $E < V(r)$. A necessary condition for the semiclassical

solution Ψ_{WKB} to be a good approximation to the exact solution of the Schrödinger equation is that the de-Broglie wavelength $\lambda(r) = h/p(r)$ varies only slightly over distances of the order of itself,

$$\left| \frac{1}{2\pi} \frac{d\lambda}{dx} \right| \ll 1 \,. \tag{2.66}$$

Ψ_{WKB} is a poor approximation near the classical turning points for which $E = V(r)$ or $p(r) = 0$. To obtain a solution for the whole space, different Ψ_{WKB} functions, each solution between classical turning points, have to be matched. Connection conditions can be obtained by using the exact of the Schrödinger equation near the turning point, assuming a simplified form of the potential, or by formally regarding $\Psi_{WKB}(r)$ as a function of a complex variable r, and integrating along a path around the turning point, thereby avoiding the divergence. For the specific example of a turning point at $r = a$, where only one side is classically accessible, and the other side is classically inaccessible, and assuming that $\Psi_{WKB}(r) \to 0$ for $|r| \to \infty$ in the classically inaccessible region, the connection condition is [1, 6]

$$\Psi_{WKB}(r) = \begin{cases} \frac{C}{2\sqrt{|p(r)|}} e^{-\frac{1}{\hbar}\left|\int_a^r p(r)dr\right|} & \text{for } V(r) > E \\ \frac{C}{\sqrt{p(r)}} \cos\left[\frac{1}{\hbar}\left|\int_a^r p(r)dr\right| - \frac{\pi}{4}\right] & \text{for } V(r) < E \end{cases} . \tag{2.67}$$

In the case of a finite one-dimensional motion of a particle in a potential well $b \leq r \leq a$, bounded by the two turning points a and b, the connection condition (2.67) leads to a quantization of the energy levels. According to the boundary condition at $r = b$, the wavefunction in the classically accessible region is

$$\Psi_{WKB}(r) = \frac{C}{\sqrt{p(r)}} \cos\left[\frac{1}{\hbar}\left|\int_b^r p(r)dr\right| - \frac{\pi}{4}\right], \tag{2.68}$$

and according to the boundary condition at $r = a$,

$$\Psi_{WKB}(r) = \frac{C'}{\sqrt{p(r)}} \cos\left[\frac{1}{\hbar}\left|\int_r^a p(r)dr\right| - \frac{\pi}{4}\right]. \tag{2.69}$$

Considering that both expressions (2.68) and (2.69) have to agree throughout the region, we obtain the quantization rule

$$\oint p(r)dr = 2\pi\hbar\left(n + \frac{1}{2}\right) \quad \text{with } n = 0, 1, \ldots , \tag{2.70}$$

and $C = (-1)^n C'$. $\oint p(r)dr = 2\int_b^a p(r)dr$ is the integral over one period of the classical particle motion.

2.1.6.2 Semiclassical Approximation for Single Electrons in a Centrally Symmetric Field

In a centrally symmetric field, the solution $\Phi(\boldsymbol{r}, t)$ can be written as the product of an angular part $Y_{l,m}(\theta, \phi)$ and a radial part $R_l(r)$, as in (2.26). It has been shown

that $u_l(r) = r R_l(r)$ satisfies the radial Schrödinger equation (2.28) with $u_l(0) = 0$. We can apply the WKB formalism to this case and set for the classical momentum

$$p(r) = \left\{ 2m \left[E - V(r) \right] - \hbar^2 \frac{l(l+1)}{r^2} \right\}^{1/2} , \tag{2.71}$$

where the electrostatic energy $V(r)$ may be obtained from a (separate) self-consistent field calculation. $p(r)$ is zero at the classical inner and outer turning points r_1 and r_2. We can then use the quantization rule (2.70) to obtain the electron energy levels $E_{n,l}$. Using (2.69), the radial wave function is given by

$$R_{n,l}(r) \propto \frac{1}{\sqrt{p(r)}} \sin \left[\frac{\pi}{4} + \frac{1}{\hbar} \int_{r_1}^{r} p(r') dr' \right] . \tag{2.72}$$

The semiclassical approximation is only valid if condition (2.66) is satisfied, which means that $l \gg 1$. If l is small, the semiclassical approximation is not valid for small r, and we have to determine the phase of $u_l(r)$ by matching the phase for large r. It can be shown that in that case we have to use [2]

$$p(r) = \left\{ 2m[E - V(r)] - \hbar^2 \frac{\left(l + \frac{1}{2}\right)^2}{r^2} \right\}^{1/2} \tag{2.73}$$

instead of (2.71).

We now introduce a screened charge $Z(r)$ and an effective charge $Q(r)$ by defining

$$V(r) = -\frac{Z(r)e^2}{4\pi\epsilon_0 r} , \quad \text{and} \tag{2.74}$$

$$F(r) = -\frac{dU(r)}{dr} = -\frac{Q(r)e^2}{4\pi\epsilon_0 r^2} . \tag{2.75}$$

$Q(r)$ is the nuclear charge reduced by the inner screening associated with the electrons at $r' < r$, and $Q(r) = Z(r) - rZ'(r)$. For each shell with principal quantum number n and average orbit radius r_n we approximate

$$V(r) \approx V_0(r) = -\frac{Z'(r_n)e^2}{4\pi\epsilon_0} - \frac{Q_n e^2}{4\pi\epsilon_0 r} , \tag{2.76}$$

with $Q_n = Q(r_n)$. We define the quantum defect Δ_{nl} as

$$\Delta_{nl} = \frac{1}{\pi\hbar} \int_{r_1}^{r_2} p(r') dr' - \frac{1}{\pi\hbar} \int_{r_1^0}^{r_2^0} p_0(r') dr' , \tag{2.77}$$

with

$$p_0(r) = \left\{ 2m[E - V_0(r)] - \hbar^2 \frac{\left(l + \frac{1}{2}\right)^2}{r^2} \right\}^{1/2} , \tag{2.78}$$

and r_1^0 and r_2^0 are the classical turning radii associated with potentials $V_0(r)$. The shell radius r_n is taken as $(r_1^0 + r_2^0)/2$. The quantum defect Δ_{nl} is zero for a hydrogenic potential $V(r)$. Applying the quantization rule (2.70), we obtain

$$\pi\hbar\left(n_r + \frac{1}{2}\right) = \int_{r_1}^{r_2} p(r')dr' \tag{2.79}$$

$$= \pi\hbar\Delta_{nl} + \int_{r_1^0}^{r_2^0} p_0(r')dr' , \tag{2.80}$$

with $n_r = n - l - 1$. Since

$$\int_{r_1^0}^{r_2^0} p_0(r')dr' = \pi\left\{\frac{e^2 m Q_n}{4\pi\epsilon_0\sqrt{-2m\left[E - \frac{e^2 Z'(r_n)}{4\pi\epsilon_0}\right]}} - \hbar\left(l + \frac{1}{2}\right)\right\}, \tag{2.81}$$

we obtain the WKB approximation for the energy levels,

$$E_{nl} = -\frac{e^2 Z'(r_n)}{4\pi\epsilon_0} - \frac{e^2 Q_n^2}{8\pi\epsilon_0 a_0 (n - \Delta_{nl})^2} , \tag{2.82}$$

with $a_0 = 4\pi\epsilon_0\hbar^2/me^2$. The first term in (2.82) is an energy shift due to outer screening, and Q_n is the effective charge including inner screening.

2.1.6.3 The Screened Hydrogenic Ionization Model

The screened hydrogenic ionization model provides a simplified description of the energy levels of ions in various charge states. It is of modest accuracy (25% rms deviation from the ionization potentials calculated using Hartree–Fock–Slater theory) but it is very fast and gives energy levels of atoms even in very exotic states. The model is motivated by the semiclassical WKB theory. We denote the population of the nth shell by P_n with $0 \le P_n \le 2n^2$. Similar to (2.82), we write the energy eigenvalue E_n of the nth shell as

$$E_n = E_n^0 - \frac{Q_n^2 e^2}{8\pi\epsilon_0 a_0 n^2} , \tag{2.83}$$

where we neglected the quantum defect Δ_{nl} given by (2.77). We assume that the screened nuclear charge Q_n depends linearly on the population of inside shells,

$$Q_n = Z - \sum_{m=1}^{n-1}\sigma(n,m)P_m - \frac{1}{2}\sigma(n,n)P_n , \tag{2.84}$$

where the coefficients $\sigma(n,m)$ describe the screening of an electron in the nth shell by one in the mth shell. For the outer screening, we assume an expression of the

Table 2.1 Screening constants for screened hydrogenic ionization model [8].

$\sigma(m,n)$	$n=1$	$n=2$	$n=3$	$n=4$	$n=5$	$n=6$	$n=7$	$n=8$	$n=9$	$n=10$
$m=1$	0.3125	0.9380	0.9840	0.9954	0.9970	0.9970	0.9990	0.9990	0.9999	0.9999
$m=2$	0.2345	0.6038	0.9040	0.9722	0.9779	0.9880	0.9900	0.9990	0.9999	0.9999
$m=3$	0.1093	0.4018	0.6800	0.9155	0.9796	0.9820	0.9860	0.9900	0.9920	0.9999
$m=4$	0.0622	0.2430	0.5150	0.7100	0.9200	0.9600	0.9750	0.9830	0.9860	0.9900
$m=5$	0.0399	0.1597	0.3527	0.5880	0.7320	0.8300	0.9000	0.9500	0.9700	0.9800
$m=6$	0.0277	0.1098	0.2455	0.4267	0.5764	0.7248	0.8300	0.9000	0.9500	0.9700
$m=7$	0.0204	0.0808	0.1811	0.3184	0.4592	0.6098	0.7374	0.8300	0.9000	0.9500
$m=8$	0.0156	0.0624	0.1392	0.2457	0.3711	0.5062	0.6355	0.7441	0.8300	0.9000
$m=9$	0.0123	0.0493	0.1102	0.1948	0.2994	0.4222	0.5444	0.6558	0.7553	0.8300
$m=10$	0.0100	0.0400	0.0900	0.1584	0.2450	0.3492	0.4655	0.5760	0.6723	0.7612

form

$$E_n^0 = \frac{1}{2}\frac{e^2}{4\pi\epsilon_0 r_n}\sigma(n,n)P_n + \sum_{m=n+1}^{\infty}\frac{e^2 P_m}{4\pi\epsilon_0 r_m}\sigma(m,n)\,, \tag{2.85}$$

where $r_n = a_0 n^2/Q_n$ is the orbit radius of the nth shell. The total ion energy is given as

$$E_{ion} = \sum_{n=1}^{\infty}\left(-\frac{Q_n^2 e^2}{8\pi\epsilon_0 a_0 n^2}\right)P_n\,. \tag{2.86}$$

Using a least-squares optimization procedure, a ten-by-ten matrix of screening constants was proposed in [8], see Table 2.1. Figure 2.2 shows the ionization energies of the different atomic shells for neutral atoms as a function of the atomic charge number Z calculated with the screened hydrogenic ionization model. Overlaid are experimentally obtained and calculated subshell ionization energies [9]. It can be seen that the simple model does describe the ionization energies well, especially for lower-Z materials.

2.2 Atomic Processes

A number of different atomic transition processes operate, depending on the environment of the atom. If energy is added to the atom (or ion), an electron is excited from a lower-level into a higher-level state. If the added energy is sufficiently large, the electron may leave the atom. This promotion of an electron into the continuum is called ionization. We generally distinguish between particle- and photon-induced excitation and ionization processes. Table 2.2 lists the most important atomic processes in x-ray–matter interaction, along with their reverse processes [10]. For molecules, the processes are even more diverse since in addition

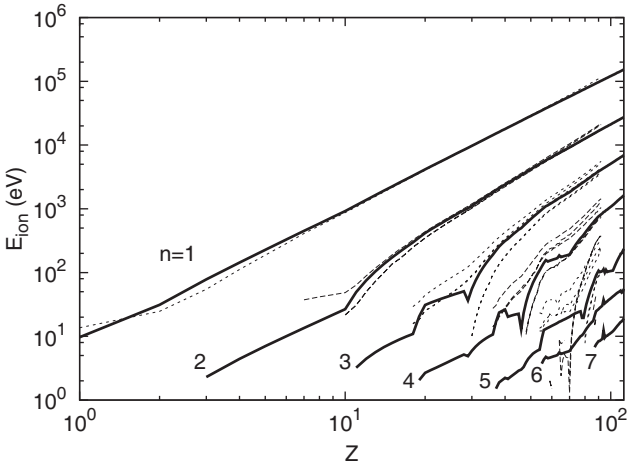

Figure 2.2 Ionization energies E_{ion} for the different shells as a function of the nucleus charge Z, calculated using the screened hydrogenic ionization model (thick). Overlaid are experimentally determined subshell ionization energies [9].

dissociation can occur. Usually only one or a few of the processes are dominant, depending on the environment and the time scale.

2.2.1 Interaction of Atoms with Photons

In many cases it is sufficient to describe the interaction of an electromagnetic field with an electron–ion system within the semiclassical model introduced in Section 1.4.2, in which the field is treated classically. In certain cases, for example for the absorption and emission of photons, it is better to consider the quantized of the electromagnetic field. Such a framework allows us to describe x-ray scattering (Section 3.2.1.1), photionization (Section 5.2), and multiphoton absorption process-

Table 2.2 Important atomic processes relevant to x-ray–matter interaction. X^q indicates an atom of type X with q electrons removed. The symbol * indicates an excited state.

Process name	Process	Inverse process
Photo ionization	$X^q + h\nu \rightarrow X^{q+1} + e^-$	Radiative recombination
Photo excitation	$X^q + h\nu \rightarrow X^{q*}$	Spontaneous emission
Electron impact ionization	$X^q + e^- \rightarrow X^{q+1} + 2e^-$	Three-body recombination
Electron impact excitation	$X^q + e^- \rightarrow X^{q*} + e^-$	Collision of the second kind
Autoionization	$X^{q*} \rightarrow X^{q+1} + e^-$	Dielectronic recombination
Inverse Bremsstrahlung absorption	$X^q + e^- + h\nu \rightarrow X^q + e^{-*}$	Inverse Bremsstrahlung

es (Section 7.2.1). We will now discuss the quantization of the free electromagnetic field [11] including the applicability of the dipole approximation in the x-ray regime, and introduce the principle of detailed balance, which is a useful tool to determine the rate of inverse processes from information about the forward processes.

2.2.1.1 Quantization of Free Electromagnetic Fields

We choose to describe the radiation field by the vector function $\boldsymbol{A}(\boldsymbol{r})$ in the radiation gauge, see (1.21) and (1.22). Gauge-invariance of observable quantities can be achieved with the minimal coupling principle by replacing $\boldsymbol{p}_i$ with $\boldsymbol{p}_i + e\boldsymbol{A}(\boldsymbol{r}_i)$ [12]. The electronic part of the nonrelativistic N-electrons Hamiltonian for an atom of nuclear charge Ze and a radiation field is given by (2.11),

$$H = \sum_{i=1}^{N} \frac{\left[\boldsymbol{p}_i + e\boldsymbol{A}(\boldsymbol{r}_i)\right]^2}{2m} + V + H_{rad} \quad \text{with} \tag{2.87}$$

$$V = -\sum_{i=1}^{N} \frac{Ze^2}{4\pi\epsilon_0 |\boldsymbol{r}_i|} + \sum_{i=1}^{N} \sum_{j=i+1}^{N} \frac{e^2}{4\pi\epsilon_0 |\boldsymbol{r}_i - \boldsymbol{r}_j|} \quad \text{and} \tag{2.88}$$

$$H_{rad} = \int \frac{\epsilon_0 \boldsymbol{E} \cdot \boldsymbol{E}^* + \boldsymbol{B} \cdot \frac{\boldsymbol{B}^*}{\mu_0}}{2} d^3x \,. \tag{2.89}$$

We introduce a quantization of the electromagnetic field by expressing $\boldsymbol{A}$ in terms of creation and annihilation operators for quanta of plane wave basis states,

$$\boldsymbol{A}(\boldsymbol{r}) = \sum_{\boldsymbol{k},\sigma} \sqrt{\frac{\hbar}{2\omega_k \epsilon_0 V}} \boldsymbol{\epsilon}_{\boldsymbol{k},\sigma} \left(a_{\boldsymbol{k},\sigma} e^{-i\boldsymbol{k}\cdot\boldsymbol{r}} + a^*_{\boldsymbol{k},\sigma} e^{i\boldsymbol{k}\cdot\boldsymbol{r}} \right) , \tag{2.90}$$

where $\boldsymbol{k}$ is the wave vector, $\boldsymbol{\epsilon}_{\boldsymbol{k},\sigma}$ are polarization vectors perpendicular to $\boldsymbol{k}$ for both polarizations $\sigma = 1, 2$, V is volume of a large box with periodic boundary conditions, and $\omega_k = kc$. a and a^* are the annihilation and creation operator for quanta of the field, respectively,

$$a_{\boldsymbol{k},\sigma} |\ldots n_{\boldsymbol{k},\sigma} \ldots\rangle = \sqrt{n_{\boldsymbol{k},\sigma}} \, |\ldots n_{\boldsymbol{k},\sigma} - 1 \ldots\rangle \,, \tag{2.91}$$

$$a^*_{\boldsymbol{k},\sigma} |\ldots n_{\boldsymbol{k},\sigma} \ldots\rangle = \sqrt{n_{\boldsymbol{k},\sigma} + 1} \, |\ldots n_{\boldsymbol{k},\sigma} + 1 \ldots\rangle \,, \tag{2.92}$$

where $|\ldots n_{\boldsymbol{k},\sigma} \ldots\rangle = \prod_{\boldsymbol{k},\sigma} |n_{\boldsymbol{k},\sigma}\rangle$ is an eigenstate of the electromagnetic field with $n_{\boldsymbol{k},\sigma}$ photons in the mode described by $\boldsymbol{k}$ and σ, often referred to as the Fock or number state. Equations 2.91 and 2.92 follow from the commutation relations

$$\left[a_{\boldsymbol{k},\sigma}, a^*_{\boldsymbol{k}',\sigma'} \right] = a_{\boldsymbol{k},\sigma} a^*_{\boldsymbol{k}',\sigma'} - a^*_{\boldsymbol{k}',\sigma'} a_{\boldsymbol{k},\sigma} = \delta_{\boldsymbol{k},\boldsymbol{k}'} \delta_{\sigma,\sigma'} \,. \tag{2.93}$$

We can rewrite H as

$$H = H_0 + H_{int} \quad \text{with} \tag{2.94}$$

$$H_0 = \sum_{i=1}^{N} \frac{\boldsymbol{p}_i^2}{2m} + V + H_{rad} \,, \tag{2.95}$$

$$H_{int} = \sum_{i=1}^{N} \frac{e}{m} \boldsymbol{p}_i \cdot \boldsymbol{A}(\boldsymbol{r}_i) + \frac{e^2}{2m} \boldsymbol{A}(\boldsymbol{r}_i)^2 \,. \tag{2.96}$$

We assume that the interaction between the atom and the field, described by H_{int}, is small and that we can treat it perturbatively. We can then describe the state of the system by $|\text{atom} + \text{rad}\rangle = |\text{atom}\rangle|\ldots n_{\boldsymbol{k},\sigma} \ldots\rangle$, where $|\text{atom}\rangle$ represents the many-particle system. Note that H_{int} is a sum of an $\boldsymbol{p} \cdot \boldsymbol{A}$ term, $H_{int}^{(1)}$, and of an $\boldsymbol{A}^2$ term, $H_{int}^{(2)}$, so that H_{int} can be written as

$$H_{int} = H_{int}^{(1)} + H_{int}^{(2)} \,, \quad \text{with} \tag{2.97}$$

$$H_{int}^{(1)} = \frac{e}{m} \boldsymbol{p} \cdot \boldsymbol{A}(\boldsymbol{r}) \tag{2.98}$$

$$= \frac{e}{m} \sum_{\boldsymbol{k},\sigma} \sqrt{\frac{\hbar}{2\epsilon_0 V \omega_k}} \boldsymbol{p} \cdot \boldsymbol{\epsilon}_{\boldsymbol{k},\sigma} \left(a_{\boldsymbol{k},\sigma} e^{-i\boldsymbol{k}\cdot\boldsymbol{r}} + a_{\boldsymbol{k},\sigma}^* e^{i\boldsymbol{k}\cdot\boldsymbol{r}} \right) \quad \text{and} \tag{2.99}$$

$$H_{int}^{(2)} = \frac{e^2}{2m} \boldsymbol{A}(\boldsymbol{r})^2 \tag{2.100}$$

$$= \frac{e^2}{m} \sum_{\boldsymbol{k},\sigma} \sum_{\boldsymbol{k}',\sigma'} \frac{\hbar}{4\epsilon_0 V \sqrt{\omega_k \omega_{k'}}} \boldsymbol{\epsilon}_{\boldsymbol{k},\sigma} \cdot \boldsymbol{\epsilon}_{\boldsymbol{k}',\sigma'} \tag{2.101}$$

$$\times \Big[a_{\boldsymbol{k},\sigma} a_{\boldsymbol{k}',\sigma'} e^{-i(\boldsymbol{k}+\boldsymbol{k}')\cdot\boldsymbol{r}} + a_{\boldsymbol{k},\sigma} a_{\boldsymbol{k}',\sigma'}^* e^{i(-\boldsymbol{k}+\boldsymbol{k}')\cdot\boldsymbol{r}}$$

$$\times \; a_{\boldsymbol{k},\sigma} a_{\boldsymbol{k}',\sigma'}^* e^{i(-\boldsymbol{k}+\boldsymbol{k}')\cdot\boldsymbol{r}} + a_{\boldsymbol{k},\sigma}^* a_{\boldsymbol{k}',\sigma'}^* e^{i(\boldsymbol{k}+\boldsymbol{k}')\cdot\boldsymbol{r}} \Big] .$$

We did not include the summation over the electrons for simplicity.

The probability of transitions per unit time of an electron from an initial atomic state i to a group of adjacent atomic continuum states f with a density (number of states/unit energy) $\rho_f(E_f)$ is given by Fermi's *Golden Rule*, here written to include the higher-order terms in H_{int} as

$$w_{i\to f} = \frac{2\pi}{\hbar} |M_{i,f}|^2 \rho_f(E_i = E_f) \,, \quad \text{with} \tag{2.102}$$

$$M_{i,f} = \langle f|H_{int}|i\rangle + \sum_{I_1} \frac{\langle f|H_{int}|I_1\rangle\langle I_1|H_{int}|i\rangle}{E_i - E_{I_1} + i\eta}$$

$$+ \sum_{I_1,I_2} \frac{\langle f|H_{int}|I_1\rangle\langle I_1|H_{int}|I_2\rangle\langle I_2|H_{int}|i\rangle}{(E_i - E_{I_1} + i\eta)(E_i - E_{I_2} + i\eta)} + \cdots \tag{2.103}$$

$|I_1\rangle, |I_2\rangle, \ldots$ are complete sets of intermediate states through which higher-order transitions occur, and $\eta \to +0$. E_i and E_f are the total energy of atom and field

before and after the transition, respectively. A more extensive discussion is given in [2].

2.2.1.2 Dipole Approximation in the X-Ray Regime

The interaction Hamiltonian (2.97) contains exponential factors of the form e^{ikr} that can be expanded as

$$e^{ikr} \approx 1 + ikr - \frac{(kr)^2}{2} + \dots \,, \tag{2.104}$$

where $k = 2\pi/\lambda$ is the magnitude of the wave vector and r is the magnitude of the radius vector. In the dipole approximation, e^{ikr} is approximated by 1. This zero-th order has been used extensively in the optical regime where it tends to be a good approximation because the wavelength is much larger than atomic dimension. In the x-ray regime, this is not necessarily the case. Nevertheless, even in the x-ray regime calculations are often performed in the dipole approximation since retaining the higher-order terms in e^{ikr} is often fairly difficult. The validity of such an approach needs to be evaluated on a case-by-case basis.

2.2.1.3 Principle of Detailed Balance

Every process has its inverse process. If we denote the forward and inverse transition rates by $w_{i\to f}$ and $w_{f\to i}$, respectively, then the ratio of these rates is given by the *principle of detailed balance*,

$$\frac{w_{i\to f}}{w_{f\to i}} = \frac{\rho_f(E)}{\rho_i(E)} \,. \tag{2.105}$$

A more extensive discussion is given in [2]. It is often useful to define the *cross section* $\sigma(v)$ for an ionization process to occur, defined as the transition rate divided by the current density of incoming electrons or photons.

The number of transitions per unit volume and unit time is given by multiplying the *reaction rate* R by the densities of the reacting particles. For a two-particle process, R is defined as

$$R = \int f(v) v \sigma(v) dv \,, \tag{2.106}$$

where $\sigma(v)$ is the velocity-dependent interaction cross section and $f(v)$ is the density distribution of particles with relative speed v. Similarly, we can define a reaction rate R for a particle irradiated by a spectral photon flux $dF(\omega)/d\omega$ as

$$R = \int \frac{dF(\omega)}{d\omega} \sigma(\omega) d\omega \,. \tag{2.107}$$

We will now discuss these atomic processes and their rates in more detail.

2.2.2
Radiative Excitation and Spontaneous Decay

In a *spontaneous decay* transition an excited ion relaxes from an upper level u to a lower level l through the emission of a photon of energy $\Delta E = E_u - E_l = \hbar\omega$ equal to the energy difference between the two states. The rate of an electric dipole transition between state u to state l is given by [18]

$$A_{u\to l} = \frac{2\pi e^2}{mc^3\epsilon_0 h^2}\Delta E^2\,|f_{u\to l}| = \frac{2\pi e^2}{mc\epsilon_0 h^2}\Delta E^2\,\frac{g_l}{g_u}\,|f_{l\to u}|\,, \tag{2.108}$$

where $g_u = 2J_u + 1$ and $g_l = 2J_l + 1$ are the statistical weights. $f_{l\to u}$ is the absorption oscillator strength

$$f_{l\to u} = \frac{2}{3}\frac{m}{\hbar^2}\Delta E\frac{1}{g_l}\sum_{M_L,M_U}\left|\langle\Psi_{l,J_l,M_l}|\sum_{i=1}^{N}\boldsymbol{r}_i|\Psi_{u,J_u,M_u}\rangle\right|^2, \tag{2.109}$$

which is a dimensionless quantity by which the classical absorption cross section,

$$\sigma_{class} = \pi r_e^2 \quad \text{with} \quad r_e = \frac{1}{4\pi\epsilon_0}\frac{e^2}{mc^2}\,, \tag{2.110}$$

has to be multiplied to give the quantum cross section $\sigma_{qm} = f_{l\to u}\sigma_{class}$. The absorption oscillator strength $f_{l\to u}$ decreases rapidly with increasing quantum number n_u which means that transitions involving low-lying excited states are much faster than those involving highly excited states. $f_{l\to u}$ relates to the absorption oscillator strength through $f_{l\to u} = -f_{u\to l}g_u/g_l$. If $\Gamma = \sum_{l<u}A_{u\to l}$ is the sum of the decay rates to all lower states l, then due to Heisenberg's uncertainty relation

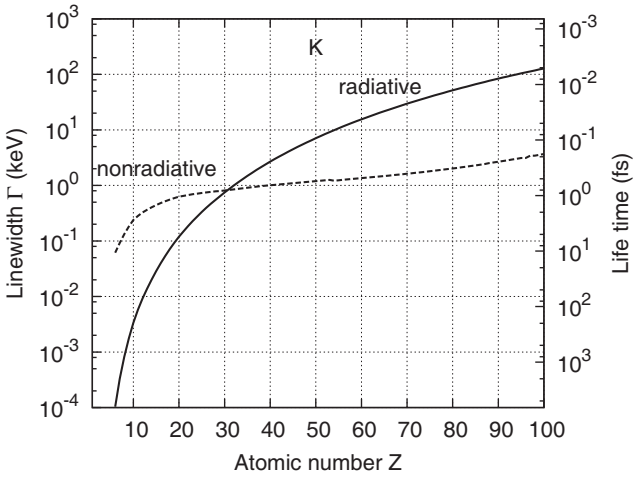

Figure 2.3 Dependence of the partial radiative and nonradiative linewidths and the corresponding vacancy lifetime on the atomic number Z for the atomic K shell [13].

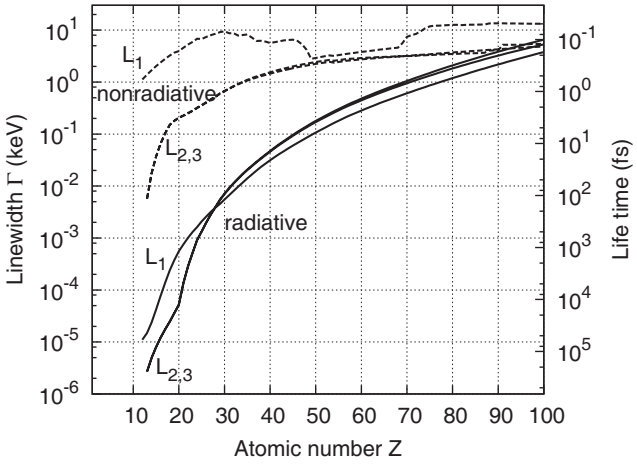

Figure 2.4 Dependence of the partial radiative and nonradiative linewidths and the corresponding vacancy lifetime on the atomic number Z for the atomic L shells [13]. L_1 and $L_{2,3}$ indicate missing 2s and 2p electrons, respectively.

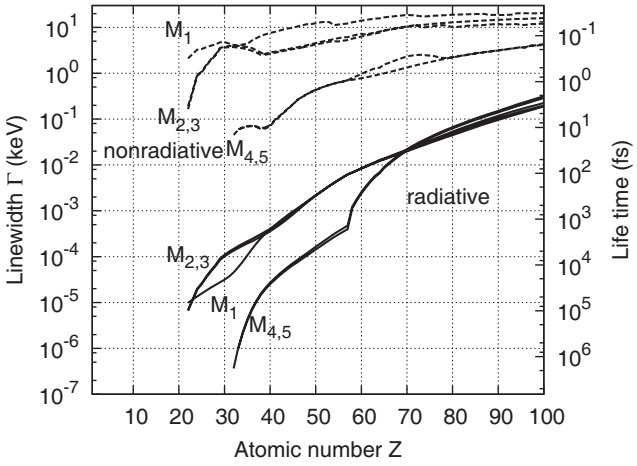

Figure 2.5 Dependence of the partial radiative and nonradiative linewidths and the corresponding vacancy lifetime on the atomic number Z for the atomic M shells [13]. M_1, $M_{2,3}$, and $M_{4,5}$ indicate missing 3s, 3p, and 3d electrons, respectively.

the spectral linewidth of the emitted light is given by $\hbar\Gamma$. Figures 2.3–2.5 show the dependence of the radiative linewidths for holes in the K, L, and M shell as a function of the atomic number Z. Generally the radiative life time decreases with increasing atomic number, and the radiative life time is smaller for inner shell holes.

The transition rate for stimulated emission, $U(\nu)B_{u\to l}$, is simply related to the transition rate $A_{u\to l}$ for spontaneous decay by

$$B_{u\to l} = \frac{c^3}{4h\nu^3} A_{u\to l} \,. \tag{2.111}$$

$U(\nu)$ is the radiation density. In stimulated emission, the presence of photons enhances the transition rate from state u to state l. The transition rate for stimulated emission also simply relates to the transition rate for absorption through photoexcitation from state l to state u, $U(\nu)B_{l\to u}$, by

$$B_{l\to u} = \frac{g_u}{g_l} B_{u\to l} = \frac{g_u}{g_l} \frac{c^3}{4h\nu^3} A_{u\to l} \,. \tag{2.112}$$

$A_{u\to l}$, $B_{u\to l}$, and $B_{l\to u}$ are called the Einstein coefficients.

2.2.3 Photoionization and Radiative Recombination

During *radiative recombination* an electron is captured into a state where it is bound by energy $E_i > 0$, and a photon is emitted while conserving energy and momentum. In the inverse process of *photoionization*, a photon excites an electron into the continuum. Using the principle of detailed balance, we can derive the *Milne relation* that connects the cross sections for these processes,

$$\frac{\sigma_{photo}(\hbar\omega)}{\sigma_{recomb}(E_e)} = \frac{2mc^2 E_e}{(\hbar\omega)^2} \frac{g_{i+1}}{g_i} \,. \tag{2.113}$$

Here, $\sigma_{photo}(\hbar\omega)$ is the photo ionization cross section as a function of the photon energy $\hbar\omega$, $\sigma_{recomb}(E_e)$ is the cross section for radiative recombination as a function of the free electron energy $E_e = \hbar\omega + E_i$, and g_{i+1} and g_i are statistical weights of the atomic states after and before ionization, respectively.

For hydrogen-like ions with nuclear charge Z, the ground-state photoionization cross section for linearly polarized light and for $\hbar\omega \gg |E_{1s}|$ is approximately

$$\sigma_K(\hbar\omega) = \frac{16\pi\sqrt{2} r_e^2 \alpha^4 Z^5}{3} \left(\frac{mc^2}{\hbar\omega}\right)^{3.5} \,, \tag{2.114}$$

where α is fine structure constant, $E_{1s} = Z^2 E_H$, and E_H is the ionization energy for hydrogen, and a_0 is the Bohr radius. Near the absorption edge for $\hbar\omega \geq |E_{1s}|$,

$$\sigma_{K'}(\hbar\omega) = \sigma_K(\hbar\omega) 2\pi \sqrt{\frac{|E_{1s}|}{\hbar\omega}} \frac{e^{-4\xi \cot^{-1}\xi}}{1 - e^{2\pi\xi}} \tag{2.115}$$

with $\xi = \sqrt{|E_{1s}|/\hbar\omega - |E_{1s}|}$. These features are illustrated in Figure 2.6 which shows the dependence of the photoionization cross section on the x-ray energy for H, C, and Ta. The jumps in the curves are due to contributions from different subshells. The photoionization cross section per electron is not strongly affected by the ionization state of the ion, except for shifts in the threshold due to shifts in the ionization energies.

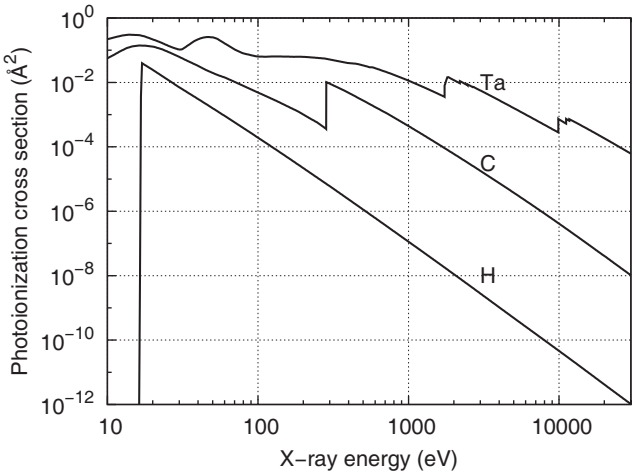

Figure 2.6 Dependence of the photoionization cross section on the x-ray energy [9].

2.2.4
Electron Impact Ionization and Three-Body Recombination

During the process of *electron impact ionization* a free electron interacts with an atom or ion and knocks out another electron. Usually the ejected electron originates from the outermost shell of the ion, but inner-shell ionization can also occur. Various semiempirical parametrizations of the cross section exist, for example the Lotz formula that gives relatively accurate results for low-Z ions, and Bethe's formula for larger impact energies. Figure 2.7 shows the near-threshold dependence of the electron impact ionization cross section on the energy of the incoming electron for some neutral and ionized elements. Unlike the photo ionization cross section, for electron impact ionization the cross section is zero at the ionization threshold, increases sharply to a maximum at a few times the binding energy, and then decreases slowly.

The inverse process to electron impact ionization is *three-body recombination*, during which two electrons simultaneously approach an ion, one electron is captured, and the second electron carries away the extra energy. Since this process requires two electrons in the vicinity of the ion, it is most likely to occur in high-density plasmas. The rate coefficient for electron impact ionization, $I(i, m \to i+1, m')$, is related to the rate coefficient for three-body recombination, $R^{(3)}(i+1, m' \to i, m)$, through the principle of detailed balance,

$$\frac{I\,(i, m \to i+1, m')}{R^{(3)}\,(i+1, m' \to i, m)} = 2\left[\frac{mc^2 T_e}{2\pi(\hbar c)^2}\right]^{3/2} \frac{g_{i+1,m'}}{g_{i,m}} \times \exp\left(-\frac{E_{i+1,m'} - E_{i,m}}{T_e}\right). \tag{2.116}$$

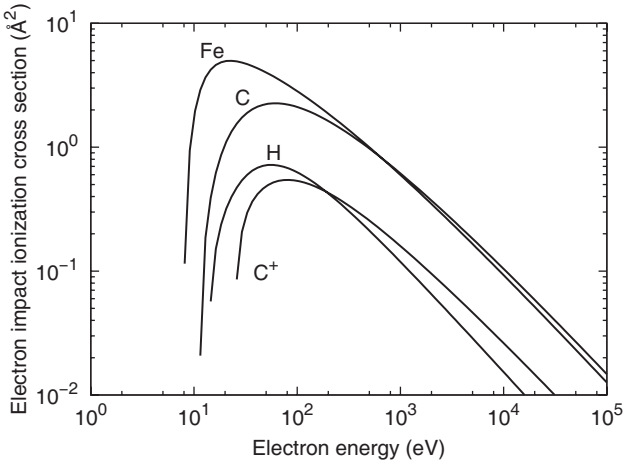

Figure 2.7 Dependence of the electron impact ionization cross section on the energy of the incoming electron for neutral H, C, and Fe, and singly ionized C [15].

Here i and $i+1$ denote the ionic charge, m the excitation state, and T_e is the electron temperature. The rate of electron-impact-ionization events per unit volume is $N_i n_e I$, and the rate of three-body-recombination events per unit volume is $N_i n_e^2 R^{(3)}$, where n_e and N_i are the electron and ion densities, respectively. Collisional ionization processes couple the outer electron states to the continuum. Recombination is most likely to occur in the uppermost states. These states are also most strongly targeted for electron impact ionization.

Generally, the *innermost* electrons are most effectively ejected by photon absorption (photoionization), whereas electron impact ionization affects primarily the outer electrons. Similarly, radiative recombination occurs preferably into the lower ionic states, which is opposite to the process of three-body recombination.

2.2.5
Electron Impact Excitation and Deexcitation

A free electron interacting with an ion may also cause *electron-impact excitation* during which a bound electron undergoes a transition to a higher/lower bound energy state. The latter (deexcitation) process is sometimes referred to as a collision of the second kind. Figure 2.8 shows electron-impact excitation cross sections for hydrogen. Similar to electron impact ionization, the cross section for electron-impact excitation starts at zero at the excitation threshold ΔE, increases sharply, and then has a maximum at a few times the excitation energy. If we denote the rate coefficients for electron impact excitation and deexcitation by $E_{l\to u}$ and $D_{u\to l}$, respectively, then we can find a relation between these two coefficients through the principle of detailed balance,

$$\frac{D_{u\to l}}{E_{l\to u}} = \frac{g_l}{g_u}\exp\left(-\frac{\Delta E}{T_e}\right). \tag{2.117}$$

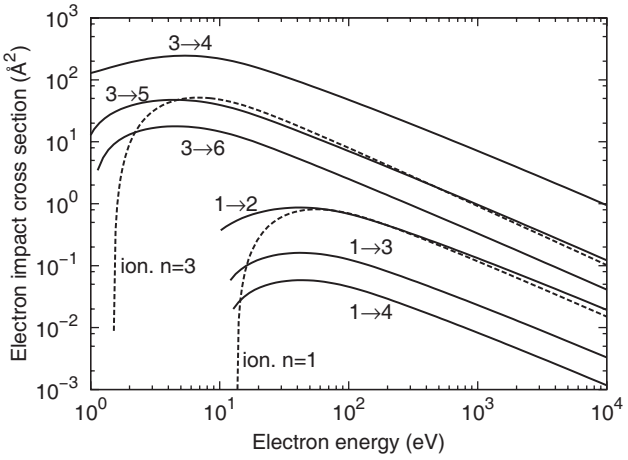

Figure 2.8 Electron impact excitation cross section of hydrogen for different shell transitions (solid lines). Overlaid are the electron impact ionization cross sections (dashed lines).

Excitation-rate coefficients tend to be highest between two states with small difference in their quantum numbers.

2.2.6 Autoionization and Dielectronic Recombination

In the process of autoionization a doubly excited ion spontaneously relaxes by ejecting a bound electron into the continuum. One excited electron imparts excitation energy to the second excited electron, which is ejected without the absorption or emission of electromagnetic radiation. Commonly the outer electron is ejected which requires that the excitation energy of the inner electron must be larger than the binding energy of the outer electron. This process occurs often after x-ray absorption since x rays are able to excite or remove core electrons, leaving behind a highly excited ion. Particularly common are Auger and Koster–Cronig transitions. During an Auger transition, a vacancy in a certain main shell is filled by an electron from a higher main shell with the emission of an electron from that same or higher shell. During a Koster–Cronig transition, a vacancy in a certain subshell is filled by an electron from another subshell in that same main shell, leading to the emission of an electron from the same or a higher main shell. Figures 2.3–2.5 show partial linewidths and lifetimes of ions with inner-shell vacancies for nonradiative (autoionizing) transitions. As discussed in Section 2.2.2, the linewidth ΔE relates to the transition rate Γ through $\Delta E = \hbar\Gamma$, and the lifetime is $1/\Gamma$.

Dielectronic recombination is a two-step process. First, an electron is captured by an ion into an excited state. The energy released is transferred to a different bound electron, so that the ion then contains two excited electrons. This first step is the inverse of the autoionization process. In the second step, the doubly excited ion relaxes through radiative decay (stabilization). Typically the lower state decays

since it has the larger transition probability. Note that if the second step were an autoionization event, this process would, instead, represent just resonant scattering.

The principle of detailed balance relates the rate coefficient for autoionization $A(i, n'l', n''l'' \rightarrow i+1, nl)$ between an ion with excited electrons in states n', l' and n'', l'' and an ion after ionization and the rate coefficient for recombination into the doubly excited states (before radiative stabilization) $R(i+1, nl \rightarrow i, n'l', n''l'')$ by

$$R\left(i+1, nl \rightarrow i, n'l', n''l''\right) = \frac{1}{2}\frac{g_{i,n'l',n''l''}}{g_{i+1,nl}}\left[\frac{2\pi(\hbar c)^2}{mc^2 T_e}\right]^{3/2} A\left(i, n'l', n''l'' \rightarrow i+1, nl\right) e^{-\frac{E_{i,n'l',n''l''} - E_{i+1,nl}}{T_e}} , \tag{2.118}$$

which has the same form as (2.116).

2.2.7 Shake Processes

Shake processes modulate the number and the energies of electrons released from an atom upon photon absorption. The departing photo electron can interact with the relaxing electron system and lose kinetic energy, leaving the system in an excited state. This effect gives rise to intense satellite structures in inner-shell spectroscopic experiments, and the intensity of these structures is proportional to the probabilities of various shake processes.

Photoemission can be described in the *adiabatic limit* and in the *sudden limit*. In the *adiabatic limit*, photoemission is assumed to be sufficiently slow so that the escaping electron feels the relaxation of the core-ionized atom. In the *sudden limit*, the photoelectron is assumed to be emitted promptly after the photon absorption event, before core relaxation has occurred. The sudden approximation (or sudden perturbation theory) is valid for high-energy photons. In this case, the absorption process is often accompanied by shake-up, shake-off, and plasmon loss processes. In *shake-up* processes, an electron is promoted into a higher, unoccupied state, which is in a sense a collective excitation. In shake-off processes, an electron is promoted into a continuum state.

It has been shown [16] that the relative probability per electron of shake from the subshell $n_1 l_1$ after ionization of the inner subshell $n_0 l_0$ can be approximated by

$$P_1(n_0 l_0; n_1 l_1) = \frac{a}{(Z-b)^2} , \tag{2.119}$$

where Z is atomic number and a and b are fitting parameters given in [16]. In this context, relative means the probability for shake with respect to the probability of an initial single $n_0 l_0$ photo ionization event. Typical relative probabilities are shown in Figure 2.9.

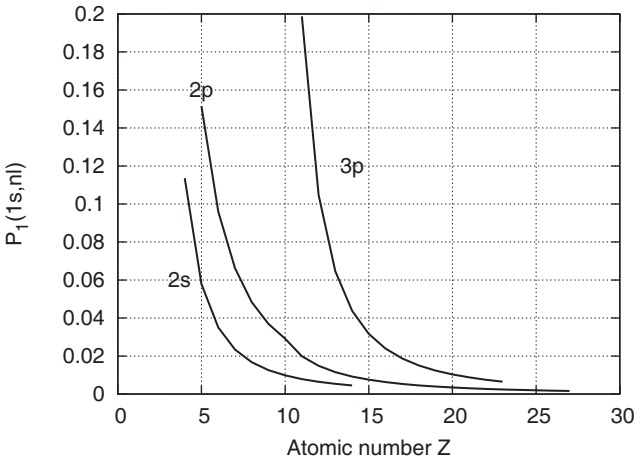

Figure 2.9 Relative probability P_1 of the occurrence of shake processes from the subshell nl, given that the subshell 1s was photoionized [16].

2.3 Effect of Plasma Environment

Low-density plasmas can usually be described by means of independent particles undergoing occasional collisions. With increasing density, when the interatomic separation is comparable to the atomic dimensions, the ions cannot be treated as isolated particles anymore, leading to a perturbation of the electronic structure and to modifications of the atomic processes. Perturbation of the electronic structure causes shifts of the energy levels and with that modifications of the partition function which describes the thermodynamic equilibrium properties of a system. In a rapidly evolving dense plasma with nonthermal level populations, the rates of various atomic processes can change significantly.

A plasma can be characterized by the degree of coupling between its constituents, which is described by the Coulomb coupling parameter $\Gamma_{A,B}$ of species A and B. $\Gamma_{A,B}$ is given by the ratio of mean potential and kinetic energies as

$$\Gamma_{AB} = \frac{|Z_A Z_B e^2|}{4\pi\epsilon_0 R_{AB} \Theta_{AB}} , \tag{2.120}$$

where $R_{AB} = (R_A + R_B)/2$ is a reduced ion-sphere radius, $R_{A,B} = (3/4\pi n_{A,B})^{1/3}$ are electron or ion sphere radii of species A and B, $n_{A,B}$ the respective densities, and $\Theta_{AB} = (m_A\Theta_B + m_B\Theta_A)/(m_A + m_B)$ is the reduced temperature in energy units. For $\Gamma_{AB} > 1$, the species A and B are strongly coupled, and for $\Gamma_{AB} < 1$ they are weakly coupled. Unless the electron temperature Θ_e is larger than the Fermi energy Θ_F,

$$\Theta_F = \frac{\hbar^2 \left(3\pi^2 n_e\right)^{2/3}}{2 m_e} , \tag{2.121}$$

the electron system is degenerate. The degree of degeneracy is characterized by a degeneracy parameter Υ,

$$\Upsilon = \frac{\Theta_F}{\Theta_e} \,. \tag{2.122}$$

For $\Upsilon \ll 1$, the electron system can be described by a Maxwellian energy distribution at thermal equilibrium.

2.3.1 Modification of Atomic Structure

Dense plasmas can be described through *physical* or *chemical* models. In the physical models, bound and free states are treated in a consistent quantum-mechanical framework. It is the most general way to describe a plasma, but its rigorous implementation is rather difficult. In the chemical models, bound and free electron states are clearly distinguished. Plasma effects are taken into account by considering the long-range attenuation of the Coulomb interaction due to plasma screening, leading to the reduction of the number of bound states. In the physical models, these effects and degeneracy are included naturally in a self-consistent way.

2.3.1.1 Physical Models

In the simplest physical model, we consider each ion as being at the origin of a sphere of radius $R_i = (3/4\pi\, n_i)^{1/3}$, where n_i is the ion density. We then perform an electronic structure calculation for the electron density $n_e(r)$ such that the sphere is charge-neutral and $dn_e(R_i)/dr = 0$. Using $n_e(r)$, various physical quantities may be inferred. In the simplest *statistical* models, we obtain the electron density and the potential energy $V(r)$ from finite-temperature Thomas–Fermi calculations [2], typically extended to include the effects of exchange forces and electron correlation. The Thomas–Fermi model treats the electrons as a partially degenerate electron gas with a continuously varying electron density $n_e(r)$ in an electrostatic potential $\Phi_{TF}(r)$ that represents the nuclear charge Ze and the electrons themselves. With this information we can calculate various thermodynamic quantities, such as free energy and pressure, as well as the average ionization. Note that due to the proximity of the ions, they are ionized even for $T = 0$. This effect is termed *pressure ionization*. *Average ion models* extend the statistical models in that an electron structure calculation is performed, resulting in an atomic shell structure, and the levels are populated according to the Fermi–Dirac distribution.

It is the nature of the physical models to neglect penetrations of neighboring ions into the sphere of radius R_i, and whereas it allows one to calculate *average* ionization, it does not provide information about the actual distribution of charge states.

2.3.1.2 Chemical Models

Plasma screening reduces the long-range part of the Coulomb force, which affects the eigenvalues and wavefunctions of the bound electrons, leading to a reduction

of the number of atomic ground states. In a charge-neutral, weakly coupled plasma ($\Gamma \ll 1$), the screened Coulomb potential of a test charge at rest can be written as

$$\Phi_D(r) = \frac{1}{4\pi\epsilon_0}\frac{Ze}{r}e^{-r/D_e}\,, \tag{2.123}$$

where D_e is the Debye length. For strongly coupled plasmas ($\Gamma \gg 1$), the ion-sphere model is more appropriate; here, a static charge Ze is surrounded by Z electrons uniformly distributed over a sphere of radius R_i, so that the potential inside the sphere is given by

$$\Phi_{IS}(r) = \frac{1}{4\pi\epsilon_0}Z_i e\left[\frac{1}{r} - \frac{1}{2}R_i\left(3 - \frac{r^2}{R_i^2}\right)\right]. \tag{2.124}$$

2.3.1.3 Energy Level Shifts

Plasma screening is mainly due to free electrons being attracted to ions. This leads to an upward energy shift of each bound state. In the simplest description, this corresponds to the reduction of the ionization threshold by some energy ΔI, termed *continuum lowering*, and the elimination of states whose binding energy is less than ΔI. At sufficiently large densities, even occupied ground states are eliminated, leading to full atomic ionization even at zero temperature. In agreement with experiments, spectral lines do not shift significantly. Continuum lowering has a direct impact on the partition function,

$$Q(T) = \sum_{n_p=1}^{\infty} g_{n_p} e^{-\frac{E_{n_p}}{T}}\,, \tag{2.125}$$

from which other thermodynamic properties such as pressure and entropy can be derived. Here n_p is the principal quantum number. Note that $Q(T)$ would diverge for an isolated ion, but since $Q(T)$ is a statistical property it is meaningless in this case. In a plasma, an ion cannot have an infinite number of states, and $Q(T)$ is finite.

Simply truncating the summation to describe the effects of continuum lowering and pressure ionization does not lead to thermodynamically consistent results, and it is better to gradually decrease the statistical weight of highly excited states with increasing density [17]. This approach is less sensitive to the number of terms in $Q(T)$ than a simple cut-off value ΔI. With increasing density, excited ions perturb nearby ions, so that quasi-molecular states and eventually conduction bands form.

In a plasma, space- and time-dependent fluctuations create a microscopic electric field that gives rise to spatially-varying perturbing configurations, so that, more realistically, one single value for ΔI cannot be applied to all ions. It is more accurate to describe the plasma as an ensemble average of perturbed ionic states than by a single average ion.

2.3.2
Modification of Atomic Processes

The study of atomic processes occurring in a plasma environment is an active area of research, but some general statements can be made [18]. Besides perturbing the atomic states, the plasma environment screens long-range forces and alters atomic transition rates, especially for processes involving outer electrons, such as electron impact ionization. Radiative rates also change since changes in the atomic wavefunctions leads to changes in oscillator strengths and Einstein coefficients. Generally, plasma screening reduces line strengths. The reduction factor increases toward the series limit since the oscillator sum rule still applies, and a reduction in total bound–bound oscillator strength is offset by increased bound–free contribution. Dielectronic recombination is a two-body process and is common in hot low-density plasmas. At larger densities, continuum lowering removes the highly excited ionic levels, so that less phase space is available for dielectronic recombination, and this process becomes less common.

References

1 Friedrich, H. (1998) *Theoretical Atomic Physics*, 2nd edn, Springer-Verlag, Berlin.
2 Landau, L.D. and Lifshitz, E.M. (2003) *Quantum Mechanics (Non-Relativistic Theory)*, Elsevier Science, Oxford.
3 Kohanoff, J. (2008) *Electronic Structure Calculations for Solids and Molecules: Theory and Computational Methods*, Cambridge University Press, Cambridge.
4 Martin, R.M. (2008) *Electronic Structure: Basic Theory and Practical Methods*, Cambridge University Press, Cambridge.
5 Brillouin, L. (1926) La mecanique ondulatoire de Schrödinger: Une methode generale de resolution par approximations successives. *C. R. Acad. Sci.*, **183**, 24–26.
6 Kramers, H.A. (1926) Wellenmechanik und halbzahlige Quantisierung. *Z. Phys.*, **39**, 828–840.
7 Wentzel, G. (1926) Eine Verallgemeinerung der Quantenbedingungen für die Zwecke der Wellenmechanik. *Z. Phys.*, **38**, 518–529.
8 More, R.M. (1982) Electronic energy-levels in dense plasmas. *J. Quant. Spectrosc. Radiat. Transf.*, **27**, 345–357.
9 Henke, B.L., Gullikson, E.M., and Davis, J.C. (1993) X-ray interactions: Photoabsorption, scattering, transmission, and reflection at $E = 50-30\,000$ eV, $Z = 1-92$. *Atom. Data Nucl. Data Tables*, **54**, 181–342.
10 Sobel'man, I.I., Vainshtein, L.A., and Yukov, E.A. (1995) *Excitation of Atoms and Broadening of Spectral Lines*, 2nd edn, Springer, Berlin.
11 Santra, R. (2009) Concepts in x-ray physics. *J. Phys. B.: At. Mol. Opt. Phys.*, **42**, 169801.
12 Greiner, W. (1994) *Quantum Mechanics – An Introduction*, 3rd edn, Springer, Berlin, Heidelberg.
13 Perkins, S.T., Cullen, D.E., Chen, M.H., Hubbell, J.H., Rathkopf, J., and Scofield, J. (1991) Tables and graphs of atomic subshell and relaxation data derived from the LLNL evaluated atomic data library (EADL), $Z = 1-100$. *LLNL Tech. Rep. UCRL-50400*.
14 Drake, G.W.F. (2006) *Springer Handbooks of Atomic, Molecular, and Optical Physics*, Springer, New York.
15 Lennon, M.A., Bell, K.L., Gilbody, H.B., Hughes, J.G., Kingston, A.E., Murray, M.J., and Smith, F.J. (1988) Recom-

mended data on the electron impact ionization of atoms and ions: Fluorine to nickel. *J. Phys. Chem. Ref. Data*, **17**, 1285–1363.

16 Kochur, A.G. and Popov, V.A. (2006) Shake up and shake off probabilities for L-, M-, and N-electrons in atoms with $Z = 3$ to 60. *Radiat. Phys. Chem.*, **75**, 1525–1528.

17 Zimmerman, G.B. and More, R.M. (1980) Pressure ionization in laser-fusion target simulation. *J. Quant. Spectrosc. Radiat. Transf.*, **23**, 517–522.

18 Salzmann, D. (1998) *Atomic Physics in Hot Plasmas*, Oxford University Press, New York, NY.

3
Scattering of X-Ray Radiation

In this chapter we review the principles of x-ray scattering. When an electromagnetic wave irradiates an atom or ion, a photon may be absorbed or scattered. If a photon is scattered and its energy is conserved, the photon is said to undergo elastic or Thomson or Rayleigh scattering. Elastically scattered light is useful for structural investigations using x rays, such as for x-ray crystallography or for coherent diffractive imaging. If the photon transfers energy to the atom and changes its wavelength, it is said that the photon undergoes inelastic, modified, Compton or Raman scattering. In the first part of this chapter we will describe scattering of photons by free charges like electrons and nuclei, followed by a description of scattering by bound electrons, crystals, and plasmas.

3.1
Scattering by Free Charges

We will first review the classical electromagnetic theory for scattering which is based on the periodic motion of charges in a time-varying electric field that leads to the emission of scattered radiation [1, 2]. The phenomenon of Compton scattering demonstrates that actual x-ray scattering does not follow classical electromagnetic theory and needs to be treated in a quantum theoretical framework. Nevertheless, we will still discuss the classical theory since scattering is often described and tabulated in units of classically derived expressions.

3.1.1
Classical Description (Thomson Formula)

We consider the case of a monochromatic plane wave with amplitude $\boldsymbol{E}_0 \exp[i(\boldsymbol{k}_0 \cdot \boldsymbol{r} - \omega t)]$ irradiating a free particle of charge q and mass m located at the origin. $\boldsymbol{E}_0$ is the electric field vector, and $\boldsymbol{k}_0$ is the wave vector of magnitude $2\pi/\lambda$. In vacuum, $c = \omega\lambda/2\pi$, where c is the velocity of light, λ is the wavelength, and ω is the frequency. The electric field accelerates the particle, and therefore radiation is emitted. In classical nonrelativistic electrodynamics, the incident and emitted radiation have the same frequency. From Maxwell equations (1.5) to (1.8) it can

High-Intensity X-rays – Interaction with Matter, First Edition. Stefan P. Hau-Riege.

be derived [3] that the amplitude of the scattered light at a position $\boldsymbol{r}$ far from the particle ($r \gg \lambda$) is given by

$$\boldsymbol{E}(\boldsymbol{r}, t) = -\frac{1}{4\pi\epsilon_0}\frac{1}{r}\frac{q^2}{mc^2}\boldsymbol{E}_0' \sin\theta\, e^{i(\boldsymbol{k}\cdot\boldsymbol{r}-\omega t)}\,, \tag{3.1}$$

which is often referred to as the Thomson equation. ϵ_0 is the vacuum permittivity, $\boldsymbol{k}$ is the wave vector of the scattered light, here $\boldsymbol{k} = k_0\boldsymbol{r}/r$, and $\boldsymbol{E}_0' = (\boldsymbol{r}\times\boldsymbol{E}_0)\times\boldsymbol{r}/r^2$. θ is the angle between $\boldsymbol{E}_0$ and $\boldsymbol{r}$ as sketched in Figure 3.1. The minus sign in (3.1) indicates that the scattered light is phase-shifted by an angle of π with respect to the incoming radiation.

We now consider the intensity of the scattered light, which is proportional to the square of the electric field amplitude. The differential scattering cross section of a particle is defined as

$$\frac{d\sigma_{i\to f}}{d\Omega} \equiv \frac{\text{radiated energy per time per solid angle}}{\text{incident energy per area per time}}\,. \tag{3.2}$$

For scattering by a free particle, it follows from (3.1) that

$$\frac{d\sigma_{i\to f}}{d\Omega} = \left(\frac{q^2}{4\pi\epsilon_0 mc^2}\right)^2 \sin^2\theta\,. \tag{3.3}$$

Integrating this differential cross section over all angles results in the total scattering cross section,

$$\sigma = \frac{8\pi}{3}\left(\frac{q^2}{4\pi\epsilon_0 mc^2}\right)^2. \tag{3.4}$$

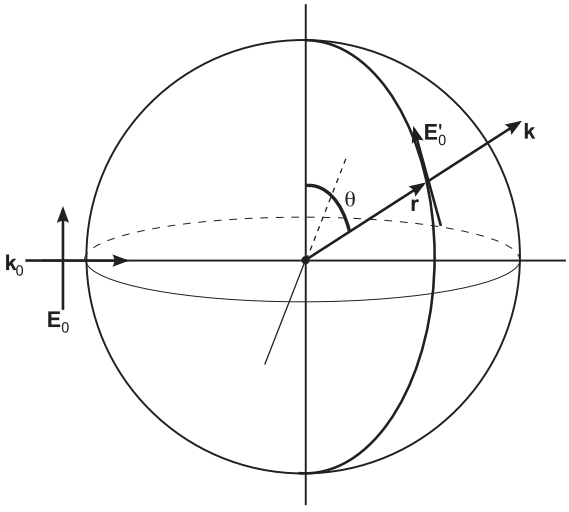

Figure 3.1 Scattering geometry for Thomson scattering.

Since $\sigma \propto m^{-2}$, scattering by atomic nuclei is much weaker than scattering by electrons and can usually be neglected.

For electrons we have $q = -e$. In this case it is common to introduce the classical electron radius,[1)]

$$r_e \equiv \frac{e^2}{4\pi\epsilon_0 mc^2} \approx 2.82 \times 10^{-13}\,\text{cm} \,. \tag{3.5}$$

The differential classical scattering cross section of a free electron can be written as

$$\frac{d\sigma_T}{d\Omega} = r_e^2 \sin^2\theta \,. \tag{3.6}$$

For unpolarized incoming light we need to average over all azimuthal angles and obtain

$$\frac{d\sigma_T}{d\Omega} = \frac{r_e^2}{2}\left(1 + \cos^2\theta\right) \,. \tag{3.7}$$

The total classical elastic scattering cross section of a free electron $\sigma_T = 8\pi r_e^2/3 \approx 0.665 \times 10^{-24}\,\text{cm}^2 = 0.665$ barn is called the Thomson cross section. From now on, we will measure the scattered light in units of light scattered classically by a free electron, $I_T = I\, d\sigma_T/d\Omega$, where I is the intensity of the incoming radiation.

3.1.2 Relativistic Quantum-Mechanical Description (Klein–Nishina Formula)

The scattering from a free electron can be described correctly only within the framework of relativistic quantum theory. Deviations from the classical theory are noticeable for short x-ray wavelengths where the photons' kinetic energy is comparable to the rest mass of the electron so that their momentum cannot be ignored. Assuming the electron is initially at rest, we can write the equations for energy and momentum conservation as [4]

$$mc^2 + \hbar c k_0 = \sqrt{m^2c^4 + p_e^2 c^2} + \hbar c k_1 \quad \text{and} \tag{3.8}$$

$$\hbar \boldsymbol{k}_0 = \hbar \boldsymbol{k}_1 + \boldsymbol{p}_e \,. \tag{3.9}$$

Here, $\boldsymbol{k}_0 = 2\pi/\lambda_0$ and $\boldsymbol{k}_1 = 2\pi/\lambda_1$ are the wave vectors of the incoming and scattered light, respectively, and $\boldsymbol{p}_e$ is the momentum of the electron after the scattering took place. It can be shown that the energy of the scattered photon $\hbar\omega_1$ is then given by [3]

$$\hbar\omega_1 = \frac{\hbar\omega_0}{1 + \frac{\hbar\omega_0}{mc^2}(1 - \cos\theta)} \,, \tag{3.10}$$

1) The classical electron radius is obtained by equating the electrostatic energy of a uniformly charged sphere of charge $-e$ to its rest mass mc^2.

where $\hbar\omega_0$ is the photon energy of the incoming radiation field and θ is the scattering angle. In the nonrelativistic limit $mc^2 \gg \hbar\omega_1$, and (3.10) simplifies to $\hbar\omega_0 - \hbar\omega_1 = \hbar^2 k^2/2m_e$ with $k = 2k_0 \sin(\theta/2)$. The magnitude of this energy shift is significant for scatterers with small mass, such as for electrons. The maximum Compton shift occurs in back-reflection for $\theta = 180°$. Using relativistic quantum mechanics, the differential scattering cross section for Compton scattering of unpolarized light can be derived to be [5]

$$\frac{d\sigma}{d\Omega} = \frac{r_e^2}{2}\left(\frac{\omega_1}{\omega_0}\right)^2\left(\frac{\omega_1}{\omega_0} + \frac{\omega_0}{\omega_1} - \sin^2\theta\right). \tag{3.11}$$

This equation is referred to as the Klein–Nishina formula. In the elastic limit $\omega_1 \to \omega_0$, and (3.11) reduces to the classical Thomson scattering result, see (3.7).

3.2 Scattering by Atoms and Ions

The amplitude of the light scattered by atoms is usually given in units of the classical scattering amplitude of a free electron, see (3.1). The proportionality factor $f(\boldsymbol{q}, \omega)$ is called the atomic form factor, often also referred to as the atomic structure factor. For small scattering angles and for photon energies much larger than atomic transition energies, f is close to the number of electrons Z in the atom. f drops rapidly for larger scattering angles [2]. In general, f is a complex number that can be calculated from the atomic properties. Around atomic resonances, f is strongly energy-dependent. The imaginary part of f relates to the absorption of photons and tends to zero for very high photon energies beyond the absorption edges.

3.2.1 Quantum-Mechanical Treatment of Scattering

In classical calculations, electrons are treated as point charges located in the vicinity of the atomic nucleus. Classical theory is not able to explain various important scattering phenomena, including inelastic Compton scattering. Realistic values for f can only be obtained from quantum theory. In such calculations, expressions for the scattered radiation are obtained assuming an electromagnetic wave falls onto an atom whose wavefunction is known in the unperturbed state. We will now calculate photon scattering from an atom by treating both the atom and the radiation together as a quantized system as introduced in Section 2.2.1.1. The primary goal is to give the reader a sense of the origin of the quantum-mechanical aspects of the atomic structure factor. There are a variety of more precise theoretical techniques available to calculate light scattering by atoms, for example the relativistic S-matrix approach [6, 7].

A simpler approximate semiclassical treatment is described in the classic book by James [8], which is based on the calculation of the time dependence of the probability current $\boldsymbol{J}$ in an atom that is exposed to a weak electromagnetic plane wave. The probability current describes the flow of the probability density in a quantum-

mechanical system. For scattering, $-e\boldsymbol{J}$ is identified with an oscillating electric current density, from which one can calculate the emitted radiation using classical electromagnetic theory. Our fully quantum theoretical approach gives results similar to this semiclassical treatment but has the advantage that it can readily be extended to higher-intensity x-ray fields.

3.2.1.1 Scattering by Atoms

Since the interaction between the radiation field with the atom is small, we follow the perturbative treatment summarized in Section 2.2.1.1. The unperturbed system can be described by the state vector

$$|\text{atom} + \text{radiation}\rangle = |q\rangle|\ldots n_{\boldsymbol{k}\sigma}\ldots\rangle \,. \tag{3.12}$$

Here, $|q\rangle$ represents the atomic state, and $|\ldots n_{\boldsymbol{k}\sigma}\ldots\rangle$ is an eigenstate of the radiation field with $n_{\boldsymbol{k}\sigma}$ photons in the mode characterized by wave vector $\boldsymbol{k}$ and polarization σ. The states $|\ldots n_{\boldsymbol{k}\sigma}\ldots\rangle$ are chosen to be orthonormal.

During the scattering process, a photon is removed from the radiation mode $\boldsymbol{k}_i\sigma_i$ and is added to the radiation mode $\boldsymbol{k}_f\sigma_f$. This two-photon process requires both an annihilation (a_i) and a creation operator (a_f^*). To first order in the interaction Hamiltonian (2.96), we therefore need to consider the $\boldsymbol{A}^2$ term $H_{int}^{(2)}$ given by (2.100), whereas the $\boldsymbol{pA}$ term (2.99) is linear in $\boldsymbol{A}$ and does not have to be considered.

We can write the initial state of the system as

$$|\text{initial}\rangle = |q_i\rangle|\ldots n_{\boldsymbol{k}_i\sigma_i}\ldots n_{\boldsymbol{k}_f\sigma_f}\ldots\rangle \,, \tag{3.13}$$

and the final state as

$$|\text{final}\rangle = |q_f\rangle|\ldots n_{\boldsymbol{k}_i\sigma_i} - 1\ldots n_{\boldsymbol{k}_f\sigma_f} + 1\ldots\rangle \,. \tag{3.14}$$

The scattering matrix element $M_{i\to f}$ given by (2.103) can then be written as

$$M_{i\to f} = \langle\text{final}|H_{int}^{(2)}|\text{initial}\rangle \tag{3.15}$$

$$= \langle q_f|\langle\ldots n_{\boldsymbol{k}_i\sigma_i} - 1\ldots n_{\boldsymbol{k}_f\sigma_f} + 1\ldots|H_{int}^{(2)} |q_i\rangle|\ldots n_{\boldsymbol{k}_i\sigma_i}\ldots n_{\boldsymbol{k}_f\sigma_f}\ldots\rangle \,. \tag{3.16}$$

Since $a_{\boldsymbol{k}\sigma}|\ldots n_{\boldsymbol{k}\sigma}\ldots\rangle = \sqrt{n_{\boldsymbol{k}\sigma}}|\ldots n_{\boldsymbol{k}\sigma} - 1\ldots\rangle$ and $a_{\boldsymbol{k}\sigma}^*|\ldots n_{\boldsymbol{k}\sigma}\ldots\rangle = \sqrt{n_{\boldsymbol{k}\sigma}+1}$ $|\ldots n_{\boldsymbol{k}\sigma}+1\ldots\rangle$, and the eigenstates are orthonormal, we can rewrite (3.16) as

$$M_{i\to f} = \langle q_f|\langle\ldots n_{\boldsymbol{k}_i\sigma_i} - 1\ldots n_{\boldsymbol{k}_f\sigma_f} + 1\ldots|\frac{\hbar}{4\epsilon_0 V\sqrt{\omega_i\omega_f}} \times \left(\boldsymbol{\epsilon}_i\cdot\boldsymbol{\epsilon}_f\right)\left[a_i a_f^* e^{i\left(\boldsymbol{k}_f-\boldsymbol{k}_i\right)\cdot\boldsymbol{r}} + a_f^* a_i e^{i\left(\boldsymbol{k}_f-\boldsymbol{k}_i\right)\cdot\boldsymbol{r}}\right] |\ldots n_{\boldsymbol{k}_i\sigma_i}\ldots n_{\boldsymbol{k}_f\sigma_f}\ldots\rangle|q_f\rangle \tag{3.17}$$

$$= r_e\frac{2\pi\hbar c^2}{\sqrt{\omega_i\omega_f}V}\left(\boldsymbol{\epsilon}_i\cdot\boldsymbol{\epsilon}_f\right) f_{i\to f}(\boldsymbol{q})\sqrt{n_i}\sqrt{n_f+1} \,, \tag{3.18}$$

with

$$f_{i\to f}(\boldsymbol{q}) = \langle q_f | e^{i\boldsymbol{q}\cdot\boldsymbol{r}} | q_i \rangle \,, \tag{3.19}$$

and $\boldsymbol{q} = \boldsymbol{k}_f - \boldsymbol{k}_i$. r_e is the classical electron radius defined by (3.5). Using the discrete form of Fermi's Golden Rule, we can write the transition rate (2.102) to the first order in $H^{(2)}_{int}$ as

$$\omega_{i\to f} = r_e^2 \frac{(2\pi)^3 \hbar c^4}{\omega_i \omega_f V^2} \left|\boldsymbol{\epsilon}_i \cdot \boldsymbol{\epsilon}_f\right|^2 |f_{i\to f}(\boldsymbol{q})|^2 n_i (n_f + 1) \delta(E_f - E_i) \,. \tag{3.20}$$

The differential scattering cross section from an atomic state i into any allowed final atomic state f is then given by

$$d\sigma_{i\to f} = \sum_{\boldsymbol{k}_f} \frac{\omega_{i\to f}}{J} \tag{3.21}$$

$$= \frac{1}{J} \int_0^\infty N(\omega) \omega_{i\to f} \, d\omega \,, \tag{3.22}$$

where

$$J = \frac{n_i c}{V} \tag{3.23}$$

is the incoming photon flux,

$$N(\omega) d\Omega \, d\omega = \frac{V}{(2\pi)^3 c^3 \hbar} \omega^2 \, d\Omega \, d\omega \tag{3.24}$$

is the photon density of states, and $d\Omega$ is a solid angle. We then obtain for the differential scattering cross section (3.22)

$$\frac{d\sigma_{i\to f}}{d\Omega} = \frac{V^2}{n_i (2\pi)^4 c^4} \frac{1}{\hbar} \int_0^\infty \omega^2 \omega_{i\to f} \, d\omega \tag{3.25}$$

$$= (n_f + 1) \frac{\omega_f}{\omega_i} |f_{i\to f}(\boldsymbol{q})|^2 \left[r_e^2 \left|\boldsymbol{\epsilon}_i \cdot \boldsymbol{\epsilon}_f\right|^2 \right] \tag{3.26}$$

$$= (n_f + 1) \frac{\omega_f}{\omega_i} |f_{i\to f}(\boldsymbol{q})|^2 \frac{d\sigma_T}{d\Omega} \,, \tag{3.27}$$

where $d\sigma_T/d\Omega = r_e^2 \left|\boldsymbol{\epsilon}_i \cdot \boldsymbol{\epsilon}_f\right|^2$ is again the classical Thomson scattering cross section. The scattering cross section (3.27) is enhanced when photons are already present in the final state ($n_f > 0$). As it is usually the case and as we will assume now, $n_f = 0$.

Elastic scattering occurs when the state of the atom does not change, so that $i = f$. In this case, the scattering by the atom is described by the atomic structure

factor $f_{n,n}(\boldsymbol{q})$, which for an atom with N electrons can be written as

$$f_{n,n}(\boldsymbol{q}) = \langle q_n | \sum_{k=1}^{N} e^{i\boldsymbol{q}\cdot\boldsymbol{r}_k} | q_n \rangle \tag{3.28}$$

$$= \int |\Psi_n(\boldsymbol{r}_1, \boldsymbol{r}_2, \ldots, \boldsymbol{r}_N)|^2 \sum_{k=1}^{N} e^{i\boldsymbol{q}\cdot\boldsymbol{r}_k} d\,V_1\, d\,V_2 \cdots d\,V_N \,. \tag{3.29}$$

Equation 3.29 is referred to as the nonrelativistic form factor approximation. We can use it to calculate the elastic structure factor of light atoms in different ionization states by calculating the electronic wavefunctions, extracting the electron densities, and simply taking the Fourier transform.

For inelastic scattering, $i \neq f$. The total inelastic scattering cross section can be obtained by summing (3.27) over all final states f. If the photon energy is much larger than the atomic transition energies, $\omega_i \approx \omega_f$, and we obtain for the intensity of the elastically scattered light

$$I_{elastic} = |f_{n,n}(\boldsymbol{q})|^2 I_T \,, \tag{3.30}$$

and the total intensity of the scattered light is given by

$$I = I_{elastic} + I_{inelastic} \tag{3.31}$$

$$= \sum_f |f_{i\to f}(\boldsymbol{q})|^2 I_T \,. \tag{3.32}$$

The derivation of (3.32) from (3.27) is based on the orthonormality of the atomic states and is described in [8].

Often $\Psi_n(\boldsymbol{r}_1, \boldsymbol{r}_2, \ldots, \boldsymbol{r}_N)$ can be approximated by a Slater determinant of one-particle states[2] as discussed in Section 2.1.4,

$$\Psi_n(\boldsymbol{r}_1, \boldsymbol{r}_2, \ldots, \boldsymbol{r}_N) = \frac{1}{\sqrt{N!}} \begin{vmatrix} \psi_1(\boldsymbol{r}_1, s_1) & \ldots & \psi_1(\boldsymbol{r}_N, s_N) \\ \vdots & & \vdots \\ \psi_N(\boldsymbol{r}_1, s_1) & \ldots & \psi_N(\boldsymbol{r}_N, s_N) \end{vmatrix} , \tag{3.33}$$

where $\psi_k(\boldsymbol{r}_i, s_i)$ are spin orbitals. The subscript k identifies a particular choice of the four quantum numbers n, l, m_l, and m_s, and $\boldsymbol{r}_i$ and s_i represent the space and spin coordinates of the ith electron. Using (3.29), the atomic structure factor is then given by the sum of the structure factors of the individual electronic wavefunctions f_k,

$$f_{n,n}(\boldsymbol{q}) = \sum_{k=1}^{N} f_k(\boldsymbol{q}) \,, \tag{3.34}$$

with

$$f_k(\boldsymbol{q}) = \int |\psi_k(\boldsymbol{r})|^2 \, e^{i\boldsymbol{q}\cdot\boldsymbol{r}} \, d\,V \,. \tag{3.35}$$

2) For open-shell systems, the wavefunction Ψ_n is usually written as a linear combination of multiple Slater determinants.

According to (3.30), the elastic part of the scattered intensity is

$$\frac{I_{elastic}(\boldsymbol{q})}{I_T} = \left| \sum_{k=1}^{N} f_k(\boldsymbol{q}) \right|^2 = |f_{n,n}(\boldsymbol{q})|^2 \,. \tag{3.36}$$

The inelastic part of the scattered intensity is then according to (3.31) and (3.32)

$$\frac{I_{inel}(\boldsymbol{q})}{I_T} = \sum_{k=1}^{N} \left(1 - |f_k(\boldsymbol{q})|^2\right) - \sum_{j,k=1, j\neq k}^{N} \left|f_{j,k}(\boldsymbol{q})\right|^2 \tag{3.37}$$

$$= Z - \sum_{k=1}^{N} |f_k(\boldsymbol{q})|^2 - \sum_{j,k=1, j\neq k}^{N} \left|f_{j,k}(\boldsymbol{q})\right|^2 \tag{3.38}$$

with $Z \equiv N$ and

$$f_{j,k} = \int \psi_j^*(\boldsymbol{r}) e^{i\boldsymbol{q}\cdot\boldsymbol{r}} \psi_k(\boldsymbol{r}) dV \tag{3.39}$$

in case electrons j and k have the same spin. If the electron spins are different, $f_{j,k} = 0$.

3.2.1.2 Tabulated Atomic Structure Factors

In the vicinity of atomic resonances, inelastic scattering beyond the form factor approximation given by (3.29) needs to be considered. Lets call $f_0(\boldsymbol{q})$ the atomic structure factor far from resonant energy levels, so that it is independent of the photon energy. We can calculate a complex correction for the atomic form factor, $\Delta f(\boldsymbol{q}, \omega) = \Delta f'(\boldsymbol{q}, \omega) + i\Delta f''(\boldsymbol{q}, \omega)$ that accounts for the dispersion. Whereas $f_0(\boldsymbol{q})$ strongly depends on the scattering angle, the angular dependence of Δf is often small and can be neglected [9]. We can then approximate $f(\boldsymbol{q}, \omega) \approx f_0(\boldsymbol{q}) + \Delta f'(\omega) + i\Delta f''(\omega)$. Values for the dispersion correction are tabulated in the International Tables for Crystallography, Vol. C [10].

The atomic structure factors that describe elastic scattering by isolated atoms and ions in their ground state are usually given in the form of fitting parameters to simple algebraic expressions, such as

$$f(q) = c + \sum_{i=1}^{n} a_i + e^{-b_i q^2} \,. \tag{3.40}$$

n is the number of terms in this expansion. Fitting parameters $\{c, a_1, a_2, \ldots, a_5\}$ for low-Z elements are given for example in [10, 11]. In (3.40), the atomic structure factor is assumed to be spherically symmetric. Since the atomic structure factor simply relates to the Fourier transform of the electron density, it is easy to deal with deviations from spherical symmetry, as for example due to chemical bonding. However, these effects are usually small and can be ignored. In case they have to be taken into account, it is useful to perform a multipole expansion of the electron density.

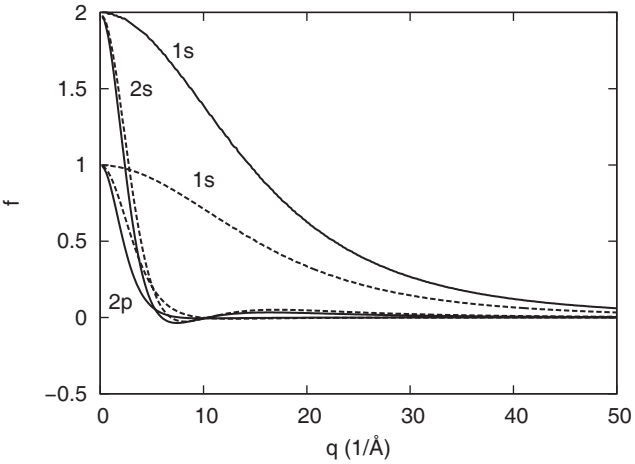

Figure 3.2 Atomic structure factors of the 1s, 2s, and 2p subshells f_n in neutral carbon (solid lines) and in carbon with a single core hole (dashed lines) [12]. Reprinted figure with permission from [12]. Copyright (2007) by the American Physical Society.

When x rays interact with atoms, photoionization often occurs, leading to the removal of electrons from different atomic subshells. In this case, we can still use the form factor approximation to calculate the elastic structure factor of ions in different ionization states by calculating the electronic wavefunctions, extracting the electron densities, and taking the Fourier transform. The atomic form factor $f(q)$ can be written as the sum of the atomic form factors $f_n(q)$ of the occupied orbitals n, see (3.34). As an example, Figure 3.2 shows the atomic structure factors of the 1s, 2s, and 2p subshells $f_n(q)$ in neutral carbon and in carbon with a single core hole. $f_n(0)$ is equal to the natural orbital occupation number. With increasing q, $f_n(q)$ drops once $1/q$ is smaller than the size of the atomic subshell. The electrons from all subshells contribute similarly to the atomic structure factor for small q, whereas for larger q only the inner subshells contribute significantly. Note that core ionization does not only affect f_{1s} but also f_{2s} and f_{2p} due to electronic rearrangement (core relaxation).

3.3
Scattering by Gases, Liquids, and Amorphous Solids

We now consider the scattering of an electromagnetic plane wave with wave vector $\boldsymbol{k}_0$ and frequency ω_0 by a system of N identical atoms, such as a gas, liquid, or amorphous solid, where each atom contains Z bound electrons. The wave vector and frequency of the outgoing light are $\boldsymbol{k}_1$ and ω_1, respectively. We denote the scattering vector by $\boldsymbol{q} \equiv \boldsymbol{k}_1 - \boldsymbol{k}_0$, as sketched in Figure 3.3, and the (negative) energy transfer from the incoming light onto the scatterer by $\hbar\omega \equiv \hbar\omega_1 - \hbar\omega_0$. At first glance it seems that the positions of the atoms are completely random, and we sim-

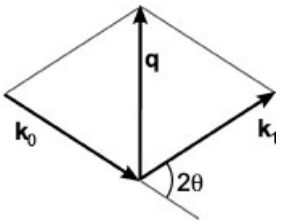

Figure 3.3 Relation of the scattering vectors.

ply would have to add the intensities of the light scattered by each atom. However, each atom occupies a finite volume in space, and atoms cannot get infinitesimally close, giving rise to structure in the material that is observable in the diffraction pattern. We will now calculate this pattern.

In a classical model, the electron number density of the system is given by

$$\tilde{\rho}(\boldsymbol{r}, t) = \sum_{k=1}^{N} \sum_{\alpha=1}^{Z} \delta \left[\boldsymbol{R}_k(t) + \boldsymbol{r}_{k,\alpha}(t) \right], \tag{3.41}$$

where $\boldsymbol{R}_k(t)$ is the position of atom k at time t, and $\boldsymbol{r}_{k,\alpha}(t)$ are the positions of all electrons belonging to atom k relative to the position of atom k. It is more convenient to consider the Fourier transform of the electron density instead,

$$\rho(\boldsymbol{q}, t) = \int e^{i\boldsymbol{q}\cdot\boldsymbol{r}} \rho(\boldsymbol{r}, t) dV \tag{3.42}$$

$$= \sum_{k=1}^{N} \sum_{\alpha=1}^{Z} e^{i\boldsymbol{q}\cdot\left[\boldsymbol{R}_k(t)+\boldsymbol{r}_{k,\alpha}(t)\right]} \tag{3.43}$$

$$= \sum_{k=1}^{N} e^{i\boldsymbol{q}\cdot\boldsymbol{R}_k(t)} \sum_{\alpha=1}^{Z} e^{i\boldsymbol{q}\cdot\boldsymbol{r}_{k,\alpha}(t)} . \tag{3.44}$$

We now derive a quantum-mechanical description of the scattering process. The ensemble average of an operator $A(\boldsymbol{r}, t)$ for the electrons of a single atom described by the wavefunction Φ is

$$\langle A(\boldsymbol{r}, t) \rangle = \int \Phi^* (\boldsymbol{r}_1, \boldsymbol{r}_2, \ldots, \boldsymbol{r}_Z, t)\, A(\boldsymbol{r}, t) \Phi (\boldsymbol{r}_1, \boldsymbol{r}_2, \ldots, \boldsymbol{r}_Z, t)\, d^Z V . \tag{3.45}$$

In this notation, the atomic structure factor in (3.29) can be written as

$$f(\boldsymbol{q}) = \langle \rho_B(\boldsymbol{q}, t) \rangle \tag{3.46}$$

$$= \langle \rho_B(\boldsymbol{q}) \rangle \tag{3.47}$$

where $\rho_B(\boldsymbol{q}, t)$ is the Fourier transform of the electron number density of the bound electrons of one atom k,

$$\rho_B(\boldsymbol{q}, t) = \sum_{\alpha=1}^{Z} e^{i\boldsymbol{q}\cdot\boldsymbol{r}_{k,\alpha}(t)} . \tag{3.48}$$

We now extend the concept of averaging over a single atom to an average over a system of atoms and denote $\langle \ldots \rangle$ as the ensemble average. We also extend (3.32) and write for the intensity of the scattered light $I(\boldsymbol{q}, t)$ by an assembly of atoms

$$\frac{I(\boldsymbol{q}, t)}{I_T} = \langle \rho(\boldsymbol{q}, t) \rho^*(\boldsymbol{q}, 0) \rangle \ , \tag{3.49}$$

where I_T is the intensity of classical Thomson scattering. We approximate the electron density in (3.44) by the product of the atomic form factor $f(\boldsymbol{q})$ and the atomic density $\rho_A(\boldsymbol{q})$,

$$\rho(\boldsymbol{q}, t) \approx \left\langle \sum_{\alpha=1}^{Z} e^{i\boldsymbol{q}\cdot\boldsymbol{r}_{j,\alpha}(t)} \right\rangle \sum_{k=1}^{N} e^{i\boldsymbol{q}\cdot\boldsymbol{R}_k(t)} \tag{3.50}$$

$$= f(\boldsymbol{q}) \rho_A(\boldsymbol{q}, t) \ , \tag{3.51}$$

with

$$\rho_A(\boldsymbol{q}, t) = \sum_{k=1}^{N} e^{i\boldsymbol{q}\cdot\boldsymbol{R}_k(t)}. \tag{3.52}$$

We can then rewrite for the intensity of the scattered light, (3.49),

$$\frac{I(\boldsymbol{q}, t)}{I_T} = \sum_{j,k}^{N} \sum_{\alpha,\beta}^{Z} \left\langle e^{i\boldsymbol{q}\cdot\left[\boldsymbol{R}_k(t) + \boldsymbol{r}_{k,\alpha}(t) - \boldsymbol{R}_j(0) - \boldsymbol{r}_{j,\beta}(0)\right]} \right\rangle \tag{3.53}$$

$$= \sum_{j\neq k}^{N} \sum_{\alpha,\beta}^{Z} \left\langle e^{i\boldsymbol{q}\cdot\left[\boldsymbol{R}_k(t) + \boldsymbol{r}_{k,\alpha}(t) - \boldsymbol{R}_j(0) - \boldsymbol{r}_{j,\beta}(0)\right]} \right\rangle$$

$$+ N \sum_{k=1}^{N} \sum_{\alpha,\beta}^{Z} \left\langle e^{i\boldsymbol{q}\cdot\left[\boldsymbol{R}_k(t) - \boldsymbol{R}_k(0)\right]} e^{i\boldsymbol{q}\cdot\left[\boldsymbol{r}_{k,\alpha}(t) - \boldsymbol{r}_{k,\beta}(0)\right]} \right\rangle \tag{3.54}$$

$$= N |f(q)|^2 F_{AA}(\boldsymbol{q}, t)$$

$$+ N \left[Z F^{ce}(\boldsymbol{q}, t) - |f(q)|^2 \right] F_S(\boldsymbol{q}, t) \ , \tag{3.55}$$

where we used the intermediate scattering functions describing the atom–atom correlations

$$F_{AA}(\boldsymbol{q}, t) = \frac{1}{N} \sum_{j,k=1}^{N} \left\langle e^{i\boldsymbol{q}\cdot\left[\boldsymbol{R}_k(t) - \boldsymbol{R}_j(0)\right]} \right\rangle \quad \text{and} \tag{3.56}$$

$$F_S(\boldsymbol{q}, t) = \left\langle e^{i\boldsymbol{q}\cdot\left[\boldsymbol{R}_k(t) - \boldsymbol{R}_k(0)\right]} \right\rangle. \tag{3.57}$$

The electron–electron correlation between the core electrons of an ion is

$$Z F^{ce}(\boldsymbol{q}, t) = \left\langle \rho_B(\boldsymbol{q}, t) \rho_B^*(\boldsymbol{q}, 0) \right\rangle. \tag{3.58}$$

The first part in (3.55) represents the elastic scattering from the bound electrons that follow the motion of the nuclei, and the second part describes the inelastic scattering by the bound electrons. Taking the Fourier transform of (3.55) with respect

to time, we obtain the intensity of the scattered light as a function of momentum and energy transfer [13],

$$\frac{I(\boldsymbol{q},\omega)}{I_T} = \frac{1}{2\pi}\int_{-\infty}^{\infty} I(\boldsymbol{q},t)e^{i\omega t}dt \tag{3.59}$$

$$= N|f(q)|^2 S_{AA}(\boldsymbol{q},\omega) + NZ\int \tilde{S}^{ce}(\boldsymbol{q},\omega-\omega')S_S(\boldsymbol{q},\omega')d\omega' , \tag{3.60}$$

where S_{AA} is the atom–atom dynamic structure factor,

$$S_{AA}(\boldsymbol{q},\omega) = \frac{1}{2\pi N}\int_{-\infty}^{\infty}\sum_{j,k=1}^{N}\left\langle e^{i\boldsymbol{q}\cdot[\boldsymbol{R}_k(t)-\boldsymbol{R}_j(0)]}\right\rangle dt , \tag{3.61}$$

$S_S(\boldsymbol{q},\omega)$ is the Fourier transform of $F_S(\boldsymbol{q},t)$, and the dynamic structure factor of the bound electrons is given by

$$\tilde{S}^{ce}(\boldsymbol{q},\omega) = S^{ce}(\boldsymbol{q},\omega) - |f(q)|^2\frac{\delta(\omega)}{Z} , \tag{3.62}$$

where $S^{ce}(\boldsymbol{q},\omega)$ is the Fourier transform of $F^{ce}(\boldsymbol{q},t)$, which is, in turn, related to the matrix elements $f_{j,k}$, compare to (3.39). Integrating (3.59) over all frequencies, we obtain the scattered intensity as a function of the scattering vector $\boldsymbol{q}$ [14],

$$\frac{I(\boldsymbol{q})}{I_T} = N|f(q)|^2 S_{AA}(\boldsymbol{q}) + NZS^A_{inc}(\boldsymbol{q}) , \tag{3.63}$$

with

$$ZS^A_{inc}(\boldsymbol{q}) = \int Z\int \tilde{S}^{ce}(\boldsymbol{q},\omega-\omega')S_S(\boldsymbol{q},\omega')d\omega' d\omega \tag{3.64}$$

$$\approx Z - \sum_{j,k}^{Z}\left|f_{jk}(\boldsymbol{q})\right|^2 , \tag{3.65}$$

where $f_{jk}(\boldsymbol{q})$ is defined by (3.39). Equation 3.63 is the generalization of the scattering from a single atom, (3.37), to an assembly of atoms.

As an example, we now consider the scattering from an amorphous sample that contains N identical atoms in a volume V and that is homogeneous and isotropic. The structure of this sample may be described by the radial distribution function $\rho(r)$. In the literature, often the pair distribution function $g(r) = \rho(r)/\rho_{ave}$ is used instead, where ρ_{ave} is the average atomic density in the sample. The average number of atoms at a distance between r and $r + dr$ from any atom is $4\pi r^2\rho(r)dr$. The intensity of the elastically scattered light is [15]

$$\frac{I(q)}{I_T} = N|f(q)|^2 S_{AA}(q) + |f(q)|^2\sum_{m=1}^{N} e^{-i\boldsymbol{q}\cdot\boldsymbol{r}_m}\int_V \rho_{ave}e^{i\boldsymbol{q}\cdot\boldsymbol{r}}dV , \tag{3.66}$$

where

$$S_{AA}(q) = 1 + \frac{4\pi}{q} \int_0^\infty r[\rho(r) - \rho_{ave}] \sin(qr) dr \,. \tag{3.67}$$

The last term in (3.66) relates to the sample shape and is usually very small, even for small angles. If we neglect this term, we can invert (3.66) to obtain the radial distribution function from a measured diffraction pattern,

$$\rho(r) = \rho_{ave} + \frac{1}{2\pi^2 r} \int_0^\infty q \frac{\frac{I(q)}{N} - |f(q)|^2}{|f(q)|^2} \sin(qr) dq \,. \tag{3.68}$$

Numerical techniques are available to reduce the effects of artifacts in $\rho(r)$ due to experimental limitations to measure $I(q)$ for large q, see for example Section 10.6 in [15].

3.4 Scattering by Plasmas

Plasmas are statistical systems of mobile charged particles, such as electrons and partially or fully ionized ions. The mobility of the particles leads to a wide variety of plasma phenomena and a very rich response to electromagnetic radiation. Similar to solids and liquids, in a plasma radiation is scattered predominantly by (free and bound) electrons. The motion of particles in a plasma is complex but correlated, giving rise to structure that is apparent in the diffraction pattern.

Particle densities and temperatures in a plasma can vary over several orders of magnitude, ranging from dilute hot plasmas over metals and semiconductors to highly condensed cold matter. Hot dilute plasmas are fairly well understood, whereas plasmas in other regimes, for example warm degenerate plasmas in which quantum effects are important, are an active area of research.

Scattering of optical light has been a useful tool to probe plasmas. It allows one to measure important basic plasma parameters, including ionization states and electron temperature and density, as well as transport properties. A major limitation of optical light is that it can only penetrate low-density plasmas since electromagnetic waves with frequencies ω smaller than the plasma frequency

$$\omega_p = \left(\frac{e^2 n}{m_e \epsilon_0} \right)^{\frac{1}{2}} \tag{3.69}$$

are reflected. Here (e) is the magnitude of the electron charge, m_e is the electron mass, and n is the electron density. For higher-density plasmas, x rays are a viable alternative to optical light. Optical light interacts primarily with the free electrons and is elastically scattered. X rays, on the other hand, interact with both the free

and bound electrons, and energy can be transferred from the light to the electrons through the Compton effect, that is inelastic scattering.

To derive an expression for the angularly and spectrally resolved scattering intensity, we consider scattering by a uniform plasma with N ions. The frequency of the incoming light is much larger than the ionization energies of bound electrons and we neglect photoabsorption processes. The number of kinematically free electrons per ion is $Z_f = Z_{ion} + Z_v$, where Z_{ion} and Z_v are the number of free (ionized) electrons and number of weakly bound (valence) electrons per ion, respectively. The number of core electrons per ion is Z_b. Electrons with binding energies larger than the Compton shift are referred to as core electrons. The nuclear charge number of the ions is $Z = Z_f + Z_b$. The total electron density ρ can be written as the sum of the core-electron part ρ_c and the free-electron part ρ_f. As before, we consider the Fourier components instead of the real space representation,

$$\rho(\boldsymbol{q}, t) = \rho_c(\boldsymbol{q}, t) + \rho_f(\boldsymbol{q}, t) \tag{3.70}$$

$$= \sum_{k=1}^{ZN} e^{i\boldsymbol{q}\cdot\boldsymbol{r}_k(t)} \,. \tag{3.71}$$

Here $\boldsymbol{r}_k(t)$ is the time-dependent position vector of the kth electron. The scattered intensity of a plasma is usually described by the total dynamical structure factor $S(\boldsymbol{q}, \omega)$ of all the electrons involved in the plasma,

$$I(\boldsymbol{q}, \omega) = N I_T S(\boldsymbol{q}, \omega) \,, \tag{3.72}$$

where I_T is the intensity due to classical Thomson scattering, $\boldsymbol{k}_0$ and $\boldsymbol{k}_1$ are the wave vectors of the incoming and scattered light, respectively, and ω is the frequency shift of the scattered light. The total dynamical structure factor is the power spectrum of the intermediate scattering function $F(\boldsymbol{q}, t)$,

$$S(\boldsymbol{q}, \omega) = \frac{1}{2\pi} \int_{-\infty}^{\infty} F(\boldsymbol{q}, t) e^{i\omega t} dt \,, \tag{3.73}$$

with

$$F(\boldsymbol{q}, t) \equiv \frac{1}{N} \left\langle \rho(\boldsymbol{q}, t) \rho^*(\boldsymbol{q}, t) \right\rangle , \tag{3.74}$$

where $\langle \ldots \rangle$ denotes again the ensemble average.

Extending (3.60) to the case of a plasma, the dynamical structure factor can be written as [13]

$$S(\boldsymbol{q}, \omega) = |f_I(\boldsymbol{q}) + d(\boldsymbol{q})|^2 \, S_{II}(\boldsymbol{q}, \omega) + Z_f S^0_{ee}(\boldsymbol{q}, \omega) + Z_B \int \tilde{S}^{ce}(\boldsymbol{q}, \omega - \omega') S_s(\boldsymbol{q}, \omega') d\omega' \,. \tag{3.75}$$

This equation is valid for a wide range of plasma parameters, even for cold dense plasmas that are degenerate. The first term relates to the density correlations due

to electrons that follow the ion motion, which are the core electrons, described by the atomic structure factor $f_I(\boldsymbol{q})$, and the screening electrons surrounding the ion, described by $d(\boldsymbol{q})$. Similar to the case of a liquid, see (3.61), the ion–ion density correlation function $S_{II}(\boldsymbol{q},\omega)$ is the power spectrum of the intermediate ion–ion scattering function

$$F_{II}(\boldsymbol{q},t) = \frac{1}{N}\sum_{k=1}^{N}\sum_{l=1}^{N}\left\langle e^{i\boldsymbol{q}\cdot[\boldsymbol{R}_k(t)-\boldsymbol{R}_l(0)]}\right\rangle, \tag{3.76}$$

where $\boldsymbol{R}_k(t)$ is the time-dependent position vector of ion k. Usually S_{II} is very small for larger values of ω since ions are much heavier than electrons, and we can assume $S_{II}(\boldsymbol{q},\omega) \approx S_{II}(\boldsymbol{q})\delta(\omega)$. The first term in (3.75) also includes the correlation of the free electrons with the ions since it can be shown that the ion–electron density correlation function depends on the ion–ion density correlation function,

$$S_{eI}(\boldsymbol{q},t) = \frac{d(\boldsymbol{q})}{\sqrt{Z_f}}S_{II}(\boldsymbol{q},\omega)\ . \tag{3.77}$$

The second term in (3.75) describes the scattering from the free electrons that do not follow the ion motion. $S^0_{ee}(\boldsymbol{q},\omega)$ is the electron–electron density correlation function without the Debye-screening feature,

$$S^0_{ee}(\boldsymbol{q},\omega) = S_{ee}(\boldsymbol{q},\omega) - \frac{|d(\boldsymbol{q})|^2}{Z_f}S_{II}(\boldsymbol{q},\omega)\ . \tag{3.78}$$

The third term in (3.75) describes inelastic scattering by core electrons. The dynamic structure factor of the core electrons is $\tilde{S}^{ce}(\boldsymbol{q},\omega-\omega')$, and, similar to (3.62), $S_S(\boldsymbol{q},\omega)$ is the power spectrum of the self-motion intermediate structure factor of the ions,

$$F_S(\boldsymbol{q},t) = \left\langle e^{i\boldsymbol{q}\cdot[\boldsymbol{R}_k(t)-\boldsymbol{R}_k(0)]}\right\rangle. \tag{3.79}$$

Very often the de-Broglie wavelength of the ions is much smaller than the interatomic spacing, so that the ions are nondegenerate, whereas the de-Broglie wavelength of the electrons is comparable or larger than the electron–electron spacing, so that quantum interference effects are significant for the electrons. If this degenerate electron gas is cold, it needs to be described by the Fermi–Dirac distribution. If the frequency of the incoming light is much larger than atomic transition energies, the last term in (3.75) can be written as

$$Z_B\, S^I_{inc}(q,\omega) \approx Z_B\, \tilde{S}^{ce}(q,0)\ . \tag{3.80}$$

The dynamic structure factor in (3.75) can be extracted from measurements of the spectrally resolved scattering signal. For a given scattering angle, it features a central peak due to elastic scattering by core electrons, and a peak due to Compton scattering at somewhat lower energies. The Compton peak is Doppler-broadened

due to the finite velocities of the free electrons, characterized by their temperature or, in case of low temperatures, the Fermi energy.

The invariance of a scattering system to time inversion requires the microreversibility of physical processes, also called the principle of detailed balance. As a consequence of detailed balance, the total density correlation function must obey the relation [16]

$$S(\boldsymbol{q}, -\omega) = e^{\frac{-\hbar\omega}{kT}} S(\boldsymbol{q}, \omega) \; . \tag{3.81}$$

Integrating the dynamic structure factor $S(q, \omega)$ over all frequencies gives the static structure factor of a plasma,

$$\begin{aligned} S(q) = {} & |f_I(q) + d(q)|^2 \, S_{II}(q) + Z_f S^0_{ee}(q) \\ & + Z_B S^I_{inc}(q) \; , \end{aligned} \tag{3.82}$$

which is an extension of the usual formula for x-ray scattering, (3.59). It describes the spectrally integrated angular dependence of the scattering signal. As described above, $Z_B S^I_{inc}(q)$ corresponds to the incoherent Compton scattering produced by the bound electrons in each ion,

$$Z_B S^I_{inc}(q) \approx Z_B - \sum_{j,k} \left| f_{j,k}(q) \right|^2 , \tag{3.83}$$

where $f_{j,k}(q)$ is given by (3.39). We can identify $f_I(q) + \rho(q)$ with the structure factor of the plasma, and $Z_f S^0_{ee}(q) + Z_B S^I_{inc}(q)$ describes the inelastic structure factor. References for various models for $S(q, \omega)$ are given in Section 10.4.3.

3.5 Scattering by Crystals

Crystals exhibit translational periodicity and can be defined as a region of matter within which identical groups of atoms, each of which is called a motif or basis, are arranged in a three-dimensional translationally periodic pattern, the lattice. The periodic arrangement has a profound effect on the physical properties of crystals, including the response to x-ray radiation. We will first review key aspects of the kinematical (or geometric) theory of diffraction. Kinematical diffraction theory is based on numerous simplifying assumptions but has been very successful in describing diffraction from imperfect crystals. We will then briefly review the dynamical theory of diffraction that describes the diffraction of a wave by a perfect crystal [17, 18]. It differs from the kinematical theory in that it accounts for the response of the crystal to the incoming radiation.

As an example, we will apply kinematical and dynamical diffraction theory to calculate the intensity of x-ray diffraction signals from single crystals. It will become apparent that dynamical diffraction theory is suitable for describing diffraction from a perfect crystal, whereas kinematical diffraction theory describes a perfectly imperfect crystal. In a perfectly imperfect crystal, different volume elements

are slightly misaligned with respect to each other without correlation, so that the light diffracted by each element adds incoherently. Most real crystals lie in between these two extremes.

3.5.1 Kinematic Diffraction by Crystals

In the kinematical diffraction theory, we assume that the incident radiation does not interact with the scattered radiation, so that the phase velocity of the light is equal to the speed of light in vacuum. This is equivalent to the assumption that the index of refraction is one. We further neglect multiple scattering in the sample, so that scattered light is not rescattered. Initially, we also neglect absorption effects.

3.5.1.1 Diffraction by a Lattice of Finite Volume

We denote $\boldsymbol{a}_1$, $\boldsymbol{a}_2$, and $\boldsymbol{a}_3$ as a set of lattice vectors with which we can express every lattice point $\boldsymbol{R}_k$ in the form $\boldsymbol{R}_k = n_1\boldsymbol{a}_1 + n_2\boldsymbol{a}_2 + n_3\boldsymbol{a}_3$, where n_1, n_2, and n_3 are integers. The positions of the n atoms in the motif are designated by $\boldsymbol{r}_j$, and the elastic scattering by each atom is described by atomic structure factors f_j. We consider scattering by atoms located within a finite volume V. To describe this restriction mathematically, we introduce a simple shape function $S(\boldsymbol{r})$,

$$S(\boldsymbol{r}) = \begin{cases} 1 & \text{if } \boldsymbol{r} \text{ inside of } V\,, \\ 0 & \text{otherwise}\,. \end{cases} \tag{3.84}$$

We can then write the atomic density of the system as

$$\rho(\boldsymbol{r}) = S(\boldsymbol{r}) \sum_{n_1=-\infty}^{\infty} \sum_{n_2=-\infty}^{\infty} \sum_{n_3=-\infty}^{\infty} \sum_{k=1}^{n} \delta\left(n_1\boldsymbol{a}_1 + n_2\boldsymbol{a}_2 + n_2\boldsymbol{a}_3 + \boldsymbol{r}_k - \boldsymbol{r}\right). \tag{3.85}$$

We consider the scattering of an incoming electromagnetic plane wave with wave vector $\boldsymbol{k}_0$. The wave vector of the outgoing light is $\boldsymbol{k}_1$. We denote the scattering vector by $\boldsymbol{q} \equiv \boldsymbol{k}_1 - \boldsymbol{k}_0$, as sketched in Figure 3.3.

The amplitude of the diffracted light in units of the amplitude of classical Thomson scattering E_T, given by (3.1), is

$$\frac{E(\boldsymbol{q})}{E_T} = \int \tilde{S}(\boldsymbol{q} - \boldsymbol{q}') \sum_{n_1=-\infty}^{\infty} \sum_{n_2=-\infty}^{\infty} \sum_{n_3=-\infty}^{\infty} \sum_{k=1}^{n} f_k(\boldsymbol{q}') e^{i\boldsymbol{q}'\cdot(n_1\boldsymbol{a}_1 + n_2\boldsymbol{a}_2 + n_3\boldsymbol{a}_3 + \boldsymbol{r}_k)}\, d\boldsymbol{q}'\,. \tag{3.86}$$

Here we used the Fourier transform of the shape function,

$$\tilde{S}(\boldsymbol{q}) = \int S(\boldsymbol{r}) e^{i\boldsymbol{q}\cdot\boldsymbol{r}}\, dV\,. \tag{3.87}$$

We define the structure factor of the crystal motif as

$$F(\boldsymbol{q}) = \sum_{k=1}^{n} f_k(\boldsymbol{q}) e^{i\boldsymbol{q}\cdot\boldsymbol{r}_k} \,. \tag{3.88}$$

It can be shown that [18]

$$\sum_{n_1=-\infty}^{\infty} \sum_{n_2=-\infty}^{\infty} \sum_{n_3=-\infty}^{\infty} e^{i\boldsymbol{q}\cdot(n_1\boldsymbol{a}_1+n_2\boldsymbol{a}_2+n_3\boldsymbol{a}_3)} \tag{3.89}$$

$$= \sum_{h=-\infty}^{\infty} \sum_{k=-\infty}^{\infty} \sum_{l=-\infty}^{\infty} \delta\left(h\boldsymbol{b}_1 + k\boldsymbol{b}_2 + l\boldsymbol{b}_3 - \boldsymbol{q}\right), \tag{3.90}$$

where

$$\boldsymbol{b}_1 = 2\pi \frac{\boldsymbol{a}_2 \times \boldsymbol{a}_3}{\boldsymbol{a}_1 \cdot (\boldsymbol{a}_2 \times \boldsymbol{a}_3)} \,, \tag{3.91}$$

$$\boldsymbol{b}_2 = 2\pi \frac{\boldsymbol{a}_3 \times \boldsymbol{a}_1}{\boldsymbol{a}_1 \cdot (\boldsymbol{a}_2 \times \boldsymbol{a}_3)}, \quad \text{and} \tag{3.92}$$

$$\boldsymbol{b}_3 = 2\pi \frac{\boldsymbol{a}_1 \times \boldsymbol{a}_2}{\boldsymbol{a}_1 \cdot (\boldsymbol{a}_2 \times \boldsymbol{a}_3)} \tag{3.93}$$

are the reciprocal lattice vectors. We can then rewrite the scattering amplitude, (3.86), as

$$\frac{E(\boldsymbol{q})}{E_T} = \sum_{h=-\infty}^{\infty} \sum_{k=-\infty}^{\infty} \sum_{l=-\infty}^{\infty} F\left(h\boldsymbol{b}_1 + k\boldsymbol{b}_2 + l\boldsymbol{b}_3\right) \tilde{S}\left(\boldsymbol{q} - h\boldsymbol{b}_1 - k\boldsymbol{b}_2 - l\boldsymbol{b}_3\right) \tag{3.94}$$

For the case of an infinitely large crystal, $S(\boldsymbol{r}) = 1$, so that $\tilde{S}(\boldsymbol{q}) = \delta(\boldsymbol{q})$. Inserting this into (3.94), we see that the diffracted light consists of regularly spaced diffraction peaks at the position of the reciprocal lattice vectors $\boldsymbol{B}_{hkl} \equiv h\boldsymbol{b}_1 + k\boldsymbol{b}_2 + l\boldsymbol{b}_3$, and that the diffraction peaks exhibit the shape of delta functions. Diffraction maxima are sometimes also called reflections from the crystal. We can use the Ewald construction to find the peaks that are observed in a two-dimensional diffraction pattern: If we draw the wave vector of the incoming light $\boldsymbol{k}_0$ from a point P to the origin in reciprocal space, then diffraction peaks occur for all outgoing wave vectors $\boldsymbol{k}_1$ for which a sphere of radius k_0 around point P, the sphere of reflection, intersects a reciprocal lattice point. This geometry is sketched in Figure 3.4. An alternative interpretation of the position of the diffraction peaks is that diffraction maxima occur in directions in which the incident beam is *reflected* by a set of lattice planes, given a specific relation between the distance of the lattice planes, d_{hkl}, and the wavelength is fulfilled,

$$2d_{hkl} \sin\theta = \lambda \,. \tag{3.95}$$

Equation 3.95 is called the Bragg equation. The vector $\boldsymbol{B}_{hkl}$ is normal to the lattice plane, and d_{hkl} is given by

$$d_{hkl} = \frac{2\pi}{|\boldsymbol{B}_{hkl}|} \,. \tag{3.96}$$

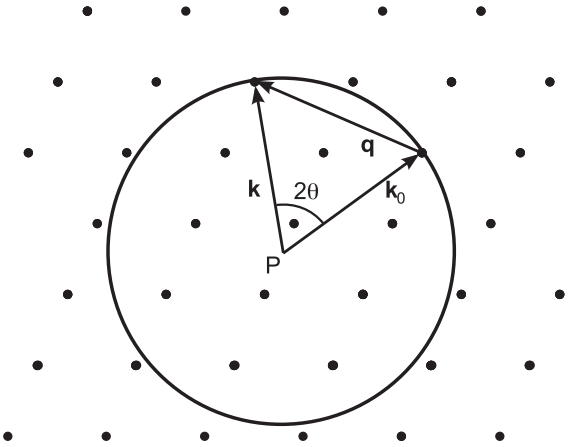

Figure 3.4 Ewald construction to determine the position of the diffraction maxima for an infinitely large crystal.

If h, k, and l have a common factor m, then the diffraction maximum can be interpreted either as the mth-order reflection from the h/m, l/m, l/m planes, or as first-order reflection from a set of planes that are parallel to the actual lattice planes but with $1/m$ of the true spacing.

For a crystal of finite size, the diffraction maxima are located at the same positions as for the infinite crystal, but their shape is now given by $\tilde{S}(\boldsymbol{q})$, which is the Fourier transform of the shape function in real space, see (3.84) and (3.87). The smaller the size of the crystal, the larger is the extent of the diffraction peaks. For example, if the crystal is a parallelepiped with N_1, N_2, and N_3 motifs in directions 1, 2, and 3, respectively, then

$$\tilde{S}(\boldsymbol{q}) = \frac{\sin\left(N_1 \boldsymbol{q}\cdot\frac{\boldsymbol{a}_1}{2}\right)}{\sin\left(\boldsymbol{q}\cdot\frac{\boldsymbol{a}_1}{2}\right)} \frac{\sin\left(N_2 \boldsymbol{q}\cdot\frac{\boldsymbol{a}_2}{2}\right)}{\sin\left(\boldsymbol{q}\cdot\frac{\boldsymbol{a}_2}{2}\right)} \frac{\sin\left(N_3 \boldsymbol{q}\cdot\frac{\boldsymbol{a}_3}{2}\right)}{\sin\left(\boldsymbol{q}\cdot\frac{\boldsymbol{a}_3}{2}\right)} \,, \tag{3.97}$$

which exhibits a center maximum around $\boldsymbol{q} = 0$. The widths of this peak are $2b_j/N_j$. This relationship is also referred to as the Scherrer equation [19, 20]. The finite size of the diffraction peaks relaxes the conditions for which diffraction maxima are observed. As shown in Figure 3.5, the diffraction peaks now have a finite extent in reciprocal space, and diffraction maxima occur whenever the Ewald sphere intersects such a peak.

3.5.1.2 Structure Factors for Monoatomic Crystals

For a monoatomic crystal, the atomic structure factor for all atoms is the same, and the structure factor of the lattice $F(\boldsymbol{q})$, given by (3.88), can be written as

$$F(\boldsymbol{q}) = f(\boldsymbol{q}) \sum_{k=1}^{n} e^{i\boldsymbol{q}\cdot\boldsymbol{r}_k} \,. \tag{3.98}$$

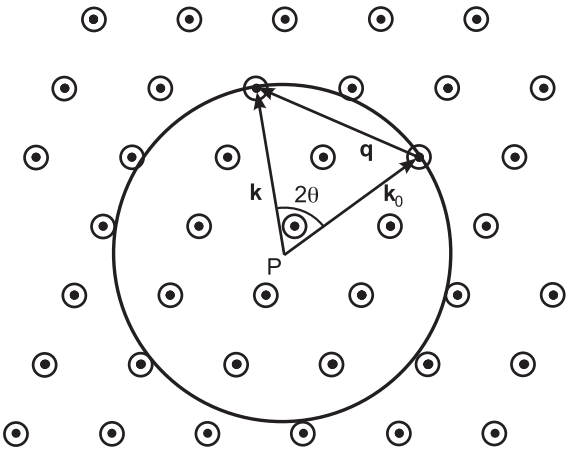

Figure 3.5 Ewald construction to determine the position of the diffraction maxima for a crystal of finite size.

$F(\boldsymbol{q})/f(\boldsymbol{q})$ is a simple geometric quantity independent of the atomic properties. For a body-centered cubic (bcc) crystal described in terms of a simple cubic lattice, the motif has two atoms, and the structure factor $F_{hkl} \equiv F(h\boldsymbol{b}_1 + k\boldsymbol{b}_2 + l\boldsymbol{b}_3)$ is given by

$$F_{hkl} = \begin{cases} 2f_{hkl} & \text{if } h+k+l \text{ is even}\,, \\ 0 & \text{otherwise}\,. \end{cases} \tag{3.99}$$

Here $\boldsymbol{b}_1$, $\boldsymbol{b}_2$, and $\boldsymbol{b}_3$ are the reciprocal lattice vectors, and $f_{hkl} \equiv f(h\boldsymbol{b}_1 + k\boldsymbol{b}_2 + l\boldsymbol{b}_3)$. For a face-centered cubic (fcc) crystal described in terms of a simple cubic lattice, the motif has four atoms, and the structure factor is given by

$$F_{hkl} = \begin{cases} 4f_{hkl} & \text{if } h,\, k, \text{ and } l \text{ are all even or all odd}\,, \\ 0 & \text{otherwise}\,. \end{cases} \tag{3.100}$$

Finally, for a hexagonal close-packed (hcp) crystal described in terms of a simple hexagonal lattice, the motif has two atoms, and the structure factor is given by

$$F_{hkl} = f_{hkl}\left\{1 + e^{2\pi i[(h+2k)/3 + l/2]}\right\}, \tag{3.101}$$

which may be real or complex, and

$$|F_{hkl}|^2 = \begin{cases} 4|f_{hkl}|^2 & \text{if } h+2k = 3n, \text{ and } l \text{ is even} \\ 3|f_{hkl}|^2 & \text{if } h+2k = 3n \pm 1, \text{ and } l \text{ is odd} \\ |f_{hkl}|^2 & \text{if } h+2k = 3n \pm 1, \text{ and } l \text{ is even} \\ 0 & \text{otherwise}\,. \end{cases} \tag{3.102}$$

3.5.1.3 Finite Temperature

At finite temperature, the atoms oscillate around their equilibrium positions. We now consider the effect of this oscillation on the diffraction pattern of an infinite crystal. To simplify the notation, we denote the position of the kth atom with atomic structure factor f_k in the system by the vector $\boldsymbol{t}_k$. If we denote the time-dependent deviation from the equilibrium position of atom k by $\boldsymbol{\delta}_k(t)$, then we can rewrite the atomic density of the system, given by (3.85), as

$$\rho(\boldsymbol{r}) = \sum_{k=1}^{n} \delta\left[\boldsymbol{t}_k + \boldsymbol{\delta}_k(t) - \boldsymbol{r}\right]. \tag{3.103}$$

The intensity of the elastically scattered light in units of the classical Thomson scattering is

$$\frac{I(\boldsymbol{q})}{I_T} = \left\langle \sum_{j=1}^{NZ}\sum_{k=1}^{NZ} f_j(\boldsymbol{q}) f_k^*(\boldsymbol{q}) e^{i\boldsymbol{q}\cdot\left[\boldsymbol{R}_j - \boldsymbol{R}_k + \boldsymbol{\delta}_j(t) - \boldsymbol{\delta}_k(t)\right]} \right\rangle, \tag{3.104}$$

where $\langle \ldots \rangle$ denote a time average. If we assume the deviation $\boldsymbol{\delta}_k(t)$ from the equilibrium positions $\boldsymbol{t}_k$ to be small, we can rewrite (3.104) as

$$\frac{I(\boldsymbol{q})}{I_T} \approx \sum_{j=1}^{NZ}\sum_{k=1}^{NZ} f_j(\boldsymbol{q}) e^{-M_j} f_k^*(\boldsymbol{q}) e^{-M_k} e^{i\boldsymbol{q}\cdot(\boldsymbol{R}_j - \boldsymbol{R}_k)} \tag{3.105}$$

$$+ \sum_{j=1}^{NZ}\sum_{k=1}^{NZ} f_j(\boldsymbol{q}) e^{-M_j} f_k^*(\boldsymbol{q}) e^{-M_k} e^{i\boldsymbol{q}\cdot(\boldsymbol{R}_j - \boldsymbol{R}_k)} \tag{3.106}$$

$$\times \left(e^{\langle(\boldsymbol{q}\cdot\boldsymbol{\delta}_k)(\boldsymbol{q}\cdot\boldsymbol{\delta}_l)\rangle} - 1 \right), \tag{3.107}$$

where

$$M_k \equiv \frac{1}{2}\left\langle (\boldsymbol{q}\cdot\boldsymbol{\delta}_k)^2 \right\rangle \tag{3.108}$$

is a measure for the square of the time average displacement in the direction of the diffraction vector. Here we have used $\langle e^{ix}\rangle \approx \langle 1 + ix - x^2/2 - ix^3/6\rangle \approx e^{-x^2}$ for small x with equal probability for x being positive and negative. The first term in (3.105) shows that the sharp crystalline reflections are reduced by the terms e^{-M_j} and e^{-M_k}. The second term represents diffuse background scattering without sharp reflection peaks since the expression $e^{\langle(\boldsymbol{q}\cdot\boldsymbol{\delta}_k)(\boldsymbol{q}\cdot\boldsymbol{\delta}_l)\rangle} - 1$ tends to zero for atoms that are far apart and are therefore uncorrelated.

For a monoatomic lattice, the intensities of the Bragg peaks are reduced by a factor of $e^{\langle(\boldsymbol{q}\cdot\boldsymbol{\delta}_k)^2\rangle}$, which is often simply written as $e^{-(q/4\pi)^2 B(T)} = e^{-(\sin\theta/\lambda)^2 B(T)}$. The temperature-dependent quantity B is called the Debye–Waller factor. Parametrizations for $B(T)$ based on experimental phonon density of states data has been derived in [21]. Figure 3.6 shows $B(T)$ as a function of temperature for aluminum and tantalum. $B(T)$ is generally lower for stiffer materials since for a given temperature, the amplitude of the lattice oscillations are smaller. Figure 3.7 shows the reduction of the Bragg reflectivity due to the atomic motion. It can be seen that this reduction is smaller for stiffer materials and for lower-order reflections.

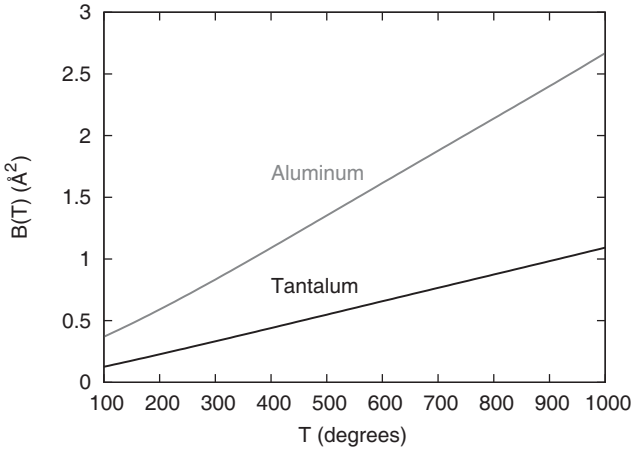

Figure 3.6 Debye–Waller factor $B(T)$ for aluminum and tantalum [21].

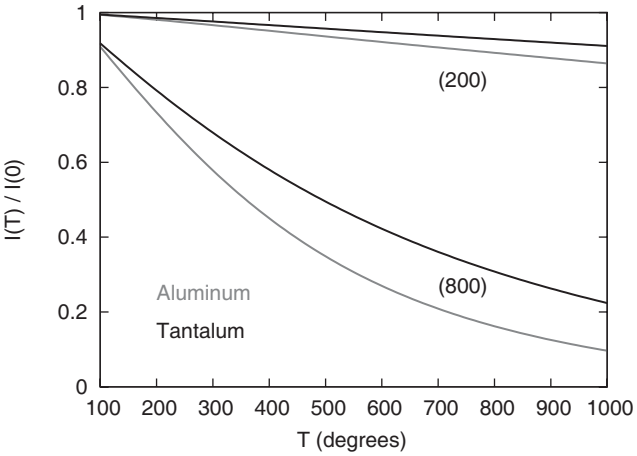

Figure 3.7 Reduction in reflectivity $I(T)$ for aluminum and tantalum for the (200) and (800) reflection [21].

3.5.1.4 Experimental Configurations

For an arbitrary incident wave vector $\boldsymbol{k}_0$, the Ewald sphere shown in Figure 3.4 will in general not pass through a second lattice point in reciprocal space. Therefore, no diffraction peaks will be observed besides the trivial forward scattered peak. To ensure the observation of nontrivial diffraction peaks, the scattering geometry has to be varied continuously, so that the Ewald sphere sweeps over a volume in reciprocal space. For example, if we irradiate the crystal by a continuous spectrum with wavelengths between λ_1 and λ_2 corresponding to parallel incoming wave vectors $\boldsymbol{k}_0^1$ and $\boldsymbol{k}_0^2$, we would observe diffraction peaks for any reciprocal lattice point that lies within the hatched region of Figure 3.8.

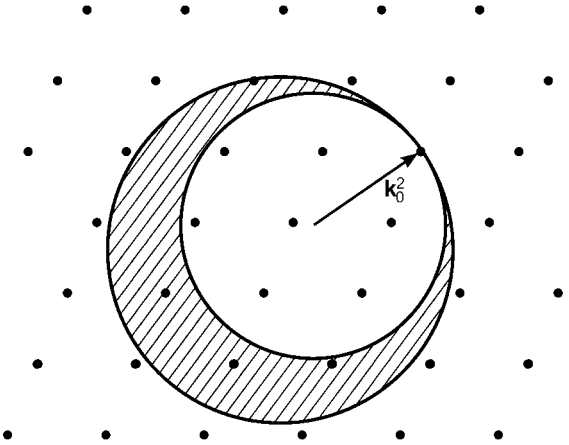

Figure 3.8 Ewald construction to determine the position of the diffraction maxima for a crystal of infinite size and a continuous spectrum.

In general, the incoming wave vector $\boldsymbol{k}_0$ is determined by three scalar variables, which can for example be taken as the wavelength λ and the scattering direction, characterized by the spherical coordinates δ and ϕ. Diffraction maxima occur whenever there exist a reciprocal lattice vector $\boldsymbol{B}_{hkl}$ such that the wave vector of the diffracted light can be written as $\boldsymbol{k}_1 = \boldsymbol{k}_0 + \boldsymbol{B}_{hkl}$. If we vary one variable continuously, we observe a diffraction pattern with sharply defined peaks. If we vary two variables continuously, for example by diffraction off a powder sample, we observe lines as the diffraction pattern. If we vary all three variables, no distinct features will be observed.

3.5.2
Dynamical Diffraction by Crystals

In the kinematical diffraction theory that we have discussed so far, we neglected the back-reflection of the reflected beam inside of the crystal. This effect is small for only a few atomic layers but becomes more significant for thicker, highly perfect crystals. This contribution can also be neglected for very imperfect crystals that are made up of small, independent diffraction units or mosaic blocks that are slightly misoriented with respect to each other. Darwin proposed the first approach for dynamical diffraction [22, 23], which is relatively intuitive and relates directly to the kinetic theory we have discussed so far, so we will follow this treatment. It is also discussed in [15]. A theoretically more satisfying approach was developed by Ewald [24] and von Laue [25] based on solving Maxwell equations directly. This theory is described in more detail in [8, 17, 18].

We will first consider reflection from a single layer of atoms, and then obtain reflection from multiple layers in the kinematical approach through simple superposition. Finally, we will present a treatment that accounts for dynamical effects.

3.5.2.1 Diffraction from a Single Layer of Atoms

We start by considering a point source of x rays called S located in front of an infinite layer of atoms arranged in unit cells in the x–y plane. The unit cells have a structure factor $F(\theta)$ and an areal density σ. The geometry is sketched in Figure 3.9a. Our goal is to obtain an expression for the scattered light at point P. We chose the origin O so that the path length $\overline{SO} + \overline{OP}$ is minimal. In [15] it is shown that the scattered electric field at point P due to linearly polarized light with an elec-

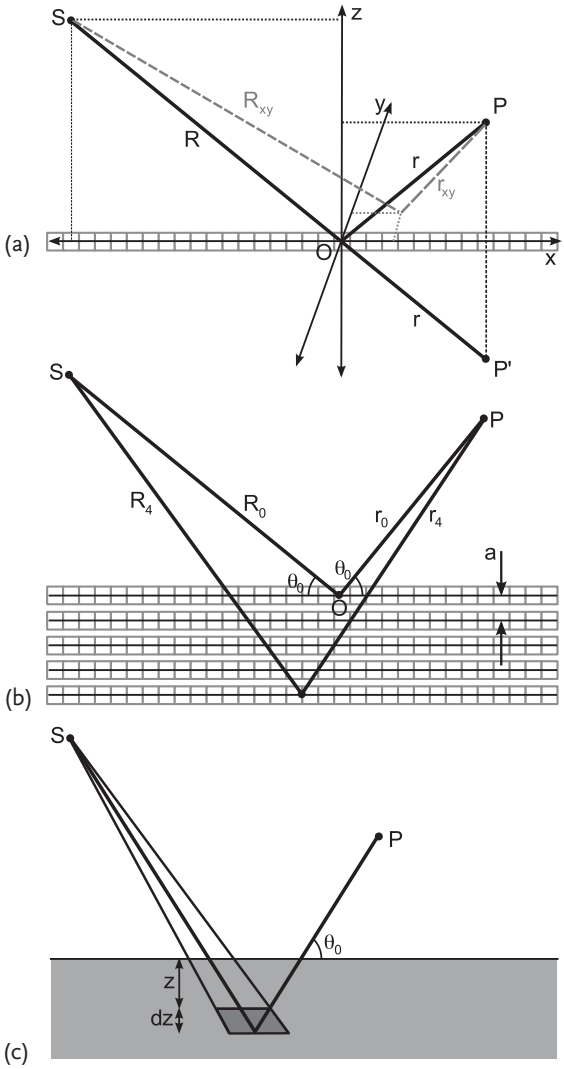

Figure 3.9 (a) Geometry to calculate the diffraction pattern from a single layer of unit cells. (b) Geometry to calculate the diffraction from several layers of unit cells. (c) Geometry to calculate the diffraction from a large mosaic crystal.

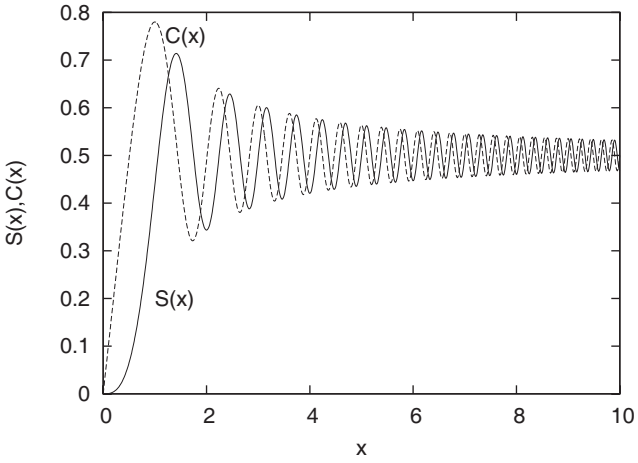

Figure 3.10 Fresnel integrals $S(x) = \int_0^x \sin(t^2)dt$ and $C(x) = \int_0^x \cos(t^2)dt$.

tric field vector $\boldsymbol{E}_0$ parallel to the y axis due to scattering from atoms in unit cells in the area element $dx\,dy$ is given by

$$dE_P = -\frac{r_e}{r_{xy}} F\left(2\theta_{xy}\right) \sigma e^{ik\left[ct-(R_{xy}+r_{xy})\right]} E_0 dx\,dy\ . \tag{3.109}$$

Integrating (3.109) over the x-y plane gives the total field in point P. Since only the area close to O contributes to the integral significantly, we approximate $\theta_{xy} \approx \theta_0$ and $r_{xy} \approx r_0$. It can be shown [15] that

$$\begin{aligned} E_P &\approx -\frac{r_e F\left(\theta_0\right) \sigma\lambda R_0}{\sin(\theta_0)(R_0+r_0)} e^{ik\left[ct-(R_0+r_0)\right]} E_0 \\ &\quad \times 2\left[C(v) - i\,S(v)\right]\left[C(u) - i\,S(u)\right] \end{aligned} \tag{3.110}$$

$$\approx i\,\frac{r_e F\left(\theta_0\right) \sigma\lambda R_0}{\sin(\theta_0)(R_0+r_0)} e^{ik\left(ct-(R_0+r_0)\right)} E_0\ , \tag{3.111}$$

with $u \equiv [2\sin^2(\theta_0)(R_0+r_0)/\lambda r_0 R_0]^{1/2} x_{\max}$ and $v \equiv [2(R_0+r_0)/\lambda r_0 R_0]^{1/2} y_{\max}$. $C(u) = \int_0^u \cos(x^2)dx$ and $S(u) = \int_0^u \sin(x^2)dx$ are the Fresnel integrals sketched in Figure 3.10. In (3.111) we assumed $u, v > 4$, so that C and S can be approximated by the value 0.5.

3.5.2.2 Kinematical Diffraction from Several Layers of Atoms

Instead of a single layer, we now consider the case of a stack of N layers of atomic unit cells, diffracting light from a point source S to a point P, as sketched in Figure 3.9b. The spacing of the layers is a. In can then be shown [15] that apply-

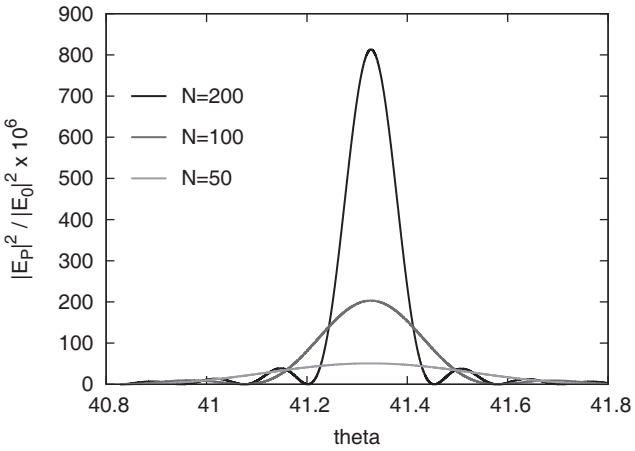

Figure 3.11 Diffracted intensity for the (220) reflection from several layers N of unit cells in (110)Ta, assuming $P = 1$ and $\lambda = 1.54\,\text{Å}$.

ing (3.111) repeatedly to each layer results in

$$E_P(\theta_0) = i\frac{r_e F(\theta_0)\,\sigma\sqrt{2\lambda^3 R_0^3 r_0}}{(R_0 + r_0)^{3/2} a \sin(2\theta_0)} e^{ik[ct-(R_0+r_0)+\rho\Delta\theta^2]} E_0 \tag{3.112}$$

$$\{C(s+u) - C(s) - i\left[S(s+u) - S(s)\right]\}, \tag{3.113}$$

with $s \equiv 2(r_0/\lambda)^{1/2}\Delta\theta$, $u \equiv 2Na\cos(\theta_B)/(r_0\lambda)^{1/2}$, and $\theta_0 = \theta_B + \Delta\theta$. Figure 3.11 shows $E_p(\theta_0)$ for the (220) reflection of (110) tantalum for different numbers of layers. For a larger number of layers N, the diffraction peak is narrower and the maximum is larger. The integrated intensity scales *linearly* with the number of layers N. The reflectivity R_N is given by

$$R_N \equiv \frac{\int_{-\infty}^{\infty} |E_p(\theta)|^2 d\theta}{|E_0|^2} \tag{3.114}$$

$$= r_e^2 N P |F(\theta_0)|^2 \frac{R_0^2}{(R_0 + r_0)^2} \frac{\lambda^3 \sigma^2 2\cos(\theta_0)}{a \sin^2(2\theta_0)}, \tag{3.115}$$

where P is the polarization factor.

Equation 3.115 is valid for a small crystal without photon absorption. We now consider the reflection from a large crystal that is made up of multiple such small crystals. We assume that the orientations of the small crystals are similar but exhibit a slight independent variation, so that the intensities of the reflected light of each small crystal add linearly. Such a perfectly imperfect crystal is called a mosaic crystal. We consider the geometry in Figure 3.9c. For the diffraction from each volume element between z and $z + dz$ we need to consider an absorption factor $\exp[-2\mu z/\sin(\theta_0)]$ for the intensity of the diffracted light, where μ is the linear absorption factor, defined as the inverse of the absorption length, so that the total

diffracted energy is

$$R \equiv \frac{\int_{-\infty}^{\infty} |E_p(\theta)|^2 d\theta}{|E_0|^2} \tag{3.116}$$

$$= r_e^2 P |F(\theta_0)|^2 \frac{R_0^2}{(R_0 + r_0)^2} \frac{\lambda^3 \sigma^2 2\cos(\theta_0)}{a \sin^2(2\theta_0)} \int_0^{\infty} e^{-\frac{2\mu z}{\sin(\theta_0)}} \frac{dz}{a} \tag{3.117}$$

$$= r_e^2 P |F(\theta_0)|^2 \frac{R_0^2}{(R_0 + r_0)^2} \frac{\lambda^3 \sigma^2}{2\mu a^2 \sin(2\theta_0)} . \tag{3.118}$$

Since $R \propto 1/\mu$, the reflectivity is higher for materials that attenuate x rays less. For very small μ, R becomes larger than 1, which is unphysical and demonstrates one of the shortcomings of the kinematic theory of diffraction.

3.5.2.3 Index of Refraction

Equation 3.111 for light scattered by a plane of unit cells also holds for scattering in the forward direction to point P' since all the path lengths are the same as for point P. In this case, $F(\theta_0)$ has to be replaced by $F(0)$. To simplify the algebra, we restrict ourselves to $R_0 \gg r_0$, and obtain from (3.111) that

$$E_{P'} = i q_0 e^{ik[ct - (R_0 + r_0)]} E_0 , \tag{3.119}$$

with

$$q_0 \equiv \frac{r_e F(0) \sigma \lambda}{\sin(\theta_0)} . \tag{3.120}$$

After transmission through a plane, the incident amplitude E_0 changes to $E_0(1 + iq_0)(1 - \beta') \approx E_0(1 + iq_0 - \beta') \approx E_0 e^{iq_0 - \beta'}$, where $0 < \beta' \ll 1$ describes the attenuation and is related to the linear absorption coefficient μ by

$$\beta' = \frac{\mu a}{2\sin(\theta_0)} . \tag{3.121}$$

Let us assume that the beam passes through several planes with spacing a, and that the angle of incidence θ_0 does not correspond to a Bragg angle, so that we can neglect the reflected beam. After passing through N planes corresponding to a distance of $l = Na/\sin(\theta_0)$, the phase of the beam has changed by $-Nq_0$, and the amplitude has changed by $\exp(-N\beta')$, so that we can write for the index of refraction

$$n = 1 - \beta' - i\beta , \tag{3.122}$$

$$\delta = \frac{q_0 \sin(\theta_0)}{ka} = \frac{r_e \lambda}{k} \rho_a F(0) , \quad \text{and} \tag{3.123}$$

$$\beta = \frac{\beta' \sin(\theta_0)}{ka} = \frac{\mu}{2k} , \tag{3.124}$$

where ρ_a is the density of unit cells in the material.[3)]

3) In the following we neglect the case of a polar crystal in which case the reflection from a plane depends on the direction of the incoming beam. This effect is discussed in [8].

It is often convenient to include the absorption processes in the atomic scattering factor $F(0)$, often simply called f, In this case, f is a complex number, and the index of refraction becomes

$$n = 1 - \frac{r_e \lambda}{k} \rho_a (f' + i f'') \,, \tag{3.125}$$

where f' and f'' indicate the real and imaginary part of f, respectively, and

$$f' = \left(\frac{k}{r_e \rho_a \lambda} \right) \delta \,, \quad \text{and} \tag{3.126}$$

$$f'' = \left(\frac{k}{r_e \rho_a \lambda} \right) \beta \,. \tag{3.127}$$

3.5.2.4 Reflection from a Perfect Crystal

We now follow Darwin's treatment for the reflected intensity from the surface of a perfect crystal [22, 23], as is also described in detail in [15]. For simplicity, we assume $R_0 \gg r_0$, which means that the incoming light resembles a plane wave. The crystal consists of lattice planes that are spaced the distance a apart. Each crystal plane is identified by an integer $j \geq 0$, and $j = 0$ corresponds to the surface of the crystal. We denote the amplitude and phase of the total transmitted wave just above the jth layer by T_j, and the amplitude and phase of the reflected light at the same position by R_j, see Figure 3.12. Our goal is to calculate the crystal reflectivity R_0 / T_0.

To allow for absorption in the crystal, we redefine q and q_0 to be complex quantities and rewrite (3.119) and (3.120) as

$$E_P = i q e^{ik[ct - (R_0 + r_0)]} E_0 \,, \tag{3.128}$$

$$E_{P'} = i q_0 e^{ik[ct - (R_0 + r_0)]} E_0 \,, \tag{3.129}$$

$$q_0 \equiv \frac{r_e F(0) \sigma \lambda}{\sin(\theta_0)} + i \frac{\mu a}{2 \sin(\theta_0)} \,, \quad \text{and} \tag{3.130}$$

$$q \equiv \frac{r_e F(\theta_0) \sigma \lambda}{\sin(\theta_0)} + i \frac{\mu a}{2 \sin(\theta_0)} \,. \tag{3.131}$$

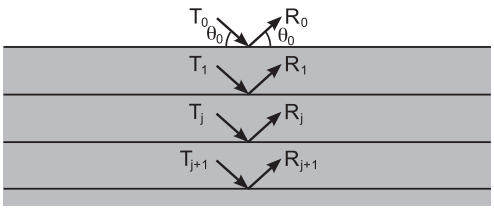

Figure 3.12 Geometry to calculate the diffraction from several layers of unit cells in a perfect crystal.

By considering the energy balance between the primary and the reflected beams, we can derive difference equations for the quantities T_j and R_j,

$$R_j = iqT_j + (1 + iq_0)e^{-i\phi} R_{j+1} , \tag{3.132}$$

$$T_{j+1} = (1 + iq_0)e^{-i\phi} T_j + iqe^{-2i\phi} R_{j+1} , \quad \text{with} \tag{3.133}$$

$$\phi \equiv ka \sin(\theta_0) . \tag{3.134}$$

From (3.132) and (3.133), we can derive a difference equation that only depends on T_{j-1}, T_j, and T_{j+1},

$$(1 + iq_0)(T_{j-1} + T_{j+1}) = \left[q^2 e^{-i\phi} + (1 + iq_0)^2 e^{-i\phi} + e^{i\phi}\right] T_j . \tag{3.135}$$

Since we are interested in the solution of this equation for a thick crystal, we set

$$T_{j+1} = xT_j \tag{3.136}$$

with $|x| < 1$ being independent of j. We can write x as

$$x = (1 - \xi)e^{-im\pi} , \tag{3.137}$$

with $|\xi| \ll 1$. If ν characterizes the deviation from the scattering geometry from the Bragg geometry,

$$ka \sin(\theta) = m\pi + \nu , \tag{3.138}$$

then it can be shown [8] that the reflectivity of a semi-infinitely thick perfect crystal is given by

$$\frac{R_0}{T_0} \approx \frac{q}{\nu - q_0 \pm \sqrt{(\nu - q_0)^2 - q^2}} , \tag{3.139}$$

where the sign in front of the square root has been chosen so that $R_0/T_0 \leq 1$.

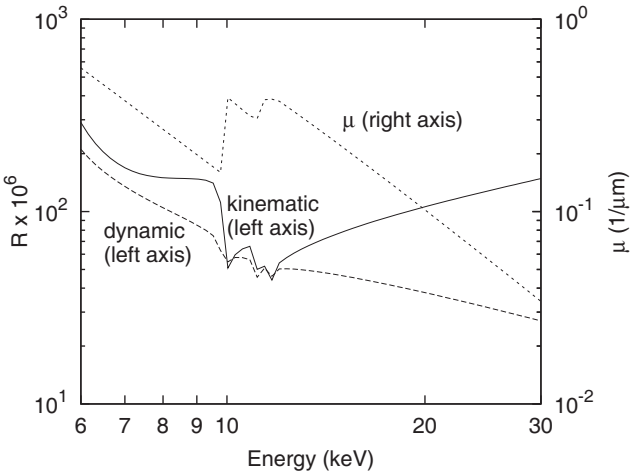

Figure 3.13 Comparison of reflectivities of (220) Ta calculated using dynamical and kinematical diffraction theory.

Figure 3.13 compares the integrated reflectivity of the (220) reflection from a Ta crystal with (110) orientation calculated using kinematical theory, see (3.116), and using dynamical theory by integrating $|R_0/T_0|^2$ from (3.139) over all angles θ. The reflectivity calculated using kinematical diffraction theory is usually much larger than the reflectivity calculated using dynamical theory since in dynamical theory the reflected light is reflected back into the sample, which is neglected in kinematical theory. This effect is very noticeable for large x-ray energies in Figure 3.13 since the physical attenuation due to photoabsorption and incoherent scattering tends to be lower. Actual crystal reflectivities typically lie between these two reflectivity values depending on their degree of imperfection.

References

1 Als-Nielsen, J. and McMorrow, D. (2001) *Elements of Modern X-ray Physics*, John Wiley & Sons, Ltd, Chichester.

2 Attwood, D. (2007) *Soft X-Rays and Extreme Ultraviolet Radiation: Principles and Applications*, Cambridge University Press, Cambridge.

3 Jackson, J.D. (1975) *Classical Electrodynamics*, 2nd edn, John Wiley & Sons, New York.

4 Compton, A.H. (1923) A quantum theory of the scattering of x rays by light elements. *Phys. Rev.*, **21**, 483–502.

5 Klein, O. and Nishina, T. (1929) Über die Streuung von Strahlung durch freie Elektronen nach der neuen relativistischen Quantendynamik von Dirac. *Z. Phys.*, **52**, 853–868.

6 Bergstrom Jr., P.M and Pratt, R.H. (1997) An overview of the theories used in Compton scattering calculations. *Radiat. Phys. Chem.*, **50**, 3–29.

7 Kissel, L., Pratt, R.H., and Roy, S.C. (1980) Rayleigh scattering by neutral atoms, 100 eV to 10 MeV. *Phys. Rev. A*, **22**, 1970–2004.

8 James, R.W. (1962) *Optical Principles of the Diffraction of X-Rays*, G. Bell and Sons, London.

9 Srinivasan, R. (1972) Applications of x-ray anomalous scattering in structural studies. In *Advances in Structure Research by Diffraction Methods* (eds W. Hoppe and R. Mason), Vol. 4, Pergamon Press, Oxford, pp. 105–197.

10 Prince, E. (ed.) (2004) *International Tables for Crystallography, Volume C: Mathematical, Physical and Chemical Tables*, 3rd edn, Springer, Berlin.

11 Waasmeier, D. and Kirfel, A. (1995) New analytical scattering-factor functions for free atoms and ions. *Acta Cryst. A*, **51**, 416–431.

12 Hau-Riege, S.P. (2007) X-ray atomic scattering factors of low-Z ions with a core hole. *Phys. Rev. A*, **76**, 042511.

13 Chihara, J. (2000) Interaction of photons with plasmas and liquid metals – photoabsorption and scattering. *J. Phys. Condens. Matter*, **12**, 231–247.

14 Chihara, J. (1987) Difference in x-ray scattering between metallic and nonmetallic liquids due to conduction electrons. *J. Phys. F: Met. Phys.*, **17**, 295–304.

15 Warren, B.E. (1990) *X-Ray Diffraction*, Dover Publications, New York.

16 Belkic, D. (2004) *Principles of Quantum Scattering Theory*, Institute of Physics Publishing, Bristol, UK.

17 Authier, A. (2001) *Dynamical Theory of X-Ray Diffraction*, Oxford University Press, Oxford.

18 Zachariasen, W.H. (1945) *Theory of X-ray Diffraction in Crystals*, John Wiley & Sons, New York.

19 Langford, J.I. and Wilson, A.J.C. (1978) Scherrer after sixty years: A survey and some new results in the determination of crystallite size. *J. Appl. Cryst.*, **11**, 102–113.

20 Scherrer, P. (1918) Bestimmung der Größe und der inneren Struktur von

Kolloidteilchen mittels Röntgenstrahlen. *Nachr. Ges. Wiss. Göttingen*, **26**, 98–100.

21 Gao, H.X. and Peng, L.-M. (1999) Parameterization of the temperature dependence of the Debye-Waller factors. *Acta Cryst.*, **A55**, 926–932.

22 Darwin, C.G. (1914) The theory of x-ray reflexion. Part I. *Philos. Mag. Ser. 6*, **27**, 315–333.

23 Darwin, C.G. (1914) The theory of x-ray reflexion. Part II. *Philos. Mag. Ser. 6*, **27**, 675–690.

24 Ewald, P.P. (1917) Zur Begründung der Kristalloptik III. *Ann. Phys.*, **54**, 519–597.

25 Laue, M. (1931) Die dynamische Theorie der Röntgenstrahlinterferenzen in neuer Form. *Ergeb. Exakten Naturwiss.*, **10**, 133–158.

4
Electromagnetic Wave Propagation

When an x-ray beam irradiates a material, the electric-field distribution and with that photon absorption are determined by wave propagation effects. The energy deposition profile, in turn, determines the nature of the x-ray–matter interaction process. In this chapter we review wave-propagation phenomena in continuous and structured materials, and specifically discuss applications to reflective multilayers and dispersive grazing incidence optics, which are of particular relevance for x-ray optics.

4.1
Electromagnetic Waves in Matter

The behavior of electromagnetic fields in matter can be described using Maxwell equations (1.23)–(1.26). For now, we will limit our discussion to infinitely extended (unbounded), homogeneous, isotropic media. We consider monochromatic plane harmonic waves, which are the simplest and most fundamental one-dimensional electromagnetic waves. They can be written as

$$\boldsymbol{E} = \boldsymbol{E}_0 e^{i(\boldsymbol{k}\cdot\boldsymbol{r}-\omega t)} \quad \text{and} \tag{4.1}$$

$$\boldsymbol{H} = \boldsymbol{H}_0 e^{i(\boldsymbol{k}\cdot\boldsymbol{r}-\omega t)} \,. \tag{4.2}$$

The actual physical electric and magnetic field are the real parts of $\boldsymbol{E}$ and $\boldsymbol{H}$. At each instant in time, $\boldsymbol{E}$ and $\boldsymbol{H}$ are constant on planes defined by $\boldsymbol{r}\cdot\boldsymbol{k} = \text{const}$. We can build arbitrary solutions to the Maxwell equation by linear superpositions of the plane waves (4.1) and (4.2).

We further assume that the medium is isotropic and linear so that it can be described by the permittivity $\epsilon(\omega)$, the permeability $\mu(\omega)$, and the conductivity $\sigma(\omega)$, so that

$$\boldsymbol{D} = \epsilon_0(\omega)\boldsymbol{E} \,, \tag{4.3}$$

$$\boldsymbol{B} = \mu(\omega)\boldsymbol{H} \,, \quad \text{and} \tag{4.4}$$

$$\boldsymbol{j} = \sigma(\omega)\boldsymbol{E} \,. \tag{4.5}$$

High-Intensity X-rays – Interaction with Matter, First Edition. Stefan P. Hau-Riege.

In the general dynamic case, $\epsilon_0(\omega)$ is a complex quantity due to absorption losses in the material.

The plane wave equations (4.1) and (4.2) have to fulfill Maxwell equations (1.23) to (1.26). We assume $\rho = 0$, that is the medium is charge-neutral. Inserting (4.1) and (4.2) into (1.23) to (1.26) results in

$$\boldsymbol{k} \times \boldsymbol{H} = -\frac{\omega}{c}\epsilon \boldsymbol{E} \,, \tag{4.6}$$

$$\boldsymbol{k} \times \boldsymbol{E} = \frac{\omega}{c}\mu \boldsymbol{H} \,, \tag{4.7}$$

$$\boldsymbol{k} \cdot \boldsymbol{E} = 0 \,, \quad \text{and} \tag{4.8}$$

$$\boldsymbol{k} \cdot \boldsymbol{H} = 0 \,. \tag{4.9}$$

Here we defined the generalized complex permittivity as

$$\epsilon(\omega) = \epsilon_0(\omega) + \frac{4\pi i \sigma}{\omega} \,. \tag{4.10}$$

From (4.6) to (4.9) it follows that (4.1) and (4.2) have to be transverse, which means (i) that they do not contain a component in the direction of the propagation direction $\boldsymbol{k}$, (ii) that $\boldsymbol{k}$, $\boldsymbol{E}$, and $\boldsymbol{H}$ form a right-handed, orthogonal coordinate system, and (iii) that

$$k = n\frac{\omega}{c} \,, \tag{4.11}$$

where $n(\omega) = \sqrt{\mu(\omega)\epsilon(\omega)/\mu_0\epsilon_0}$ is the complex index of refraction.

We limit our discussion to nonmagnetic materials so that $\mu = \mu_0$. In the x-ray regime, it is useful to express the complex index of refraction as $n = \sqrt{\epsilon} = 1 - \delta + i\beta$, where δ and β are small numbers. For a plane wave propagating in the positive x-direction, we obtain for the exponential part of the wavefunctions (4.1) and (4.2)

$$e^{i(\boldsymbol{k}\cdot\boldsymbol{r}-\omega t)} = e^{i\left[\frac{\omega}{c}(1-\delta)x-\omega t\right]}e^{-\frac{\omega}{c}\beta x} \,. \tag{4.12}$$

This wave decreases exponentially with increasing distance x in the direction of propagation. The distance $d = c/2\omega\beta = \lambda_0/4\pi\beta$ at which wave intensity decreases to $1/e$ of its value is called the *penetration depth*. $\lambda_0 \equiv c/\omega$ is the wavelength in vacuum. The velocity at which planes of constant phase propagate is given by

$$v = \frac{c}{1-\delta} \,. \tag{4.13}$$

Since the real part of the generalized permittivity ϵ is $(1-\delta)^2 - \beta^2$, and the imaginary part is $2\beta(1-\delta)$, the phase velocity v depends on the conductivity σ and the absorption loss in the medium through the imaginary part of ϵ.

4.1.1
Scalar Wave Propagation

In this section we assume that the medium is nondispersive. The effects of dispersion on wave propagation are discussed in Section 4.4. The medium is allowed to be inhomogeneous, so that the dielectric constant $\epsilon(\boldsymbol{r})$ depends on the position $\boldsymbol{r}$, but ϵ is assumed to be time-independent. We can then rearrange Maxwell equations to obtain [1]

$$\nabla^2 \boldsymbol{E} + 2\nabla(\boldsymbol{E} \cdot \nabla n) - \frac{n^2}{c^2}\frac{\partial^2 \boldsymbol{E}}{\partial t^2} = 0 \,. \tag{4.14}$$

A similar equation can be obtained for the magnetic field $\boldsymbol{H}$. This is very similar to a wave equation for each component of the electric field vector $\boldsymbol{E}$, except that the middle term in (4.14) couples the different component of $\boldsymbol{E}$. Whenever boundary conditions are imposed on a propagating wave, the various components of $\boldsymbol{E}$ (and $\boldsymbol{H}$) couple. In certain cases we can neglect the middle term in (4.14) and obtain an approximate wave equation for each component $u(\boldsymbol{r}, t)$ of $\boldsymbol{E}$ and $\boldsymbol{H}$,

$$\nabla^2 u - \frac{n^2}{c^2}\frac{\partial^2 u}{\partial t^2} = 0 \,. \tag{4.15}$$

Evidently, this scalar diffraction theory is much simpler than the vector theory, but it is only accurate when the diffracting structures are much larger than the wavelength.

We now consider a monochromatic continuous wave that is incident on a transverse (x, y) plane at $z = 0$, with a component of propagation in the positive z direction. We denote the field at $z = 0$ by $u(x, y, 0)$. $u(x, y, 0)$ is a very general expression for a wavefront and can describe anything from the evanescent wave inside a reflection optic to the exit wave of a photolithography mask. Our goal is to calculate the field $u(x, y, z)$ at any point $z > 0$ in a homogeneous medium. It is convenient to decompose the two-dimensional field at $z = 0$ into an angular spectrum of component plane waves, each traveling in a unique direction,

$$A(f_x, f_y, 0) = \int_{-\infty}^{\infty}\int_{-\infty}^{\infty} u(x, y, 0) e^{-2\pi i(f_x x + f_y y)} dx\, dy \,. \tag{4.16}$$

Each exponential function $e^{-2\pi i(f_x x + f_y y)}$ at $z = 0$ may be regarded as a plane wave propagating with a wave vector $\boldsymbol{k} = 2\pi/\lambda(\gamma_1 \boldsymbol{e}_x + \gamma_2 \boldsymbol{e}_y + \gamma_3 \boldsymbol{e}_z)$, where the direction cosines fulfill $\gamma_1^2 + \gamma_2^2 + \gamma_3^2 = 1$ and are given by

$$\gamma_1 = \lambda f_x \,, \tag{4.17}$$

$$\gamma_2 = \lambda f_y \,, \quad \text{and} \tag{4.18}$$

$$\gamma_3 = \sqrt{1 - \gamma_1^2 - \gamma_2^2} \,. \tag{4.19}$$

Here, $\boldsymbol{e}_x$, $\boldsymbol{e}_y$, and $\boldsymbol{e}_z$ are the Cartesian unit vectors. Each component plane wave propagates according to

$$A(f_x, f_y, z) = A(f_x, f_y, 0)e^{i\frac{2\pi}{\lambda}\gamma z} . \tag{4.20}$$

Using the inverse Fourier transformation, we can then obtain $u(x, y, z)$ at $z > 0$,

$$u(x, y, z) = \int_{-\infty}^{\infty}\int_{-\infty}^{\infty} A(f_x, f_y, z)e^{2\pi i(f_x x f_y y)} d f_x d f_y . \tag{4.21}$$

Equations 4.16, 4.20, and 4.21 describe how an arbitrary wavefront propagates from a plane at $z = 0$ to a plane at $z > 0$. We note that γ is imaginary when $\alpha^2 + \beta^2 > 1$. According to (4.20), this corresponds to rapidly attenuated evanescent waves, which are components in the spectrum of $u(x, y, 0)$ that are incompatible with a wave of wave vector $\boldsymbol{k}$ propagating in the positive z direction.

The numerical implementation of the wavefront propagation is usually done using efficient algorithms based on the fast-Fourier transformation (FFT). This description can readily be extended to nonmonochromatic cases and to include attenuation, refraction, dispersion, and even nonlinear propagation [1].

4.1.2 Laser Modes

Triggered primarily by the advent of x-ray free-electron lasers, the issue of laser light propagation in the x-ray regime has gained in significance. The cross-sectional intensity distribution of a propagating laser field is usually described in terms of electromagnetic radiation modes. Transverse electromagnetic (TEM) modes are radiation patterns with zero electric or magnetic field components in the light propagation direction, such as a plane wave. In lasers with cylindrical symmetry, TEM modes are usually best described by a combination of a Gaussian beam profile and a Laguerre Polynomial. In cylindrical coordinates, the intensity of the light at point (r, ϕ) for the mode TEM_{pl} is [2]

$$I_{pl}(r, \phi) = I_0 \frac{2p!}{(1 + \delta_{l0})\pi(p + l)!}\rho^l \left[L_p^l(\rho)\right]^2 \cos^2(l\phi)\exp^{-\rho} , \tag{4.22}$$

where $L_p^l(\rho)$ is the associated Laguerre polynomial of radial order p and azimuthal order l, $\rho = 2r^2/w^2$, and w is the spot size. Figure 4.1 shows the lowest order cylindrical TEM modes. The spot size as a function of the propagation distance z is given by

$$w^2(z) = w_0^2\left(1 + \frac{z^2}{b^2}\right), \tag{4.23}$$

where w_0 is the minimum beam radius of the lowest order mode TEM_{00}, which is Gaussian, b the confocal parameter in terms of which $w_0 = \sqrt{2b/k}$, where k is the

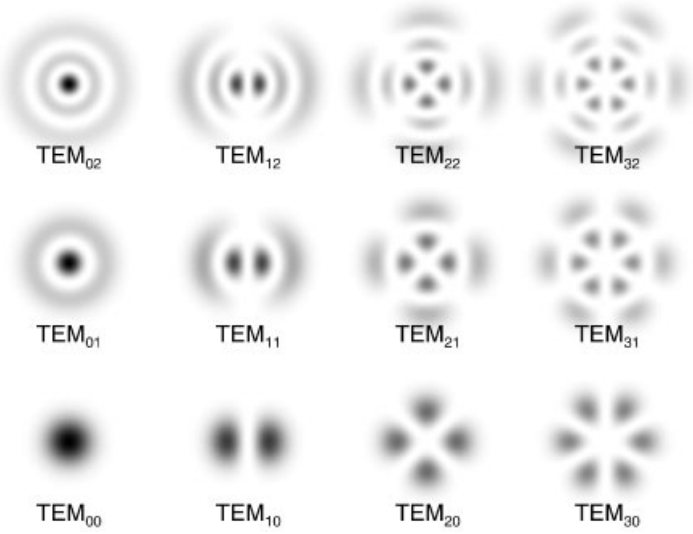

Figure 4.1 Lowest-order cylindrical transverse electromagnetic modes.

wavenumber. The radius of curvature of the phase front at any position z is given by

$$R(z) = \frac{z^2 + b^2}{z} \,. \tag{4.24}$$

Of particular practical importance is the Gaussian TEM_{00} mode which often dominates. Since $L_0^0 = 1$ [2], the areal photon density of this mode is of the form

$$\rho(x, y, z) = A_{peak}(z) e^{-2\frac{x^2+y^2}{w(z)^2}} \,, \quad \text{with} \tag{4.25}$$

$$A_{peak}(z) = \frac{2N}{\pi w(z)^2} \,, \tag{4.26}$$

where N is the total number of photons per mode. The full-width-at-half-maximum (FWHM) of the beam is given by

$$w_{FWHM}(z) = \sqrt{2 \ln 2} w(z) \,. \tag{4.27}$$

4.2
Reflection and Refraction at Interfaces

We now consider an electromagnetic wave entering a medium. The medium is assumed to be quasi-semi-infinite in extent, otherwise diffraction effects would need to be considered. At the interface, the incoming wave is both reflected and transmitted. The propagation direction of the transmitted light may be different from

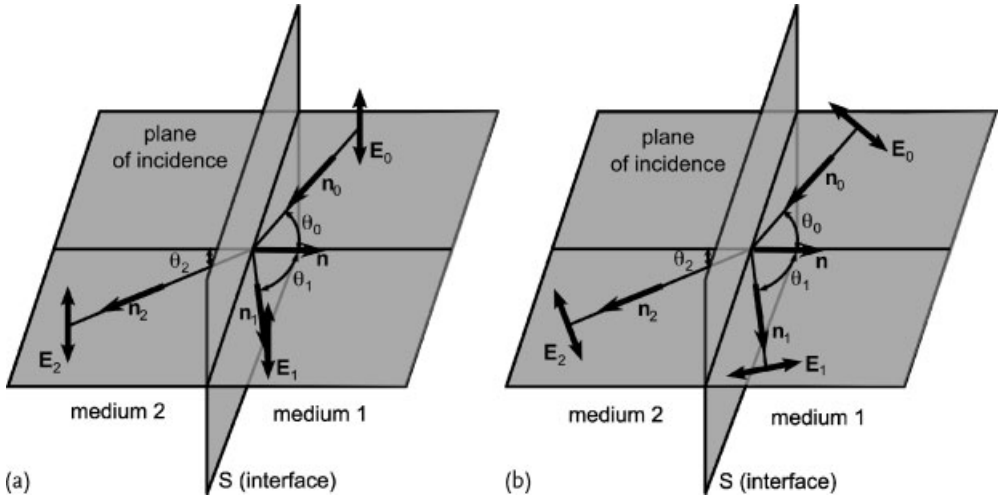

Figure 4.2 Geometry for refraction and reflection. (a) Transverse electric (TE) polarization, often also called s-polarization, and (b) transverse magnetic (TM) polarization, often also called p-polarization.

the propagation direction of the incoming light, a phenomenon called refraction. We assume that each medium is homogeneous and isotropic, and that their optical properties can be characterized by complex indices of refraction n_1 and n_2. This seemingly simple problem gives rise to a large variety of optical phenomena, including total reflection, evanescent waves, polarization, and various dispersive processes that can even change the temporal pulse structure of the reflected light [3].

We consider the geometry shown in Figure 4.2 in which a plane electromagnetic wave is incident on the boundary plane S between media (1) and (2). We denote the surface normal by $\boldsymbol{n}$, and the propagation direction of the incident wave by $\boldsymbol{n}_0$. The plane spanned by the vectors $\boldsymbol{n}$ and $\boldsymbol{n}_0$ is the *plane of incidence*. The incoming field induces oscillatory motions of free and bound charges near the interface, creating a secondary field in media (1) and (2). Maxwell's equations require certain boundary conditions at the interface S to be fulfilled. These boundary conditions determine the fields in media (1) and (2), and lead to the conditions that [4]

1. $\boldsymbol{n}$, $\boldsymbol{n}_0$, $\boldsymbol{n}_1$, $\boldsymbol{n}_2$ are all coplanar and lie in the plane of incidence,
2. the planes of constant phase of transmitted and reflected waves are normal to the plane of incidence,
3. the incident angle θ_0 is equal in magnitude to the angle of reflection θ_1, and
4. Snell's law holds,

$$n_1 \sin\theta_1 = n_2 \sin\theta_2 \ . \tag{4.28}$$

In general, θ_1 and θ_2 may be complex.

It is convenient to treat the two polarization components of the incident wave separately: For the transverse electric (TE) component, the *electric* field vector of

incoming light is perpendicular to the plane of incidence, and for the transverse magnetic (TM) component the *magnetic* field vector is perpendicular to the plane of incidence (and the electric field vector of incoming light lies in the plane of incidence). The geometries of both cases are sketched in Figure 4.2. The relationships between the electric field vectors of the incident light E_0, the reflected light E_1, and the refracted (transmitted) light E_2 is described by the *Fresnel equations*, which can be derived from Maxwell's equations [4]. For the case of TE- or s-polarization, these relations are given by

$$E_1 = \frac{n_1 \cos\theta_1 - n_2 \cos\theta_2}{n_1 \cos\theta_1 + n_2 \cos\theta_2} E_0 \,, \quad \text{and} \tag{4.29}$$

$$E_2 = \frac{2 n_1 \cos\theta_1}{n_1 \cos\theta_1 + n_2 \cos\theta_2} E_0 \,. \tag{4.30}$$

Similarly, for TM- or p-polarization, these relations are given by

$$E_1 = \frac{n_1 \cos\theta_2 - n_2 \cos\theta_1}{n_1 \cos\theta_2 + n_2 \cos\theta_1} E_0 \,, \quad \text{and} \tag{4.31}$$

$$E_2 = \frac{2 n_1 \cos\theta_1}{n_2 \cos\theta_1 + n_1 \cos\theta_2} E_0 \,. \tag{4.32}$$

In general, both the transmitted and reflected waves have phases that are different from the phase of the incident light. For normal incidence, $\theta_0 = 0$, the cases of TE- and TM polarization cannot be distinguished. Writing $n_j = 1 - \delta_j + i\beta_j$ ($j = 1, 2$), we obtain from (4.29) and (4.30) or from (4.31) and (4.32) that

$$E_1 = \frac{\delta_2 - \delta_1 + i(\beta_1 - \beta_2)}{2 - (\delta_1 + \delta_2) + i(\beta_1 + \beta_2)} E_0 \,, \quad \text{and} \tag{4.33}$$

$$E_2 = \frac{2(1 - \delta_1 + i\beta_1)}{2 - (\delta_1 + \delta_2) + i(\beta_1 + \beta_2)} E_0 \,. \tag{4.34}$$

The mean energy flow or the mean intensity is given by the real part of the Poynting vector $\bar{\boldsymbol{S}}$. In our case of a plane wave,

$$\bar{\boldsymbol{S}}_j = \frac{1}{2} \Re \left\{ \boldsymbol{E}_j \times \boldsymbol{H}_j^* \right\} = \Re \left\{ \frac{n_j}{2} |E_j|^2 \right\} \boldsymbol{n}_j \,, \tag{4.35}$$

where $j = 1, 2$ and $n_0 = n_1$. The energy per unit area incident (or leaving) the interface is $\boldsymbol{n} \cdot \bar{\boldsymbol{S}}_j$. We define the *reflection* and *transmission coefficients* as

$$R = \frac{\boldsymbol{n} \cdot \bar{\boldsymbol{S}}_1}{\boldsymbol{n} \cdot \bar{\boldsymbol{S}}_0} = \left| \frac{E_1^2}{E_0^2} \right| , \quad \text{and} \tag{4.36}$$

$$T = \frac{\boldsymbol{n} \cdot \bar{\boldsymbol{S}}_2}{\boldsymbol{n} \cdot \bar{\boldsymbol{S}}_0} = \Re \left\{ \frac{n_2 \cos\theta_2}{n_1 \cos\theta_0} \right\} \left| \frac{E_2^2}{E_0^2} \right| , \tag{4.37}$$

respectively. It can be shown that the energy is conserved, so that $R + T = 1$.

4.2.1 Electromagnetic Field in the Reflecting Medium

To understand the energy deposition of an x-ray beam in a material, it is not only important to consider the magnitude but also the polarization direction of the transmitted light, since that affects the emission of photoelectrons. We now consider the case in which the incoming wave travels from a dielectric with $\beta_1 = 0$ into a medium with index of refraction $n_2 = n = 1 - \delta + i\beta$. We continue to assume that $\mu_1 = \mu_2 = \mu_0$. For TE-polarized light, the angle of refraction θ_2 is complex, and the magnetic field of the refracted light is elliptically polarized and not completely transverse to the electric field. As we will show now, this deviation from a planar wave is small in the x-ray regime since the index of refraction is close to one.

We define

$$k_z = k_2 \cos\theta_2 \,. \tag{4.38}$$

We call the angle between the z axis and the actual propagation direction in medium (2), given by the constant-phase surfaces, η_{TE}. It can be shown that [5]

$$\tan\eta_{TE} = \frac{k_x}{k_z'} = \frac{k_x}{|k_z|\cos\alpha} \,, \tag{4.39}$$

with $k_x = k_1 \sin\theta_0 = k_2 \sin\theta_2$, $k_1 = n_1\omega c$, and k_z' denotes the real part of k_z. The surfaces of constant amplitude on the other hand are parallel to the interface $z = \text{const}$. The direction of the time-averaged Poynting vector makes an angle η with the z axis. Further, the magnetic field is elliptically polarized with a minor-axis-to-major-axis ratio of [5]

$$\tan\tau = \frac{\left(1 - \sqrt{1 - \sin^2 2\tau}\right)}{\sin 2\tau} \quad \text{with} \tag{4.40}$$

$$\sin 2\tau = \frac{2k_x k_z''}{|k_z|^2 + k_x^2} \,. \tag{4.41}$$

The minor-axis-to-major-axis ratio (4.40) is typically very small in the x-ray regime and can usually be neglected. For TM-polarized light, the electric field vector behaves similarly to the magnetic field vector in the TE case. In this case, the angle of the refracted light with the z axis is

$$\tan\eta = \frac{\tan\eta_{TE}}{1 + \tan\alpha\tan\delta} \,, \tag{4.42}$$

where α is the phase of $k_z = |k_z|e^{i\alpha}$, and δ is the phase of $\epsilon_2 = |\epsilon_2|e^{i\delta}$.

4.2.2 Polarization by Reflection

Of particular interest in x-ray spectroscopy and beam characterization is the phenomenon of polarization by reflection when light irradiates a surface near the *Brewster angle*, and only one polarization component is reflected. We consider the case

of an electromagnetic wave impinging on the planar interface between vacuum and a medium with a complex index of refraction. Using (4.29) and (4.31), we can calculate the amplitude of the reflected light. As an example, Figure 4.3 shows this amplitude in units of the amplitude of the incoming light when an 8-keV x-ray beam irradiates a semi-infinite piece of silicon, as a function of the grazing angle of incidence ϕ. For very small angles ϕ, the amplitude of the reflected light is quite appreciable. This is the phenomenon of total reflection and is discussed in more detail in Section 4.2.3. For larger angles of incidence, the material does not reflect the light appreciably since in the x-ray regime the index of refraction is close to one.[1)] Another feature that can be observed in Figure 4.3 is that the reflectivity of TM-polarized light drops sharply at around $\phi \approx 45°$. Considering the simplified case in which absorption effects can be neglected, $\beta = 0$, R_{TM} is given by

$$R_{TM} = \frac{\tan^2(\theta_0 - \theta_2)}{\tan^2(\theta_0 + \theta_2)} \,. \tag{4.43}$$

Equation 4.43 shows that R_{TM} tends to zero when $\theta_0 + \theta_2$ approaches $\phi \approx 90°$. The angle θ_0 at which this phenomenon occurs is the *Brewster angle*. In the x-ray regime, the Brewster angle is always around $\phi \approx 45°$. The Brewster angle is also called the polarizing angle because under this angle the p-component of the incident light is filtered out, and only the s-component is reflected.

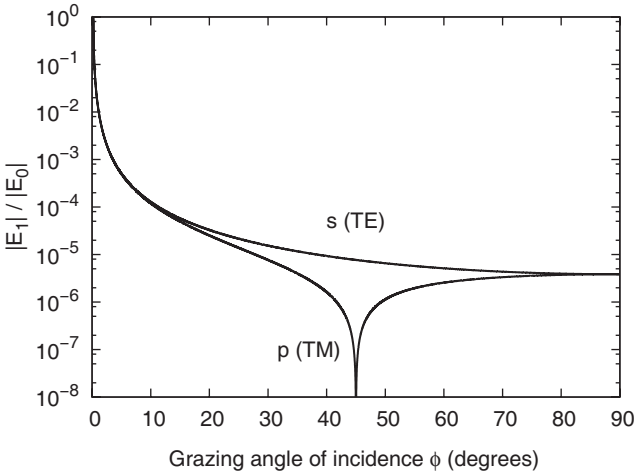

Figure 4.3 Amplitude of the reflected light $|E_1|$ in units of the amplitude of the incoming light $|E_0|$ for an 8-keV x-ray beam irradiating a slab of silicon.

1) This discussion excludes reflection associated with lattice resonances (Bragg diffraction). A unified treatment combining the effects of the lattice and macroscopic electromagnetic theory can be done in the framework of dynamical diffraction theory as described below. A computational method for this case is described in [6].

4.2.3 Critical Angle

As apparent from Figures 4.3 and 4.4, the reflectivity of a slab in vacuum approaches unity for very small grazing angles $\phi \to 0$. This phenomenon is called *total reflection* and occurs when light from a medium of higher optical density (larger index of refraction) impinges on a medium with lower optical density (smaller index of refraction). In the x-ray regime, the real part of the index of refraction $n = 1 - \delta + i\beta$ is usually slightly less than one, so that total reflection can occur when the incoming medium is vacuum. For simplicity, we first consider the absorption-free case of $\beta = 0$. We obtain from Snell's law (4.28) that total reflection occurs when

$$\sin\theta_2 = \frac{\sin\theta_1}{1-\delta} > 1 \,, \tag{4.44}$$

which can only be fulfilled for complex θ_2. A complex diffracting angle means that a phase shift occurs at the interface and that an attenuation factor is present. In this case, no energy flows into the medium on average, with $R = 1$ and $T = 0$, so that we have a perfectly reflecting mirror. We can define a critical grazing-incidence angle for total reflection ϕ_c as

$$\cos(\phi_c) = 1 - \delta \,, \tag{4.45}$$

and for small values of δ, we obtain

$$\phi_c \approx \sqrt{2\delta} \,. \tag{4.46}$$

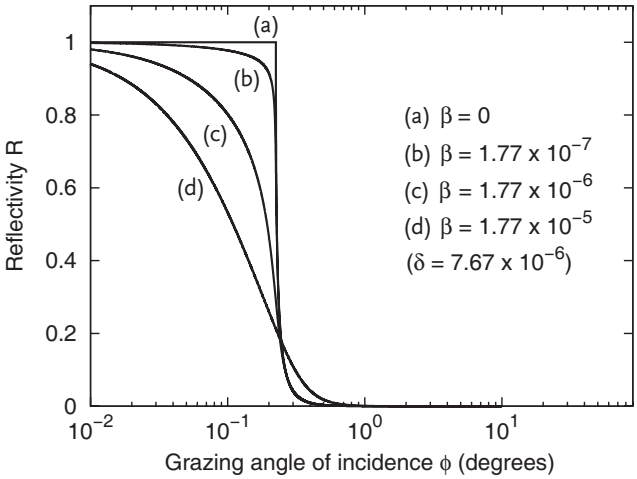

Figure 4.4 Reflectivity R of an 8-keV x-ray beam from the surface of a slab for different hypothetical values of β. Case (b) corresponds to the optical constants of silicon. The transmissivity can be calculated from $T = 1 - R$.

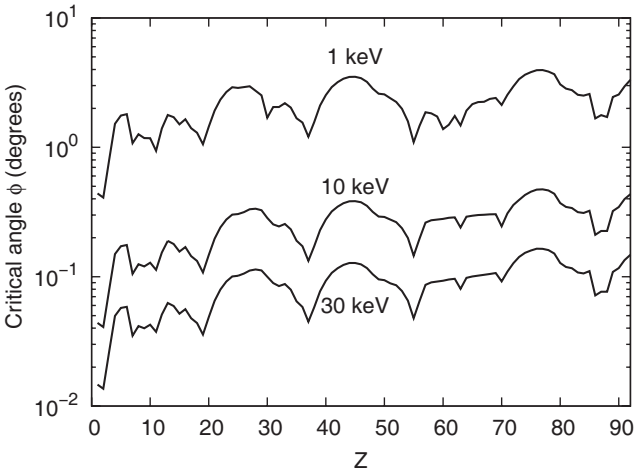

Figure 4.5 Critical angle (grazing incidence) as a function of the atomic charge number Z [7].

For an absorbing medium with $\beta > 0$, the reflectivity below the critical angle is somewhat depressed as shown in Figure 4.4, depending on the magnitudes of β and δ. Figure 4.5 shows the critical angle as a function of charge number Z for different x-ray energies. The critical angle increases weakly with Z, and it drops significantly with increasing x-ray energy.

4.2.4
Evanescent Waves for Grazing-Incidence Reflection

For a grazing angle of incidence less than the critical angle, the electric field inside the medium is not zero, even for the theoretical case of $\beta = 0$. There is an instantaneous energy flow across the surface that oscillates and whose time-average is zero. For $\beta > 0$, part of this energy leaking into the material as an evanescent wave is absorbed. The penetration of x rays into the material d_x is given by [8]

$$d_x = \frac{\lambda\rho}{4\pi\beta} \quad \text{with} \tag{4.47}$$

$$\rho = \sqrt{\frac{1}{2}\left[\sin^2\phi - 2\delta + \sqrt{\left(\sin^2\phi - 2\delta\right)^2 + 4\beta^2}\right]}\,. \tag{4.48}$$

Here, λ is wavelength, and δ and β are real and imaginary optical constants. Figure 4.6 shows d_x as a function of the grazing angle of incidence ϕ for different materials. It can be seen that d_x is quite small for small ϕ. Near and below the critical grazing angle, the penetration depth becomes constant. For near normal incidence ($\phi \to 90°$), $\rho \to 1$, and the penetration depth approaches $d_x \to \lambda/4\pi\beta$.

The dependence of d_x on the angle of incidence ϕ has a profound effect on the x-ray dose, defined as the x-ray energy deposited per unit volume in the material.

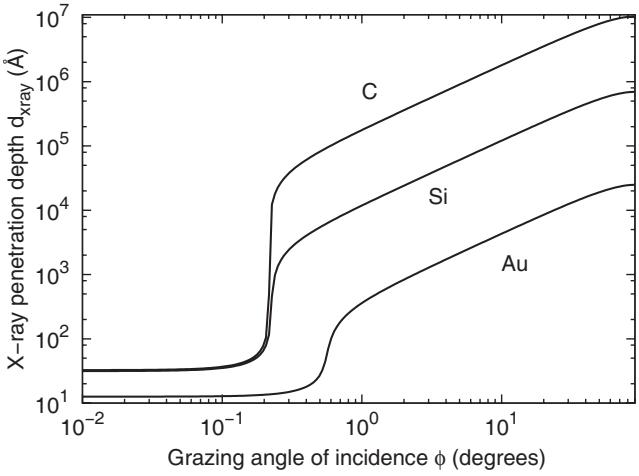

Figure 4.6 X-ray penetration depth as a function of grazing angle of incidence for graphite, silicon, and gold.

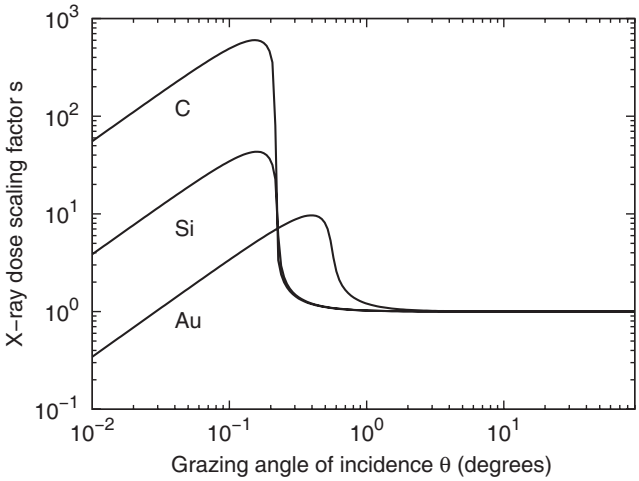

Figure 4.7 X-ray dose scaling factor s (4.49) as a function of grazing angle of incidence for graphite, silicon, and gold.

The cross-sectional area of a beam irradiating a surface under glancing angle ϕ increases by a factor of $(\sin\theta)^{-1}$ compared to normal incidence, so that the irradiance is smaller by a factor of $\sin\phi$. However, the x-ray intensity inside the material that determines the x-ray dose scales as

$$s = \sin\phi \frac{d_x(0)}{d_x(\phi)} R(\phi) \,, \tag{4.49}$$

where $R(\phi)$ is the reflectivity given by (4.36). We plotted s as a function of grazing angle of incidence ϕ for different materials in Figure 4.7. Somewhat surprisingly at first glance, s is approximately constant for large ϕ, suggesting that decreasing the grazing angle of incidence does *not* change the x-ray dose inside of the material significantly. For much smaller angles, s increases rapidly near the critical angle, and then decreases again since the x-ray penetration depth d_x levels off below the critical angle. This dependence of the x-ray dose on the angle of incidence is similar for most materials. Notice, however, that the dependence of the actual energy density in the material will be quite different since electron transport plays an important role. This is discussed in more detail in Section 1.5.3 and Chapter 5.

4.3 Reflection by Thin Films, Bilayers, and Multilayers

In the x-ray regime, reflection from a single interface is rather weak as shown in Figure 4.3, except for lattice resonances (Bragg reflection) discussed in Section 3.5, and for very small values of the grazing angle of incidence for which total reflections occurs, see Figure 4.5. In order to achieve larger reflectivity values at larger grazing angles of incidence, several layers of different materials can be stacked to produce multiple reflecting interfaces [9]. A useful design are multilayer interference coatings fabricated by depositing layers of alternating materials, typically each with very different atomic charge numbers to maximize the optical contrast. When the bilayer thickness d is in agreement with Bragg's law [10],

$$m\lambda = 2d \sin\phi \ , \tag{4.50}$$

interference effects can lead to relatively large reflectivities even for larger values of ϕ. In (4.50), $m = 1, 2, \ldots$, and ϕ is the grazing angle of incidence inside the material. When refraction is considered, ϕ should be taken as an average value over the multilayer components. The multilayer period d, averaged over the beam area, has to be precise to within a fraction of an atomic layer, and the roughness of the multilayer has to be tightly controlled [11]. Another important factor for fabricating high-reflectivity multilayers is material stability, including compound formation at the interfaces and material interdiffusion.

4.3.1 Optical Properties of a Multilayer Stack

We now provide an algorithm to calculate the optical properties, such as reflection and transmission coefficients, of a multilayer stack. This treatment closely follows the procedure outlined by Windt [12]. We consider a plane harmonic wave irradiating a multilayer stack of N layers, corresponding to $N + 1$ interfaces. The thickness and the complex index of refraction of the ith layer are d_i and n_i, respectively. The indices of refraction above and below the stack are n_0 and n_{N+1}, respectively. The

net reflection (r_i) and transmission (t_i) coefficients of the ith layer are

$$r_i = \frac{r_{ij} + r_j e^{2i\beta_i}}{1 + r_{ij} r_j e^{2i\beta_i}} , \quad \text{and} \tag{4.51}$$

$$t_i = \frac{t_{ij} t_j e^{2i\beta_i}}{1 + r_{ij} r_j e^{2i\beta_i}} , \tag{4.52}$$

where

$$\beta_i = \frac{2\pi d_i n_i \cos\theta_i}{\lambda} . \tag{4.53}$$

The angles θ_i can be determined from Snell's law (4.28),

$$n_i \sin\theta_i = n_j \sin\theta_j , \tag{4.54}$$

where θ_i are in general complex quantities. Using (4.29) and (4.30), we obtain for s-polarized light

$$r_{ij} = \frac{n_i \cos\theta_i - n_j \cos\theta_j}{n_i \cos\theta_i + n_j \cos\theta_j} , \quad \text{and} \tag{4.55}$$

$$t_{ij} = \frac{2 n_i \cos\theta_i}{n_i \cos\theta_i + n_j \cos\theta_j} , \tag{4.56}$$

whereas for p-polarized light, according to (4.31) and (4.32),

$$r_{ij} = \frac{n_i \cos\theta_j - n_j \cos\theta_i}{n_i \cos\theta_j + n_j \cos\theta_i} , \quad \text{and} \tag{4.57}$$

$$t_{ij} = \frac{2 n_i \cos\theta_i}{n_i \cos\theta_j + n_j \cos\theta_i} . \tag{4.58}$$

In order to compute the net reflection r and net transmission t of the multilayer stack, (4.51) and (4.52) have to be applied recursively, starting from the bottom-most layer, $i = N$, $j = N + 1$. This calculation can be performed efficiently using matrix methods. The reflectance R and transmittance T are then given by

$$R = |r|^2 , \quad \text{and} \tag{4.59}$$

$$T = \Re\left\{\frac{n_{N+1}\cos\theta_{N+1}}{n_0 \cos\theta_0}\right\} |t|^2 . \tag{4.60}$$

Equations 4.59 and 4.60 are analogous to the corresponding (4.36) and (4.37) for a single interface. From energy conservation we obtain the absorptance as

$$A = 1 - R - T , \tag{4.61}$$

which measures the amount of light absorbed in the multilayer. The phases of the reflected and transmitted light are

$$\Phi_r = \arctan\left(\frac{\Im\{r\}}{\Re\{r\}}\right), \quad \text{and} \tag{4.62}$$

$$\Phi_t = \arctan\left(\frac{\Im\{t\}}{\Re\{t\}}\right), \quad \text{respectively} . \tag{4.63}$$

4.3.2
Field Intensity in the Multilayer Stack

Of particular importance for high-intensity x-ray–matter interaction is the field intensity distribution inside of a multilayer stack, which can be calculated from propagating the waves inside it. At the interface of the ith and jth layer, we have both a positive- (propagating toward the substrate) and a negative-going (propagating toward the surface) electromagnetic plane wave associated with both layers. By solving Maxwell's equations, it can be shown that the field amplitudes at a distance z_i above the interface are given by [12]

$$E_i^+(z_i) = \frac{1}{t_{ij}} e^{-i\beta_i(z_i)} E_j^+(0) + \frac{r_{ij}}{t_{ij}} e^{-i\beta_i(z_i)} E_j^-(0) \,, \quad \text{and} \tag{4.64}$$

$$E_i^-(z_i) = \frac{r_{ij}}{t_{ij}} e^{i\beta_i(z_i)} E_j^+(0) + \frac{1}{t_{ij}} e^{i\beta_i(z_i)} E_j^-(0) \,, \tag{4.65}$$

for the positive and negative directions, respectively, where

$$\beta_i(z_i) = \frac{2\pi z_i n_i \cos\theta_i}{\lambda} \,. \tag{4.66}$$

$E_j^+(0)$ and $E_j^-(0)$ are the field amplitudes at the top of the jth layer. Starting from the bottom layer $i = N$, $j = N+1$, with $E_{N+1}^+(0) = 1$ and $E_{N+1}^-(0) = 0$, the field amplitudes can be calculated recursively. Finally all the field amplitudes are divided by $E_0^+(0)$ to ensure that $E_0^+(0) = 1$, which means the problem is normalized so that the incident electric field amplitude has unit magnitude. The field intensity inside the multilayer is then proportional to $|E^+(z) + E^-(z)|^2$.

4.3.3
Multilayers in the X-Ray Regime

Multilayers can be optimized for different properties, such as for the maximum peak reflectivity, the broadest or narrowest bandwidth, or the lowest radiation dose especially in the top layers. A useful parameter to characterize a multilayer design is the ratio of the high-Z layer thickness d_H to multilayer period $d = d_H + d_L$,

$$\Gamma = \frac{d_H}{d_H + d_L} = \frac{d_H}{d} \,. \tag{4.67}$$

Inside a multilayer, the incoming and reflected light interfere to form a standing wave, that is designed so that (i) the intensity minima are located in the high-Z layers to minimize absorption, and (ii) the Bragg condition (4.50) is fulfilled. To maximize reflection, the spacer between the high-Z layers is chosen such that as little light is absorbed as possible. A survey of recently experimentally tested multilayer mirrors can be found in [13]. Typical material pairs used around 8-keV photon energies are Ni/C, Ni/BN, W/Si [14], and Pt/C [15]. Figure 4.8 shows the reflectivity of a Ni/BN multilayer with 50 bilayer pairs, each of thickness $d = 5.5\,\text{nm}$, and

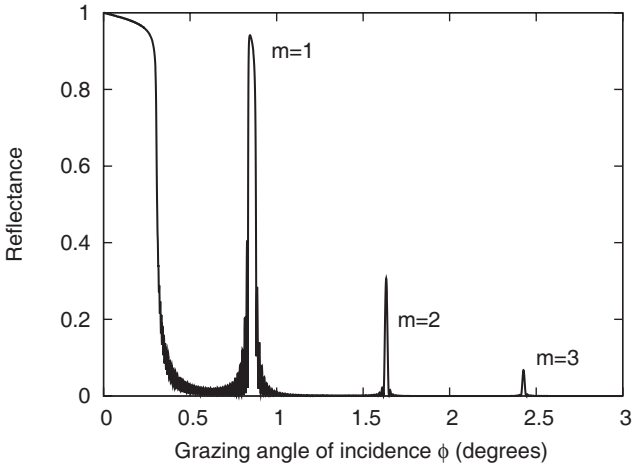

Figure 4.8 Reflectivity of a Ni/BN multilayer.

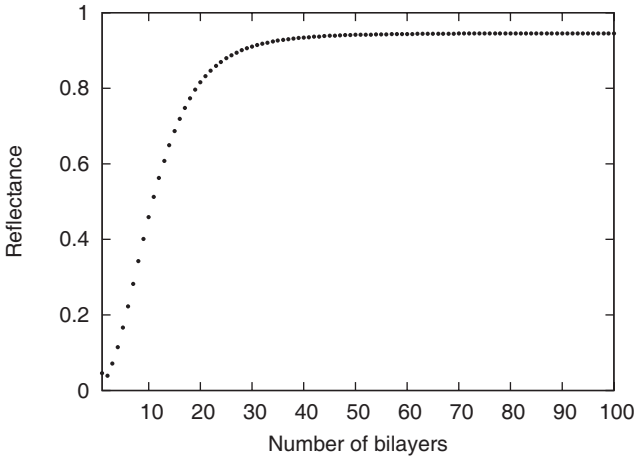

Figure 4.9 Peak reflectivity of a Ni/BN multilayer as a function of the number of bilayers.

$\Gamma = 0.4$, irradiated with 8-keV x-ray light. The polarization of the light has a negligible effect on the reflectance. Indicated are the reflectance peaks corresponding to different orders m, see (4.50).

Figure 4.9 shows the peak reflectivity of a Ni/BN multilayer with a bilayer thickness $d = 5.5\,\text{nm}$, and $\Gamma = 0.4$, irradiated with 8-keV x-ray light at a grazing angle of incidence of 0.8°, as a function of the number of bilayers. In this calculation we only considered the first-order reflection $m = 1$. It can be seen that the reflectivity quickly saturates for only a few bilayers since the x-ray penetration is small for grazing incidence.

Figure 4.10 shows the field intensity inside a multilayer normalized to the incident field, $|E|^2/|E_0^+(0)|^2$. The incoming medium (vacuum) is located at $z < 0$.

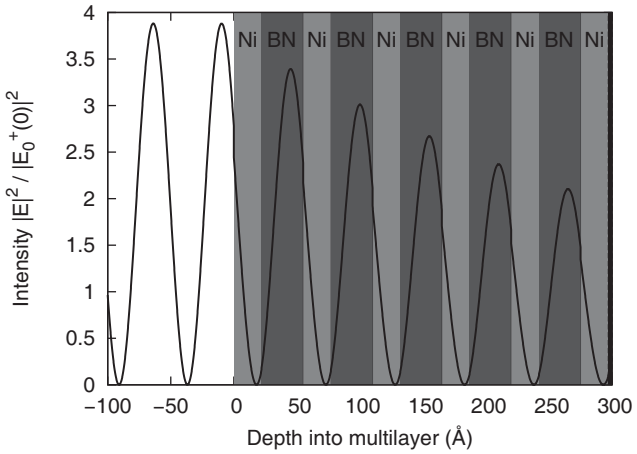

Figure 4.10 Field intensity inside a Ni/BN multilayer as a function of the depth into the multilayer. The atomic charge number of Ni is $Z = 28$, and the average charge number of BN is $Z = 6$.

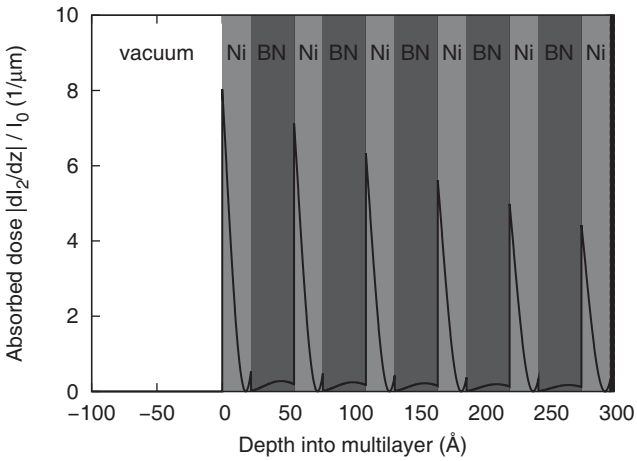

Figure 4.11 Absorbed dose inside a Ni/BN multilayer as a function of the depth into the multilayer.

Since the incoming and reflected light interfere and form a standing wave, the intensity in the vacuum is not unity but oscillates. Inside the multilayer structure, the field is small in the high-Z Ni layer and larger in the BN spacer layers that absorb less light. Additionally, the field decreases as we go into the multilayer $z > 0$.

In order to determine the heating of the multilayer, we need to calculate the absorbed dose which is a function of the field intensity. Let I_2 be the intensity in the multilayer stack, then the absorbed dose is given by

$$\left| \frac{d\, I_2}{dz} \right| = \Im \left\{ \frac{4\pi}{\lambda} n_2 \cos \theta_2 \right\} I_2 \, . \tag{4.68}$$

Figure 4.11 shows the absorbed dose for the multilayer intensity shown in Figure 4.10. Even though the maximum field intensity occurs in the spacer material, the maximum of the absorbed dose still lies in the high-Z layer, as is usually the case for high-reflectivity x-ray multilayers [16].

In order to reduce the absorbed dose and therefore the damage to a multilayer, it is generally desirable to reduce the thickness d_H of the high-Z layer since then radiation is able to penetrate deeper into the material, thereby spreading the dose over a larger volume, and the absorption in each high-Z layer is reduced. This approach has practical limitations since such multilayers are more difficult to fabricate, and are potentially less stable, especially at the interfaces.

4.3.4 Reflection by Thin Films and Bilayers

Often it is advantageous to grow mirror materials as thin films on a substrate. Since the penetration depth under grazing incidence is rather small, see Figure 4.6, very thin films are usually sufficient. On the basis of the general analysis in the previous section, we now give simple (but exact) formulas to calculate the reflection coefficients for single and bilayer films on substrates.

Thin Films We denote the indices of refraction of the ambient, the film, and the substrate by n_a, n_f, and n_s, respectively, the film thickness by d_f, and the off-normal angle of incidence by θ_a. n_f and n_s are in general complex numbers. We further define

$$\beta = \frac{2\pi}{\lambda} d_f n_f \cos\theta_f \,, \tag{4.69}$$

where θ_f is determined from Snell's law, $n_a \sin\theta_a = n_f \sin\theta_f = n_s \sin\theta_s$. According to (4.51), the reflectance coefficient of film is given by

$$r = \frac{r_{af} + r_{fs} e^{2i\beta}}{1 + r_{af} r_{fs} e^{2i\beta}} \,, \tag{4.70}$$

where r_{af} and r_{fs} are defined through (4.55) and (4.57) for s- and p-polarized light, respectively.

Bilayers We denote the indices of refraction of the ambient, the top film, the bottom film, and the substrate by n_a, n_{f1}, n_{f2}, and n_s, respectively, the corresponding film thicknesses by d_{f1} and d_{f2}, and the off-normal angle of incidence by θ_a. As for thin films (above), n_{f1}, n_{f2}, and n_s are in general complex numbers. We further define

$$\beta_1 = \frac{2\pi}{\lambda} d_{f1} n_{f1} \cos\theta_{f1} \,, \quad \text{and} \tag{4.71}$$

$$\beta_2 = \frac{2\pi}{\lambda} d_{f2} n_{f2} \cos\theta_{f2} \,, \tag{4.72}$$

where θ_{f1} and θ_{f2} are determined from Snell's law, $n_a \sin\theta_a = n_{f1}\sin\theta_{f1} = n_{f2}\sin\theta_{f2} = n_s \sin\theta_s$. According to (4.51), the reflectance coefficient of the bilayer stack is then given by

$$r = \frac{r_{af} + r_{f1}e^{2i\beta_1}}{1 + r_{af1}r_{f1}e^{2i\beta_1}}, \quad \text{with} \tag{4.73}$$

$$r_{f1} = \frac{r_{f1f2} + r_{f2s}e^{2i\beta_2}}{1 + r_{f1f2}r_{f1s}e^{2i\beta_2}}, \tag{4.74}$$

where r_{af1}, r_{f1f2}, and r_{f2s} are defined through (4.55) and (4.57) for s- and p-polarized light, respectively.

4.4 Dispersive Interaction of Wavepackets with Materials

At any instant of time, any electromagnetic pulse or wavepacket can be written as a superposition of harmonic waves of infinite length and duration. The constant-phase surface of each harmonic wave propagates with the phase velocity v given by (4.13). The damping of the harmonic waves is determined by the magnitude of $\beta(\omega)$. A pulse propagates without distortion only if δ and β are not frequency-dependent. If in addition $\beta = 0$, the pulse will also not be attenuated. However, usually δ and β are frequency-dependent, and the harmonic component waves suffer relative displacements and change in magnitude in a medium. Such media are called *dispersive*.

We will now estimate the effect of such a dispersion on a wavepacket. We consider a plane pulse characterized by $u(z,t)$ propagating in the z direction of a dispersive medium. We assume that the spectrum is centered around the frequency ω_0, that the time-domain envelope at $z = 0$ has the shape of a Gaussian function, and that at time $t = 0$ the center of the Gaussian is at position $z = 0$,

$$u(z=0,t) = A_0 e^{-\frac{t^2}{\tau^2}} e^{-i\omega_0 t}. \tag{4.75}$$

The time-domain Fourier transform of (4.75) is

$$A(\omega) = \frac{1}{\sqrt{2\pi}} \int_{-\infty}^{\infty} u_0(z=0,t) e^{i\omega t} dt \tag{4.76}$$

$$= A_0 \frac{\tau}{\sqrt{2}} e^{-\frac{1}{4}\tau^2(\omega-\omega_0)^2}. \tag{4.77}$$

At time $t \geq 0$ and for $z \geq 0$, $u(z,t)$ can then be calculated from

$$u(z,t) = \frac{1}{\sqrt{2\pi}} \int_{-\infty}^{\infty} A(\omega) e^{i[k(\omega)z - \omega t]} d\omega. \tag{4.78}$$

Expanding the wavenumber $k(\omega)$ in a Taylor series around ω_0,

$$k(\omega) \approx k(\omega_0) + \frac{dk}{d\omega}(\omega - \omega_0) + \frac{d^2k}{d\omega^2}\frac{(\omega - \omega_0)^2}{2} , \tag{4.79}$$

and defining the *group velocity* as $v_g = d\omega/dk$, we obtain

$$u(z,t) = \frac{A_0\tau}{2\sqrt{\pi}} e^{i\left[k(\omega_0)z - \omega_0 t\right]} \tag{4.80}$$

$$\int_{-\infty}^{\infty} e^{-\frac{\tau^2\omega^2}{4}} e^{i\left(\frac{z}{v_g} - t\right)\omega} e^{ik''z\frac{\omega^2}{2}} d\omega . \tag{4.81}$$

$$= A_0\tau \left[\frac{e^{-\frac{\left(z - tv_g\right)^2}{v_g^2(\tau^2 + 2ik''z)}}}{\sqrt{\tau^2 + 2ik''z}} \right] e^{i\left[k(\omega_0)z - \omega_0 t\right]} , \tag{4.82}$$

where we abbreviate the second derivative of the wavenumber with respect to the angular frequency by $k'' = d^2k/d\omega^2$.

For a dispersion-less medium, $k'' = 0$, and we obtain

$$u(z,t) = A_0 e^{i\left[k(\omega_0)z - \omega_0 t\right]} e^{-\frac{\left(t - \frac{z}{v_g}\right)^2}{\tau^2}} , \tag{4.83}$$

which is still a wavepacket at any z, modulated by a Gaussian envelope, and with the same temporal width. The envelope is not distorted during propagation. The speed of propagation is v_g. If the medium does exhibit dispersion, $k'' \neq 0$, the pulse envelope changes with time. The center of the pulse still travels with velocity v_g.

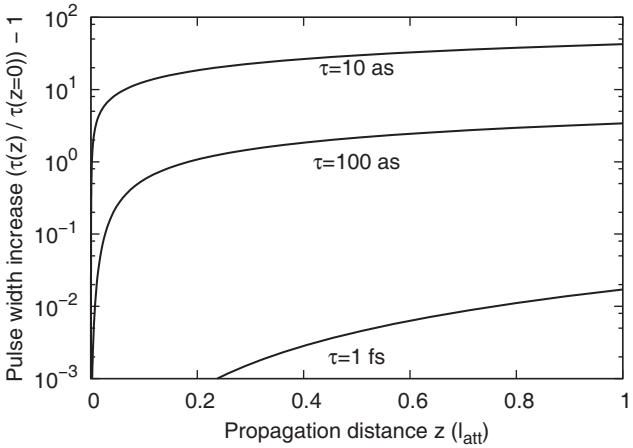

Figure 4.12 Increase in the pulse width of a Gaussian pulse as a function of the propagation distance in silicon for a photon energy of 8 keV. The distance is given in units of the photon attenuation length l_{att}.

Neglecting attenuation, the pulse shape remains Gaussian. The pulse width in this case increases with time as

$$\tau(z) = \tau(z=0)\sqrt{1 + \frac{4k''^2 z^2}{\tau(z=0)^2}} \,. \tag{4.84}$$

The factor in parenthesis in (4.82) also affects the phase of the pulse. Figure 4.12 shows the increase of the pulse width of a Gaussian pulse in bulk silicon with a center wavelength of 1.55 Å, corresponding to a photon energy of 8 keV. It can be seen that pulse length below about 1 fs significantly increase in temporal width over the distance of one attenuation length since shorter pulses span a larger width in reciprocal space, and with that span a larger range of phase velocities. Non-Gaussian pulses can behave differently: For example, especially chirped pulses may actually first compress and then later expand.

4.4.1 Interaction with Optical Elements

The response of a plane pulse on an optical element can be calculated using a technique similar to the one we used to obtain the response of a dispersive medium. We assume again that a plane pulse characterized by $u_I(z,t)$ is propagating in the z direction. We further assume that this pulse impinges on a reflective optical element at $z = 0$, such as a planar mirror. Let the spectrum be centered around ω_0. Similar to above, we define the temporal spectrum of $u_I(z=0,t)$, called $A_I(\omega)$, through (4.76). We can describe the response of the optical element by the function $r(\omega)$ such that

$$A_R(\omega) = r(\omega) A_I(\omega) \,, \tag{4.85}$$

and the reflected wave is then given by

$$u_R(z=0,t) = \frac{1}{\sqrt{2\pi}} \int_{-\infty}^{\infty} A_R(\omega) e^{i\omega t} d\omega \,, \tag{4.86}$$

with $r(-\omega) = r^*(\omega)$.

An important special case is the effect of an optic to a delta-function-like pulse $E_I(t) = \delta(t)$. In this case $A_I(\omega) = 1/\sqrt{2\pi}$, and the impulse response $A_R(\omega)$ is given by Green's function

$$G_R(t) = \frac{1}{2\pi} \int_{-\infty}^{\infty} r(\omega) e^{i\omega t} d\omega \,. \tag{4.87}$$

Then $u_R(t)$ in (4.86) can be written as a convolution integral,

$$u_R(z=0,t) = \frac{1}{\sqrt{2\pi}} \int_{-\infty}^{\infty} G_R(\tau) E_I(t-\tau) d\tau \,. \tag{4.88}$$

An example of the application of this formalism to the reflection of attosecond x-ray pulses can be found in [17].

4.5 Kramers–Kronig Relation

Methods for measuring $\beta(\omega)$ through absorption experiments of thin foils or gases are relatively well established. The direct measurement of $\delta(\omega)$ has proven to be much more difficult. Using the *Kramers–Kronig relations*, we can relate $\beta(\omega)$ to $\delta(\omega)$ through the atomic scattering factor. As shown in (3.126) and (3.127), β and δ relate to $f = f' + i f''$ through

$$f' = \left(\frac{k}{r_e \rho_a \lambda}\right) \delta \,, \quad \text{and} \tag{4.89}$$

$$f'' = \left(\frac{k}{r_e \rho_a \lambda}\right) \beta \,. \tag{4.90}$$

where r_e is the classical electron radius, ρ_a the atomic number density, λ the wavelength (in vacuum), and k the wavenumber. We then exploit general relationships between f' and f'', the *Kramers–Kronig relations*, [18]

$$f'(\omega) = \frac{1}{\pi} P \int_{-\infty}^{\infty} \frac{f''(\omega')}{(\omega' - \omega)} d\omega' \tag{4.91}$$

$$= \frac{2}{\pi} P \int_{-\infty}^{\infty} \frac{\omega' f''(\omega')}{(\omega'^2 - \omega^2)} d\omega' \,, \tag{4.92}$$

$$f''(\omega) = -\frac{1}{\pi} P \int_{-\infty}^{\infty} \frac{f'(\omega')}{(\omega' - \omega)} d\omega' \tag{4.93}$$

$$= -\frac{2\omega}{\pi} P \int_{-\infty}^{\infty} \frac{f'(\omega')}{(\omega'^2 - \omega^2)} d\omega' \,, \tag{4.94}$$

The P in front of the integral denotes the *principal value*, meaning that the integral over ω' is performed from $-\infty$ to $(\omega - \epsilon)$, and from $(\omega + \epsilon)$ to ∞, and then we take the limit $\epsilon \to 0$. The Kramers–Kronig relations result mathematically from the analytic behavior of f, which can be shown to be equivalent to the causality of the physical system [19].

References

1 Goodman, J.W. (2004) *Introduction to Fourier Optics*, Roberts & Company Publishers, Greenwoood Village, CO.

2 Arora, R.K. and Lu, Z. (1994) Graphical study of Laguerre-Gaussian beam modes. *IEE Proc. Microw. Antennas Propag.*, **141**, 145–150.

3 Stratton, J.A. (1941) *Electromagnetic Theory*, McGraw-Hill Book Comp., New York.

4 Jackson, J.D. (1975) *Classical Electrodynamics*, 2nd edn, John Wiley & Sons, New York.

5 De Roo, R. and Tai, C. (2003) Plane wave reflection and refraction involving a finitely conduction medium. *IEEE Antennas Propag. Mag.*, **45**, 54–61.

6 Huang, X. and Dudley, M. (2003) A universal computation method for two two-beam dynamical x-ray diffraction. *Acta Cryst. A*, **59**, 163–167.

7 Henke, B.L., Gullikson, E.M., and Davis, J.C. (1993) X-ray interactions: photoabsorption, scattering, transmission, and reflection at $E = 50{-}30\,000$ eV, $Z = 1{-}92$. *Atom. Data Nucl. Data Tables*, **54**, 181–342.

8 London, R.A., Bionta, R.M., Tatchyn, R.O., and Roesler, S. (2001) *Computational Simulations of High-Intensity X-Ray Matter Interaction* (eds R.O. Tatchyn, A.K. Freund, and T. Matsushita), *Proc. SPIE*, **4500**, 51–62.

9 Spiller, E. (1972) Low-loss reflection coatings using absorbing materials. *Appl. Phys. Lett*, **20**, 365–367.

10 Rosenbluth, A.E. and Forsyth, J.M. (1981) *The Reflecting Properties of Soft X-Ray Multilayers. AIP Conf. Proc.*, **75**, 280–285.

11 Spiller, E., Stearns, D., and Krumrey, M. (1993) Multilayer x-ray mirrors: Interfacial roughness, scattering, and image quality. *J. Appl. Phys.*, **74**, 107–118.

12 Windt, D.L. (1998) IMD – software for modeling the optical properties of multilayer films. *Comput. Phys.*, **512**, 360–370.

13 Lawrence Berkeley National Laboratory Center for X-ray Optics. *PXRMS Multilayer Survey*.http://henke.lbl.gov/multilayer/survey.html. Last access: 29 May 2011.

14 Salditt, T., Lott, D., Metzger, T.H., Peisl, J., Vignaud, G., Hoj, P., Schärpf, O., Hinze, P., and Lauer, R. (1996) Interfacial roughness and related growth mechanisms in sputtered W/Si multilayers. *Phys. Rev. B*, **54**, 5860–5872.

15 Spiga, D., Pareschi, G., Citterio, O., Banham, R., Basso, S., Cassanelli, M., Cotroneo, V., Negri, B., Grisoni, G., Valsecchi, G., and Vernani, D. (1998) Development of multilayer coatings (Ni/C-Pt/C) for hard x-ray telescopes by e-beam evaporation with ion assistance. *Proc. SPIE*, **5488**, 813–819.

16 Hau-Riege, S.P., London, R.A., Chapman, H.N., and Bergh, M. (2007) Soft-x-ray free-electron-laser interaction with materials. *Phys. Rev. E*, **76**(4), 046403.

17 Hau-Riege, S.P. and Chapman, H.N. (2007) Reflection of attosecond x-ray free electron laser pulses. *Rev. Sci. Instrum.*, **78**, 013104.

18 de Laer Kronig, R. (1926) On the theory of dispersion of x-rays. *J. Opt. Soc. Am.*, **12**, 547–556.

19 Toll, J.S. (1956) Causality and the dispersion relation: Logical foundations. *Phys. Rev.*, **104**, 1760–1770.

5
Electron Dynamics

In this chapter we discuss the dynamics of electrons in x-ray-irradiated materials. Following the absorption of x rays by electrons, it is the behavior of the electrons that determines the material evolution. X rays are absorbed primarily through photoionization. The decrease of the intensity dI of an x-ray beam upon passage through a segment of material of length dx can be described by the linear attenuation coefficient α,

$$dI = -\alpha I(x)dx \,, \tag{5.1}$$

where $I(x)$ is the intensity of the x-ray beam at position x. Integrating (5.1) over x under the assumption that α is constant results in the transmitted intensity through a layer of thickness d, often referred to as the *Beer–Lambert law*,

$$I = I_0 e^{-\alpha d} \,. \tag{5.2}$$

X-ray absorption induces the generation of a whole spectrum of electrons in the sample. The process is initiated by the emission of photoelectrons with kinetic energies on the order of the x-ray energy (typically several keV) that propagates through the sample and excites electrons, ions, and atoms. For linearly polarized light, photoelectrons are emitted preferentially in the direction of the electric field vector of the light, which is perpendicular to the direction of light propagation. The photoionized ions decay through x-ray fluorescence or through Auger relaxation, the latter leading to the emission of a lower-energy Auger electron (typically hundreds of eV in low-Z materials). Both photo- and Auger electrons propagate through the material and are elastically and inelastically scattered. Inelastic scattering leads to deceleration of the electrons. Typical energy losses per scattering event due to electron–phonon scattering are on the order of 0.05 eV, due to plasmon excitation between 5 and 25 eV at solid density, due to valence electron excitation and ionization between 5 and 25 eV, and due to core electron excitation and ionization between 10 and 1000 eV. Atomic ionization by fast electrons occurs primarily through electron-impact ionization, leading to the emission of a large number of secondary electrons. These processes taken together are referred to as electron *cascades*. Following the electron–electron thermalization, the lower-energy electrons couple with the ions. In case of solids, phonons are excited. Both electronic and ionic heat conductions lead to further dissipation of the absorbed x-ray

High-Intensity X-rays – Interaction with Matter, First Edition. Stefan P. Hau-Riege.

energy. We consider *electron dynamics* to be the sum of all these processes, and it determines, along with the x-ray absorption characteristics, the energy distribution in the sample following x-ray irradiation and the time scale for energy dissipation.

In this chapter, we will discuss the electron dynamics in x-ray-irradiated materials in more detail, including a discussion of the anisotropy of the emission of the photoelectrons, the elastic and inelastic scattering of electrons in solids and plasmas, and the escape of energetic electrons from the sample that leads to electrostatic charging. To put these concepts into perspective, we will start out with an overview of the processes involved in the transition of a solid into a plasma.

5.1 Transition of Solids into Plasmas

An x-ray beam of sufficiently large flux can transform a solid into a plasma. During this transition the material will enter various transient states. A unified theoretical description of these states is often very difficult. Only the initial condensed matter state and the final hot plasma state are relatively well understood, whereas transient cold- and warm-dense-plasma states are an active area of research.

We now consider a crystal at room temperature and solid density. In a crystal, atomic vibrations are traveling sound waves, also called phonons. Electronic states are well described in terms of energy bands and Bloch functions [1]. Core electrons are associated with a narrow band of propagating states. Even electrons with energies much larger than the Fermi energy are Bragg reflected due to the periodicity of the crystal, giving rise to energy gaps at the Brillouin zone boundaries. Because of the Bragg reflection, we have to use an effective mass instead of the free electron mass to describe the electron dynamics.

In a hot plasma, no long-range order exists for the ions but only short-range correlations, so that phonons do not propagate efficiently. Free electrons have well-defined energies in reciprocal space, and bound electrons are localized on specific ions instead of forming energy bands. Ions typically have definite charge states that can be determined from the Saha equation. In many cases, a classical treatment of this plasma is sufficient.

Upon heating a material that was originally in a condensed-matter state, electrons are excited to higher energies, so that bound and free electrons are less able to screen nuclear charges. Therefore, the self-consistent electrostatic potential grows stronger, the spacing of the energy levels increases, and emission lines shift to shorter wavelengths. In liquid metals and cold plasmas, the core bands become very narrow due to the stronger potential and the spoiled resonant hopping for propagating states associated with the disorder. The band gaps between states above the Fermi energy become smaller due to the loss of Bragg scattering, so that the electron mass is closer to the free-electron mass. A cold-dense plasma is typically strongly coupled and degenerate, requiring a quantum-mechanical treatment of the many-body interactions, for example through quantum-kinetic equa-

tions. In such systems, electrons and ions need to be described as quasi-particles with density-dependent self-energies that move inside a dense, interacting medium. Charge screening in this medium depends on the velocity of the test charge, leading to both static and dynamic screening effects. In simplified treatments, cold- and warm dense matter states are treated through modifications of semiclassical models, including effects known from hot dense plasma theory, such as continuum lowering, pressure ionization, and modification of atomic transition rates.

An important element of the complex solid–plasma transformation is the dynamics of the electronic system. The first step is x-ray absorption associated with the emission of photoelectrons, which we will describe now.

5.2
Directional Emission of Photoelectrons

At sufficiently low x-ray energies, the photoionization process can be treated non-relativistically. Similar to the treatment of scattering by atoms in Section 3.2.1.1, we follow the perturbative treatment summarized in Section 2.2.1.1 to describe the photoionization process. During photoabsorption, a photon is removed from the radiation mode $\boldsymbol{k}_i\sigma_i$. This single-photon process requires one annihilation step, described by the photon annihilation operator a. To first order in the interaction Hamiltonian (2.96), we therefore need to consider only the $(\boldsymbol{p}\cdot\boldsymbol{A})$ term $H^{(1)}_{int}$ given by (2.99). We can write the initial state of the system as

$$|\text{initial}\rangle = |q_i\rangle|\ldots n_{\boldsymbol{k}_i\sigma_i}\ldots\rangle\ , \tag{5.3}$$

and the final state as

$$|\text{final}\rangle = |q_f\rangle|\ldots n_{\boldsymbol{k}_i\sigma_i} - 1\ldots\rangle\ . \tag{5.4}$$

The photoabsorption matrix element $M_{i\to f}$ given by (2.103) can then be written as

$$M_{i\to f} = \langle\text{final}|\, H^{(1)}_{int}|\text{initial}\rangle \tag{5.5}$$

$$= \langle q_f|\langle\ldots n_{\boldsymbol{k}_i\sigma_i} - 1\ldots|\, H^{(1)}_{int}|q_i\rangle|\ldots n_{\boldsymbol{k}_i\sigma_i}\ldots\rangle \tag{5.6}$$

$$= \frac{e}{m}\sqrt{\frac{\hbar}{2\epsilon_0 V\omega_k}}\sqrt{n_i}\, f\ , \tag{5.7}$$

with

$$f = \langle q_f|\boldsymbol{p}\cdot\boldsymbol{\epsilon}_{k_i\sigma_i}e^{i\boldsymbol{k}_i\cdot\boldsymbol{r}}|q_i\rangle\ . \tag{5.8}$$

Using Fermi's Golden Rule, we can write the transition rate (2.102) to the first order in $H^{(1)}_{int}$ as

$$\omega_{i\to f} = r_e\frac{(2\pi)^2c^2}{mV\omega_k}\rho_f(E_f,\boldsymbol{\epsilon}_{out})n_i|\,f|^2\ , \tag{5.9}$$

where ϵ_{out} denotes the emission direction of the ejected photoelectron. The cross section for photoabsorption is then

$$\frac{d\sigma_a}{d\Omega} = \frac{\omega_{i\to f}}{J} \tag{5.10}$$

$$= r_e |f|^2 \frac{(2\pi)^2 c}{m\omega_k} \rho_f \left(E_f, \epsilon_{out}\right). \tag{5.11}$$

We limit ourselves to the single-ion treatment and ignore modifications by chemical bonding and coherence effects between multiple atoms for now. For linearly polarized light, which we consider here, the cross section is a function of the angle between the electric field vector, also called the polarization direction of the photon, and the direction of the ejected electron.

The exponential term in (5.8) complicates the calculation of f, and so it is often expanded into multipole moments. For low x-ray energies, photoelectrons are ejected primarily in the direction of the electric field vector $\epsilon_{k_i\sigma_i}$ of the incident radiation, that is perpendicular to the propagation direction of light. The photoionization process is then to a good approximation a dipole transition, and the angular distribution of the ejected electron can be specified by a single parameter as [2]

$$\frac{d\sigma_{n,l}}{d\Omega} = \frac{\sigma_{n,l}}{4\pi}\left[1 + \beta_{n,l} P_2(\cos\theta)\right], \tag{5.12}$$

where $P_2(x)$ is the Legendre polynomial of order 2, θ is the angle between polarization and electron direction as shown in Figure 5.1, and $\sigma_{n,l}$ is the total cross section. The asymmetry parameter $\beta_{n,l}$ depends on n and l. In this approximation, the maximum of the angular electron distribution lies in the direction of the polarization direction of the photon, which is perpendicular to the propagation direction of the photon. Figure 5.2 shows $(d\sigma/d\Omega)/\sigma$ for argon for photoionization from the 1s, 2s, 3s, 2p, and 3p shells for 5-keV electron energy and $\phi = 0^o$. For ionization from the s shells, $\beta_{n,0} = 2$.

At larger photon energies, higher-order multipole contributions become significant, and the angular distribution of the ejected electrons depends also on the direction of the incoming photon. High-energy photons have sufficient linear momentum to bias the ejection of the photoelectron into the direction of the incoming

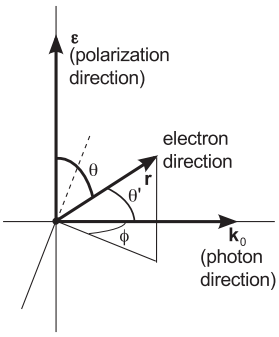

Figure 5.1 Geometry of the emission directions of photo electrons.

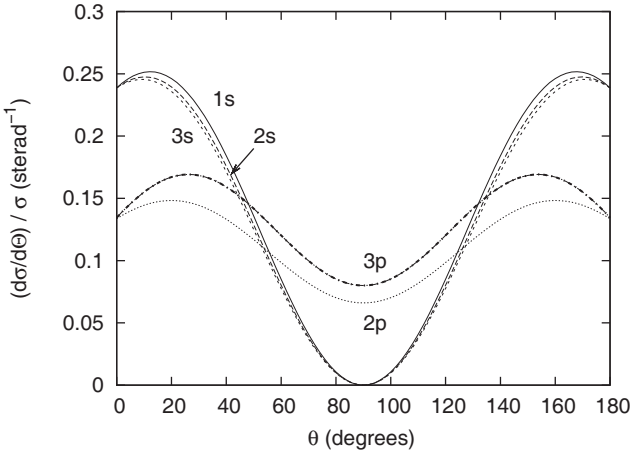

Figure 5.2 Differential cross section for photo electrons from argon for linearly polarized light for $\phi = 0$ and an electron energy of 5 keV [2].

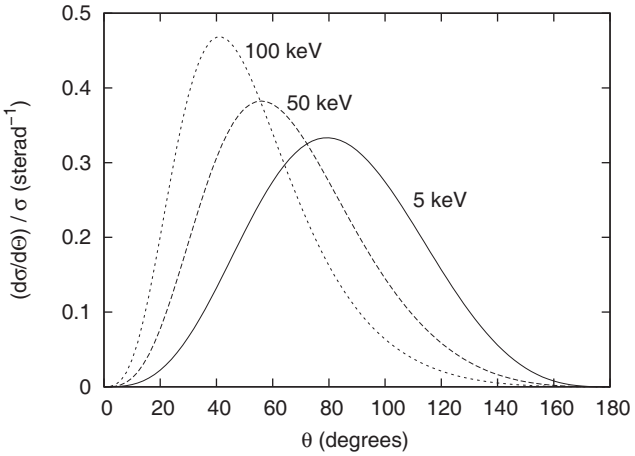

Figure 5.3 Differential cross section for photo electrons from carbon from the 1*s* shell (unpolarized light) for different photon energies [3].

photon so that forward emission dominates. For linearly polarized light, the differential cross section can approximately be written as [2]

$$\frac{d\sigma_{n,l}}{d\Omega} = \frac{\sigma_{n,l}}{4\pi}\left[1 + \beta P_2(\cos\theta) + (\delta + \gamma\cos^2\theta)\sin\theta\cos\phi\right], \tag{5.13}$$

where ϕ is the angle between the photon direction and the electron direction projected onto a plane perpendicular to the polarization, as sketched in Figure 5.1.

Figure 5.3 shows $(d\sigma/d\Omega)/\sigma$ for photoionization from the 1s shell of carbon for different photon energies of unpolarized light [3]. In these calculations the carbon atom was treated as a point charge without screening while neglecting the effect

of the outer-shell electrons. This is justified since the angular electron distribution is nearly independent of the screening from the outer electrons at high and intermediate energies. Screening is important only for calculating the total cross section $\sigma_{n,l}$.

5.3 Electron Scattering

Because of its wave-like nature, an electron can be described as a matter wave. The associated wavelength is called the *de-Broglie wavelength*. The de-Broglie equation relates the wavelength λ of a particle to the particle momentum p,

$$\lambda = \frac{h}{p} . \tag{5.14}$$

Particles with greater kinetic energy have a larger momentum and a shorter wavelength. Figure 5.4 shows the wavelengths of electrons as a function of their kinetic energy. The interaction between an electron and the atoms in a solid depends on the relative magnitudes of the de-Broglie wavelength and the interparticle distance. If the electron is fast, its de-Broglie wavelength is short, and the electron interaction with the ions can be described as a series of independent single-atom interactions, whereas slow electrons interact with several neighboring atoms simultaneously.

When electrons propagate through a material, they are elastically and inelastically scattered. Elastic scattering events lead to changes in the direction of the electrons, whereas inelastic scattering events cause them to slow. The inverse total mean free path of an electron, λ_{total}^{-1}, is the sum of the inverse mean free paths

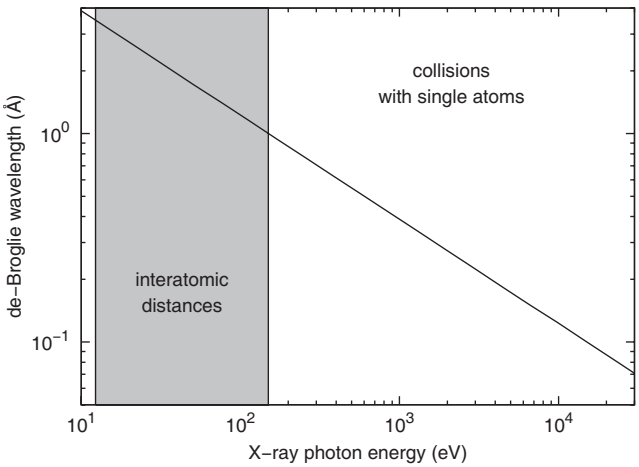

Figure 5.4 De-Broglie wavelength of electrons as a function of kinetic energy. Typical interatomic distances range between 1 and 3.5 Å.

associated with elastic and inelastic scattering, $\lambda_{elastic}^{-1}$ and $\lambda_{inelastic}^{-1}$, respectively,

$$\frac{1}{\lambda_{total}(E)} = \frac{1}{\lambda_{elastic}(E)} + \frac{1}{\lambda_{inelastic}(E)} \,. \tag{5.15}$$

During each inelastic scattering event, the electron loses energy. Often the slowdown can be assumed to be quasi-continuous. The *stopping power* is defined as the energy loss of an electron per unit length in the target along the path of the electron. It determines the *electron range*, defined as the straight-line penetration distance, the rate of secondary-electron production, the lateral energy distribution (*straggle*), the depth distribution of x-ray production, and the generation and distribution of electron–hole pairs. Figure 5.5 shows the electron stopping power in silicon, copper, and gold as a function of the electron energy. The stopping power is found to be very similar in different materials. A useful approximation for the range of monoenergetic electrons in aluminum is

$$R = aE\left(1 - \frac{b}{1 + cE}\right), \tag{5.16}$$

where E is the electron energy, $a = 5.37 \times 10^{-4}\,\mathrm{g/cm^2\,keV}$, $b = 0.9815$, and $c = 3.1230 \times 10^{-3}\,\mathrm{keV^{-1}}$ [4]. $R\rho$ as a function of E is shown in Figure 5.6. Just as the stopping power is similar in different materials, this equation gives a reasonable approximation of the electron range in different materials when it is linearly scaled by the mass density. For 20-keV electrons, the interaction volume in the material is on the order of a few micrometers. As we discuss below, at high electron energies the experimental data agrees with Bethe's law, whereas at lower energies significant deviations occur since basic assumptions of this model are not fulfilled. Good agreement has been found with stopping-power values computed

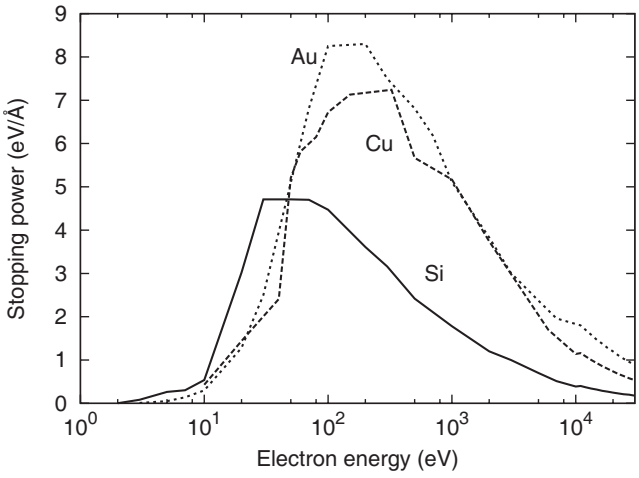

Figure 5.5 Electron stopping power of silicon, copper, and gold as a function of electron energy [7].

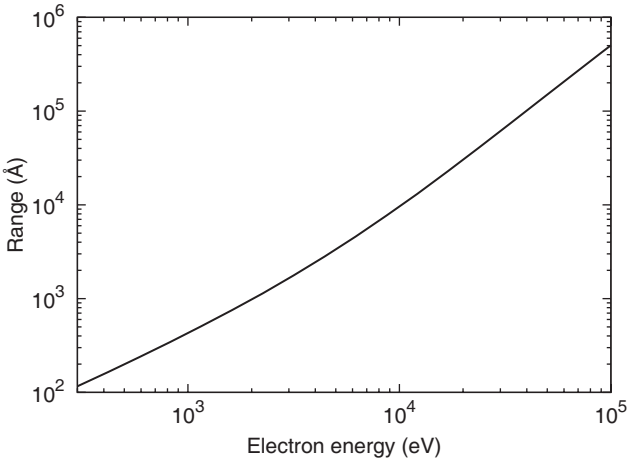

Figure 5.6 Range of monoenergetic electrons in aluminum [4].

from a dielectric model of solids [5]. Note that for low-Z materials, scattering from valence electrons is a major energy loss mechanism for electrons between 10 eV and 10 keV. The contribution from core-level electrons is less than 10% [5, 6].

5.3.1 Elastic Electron Scattering

We now discuss the process of elastic scattering of an electron by an atom. We assume that the interaction with the atom can be described by an effective central potential $V(\boldsymbol{r})$. We further assume $V(\boldsymbol{r})$ to be short-ranged, as is the case for neutral atoms or for ions in a metal or plasma where mobile charges screen the long-range part of the potential. We consider the stationary problem of an incident beam of electrons with one electron per unit volume with linear momentum $mv = \hbar K$ per electron propagating in the z direction. The wavefunction of this beam is e^{iKz}. At large distances, the wavefunction of the scattered particles is a spherical wave proportional to e^{iKr}/r. This treatment is valid for a spinless particle. Including spin effects would require the introduction of a spin density matrix, spin polarization, and relativistic effects. At large distances, the wavefunction $\Psi(\boldsymbol{r})$ describing the elastic scattering process has to satisfy the boundary conditions

$$\Psi(\boldsymbol{r}) \to e^{iKz} + f(\theta, \phi)\frac{e^{iKr}}{r} \quad \text{for} \quad r \to \infty\,, \tag{5.17}$$

where $f(\theta, \phi)$ is the scattering amplitude. The differential elastic cross section is then given by

$$\frac{d\sigma}{d\Omega} = |f(\theta, \phi)|^2\,. \tag{5.18}$$

By considering the asymptotic behavior of (5.17), it can be shown that the scattering amplitude is given by [8]

$$f(\theta, \phi) = -\frac{m}{2\pi\hbar^2} \int d^3 r e^{-iK' \cdot r} V(\boldsymbol{r}) \Psi(\boldsymbol{r}) \,, \tag{5.19}$$

where $\boldsymbol{K}'$ is the linear momentum of the scattered electron.

5.3.1.1 Elastic Scattering of Fast Electrons

The propagation of fast electrons in materials is almost like that of free electrons, and electron collisions can be treated in the single atom picture. In this regime, the first Born approximation is valid: If the electron kinetic energy E is much larger than the atomic potential energy $e^2 Z^2 / 2a_0$, scattering is weak, and $\Psi(\boldsymbol{r}) \approx e^{iKz}$. We can then approximate (5.19) by

$$f(\theta, \phi) = -\frac{m}{2\pi\hbar^2} \int d^3 r e^{i\boldsymbol{q} \cdot \boldsymbol{r}} V(\boldsymbol{r}) \,, \tag{5.20}$$

where $\boldsymbol{q} = \boldsymbol{K} - \boldsymbol{K}'$ is the scattering vector that describes the momentum loss of the incident electron. As an example, we now consider a screened Coulomb potential,

$$V(r) = -\frac{1}{4\pi\epsilon_0} \frac{Ze^2}{r} e^{-\frac{r}{a}} \,, \tag{5.21}$$

where the screening length a is defined as

$$a = \frac{a_0}{Z^{1/3}} \,. \tag{5.22}$$

The magnitude of screening is usually described by the dimensionless screening parameter $\alpha = 1/2K^2 a^2$. Screening can occur through the bound electrons of the atom, or by quasi-free electrons in a plasma or metal. Using (5.18) and (5.20), we obtain the differential cross section

$$\frac{d\sigma}{d\Omega} = \frac{1}{(4\pi\epsilon_0)^2} \frac{e^4 Z^2}{4E^2} \frac{1}{(1 - \cos\theta + \alpha)^2} \,, \tag{5.23}$$

which is the screened Rutherford formula. Note that the screened Rutherford cross section (5.23) does not diverge for small scattering angles θ since the long-range part of the potential is screened. The total elastic scattering cross section is given by

$$\sigma_{elastic} = \int \frac{d\sigma}{d\Omega} d\Omega \tag{5.24}$$

$$= \frac{1}{(4\pi\epsilon_0)^2} \frac{\pi e^4 Z^2}{E^2} \frac{1}{\alpha(2 + \alpha)} \,. \tag{5.25}$$

Elastic scattering leads to directional changes of the electron without energy loss. According to (5.25), the magnitude of this process scales as Z^2/E^2. For $\alpha \to 0$, the

cross section per atom for scattering larger than an angle Φ_0 can be estimated as [9]

$$\sigma(\theta > \Phi_0) = 1.62 \times 10^{-20} \left(\frac{Z}{E\,[\mathrm{keV}]} \right)^2 \cot^2 \left(\frac{\Phi_0}{2} \right) [\mathrm{cm}^2] \,. \tag{5.26}$$

In gases and amorphous materials, the constituent atoms can be treated as independent scatterers. In crystals, interference effects need to be taken into account, and, similar to the case of photons, Bragg diffraction of electrons may occur.

5.3.1.2 Elastic Scattering of Slow Electrons

For slower electrons, the first Born approximation does not hold. In this case the partial wave expansion method provides a much more accurate description of elastic scattering [10]. This method works well for spherically symmetric potential where $V(\boldsymbol{r}) = V(r)$. In the method of partial waves, the scattering amplitude f is written as a sum of contributions from different angular momenta, given in terms of phase shifts. The incoming plane wave is decomposed into spherical waves, called partial waves, each with a different angular momentum. We calculate the phase shift to the wavefunction at large r associated with the spherically symmetric potential. Finally, these phase-shifted partial waves are superimposed to obtain the original plane wave and the scattered wave. The scattering amplitude can be expanded as

$$f(\theta, \phi) = \sum_l (2l + 1)\, f_l(k)\, P_l(\cos\theta) \,, \tag{5.27}$$

where $P_l(x)$ are the Legendre polynomials of order l. The partial wave scattering amplitudes $f_l(k)$ are given by [10]

$$f_l(k) = \frac{1}{k} e^{i\delta_l(k)} \sin\delta_l(k) \,. \tag{5.28}$$

The phase shifts $\delta_l(k)$ can be obtained from the respective radial wave equations for each partial wave. The total scattering cross section is given by

$$\sigma = \frac{4\pi}{k^2} \sum_{l=0}^{\infty} (2l + 1) \sin^2\theta_l \,. \tag{5.29}$$

The associated *mean free path* is given by

$$\lambda_{elastic(E)} = \frac{1}{N \sigma_{elastic}(E)} \,, \tag{5.30}$$

where N is the atomic density.

5.3.1.3 Elastic Scattering in Solids

Various multiple-particle effects can approximately be accounted for by modifying the interaction potential $V(r)$. A common example are exchange effects, in which the incident electron is absorbed and another one is emitted instead. To describe

solid-state effects for atoms bound in solids, $V(r)$ can be replaced by a modified potential obtained within the muffin-tin model [1]. The muffin-tin potential is constant in the interstitial region between the atoms and has the form of an isolated atom near each atom up to a radius R_S, so that

$$V_{solid}(r) = \begin{cases} V(r) - V(R_S) & \text{for} \quad r \leq R_S \ , \\ 0 & \text{otherwise} \ . \end{cases} \tag{5.31}$$

R_S is chosen to be less than the Wigner–Seitz radius so that the atomic potentials do not overlap. A schematic of this potential is shown in Figure 5.7. Figure 5.8 shows the elastic mean free path of diamond calculated using this method [11].

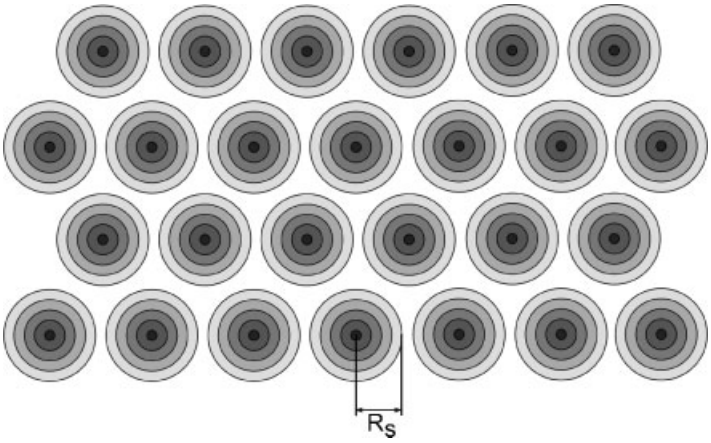

Figure 5.7 Schematics of the muffin-tin potential. The potential is constant in the interstitial regions (white).

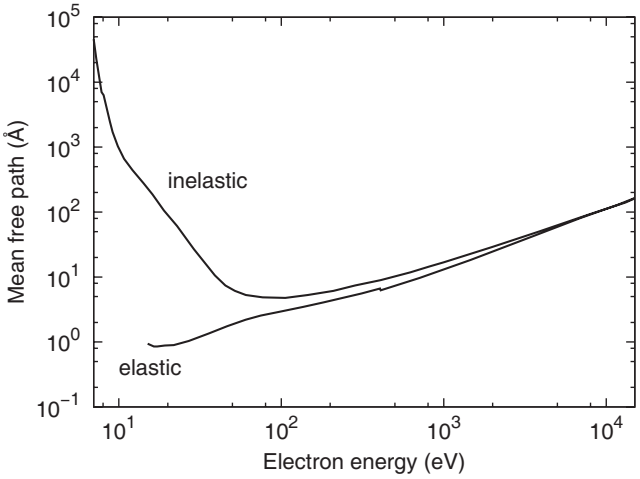

Figure 5.8 Calculated inelastic and elastic mean free paths λ of diamond [11, 12].

In these calculations, the radial charge density of a carbon atom was determined, then the muffin-tin potential for the atoms embedded in solids was constructed using various approximations for the exchange potential, and finally the phase shifts were derived. The results show that for large energies, the elastic mean free path is proportional to the ratio of electron density and mass density. In Figure 5.8, the mean free path for electron energy larger than 400 eV was taken from the NIST database [12].

5.3.2 Inelastic Electron Scattering

Inelastic scattering transfers energy from the incoming electrons to the ions, atoms, and other electrons, leading to the creation of secondary electrons and x rays. Similar to our treatment of elastic scattering, we will distinguish the cases of inelastic scattering of fast and of slow electrons.

5.3.2.1 Inelastic Scattering of Fast Electrons

Bethe calculated the mean rate at which an electron loses energy through collisions in passing through matter. The *Bethe stopping power* for fast electrons based on single-ion interactions is given by [13]

$$-\frac{dE}{ds} = \frac{2\pi e^4 NZ}{(4\pi\epsilon_0)^2 m_0 v^2}\left\{\ln\left[\frac{(\gamma+1)E^2}{2I^2}\right] - \left(\frac{2}{\gamma} - \frac{1}{\gamma^2}\right)\ln 2 + \frac{1}{\gamma^2} + \frac{1}{8}\left(1-\frac{1}{\gamma}\right)^2\right\}. \tag{5.32}$$

The kinetic energy of the electron E is assumed to be larger than a few times the atomic binding energies. Here $-e$ is the electron charge, N is atomic number density, and $\gamma = 1 + E/mc^2 = 1/(1 - v^2/c^2)^{1/2}$. I is the mean excitation energy of the material describing the mean energy loss per scattering event, averaged over all atomic shells, given by

$$I = \left[\prod_i (\hbar\omega_i)^{f_i}\right]^{1/Z}, \tag{5.33}$$

where f_i are the oscillator strength of transitions with transition energies $\hbar\omega_i$. According to the oscillator sum rule, $\sum_i f_i = Z$ [10].

Various modifications to the Bethe equation (5.32) have been suggested, including the extension to lower energies by removing the divergence of (5.32) for small I, and by treating compound materials by using mass-fraction average quantities. Some extensions are described in [7].

5.3.2.2 Inelastic Scattering of Slow Electrons

Inelastic scattering of slow electrons is very important in order to understand the electron dynamics in x-ray-excited materials. For example, in solid-density carbon,

a 250-eV Auger electron can generate 20 to 40 slower electrons, depending on the band structure. These processes typically occur on a time scale of 100 fs [11].

At lower energies, the electron is scattered by multiple ions in the solid and interacts with the background electrons, and a different approach to calculate the stopping power is needed. The interaction is typically rather strong and includes multiple ionization events, requiring a quantum-mechanical treatment that includes rather complicated nonlocal exchange terms. In semiconductors, the passage of hot electrons with energies of less than 10 eV is very well understood, but interactions with energies between 10 and 100 eV are not.

A common way to describe the passage of a charged particle through matter is to consider its electric field in the solid, described by its dielectric response function $\epsilon(\boldsymbol{q}, \hbar\omega)$. This function is the ratio of externally applied potential and the total potential in the material, so it describes the response of a medium to an energy transfer $\hbar\omega$ and momentum transfer $\boldsymbol{q}$. The probability for energy loss $\hbar\omega$ per unit distance traveled is [14]

$$p(E, \hbar\omega) = \frac{1}{\pi E a_0} \int_{q-}^{q+} \Im\left\{-\frac{1}{\epsilon(q, \hbar\omega)}\right\} \frac{dq}{q} \quad \text{with} \tag{5.34}$$

$$q_{\pm} = \frac{\sqrt{2m}}{\hbar}\left(\sqrt{E} \pm \sqrt{E - \hbar\omega}\right). \tag{5.35}$$

The stopping power is given by

$$-\frac{dE}{ds} = \int \hbar\omega\, p(E, \hbar\omega) d\hbar\omega \ . \tag{5.36}$$

Expression (5.35) for $q_{\pm}$ assumes a free particle-like behavior, thereby neglecting the energy gap, so that the free mass instead of the effective electron mass is used.

The term $\Im\{-1/[\epsilon(q, \hbar\omega)]\} dq/q$ is also called the *energy loss function* that satisfies the oscillator-strength sum rule relating the total energy loss to the effective number of free electrons per atom,

$$Z_{eff} = \frac{2}{\pi\hbar^2 \Omega_p^2} \int_0^{\infty} dE\, E \Im\left\{-\frac{1}{\epsilon\left(\boldsymbol{q}, \frac{E}{\hbar}\right)}\right\} \ . \tag{5.37}$$

Here $\Omega_p = \sqrt{Ne^2/m_e\epsilon_0}$, N is the density of atoms, and E is energy loss of the incoming particle.

Note that $\epsilon(q = 0, \hbar\omega)$ is simply the dielectric constant of light for the medium. This quantity can be measured directly through optical experiments. Ashley *et al.* [5, 6, 15] proposed that this information can be used to approximate $\epsilon(q \neq 0, \hbar\omega)$.

Integrating $p(E, \hbar\omega)$ over all electron energies E gives the inverse of the inelastic mean free path (IMFP) $\lambda_{inelastic}$,

$$\lambda_{inelastic}(E) = \frac{1}{\int p(E, \omega) d\omega} \ . \tag{5.38}$$

The IMFP is the average for diamond distance traveled between inelastic collisions. As shown in Figure 5.8 the IMFP for diamond is large below 10–15 eV, drops to a minimum of 5–10 Å between 30–100 eV, and then rises monotonically above 100 eV. To obtain the results shown in Figure 5.8, first principle calculations [16] have been used for energies below 10 eV. For energies above 50 eV, results are based on the dielectric response theory. Between 10 and 50 eV, the IMFP was simply interpolated. The IMFP can be calculated from optical data using the formalism developed by Penn [17]. Below 200 eV, it shows a strong dependence on the details of the electronic band structure. The stopping power is given by the integral of $\hbar\omega\, p(q,\hbar\omega)$ over all energy transfers, which can be used to calculate the range of an electron. The range R_0 of an electron of energy E is defined as the distance to slow an electron to an energy E_{min}, often taken as 10 eV,

$$R_0(E) = \int_{E_{min}}^{E} \frac{dE'}{-\frac{dE(E')}{ds}} \,. \tag{5.39}$$

For energies E larger than 100 eV, theory and experiments tend to agree well. Below 100 eV, both performing experiments and developing theories are very difficult. In the experiments, uncertainties in the sample preparation and experiment-specific effects make measurements challenging, and in the theory, exchange and correlation become more important, and the complex structure of the energy bands strongly affects the dynamics of the scattered electrons.

5.4 Energy Loss Mechanisms

When an electron traverses a medium, it dissipates its energy through various channels, including plasmon, photon, and atomic excitation. General information about the stopping of charged particles is contained in the energy loss function $\Im\{-1/[\epsilon(q,\hbar\omega)]\}dq/q$, but it does not give detailed information about the dominant interaction event. For example, it may describe both electron excitation and ionization events, as well as contributions from valence and core electrons, but the details are not directly accessible. We will now discuss two of these mechanisms, plasmon and phonon excitation, in more detail.

5.4.1 Energy Loss through Plasmon Excitation

One of the most important energy-loss mechanisms is plasmon excitation. The valence electrons in a metal or the free electrons in a plasma are often described well by the free-electron gas approximation. Such electrons may undergo collective

oscillations of frequency ω_p, called the plasma frequency, given by

$$\omega_p = \sqrt{\frac{e^2 n}{m\epsilon_0}} \,. \tag{5.40}$$

A plasmon is a quantum of a plasma oscillation with energy $\hbar\omega_p$. The mean free path associated with plasmon excitations can be calculated from the *Quinn formula [*18*]*,

$$\lambda_p = \frac{2a_0 E}{\hbar\omega_p}\left[\ln\left(\frac{\sqrt{p_f^2 + 2m\hbar\omega_p} - p_f}{p - \sqrt{p^2 - 2m\hbar\omega_p}}\right)\right]^{-1} \quad \text{with} \tag{5.41}$$

$$p = \sqrt{2mE} \quad \text{and} \tag{5.42}$$

$$p_f = \sqrt{2mE_f} \,. \tag{5.43}$$

Here E_f is the Fermi energy. Even in insulators, plasma resonances occur since electrons can be excited into the conduction band where they strongly interact with the other valence electrons. Note that the hole that is left behind in this case may also scatter and ionize further. These collective modes can also be described using the dielectric function $\epsilon = \epsilon_1 + i\epsilon_2$. For $\omega \to \omega_p$, ϵ_2 is small and ϵ_1 vanishes, leading to a strong peak in the electron loss function.

5.4.2
Energy Loss through Phonon Excitation

An important energy-loss mechanism of very slow electrons with kinetic energies below 20 eV traversing a crystalline material is phonon excitation [19]. The atoms of a crystalline lattice collectively vibrate about their equilibrium positions. The quanta of the collective oscillation modes are called *phonons*. Each collective mode can be associated with a frequency ω and a wave vector $\boldsymbol{k}$. The energy of a phonon is $\hbar\omega$. Phonons with $\omega(k = 0) = 0$ are called acoustic phonons, and phonons with $\omega(k = 0) \neq 0$ are called optical phonons. Since phonons disturb the perfect periodicity of a crystal, electrons are scattered by phonons. The maximum energy transfer during a scattering event with acoustic phonons is typically much smaller than for optical phonons.

Phonon scattering is significant only in a limited temperature regime. The temperature has to be sufficiently large so that phonons are present, but it has to be below the melting point so that the crystal structure is still intact. To analyze electron–phonon scattering, we have to evaluate the deviation of the Coulomb potential experienced by conduction-band electrons when the ions are displaced from their zero-temperature equilibrium position. Phonon scattering is well understood for very low electron energies of a few electron volts, especially for semiconductors. For these electron energies, the electron–phonon scattering rate is proportional to the density of states of the electrons. For large electron energies E the electron–phonon scattering rate drops rapidly, approximately proportional to $1/\sqrt{E}$ [20, 21].

In insulators, the band structure affects ionization from the valence band, and very slow electrons below the ionization threshold undergo both elastic and inelastic collisions with phonons as well as with impurities and atomic vacancies. The energy transfer during inelastic electron–phonon scattering is typically very small and not sufficient to induce atomic ionization. In metals, electron–electron interaction dominates over phonon scattering.

5.5 Electron Dynamics in Plasmas

Unlike in a solid, in a plasma both electrons *and ions* are quasi-free. Collisions of electrons with charged particles are very different from collisions with neutrals due to the long-range nature of the Coulomb force. This effect is compensated somewhat by the screening of charges in the presence of mobile charges. The average particle distance is given by $r_d = n^{-1/3}$, and the distance of closest approach is approximately $r_c = e^2/4\pi\epsilon_0 T$. The ratio $\alpha = r_d/r_c$ determines the nature of the plasma. For $\alpha \ll 1$, the plasma is strongly coupled, that is it is cold and dense, and collisions damp plasma oscillations. These kinds of plasmas do not follow the conventional plasma dynamics. On the other hand, for $\alpha \gg 1$, strong electrostatic interaction events are rare, and the plasma is weakly coupled. It can then be well described by the Fokker–Planck equation [22]. In this regime, collisions have only a small effect on plasma oscillations.

Binary collisions are sufficient to describe the particle dynamics in weakly coupled plasmas, and even for those it needs to be modified to account for collective effects such as Debye shielding. Debye shielding is the screening of charges in a plasma. The Debye shielding length is the distance in the plasma over which the electric field of a charged particle is shielded. Whereas in ideal plasmas many particles are within the Debye shielding length, in solid-density plasmas this is usually not the case. In addition, these systems are often degenerate.

The situation is more complicated when high-Z atoms are present since they are typically only partially ionized. The relevant equilibrium state in these plasmas is determined by electron impact ionization and three-body recombination, and can be described by the Saha equation for a hot plasma. However, the Saha equation becomes invalid for high densities and low temperatures since electrons are then degenerate and the atomic energy levels are distorted due to continuum lowering, as discussed in Section 2.3.1.3.

5.6 Statistical Description of Electron Dynamics

So far we have considered primarily the microscopic aspects of the electron dynamics. Microscopic particle methods are useful for describing the evolution of small systems. For larger systems, it is usually only manageable to consider a transport

approach in which the state of the system is described by a collective density function $\rho(\boldsymbol{r}, \boldsymbol{v}, t)$, which is the average particle density with velocity $\boldsymbol{v}$ at point $\boldsymbol{r}$ at time t. This approach is especially useful for systems with regular structure, such as spheres, in which case a one-dimensional treatment may be sufficient.

The function $\rho(\boldsymbol{r}, \boldsymbol{v}, t)$ gives a statistical description of a classical system in phase space. $\rho(\boldsymbol{r}, \boldsymbol{v}, t)$ can be obtained by solving the semiclassical Boltzmann equation [23],

$$\partial_t \rho + \boldsymbol{v} \partial_{\boldsymbol{r}} \rho + \boldsymbol{a} \partial_{\boldsymbol{v}} \rho = \Omega(\rho, \boldsymbol{r}, \boldsymbol{v}, t) \,, \tag{5.44}$$

where Ω is a source/collision term that contains information about first-principle microscopic processes. Using (5.44), we can follow nonequilibrium processes in plasmas, as described in more detail in Section 9.3.1.4.

Often hydrodynamic models are used instead which are a simplified form of the Boltzmann equation. Here, various assumptions are often made, for example only the collective transport component of the velocity is treated, the electrons are assumed to thermalize among themselves instantly, and an equilibrium of the local force is assumed. Hydrodynamic methods are described in more detail in Section 9.4.

5.7 Bremsstrahlung Emission and Inverse Bremsstrahlung Absorption

When a free electron travels through a plasma, it can emit and absorb electromagnetic radiation by scattering off other charges, while still staying free [24]. We will now discuss such scattering processes for ions and electrons.

5.7.1 Electron–Ion Bremsstrahlung

We first consider the case of an electron scattered by an ion. Charged particles are accelerated during collisions, which, according to classical theory, leads to the emission of electromagnetic radiation. The *Larmor formula* gives the total radiated power by a particle of charge q undergoing acceleration a in the nonrelativistic case as [25]

$$I = \frac{1}{4\pi\epsilon_0} \frac{2q^2}{3c^3} a^2 \tag{5.45}$$

which can be derived from Maxwell's equations. The acceleration of electrons in a plasma is typically much larger than for ions since the electron mass is smaller. Since $I \propto a^2$, electrons emit substantially more power than ions. Generally, large impact parameters correspond to the emission of soft (long-wavelength) radiation. This part of the spectrum is also affected most by screening of the nuclear charge by bound and quasi-free electrons in a plasma.

In quantum theory it can be shown that there is a finite probability for the emission of a photon when a particle is accelerated. This theory also limits the highest photon energy that can be emitted to the kinetic energy of the incoming particle. For very large particle velocities, a relativistic treatment is required, and the momentum of the emitted photons has to be taken into account [26].

5.7.2 Electron–Electron Bremsstrahlung

The radiation pattern of two colliding electrons is substantially different from the case of an electron colliding with an ion. In the classical case, in which photon recoil is neglected, a closed system of particles *with the same charge-to-mass ratio* cannot emit dipole radiation [27]. Electron–electron systems do not have a dipole moment, and Bremsstrahlung consists predominantly of the much weaker quadrupole radiation. Also, for a given electron energy, the maximum photon energy is smaller than in the electron–ion collision case since the recoil energy is appreciable.

5.7.3 Inverse Bremsstrahlung Absorption

Similar to the atomic processes discussed in Section 2.2, Bremsstrahlung emission has also an inverse free–free absorption process called *inverse Bremsstrahlung*. The formula for this process is

$$e + X + h\nu \rightarrow X' + e' \,, \tag{5.46}$$

where X and X' stand for the initial and final state of the ion, respectively, and e and e' stand for the initial and final state of the electron, respectively. Usually, the state of the ion does not change, so that $X = X'$.

The total emission coefficient from a high-temperature ionized gas of temperature T can be estimated to be [24]

$$J = \frac{1}{(4\pi\epsilon_0)^3}\frac{32\pi}{3}\left(\frac{2\pi kT}{3m}\right)^{1/2}\frac{Z^2e^6}{mc^3h}N_+N_e \,, \tag{5.47}$$

where N_+ is the density of ions with charge Ze, and N_e is the density of the electrons. We are specifically interested in the inverse process in order to understand how inverse Bremsstrahlung affects x-ray absorption. Using the principle of detailed balance discussed in Section 2.2.1.3, one can derive a spectral absorption coefficient κ_ν as [24]

$$\kappa_\nu = \frac{1}{(4\pi\epsilon_0)^3}\frac{4}{3}\left(\frac{2\pi}{3mkT}\right)^{1/2}\frac{Z^2e^6}{hcm\nu^3}N_+N_e \,. \tag{5.48}$$

κ_ν decreases with increasing temperature and for increasing photon energies, suggesting that inverse Bremsstrahlung absorption has an appreciable effect only for soft x rays but can be neglected for harder radiation.

5.8
Charge Trapping in Small Objects

Besides being scattered and thereby transferring energy to the surrounding electrons and ions, energetic electrons may simply leave the object. When an electron escapes, it carries energy with it and effectively reduces the temperature of the object. X rays interact with materials primarily through photoionization, leading to the emission of energetic photoelectrons. Subsequent Auger decay and electron impact ionization lead to the generation of additional, slower electrons. Electrons may escape the material initially, leaving a positive charge behind. When the positive charge becomes sufficiently large, the total electron energy, given by the sum of the potential energy $-e\Phi$ and of the kinetic energy, becomes negative, and the electrons are electrostatically trapped, meaning that they cannot escape from the object. These electrons are called *quasi-free* electrons.

In the following we will consider two simplified cases, (i) electrostatic trapping by a small solid sphere that is semitransparent to x rays, and (ii) electrostatic trapping by semi-infinite solids and thin films. We will only consider the escape of the high-energy photoelectrons, assuming that the low-energy Auger and secondary electrons are already trapped.

5.8.1
Charge Trapping in Solid, Spherical Objects

We first consider the case of a spherically symmetric solid sphere with net charge $\rho_c(r)$. Conceptionally we divide the sphere of radius r_0 into infinitesimally thin shells of radius r. A photoelectron with kinetic energy $E_{kin} = E_{x\text{-}ray} - E_b$, generated by a photon of energy $E_{x\text{-}ray}$ at a position $r \leq r_0$, may escape from the object if

$$E_{kin} > e\Phi_{crit}(r) = \frac{eQ(r_0)}{4\pi\epsilon_0 r_0} - \int_{r_0}^{r} \frac{eQ(r')}{4\pi\epsilon_0 r'^2}\, dr' \,. \tag{5.49}$$

E_b is the electron binding energy, and $Q(r) = 4\pi \int_0^r \rho_c(r') r'^2\, dr'$ is the charge within radius r. For a homogeneously charged sphere, (5.49) can be simplified to

$$\Phi_{crit}(r) = \frac{\rho_c}{2\epsilon_0}\left(r_0^2 - \frac{r^2}{3}\right). \tag{5.50}$$

Since $\Phi_{crit}(r)$ is largest at the center of the particle, electrons originating from there are trapped first, while the electrons from the outer layers can still escape until the potential reaches E_{kin}/e there, as well. During this time, the potential at the center of the sphere increases *beyond* $\Phi_{crit}(r)$. Figure 5.9 shows typical values of Φ_{crit} as a function of the particle radius for different ionization states. The finite width of the curves corresponds to the different point of origin of the energetic electron r. For example, a 7.4-keV electron is trapped in a singly ionized carbon sphere of radius 35 Å, regardless of whether the electron originated near the center or near the edge of the object.

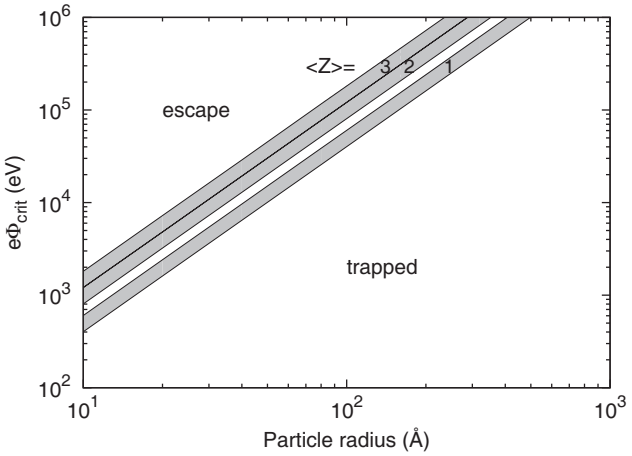

Figure 5.9 Electron kinetic energy required to overcome the electrostatic attraction of the positive object as a function of the particle radius and the average ionization state $\langle Z \rangle$. The object is assumed to consist of carbon atoms of density 1/15 Å^{-3}, corresponding to a mass density of 1.33 g/cm^3.

5.8.2 Charge Trapping in Semi-infinite Objects and Thin Films

The second geometry we consider is a circular beam of radius r_0 irradiating a semi-infinite solid or a thin free-standing film. We assume the x-ray intensity to be uniform across the beam. The beam irradiates an area A that is elliptically shaped with half axes r_0 and $r_0/\cos\theta$ where θ is the off-normal angle of incidence. Electrons will escape from the object until a sufficiently large positive charge has been accumulated so that the total energy of the liberated electrons becomes negative. In this case, this will occur first in the center of the beam, while electrons can still escape from the outer part of the ellipse until the potential exceeds E_{kin}/e everywhere. In a simple model, we neglect the variation of the potential across the illumination spot and assume that the object emits electrons until the potential E_{kin}/e is reached everywhere. It can be shown that in this case the surface charge density across the spot is given by [28]

$$\sigma(x,y) = \frac{Q}{\frac{4\pi r_0^2}{\cos\theta}\sqrt{1-\frac{x^2}{r_0^2}-\frac{y^2\cos^2\theta}{r_0^2}}}\,, \tag{5.51}$$

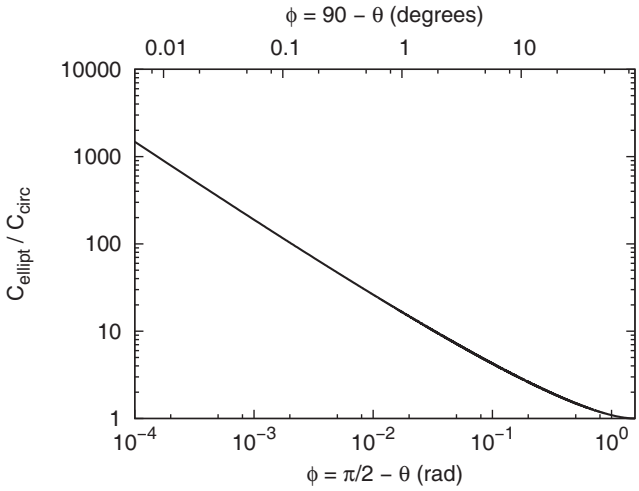

Figure 5.10 C_{ellipt}/C_{circ} as a function of the grazing angle of incidence ϕ.

and E_{kin} relates to the total charge in the spot by

$$\frac{E_{kin}}{e} = \frac{Q}{C_{ellipt}} \quad \text{with} \tag{5.52}$$

$$C_{ellipt} = C_{circ} \cdot \pi \left\{ \int_0^\infty \left[x(1+x)(\cos^{-2}\theta + x) \right]^{-1/2} dx \right\}^{-1}, \quad \text{and} \tag{5.53}$$

$$C_{circ} = 8\epsilon_0 r_0 \, . \tag{5.54}$$

Figure 5.10 shows C_{ellipt}/C_{circ} as a function of $\phi = \pi/2 - \theta$.

The charge Q that can escape from a semi-infinite solid is approximately given by $C_{ellipt}E_{kin}/e$. For a beam of radius $r_0 = 100$ µm incident on a solid at a grazing angle of $\phi = 5°$, $C_{ellipt} \approx 3.3 \times 10^{-14}$ F, so that a total charge of $Q \approx 3.3 \times 10^{-10}$ C is required to trap electrons with $E_{kin} = 10$ keV. The penetration depth of the x rays into the material d_x is given by (4.47). Using (5.51), we can estimate the charge density in the center of the beam when trapping occurs as $\sigma(0,0)/d_x$. For silicon, only a small fraction of the photoelectrons ($\approx 2.5 \times 10^{-9}$) have to escape until trapping occurs, which means that a semi-infinite solid essentially stays neutral under x-ray irradiation.

Even for thin films, the charging is a relatively weak effect. For a film of thickness d, the charge density can be estimated as $\sigma(0,0)/\min(d_x, d)$. Taking as an example an x-ray beam of radius 50 µm irradiating a 10-nm-thick silicon under normal incidence, an escaped charge density corresponding to an average ionization of only 1.4×10^{-5} leads to trapping of 10-keV photo electrons.

References

1 Ashcroft, N.W. and Mermin, N.D. (1976) *Solid State Physics*, Brooks Cole, New York.

2 Cooper, J.W. (1993) Photoelectron-angular-distribution parameters for rare-gas subshells. *Phys. Rev. A*, **47**, 1841–1851.

3 Tseng, H.K., Pratt, R.H., Yu, S., and Ron, A. (1978) Photoelectron angular distributions. *Phys. Rev. A*, **17**, 1061–1079.

4 Kobetich, E.J. and Katz, R. (1968) Energy deposition by electron beams and γ rays. *Phys. Rev.*, **170**, 391–396.

5 Ashley, J.C., Tung, J.C., and Ritchie, R.H. (1978) Inelastic interactions of electrons with polystyrene: Calculations of mean free paths, stopping powers, and CSDA ranges. *IEEE Trans. Nucl. Sci.*, **25**, 1566–1570.

6 Ashley, J.C. and Anderson, V.E. (1981) Interaction of low energy electrons with silicon dioxide. *J. Electron Spectrosc. Relat. Phenom.*, **24**, 127–148.

7 Luo, S., Zhang, X., and Joy, D.C. (1991) Experimental measurements of electron stopping power. *Radiat. Eff. Defects*, **117**, 235–247.

8 Dapor, M. (2003) *Electron-Beam Interactions with Solids*, Springer-Verlag, Berlin.

9 Joy, D.C. (1995) *Monte Carlo Modeling for Electron Microscopy and Microanalysis*, Oxford Series in Optical and Imaging Sciences, Oxford University Press, New York.

10 Friedrich, H. (2005) *Theoretical Atomic Physics*, 3rd edn, Springer, Berlin.

11 Ziaja, B., London, R.A., and Hajdu, J. (2005) Unified model of secondary electron cascades in diamond. *J. Appl. Phys.*, **97**, 064905.

12 Jablonski, A. and Powell, C. (2003) NIST electron elastic-scattering cross-section database: Version 3.1. *Tech. Rep. NIST Standard Reference Database 64*, National Institute of Standards and Technology (NIST), Gaithersburg, MD. http://www.nist.gov/srd/nist64.cfm. Last access: 22 May 2011

13 Bethe, H. and Ashkin, J. (1953) Passage of radiations through matter. In *Experimental Nuclear Physics* (ed. E. Segre), John Wiley & Sons, New York, p. 253.

14 Ritchie, R.H. (1959) Interaction of charged particles with a degenerate Fermi-Dirac electron gas. *Phys. Rev.*, **114**, 644–654.

15 Tanuma, S., Powell, C.J., and Penn, D.R. (1988) Calculations of electron inelastic mean free paths for 31 materials. *Surf. Interface Anal.*, **11**, 577–589.

16 Watanabe, T. (2001) Impact excitation of carriers in diamond under extremely high electric fields. *Jpn. J. Appl. Phys.*, **40**, L715–L717.

17 Penn, D.R. (1987) Electron mean-free-path calculations using a model dielectric function. *Phys. Rev. B*, **35**, 482–486.

18 Quinn, J. (1962) Range of excited electrons in metals. *Phys. Rev.*, **126**, 1453–1457.

19 Lundstrom, M. (2000) *Fundamentals of Carrier Transport*, 2nd edn, Cambridge University Press, Cambridge, UK.

20 Chen, Y. and Tang, T. (1989) Impact ionization coefficient and energy distribution function at high fields in semiconductors. *J. Appl. Phys.*, **65**, 4279–4286.

21 Jung, H.K., Taniguchi, K., and Hamaguchi, C. (1995) Impact ionization model for full band Monte Carlo simulation in GaAs. *J. Appl. Phys.*, **79**, 2473–2480.

22 Sharkofsky, I.P., Johnston, T.W., and Bachynski, M.P. (1966) *The Particle Kinetics of Plasmas*, Addison Wesley Publishing Company, Inc., London

23 Huang, K. (1987) *Statistical Mechanics*, John Wiley & Sons, New York.

24 Zel'dovich, Y.B. and Raizer, Y.P. (2002) *Physics of Shock Waves and High-Temperature Hydrodynamic Phenomena*, Dover Publications, Mineola, NY.

25 Larmor, J. (1897) A dynamical theory of the electric and luminiferous medium. Part III. Relations with material media. *Philos. Trans. R. Soc. Lond. A*, **190**, 205–493.

26 Lienard, A. (1898) Electric and magnetic fields produced by a point charge moving on an arbitrary path by means of

retarded potentials. *Écl. Électr.*, **16**, 360–365.

27 Haug, E. and Nakel, W. (2004) *The Elementary Process of Bremsstrahlung*, World Scientific, Singapore.

28 Smythe, W.R. (1968) *Static and Dynamics Electricity*, 3rd edn, McGraw-Hill Publishing, New York.

6
Short X-Ray Pulses

Recent advances in ultrafast optics have made it possible to generate high-intensity laser pulses in the visible regime that are shorter than a few femtoseconds (1 fs = 10^{-15} s) [1]. These pulses can be generated directly from rather compact and reliable laser oscillators and are orders of magnitude shorter in duration than what can be measured with modern sampling oscilloscopes. Therefore, novel techniques had to be developed to characterize them. Femtosecond pulses can be used to study transient phenomena in physical, chemical, and biological systems, including plasmas, and allow us to track changes even of the nuclear structure. Short pulses are also needed to study dynamic behavior of matter on short time scales, such as for atomic-resolution real-time observation of electron dynamics, which occurs within attoseconds (1 as = 10^{-18} s). However, the ultimate limit to the pulse length is set by the laser-field oscillation cycle, which is about one fs in the visible regime and therefore not sufficiently short to study sub-fs phenomena.

In principle, sub-fs phenomena can be studied using x-ray pulses, for which the duration of one wave cycle is approximately one attosecond. Historically, x rays have been used mainly as spatial probes. More recently, short-duration x-ray pulses of sufficient intensity have become available, and x rays can now also be used for time-resolved measurements.

Femtosecond and shorter x-ray pulses are particularly useful for probing ultrafast material dynamics. Such pulses allow the investigation of transient responses of atoms and molecules, high-intensity matter interaction, and basic properties of femtosecond radiation. In particular, processes in atoms and molecules often cannot be resolved with picosecond radiation. For example, for hydrogen with an electron in state n, the radius of the electron orbit R_n is proportional to n^2. In a semiclassical picture of a wavepacket circulating around the proton, the classical round-trip time is

$$T_R = \frac{4n^2h^3\epsilon_0^2}{e^4 m_e} \,. \tag{6.1}$$

For $n = 26$, we obtain $T_R \approx 100$ fs, which can easily be resolved with a one-femtosecond pulse. The spatial extent of a short pulse of one femtosecond duration is $ct = 300$ nm. Such pulses may also be sufficient to resolve the bending and vibration of chemical bonds, as well as some chemical reactions for which time

High-Intensity X-rays – Interaction with Matter, First Edition. Stefan P. Hau-Riege.

scales are also on the order of 100 fs. Plasma processes occur on a large range of time scales, depending on the density and the temperature.

Typically, pump-probe schemes are employed to study the fast dynamics in matter. Until recently, mainly long-wavelength-pump and x-ray-probe beams have been used for this purpose. For many phenomena, for example to study inner-shell atomic effects, the pump beam also needs to be an x-ray source of sufficiently high intensity. The recent advent of the x-ray free-electron laser (FEL) has led to significant progress in this field, providing x-ray pulses with pulse lengths around 10 to 300 fs [2]. It will take some time to thoroughly explore x-ray–matter interaction in this regime. Eventually, shorter sub-fs x-ray pulses will become necessary since many fundamental processes such as chemistry and semiconductor carrier dynamics operate in this time regime. Possibly *shaped* intense short x-ray pulses will become available some day which could be used to control the quantum dynamics of electrons.

6.1 Characteristics of Short X-Ray Pulses

We will first discuss the fundamental properties of short x-ray pulses, including coherence and photon statistics, pulse chirping, bandwidth limitations, and the propagation of short x-ray pulses in free space.

6.1.1 Coherence and Photon Statistics

An x-ray pulse can be characterized by multiple properties, including coherence and photon statistics. As discussed in Section 1.3.3, coherence describes the stability of light and is a measure for the correlation of the electric field at different points in space and time. For example, a sinusoidal wave that exists everywhere in space is perfectly coherent since if the electric field is known at a few locations and times, it is known everywhere for all times. In practice, waves are only partially coherent, which means that coherence exists only over a limited distance or for a limited time duration. The coherence time τ_c is the time duration over which a wave train remains stable. Assuming we know the phase at t_1, then there is a high probability that we know the phase at t_2 if $t_2 - t_1 \ll \tau_c$. This also holds the other way around: If we know the phase at t_1, then the probability that we know phase at t_2 is low when $t_2 - t_1 \gg \tau_c$. For perfectly coherent light, such as perfectly monochromatic light, τ_c is infinite.

To illustrate the meaning of the statistical properties of a photon stream, we can consider measuring the distribution of photons in an x-ray beam by counting the number of photons in short beam segments. For perfectly coherent light, it can be shown that these fluctuations follow Poissonian statistics [3]. Denoting the probability of finding n photons in such a beam segment as $P(n)$, it can be shown that

$$P(n) = \frac{\bar{n}^n}{n!} \exp(-\bar{n}) \,, \tag{6.2}$$

where $\bar{n}$ is the average count value. For such a Poisson distribution, the variance of n equals the mean value, so that $\sigma_n^2 \equiv \langle n^2 \rangle - \langle n \rangle^2 = \bar{n}$, and the standard deviation is $\sigma_k = \sqrt{\bar{n}}$. Comparing the actual photon counting statistics to the Poissonian distribution (6.2) can then be used to classify x-ray pulses [4]. For light with Poissonian statistics, $\sigma_n^2 = \bar{n}$, as for perfectly coherent light. Light is said to follow super-Poissonian statistics when $\sigma_n^2 > \bar{n}$, so that the counting statistics is broader than for Poisson distributions, which is very common. Some examples include thermal light from a black body, when only a single mode is considered, partially coherent light, and incoherent light. Partially coherent light is also called chaotic light and is characterized by a finite coherence time τ_c. Finally, light is said to follow sub-Poissonian statistics when $\sigma_n^2 < \bar{n}$. This narrow distribution is not consistent with the classical theory of light and can only be understood within quantum optics [5, 6].

6.1.2 Chirped X-Ray Pulses

For chirped x-ray pulses, the photon energy varies along the length of the pulse, so that the x-ray energy and time are coupled. Such pulses can be used to study processes on time scales shorter than the pulse length. For example, in Laue diffraction experiments, different x-ray energies give different diffraction patterns, and in this way the time dependence of the diffraction could be mapped onto space [7]. As we will discuss below, chirped x-ray pulses may also be used to reduce the pulse duration through time-compression or time-slicing. We now review the properties of chirped coherent x-ray pulses.

We consider a linearly polarized coherent photon pulse that is observed at a fixed point in space. The pulse may be described by its real-valued electric field strength,

$$E(t) = A(t)\cos\left(\Phi_0 + \omega_0 t\right), \tag{6.3}$$

where ω_0 is the carrier frequency, $A(t)$ is the envelope function, and Φ_0 is the absolute phase. The absolute phase is not very important if $A(t)$ does not vary much over the oscillation period T, as is currently the case for x rays.

The real-valued electric field strength of *chirped* x-ray pulses can be written as

$$E(t) = A(t)\cos\Phi(t) \tag{6.4}$$

with

$$\Phi(t) = \Phi_0 + \omega_0 t + \Phi_a(t)\,. \tag{6.5}$$

As in (6.3), ω_0 is the carrier frequency, $A(t)$ is the slowly varying envelope function, and Φ_0 is the absolute phase. The additional term $\Phi_a(t)$ is the chirp of the pulse. We can define an instantaneous pulse frequency,

$$\omega(t) = \frac{d\Phi(t)}{dt} = \omega_0 + \frac{d\Phi_a(t)}{dt}\,. \tag{6.6}$$

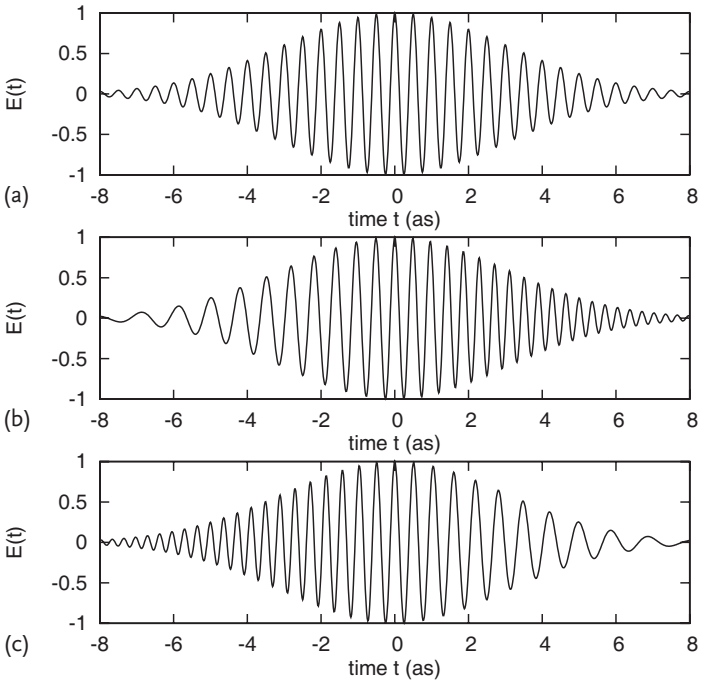

Figure 6.1 Electric field $E(t)$ in arbitrary units for (a) an unchirped pulse, (b) an up-chirped pulse, and (c) a down-chirped pulse.

In case $d\Phi_a(t)/dt > 0$, the instantaneous pulse frequency increases with time and the pulse is called *up-chirped*, whereas for $d\Phi_a(t)/dt < 0$, the instantaneous pulse frequency decreases with time and the pulse is *down-chirped*. Figure 6.1 shows examples for the evolution of the electric field of a Gaussian pulse for the cases of (i) an unchirped pulse at a wavelength of 1.5 Å with a vanishing absolute phase $\Phi_0 = 0$ and a pulse duration $\Delta t = 5$ as, (ii) an up-chirped pulse with $d\Phi_a/dt = 0.5/\text{as}^2\, t^2$, and (iii) a down-chirped pulse with $d\Phi_a/dt = -0.5/\text{as}^2\, t^2$. The pulse parameters were chosen to demonstrate the concept of up- and down-chirp clearly and cannot be achieved yet with today's technology.

6.1.3 Bandwidth-Limited X-Ray Pulses

There is a fundamental inequality for the pulse duration, taken as the full-width-at-half-maximum (FWHM) τ_p, and the spectral width, taken as the FWHM of the spectral intensity $\Delta\omega_p$,

$$\Delta\omega_p \tau_p \geq 2\pi \ . \tag{6.7}$$

For a coherent Gaussian pulse, $\Delta\omega_p \tau_p = 2\pi$, and the pulse is called *unmodulated* or *bandwidth-limited*. Figure 6.2 shows the spectral width $\Delta\omega_p$ of such bandwidth-

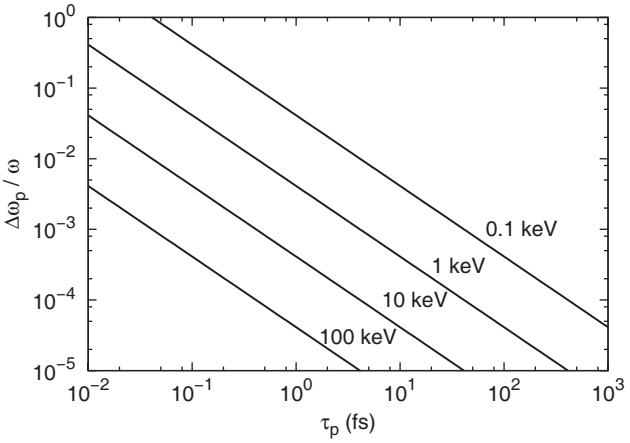

Figure 6.2 Spectral width $\Delta\omega_p$ of bandwidth-limited ultrashort coherent x-ray pulses as a function of the pulse length τ_p for different x-ray energies.

limited coherent x-ray pulses as a function of the pulse length τ_p for different x-ray energies. For a given x-ray energy and pulse length, the spectral width of the pulse has to be at least as large as $\Delta\omega_p$. For $\tau_p = 1$ fs, the spectral bandwidth is $\hbar\Delta\omega_p \geq 4.14$ eV. In the optical regime, such a short pulse would be very distorted, whereas in the x-ray regime, $\hbar\Delta\omega_p$ is much smaller than the pulse energy, and the pulse is similar to a long pulse.

Currently, most x-ray free-electron-laser radiation sources are based on the SASE (self-amplification-of-spontaneous-emission) scheme, which starts from random noise and behaves in the linear regime like a chaotic light source [8]. It has been shown that SASE light is composed of a number of coherent modes in the time domain, each represented by an intensity spike [9]. In the frequency domain, a similar spike structure occurs, and each spike corresponds to an individual coherence region [10]. The spike width can be used to determine the pulse duration of the chaotic radiation [10, 11]: The average time-bandwidth product for an ensemble of SASE pulses relates to the number M of coherent modes in the SASE pulse through

$$M = 2\bar{\sigma}_\omega \bar{\sigma}_t \,, \tag{6.8}$$

where $\bar{\sigma}_\omega$ is the root-means-square (RMS) SASE gain bandwidth, and $\bar{\sigma}_t$ is the RMS spike length. The energy fluctuation of the pulses is $\sigma_W/\langle W\rangle = 1/\sqrt{M}$, where W is the output energy per pulse.

As discussed in Section 4.4.1, when a short pulse interacts with an optic, the pulse shape may change, depending on the spectral bandpass $E_{bandpass}$ and the impulse response of the optic. Only when the bandpass energy $E_{bandpass}$ is larger than the bandwidth of the input pulse $\hbar\Delta\omega_p$ and the phase of the impulse response does not vary significantly over this energy range can the pulse length be preserved. To illustrate this concept, we consider a diffraction grating as is of-

ten used in the VUV (vacuum ultraviolet) and EUV (extreme ultraviolet) spectral regime. The path length difference between each groove is given by $n\lambda$, where n is the reflection order. With the grating length L and the line density N, the total optical path difference is $\Delta l = LNn\lambda$, so that the time stretch due to the grating is

$$\Delta\tau = LNn\frac{\lambda}{c} \tag{6.9}$$

$$= R_G\frac{\lambda}{c}\,. \tag{6.10}$$

The diffraction-limited resolving power is given by $R_G = LNn$. Note that this is an approximation since we assumed a uniform illumination and an infinitely large grating in one direction. Using a single grating always leads to some pulse stretching due to a spatial chirp which is a shear to the output beam. We could reverse the pulse stretch by using a second grating.

Similar to the case of an optical grating, a reduced bandwidth will lengthen a pulse in the x-ray regime. The bandpass of monochrometers and other optics must be greater than the spectral width of the x-ray pulse in order to preserve the pulse length. For example, when pulses are Bragg reflected from crystals, their temporal duration may be extended to a few femtoseconds, which is consistent with the energy-time uncertainty relationship for a chosen reflection.

6.1.4 Propagation in Free Space

As we will discuss in Section 7.5.1, current x-ray pulse intensities are much too small for nonlinear effects in vacuum to significantly affect the propagation of x-ray beams. We can therefore treat the propagation of short x-ray pulses using the linear formalism developed in Section 4.1.1. Since the index of refraction of vacuum is $n = 1$, (4.14), which describes the evolution of the electric field, simplifies to the linear wave equation,

$$\nabla^2\boldsymbol{E} - \frac{1}{c^2}\frac{\partial^2\boldsymbol{E}}{\partial t^2} = 0\,. \tag{6.11}$$

Equation 6.11 is satisfied by each component of the electric field. Therefore, the pulse shape of ultrashort pulses propagating in space is conserved. In matter, the intensity profile of an x-ray pulse is only preserved in nonabsorbing and nondispersive media, assuming that the electric field strengths are sufficiently small so that nonlinear effects can be neglected. As we have shown in Section 4.4, materials are usually dispersive and distort the pulse shape of subfemtosecond pulses significantly during propagation.

6.2
Generating Short X-Ray Pulses

Various methods have been suggested to generate short x-ray pulses. Compact, table-top optical lasers with output energies on the order of mJ and ps pulse durations can be used to irradiate solids and generate high-temperature plasmas which emit x rays. By combining this approach with rapid cooling of the target, sub-ps x-ray pulses can be generated. At the other end of the spectrum of possibilities are large-scale x-ray facilities. The highest-intensity short x-ray pulses in the laboratory are currently generated by x-ray free-electron lasers. We will now discuss the most important short-pulse x-ray sources and techniques to reduce the pulse lengths even further. This discussion extends on the more general description of x-ray light sources in Section 1.3.

6.2.1
Short-Pulse X-Ray Sources

Early devices to generate x rays such as x-ray tubes, electrical discharges, and even the first synchrotron sources were able to produce pulses as short as several nanoseconds. Recent advances in different areas of x-ray–matter interaction have enabled the development of pulsed x-ray sources with pulse lengths on the order of picoseconds, femtoseconds, and even attoseconds. Figure 6.3 shows where these new sources prevail in x-ray energy and pulse length space. Virtually all short-pulse x-ray sources involve accelerated electrons, and often short-pulse optical lasers are engaged, as well. A high degree of coherence in the photon output is generally beneficial to achieve high x-ray intensities since it simplifies focusing the beam.

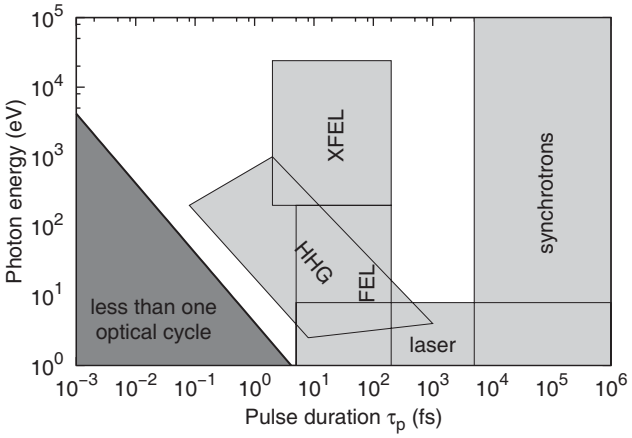

Figure 6.3 Source characteristics of different short-pulse x-ray sources. The bottom left of the diagram indicates the regime in which the pulse length is shorter than a single optical cycle. Reprinted figure with permission from [12].

6.2.1.1 High-Harmonic Generation

Intense optical laser pulses may be converted directly into x rays through high-harmonic generation, a nonlinear optical process, by focusing a sub-ps coherent visible-light laser to more than $10^{14}\,\mathrm{W/cm^2}$ and irradiating a gas jet or a solid target. At such intensities, the target ions are field-ionized, and the electrons are accelerated by the later part of the laser field's wave cycle. The accelerated electrons then coherently emit high-harmonic radiation. Harmonics beyond the 300th order have been achieved, corresponding to soft x-ray radiation up to 1 keV. Since the high-harmonics generation utilizes only a fraction of the optical cycle (a few fs in duration), the pulse length is a few hundred attoseconds.

This process cannot be described as regular *n*-photon excitation in the context of perturbation theory, in which the electron is treated in its bound state, since that cross section would be quite small. Instead, a simple *three-step model* has been very successful in describing the process of high-harmonic generation [13, 14]. The ion is ionized when the laser field is close to its peak, and the electron is driven away from the ion. When the field reverses, the electron is accelerated back toward the ion while gaining kinetic energy. When it eventually reaches the ion again and recombines, a photon with the energy $\hbar\omega_c$ is emitted that is equal to the sum of the ionization energy I_p plus the electron's kinetic energy.

The acceleration of the electrons occurs on time scales that are on the order of the cycle length of the driving laser field and leads to the emission of EUV and soft x-ray light in integer multiples of the fundamental frequency of the optical laser light. The maximum photon energy $\hbar\omega_{\max}$ that can be generated is limited by the maximum kinetic energy the electron can attain, which can be shown to be limited by

$$\hbar\omega_{max} = 3.17\,U_p + I_p\ , \tag{6.12}$$

where U_p is the ponderomotive potential. The emitted radiation exhibits a high degree of temporal and spatial coherence. High-harmonic generation has been demonstrated for photon energies up to 1 keV [15, 16].

6.2.1.2 Thomson Scattering

When an intense optical laser irradiates an energetic electron beam normal to the propagation direction of the electrons, for example in a storage ring, relativistic 90° Thomson scattering occurs colinear with the propagation direction of the electrons [17, 18]. Because of the momentum transfer from the electrons to the photons, the scattered photons can obtain energies of up to several keV. This process allows for the production of ultrashort, directed x-ray pulses.

6.2.1.3 Ultrafast X-Ray Tubes

A short-pulse optical laser can be used to generate ultrashort electron pulses from a heated cathode, which are then accelerated in a DC field to energies of several keV. When the electrons collide with the atoms of the anode material, bremsstrahlung is emitted. The emitted radiation is incoherent and continuous, and some of it lies in the x-ray spectral regime. Similar to x-ray pulses from laser-driven plasmas, the

duration of the x-ray pulses from an ultrafast x-ray tube is governed by the penetration depth of the electrons inside the anode material. The number of emitted photons is limited for sub-ps x-ray pulses by electrostatics: when too many electrons are ejected from the cathode material, the electrons experience a Coulomb repulsion that increases the pulse length. Increasing the accelerating voltage leads to shorter pulses. Ultrafast x-ray pulses have been demonstrated in the ns, ps, and fs regime [19–21].

6.2.1.4 Laser Plasma Sources

Ultrashort optical laser pulses can be used to produce short x-ray pulses by irradiating solid-density materials and creating a high density of excited atoms and a large number of energetic free electrons through inverse bremsstrahlung absorption. This hot dense plasma emits black-body radiation in the form of bremsstrahlung when the electrons are scattered by the ions. For sufficiently large laser intensities, the plasma also emits characteristic *K-α* radiation. The radiation is emitted into a solid angle of 4π and is not coherent. The hot plasma cools down by expanding on a time scale of typically less than a picosecond, so that the emitted x-ray pulses have few hundred femtoseconds time duration. The emitted pulses are perfectly synchronized with the pump laser. The principle was first demonstrated by Murnane [22].

6.2.1.5 Synchrotrons

In a *cyclotron*, charged particles are accelerated by electric and magnetic fields and move on outward-spiralling trajectories as the particle energy increases. Whereas in a cyclotron the electric and magnetic fields are constant in time, the fields in a *synchrotron* are carefully synchronized with the charged particles' motion so that they stay on their paths. Energy loss through bremsstrahlung emission is compensated by electric fields in RF (radio-frequency) cavities. A *storage ring* is a particular kind of synchrotron in which the charged particles (typically electrons) are kept circulating for a long time, up to several hours. A schematic of a storage ring is shown in Figure 6.4a. The electron current reaches up to one Ampere. Nowadays, storage rings are a mature and reliable technology. They support a large user community because each ring has several tens of beamlines. The emitted synchrotron radiation is collimated and stable, but the pulse length of 100 ps is relatively long. More complicated setups such as pulse slicing and streak cameras are used to improve the time resolution.

Insertion devices such as wigglers and undulators are used to mildly accelerate the electrons out of their synchrotron path to generate radiation. Undulators are periodic dipole-magnet arrangements with alternating magnetic fields, which are used to produce intense radiation that is concentrated in a narrow spectral band. Undulators are typically characterized by a dimensionless parameter [23]

$$K = \frac{e B \lambda_u}{2\pi m c}\,, \tag{6.13}$$

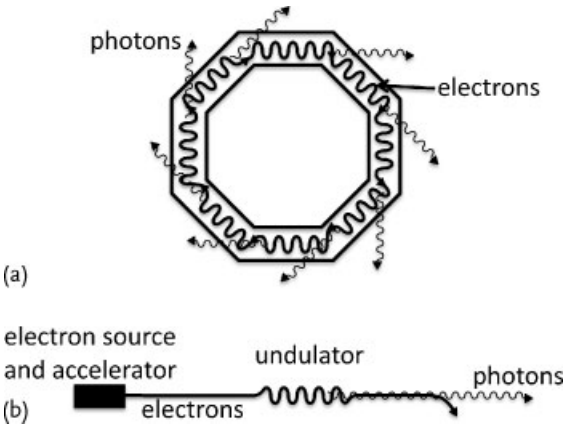

Figure 6.4 (a) Schematic of a synchrotron light source. The straight sections contain periodic magnetic structures (wigglers and undulators) that cause the emission of synchrotron radiation. (b) Schematic of a free-electron laser.

where $-e$ is the electron charge, B is the magnetic field, λ_u is the magnetic field undulation period, m is the electrons mass, and c the velocity of light. For $K \ll 1$, the oscillation amplitude is small, and light is emitted into a narrow spectral band. λ_u is chosen such that the electron bremsstrahlung induced by the magnetic field undulations interferes constructively. With increasing number N of magnetic field periods, the undulator brightness increases by a factor of up to N^2 over the radiation from a simple bending magnet due to constructive interference and the small emission angle which is reduced by a factor of $1/N$. For $K \gg 1$, the oscillation period is larger, and the radiation from each field period sums up incoherently. This kind of insertion device is called a wiggler and generates a much broader spectrum than an undulator. A wiggler behaves more like a series of bending magnets than an undulator. Wigglers and undulators emit radiation of only limited spatial coherence. The output radiation is strongly polarized and, for an undulator, collimated to within a few arcseconds.[1)]

In the course of the development of storage rings, the electron bunch length that determines the photon pulse duration has been reduced to a few tens of picoseconds by increasing the kinetic energy of the electrons. The maximum kinetic energy of the electrons is limited by the maximum available magnetic field that determines the radius of curvature of the electron trajectory and is typically on the order of a few GeV. The lower limit for the electron-bunch length is on the order of 1 ps. The bunches are typically spaced a few tens of nanoseconds apart. The short pulse length coupled with the ability to select a narrow spectral region makes synchrotrons very versatile devices. For a given electron energy, the emittance of the beam can be reduced and thereby the brightness of the radiation can be increased by increasing the circumference of the synchrotron. In the limit of a linear accel-

1) $1\,\text{arcsec} = 1/60\,\text{arcmin} = 1/3600°$.

erator, several GeV electron bunches can be produced that emit diffraction-limited 10-keV x-ray pulses.

In future technologies, it is anticipated that partial x-ray lasing may be achieved through the self-amplification-of-spontaneous-emission (SASE) principle, thereby increasing the emission ten to one hundred times. In the SASE process, a resonance between the electron bunch and synchrotron radiation occurs, which is initiated by shot noise. This principle is described in more detail in Section 6.2.1.7 on x-ray free-electron lasers.

X-ray pulses shorter than 1 ps down to 1 fs can be achieved by *electron-bunch slicing*, a technique in which an electron bunch interacts with the radiation from an intense fs optical laser [24], extracting a short segment of the pulse. Preserving the full pulse energy when decreasing the pulse length is more difficult. Techniques have been suggested to use the full electron bunch through *electron-bunch compression*, for example by chirping the electron energy along the length of the pulse and then compressing it in a magnetic chicane to sub-ps length [25] and below [26].

6.2.1.6 Energy Recovery Linacs

In an energy recovery linac, a low-emittance and highly monochromatic electron beam circulates through a ring-like transport line, which contains multiple insertion devices and is then returned to the linear accelerator (linac) in which the beam energy is recovered in the superconducting structure. Since the beam is not stored in the ring, the very small beam emittance from the linac is nearly completely preserved during the single travel through the ring, leading to very-high-brightness emission. Energy recovery linacs are now in the research and development phase. They are anticipated to be operated in one of two modes. In the first, high current mode, electron currents are on the order of 100 mA, and high-brightness 1-ps-long pulses are emitted. In the second, short-bunch mode, short pulses on the order of tens of fs are produced, but using much lower electron currents.

6.2.1.7 X-Ray Free-Electron Lasers

A schematic of a free-electron laser is shown in Figure 6.4b. X-ray free-electron lasers can be seen as an extension of an undulator insertion device. In an undulator, the bremsstrahlung radiation that is emitted by each accelerated electron interferes constructively, but radiation emitted by different electrons does not. Therefore, the x-ray radiation is proportional to the number of electrons N_e in a pulse. In an x-ray free-electron laser, the electron density is so much increased, for example by compressing the electron bunch, that the bremsstrahlung radiation is sufficiently intense to interact with the electron cloud itself, given rise to the phenomenon of *microbunching*. This process is illustrated in Figure 6.5. Because of this microbunching, the electron radiation is correlated and the radiation adds coherently, up to a factor of N_e^2. Microbunches can form spontaneously from noise. This mode of operation of a free-electron laser is called *self-amplification-of-spontaneous-emission* (*SASE*) [27]. Instead of starting from noise, the electron bunching may also be initiated with a laser. In this case, it is a *seeded* FEL [28, 29].

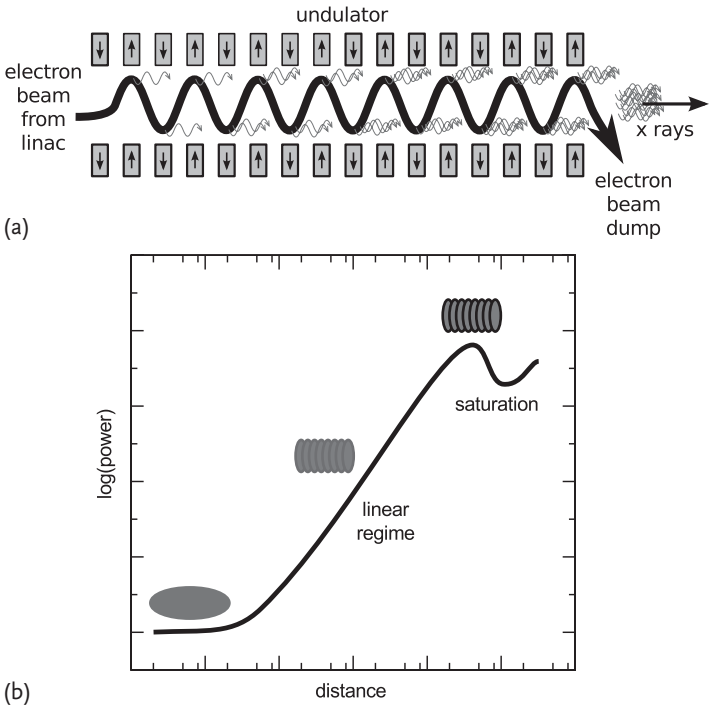

Figure 6.5 Sketch of the self-amplification-of-spontaneous-emission (SASE) process (a) in an undulator resulting from the interaction of the electrons with the synchrotron radiation they emit. (b) Here the longitudinal density modulation (microbunching) of the electron bunch is shown together with the resulting exponential growth of the radiation power along the undulator. Note that for x-ray free-electron lasers, the number of microbunches is much larger (on the order of 10^5) [30].

LEUTL at the Advanced Photon Source (APS) was the first SASE free-electron laser that achieved saturation in the visible spectrum [31]. At the Tesla Test Facility (TTF) at the Deutsches Synchrotron (DESY), saturation of a SASE free-electron laser was achieved at a wavelength of 100 nm [27]. This facility has recently been rebuilt to operate down to 6 nm, and its name was changed from VUV-FEL to FLASH [32]. The pulse lengths are less than 25 fs, and the energy for a pulse is up to 200 μJ. The Linac Coherent Light Source (LCLS) is the first x-ray free-electron laser that provides photon pulses between 0.5 and 10 keV. Each pulse is 10 to 300-fs long [2], and the pulse energy is up to 3 mJ [33]. Since the LCLS is currently operated in the SASE mode, its pulses exhibit limited temporal but quasi-full spatial coherence. In the near future, the Japanese x-ray free-electron laser near SPring 8 and the European x-ray free-electron lasers are expected to become available [34]. These sources require extreme electron-beam characteristics with respect to beam energy, emittance, peak current, and stability. X-ray free-electron lasers typically produce pulses that are shorter than a ps, and recently even fs-pulse lengths have been demonstrated [2]. Currently, the longitudinal coherence and the pulse-

shaping abilities are limited, but this can be greatly improved by using seeding and oscillator techniques. The spectral bandwidth $\Delta E/E$ of LCLS is on the order of 10^{-4}. Free-electron lasers can also be used as amplifiers, oscillators, and harmonic generators. The most recent x-ray free-electron-laser facilities use pulsed linacs and emit macro (composite) pulses at rates ranging from 1 to 120 Hz, and can also be operated in a burst mode with multiple pulses per macro pulse. Future continuous-wave (CW) superconducting linac-based free-electron lasers hold the promise of a high repetition rate with even pulse spacing in time, operating at tens of kHz to a MHz. Further developments on the electron gun are required to realize this concept. These next-generation facilities are expected to deliver transform-limited pulses of unprecedented intensity.

As a historical note, the subpicosecond-pulse source (SPPS) [26] was the first step toward the world's first hard x-ray free-electron laser, the LCLS. In the fine-focus test beam (FFTB) branch of the SLAC LINAC, 80-fs-long electron beams were produced and then used to generate short incoherent x-ray pulses in an undulator. The x-ray output was a highly collimated beam of 0.01 mrad with 10^7 photons and a few percent bandwidth.

6.2.2
Reducing Pulse Lengths through Time-Slicing

It is possible to chirp x-ray free-electron-laser pulses by creating an energy gradient along the length of an electron bunch using RF phasing or longitudinal wave fields in the accelerating structure [35]. As discussed in Section 6.1.2, chirped x-ray pulses exhibit a time-dependent wavelength which is equivalent to a time-correlated energy spread. Such a pulse can be used to create a shorter pulse through *time-slicing* in which a small temporal section of the x-ray pulse is selected. This leads to a proportional decrease in the total pulse energy.

Time-slicing can be implemented by using a monochromator of appropriate bandwidth to extract a short segment of the x-ray pulse [36], keeping only a fraction of the pulse energy. It has been proposed that in the x-ray regime, time-slicing could be achieved by using an off-axis transmissive zone plate in combination with a slit-like aperture: A circular zone plate focuses light to a point on its optical axis, and the distance of this focal point from the center of the zone plate is a function of the wavelength. When the illumination is restricted to a small area near the outer edge of the zone plate, it still converges to the focal point on the axis of the zone plate, giving the appearance that the small beam has been deflected sideways. This is similar to the behavior of a grating except that in the case of the zone plate the light is also focused. A screen perpendicular to the axis of the zone plate at a distance of the mid-pulse focus will see a small spot of light moving across the screen during the pulse. Placing an aperture slit through the screen in the path of the spot produces a brief pulse of light downstream [37]. For applications at x-ray free-electron lasers, it is necessary to fabricate the zone plates from low-Z materials in order to prevent radiation damage. The focal length f_0 at a design wavelength λ_0 of a zone plate will have a central radius of $r_1 = \sqrt{\lambda_0 f_0}$, and the focal lengths at other

wavelengths will be $f(\lambda) = r_1^2/\lambda$. As an example, at the x-ray free-electron-laser LCLS, a pulse chirp of 2% may be achieved [35], which would lead to a pulse length reduction of a factor of 4. For chirps of less than 0.25%, it is currently not possible to fabricate appropriate zone plates.

Another way to shorten the duration of x-ray light pulses is to use ultrafast shutters. It was shown that laser-induced acoustic pulses in crystals can modulate and switch the x-ray transmission properties by making use of the Borrmann effect. This technique could potentially be employed to generate subpicosecond pulses [38].

More recently it has been proposed [39] and demonstrated [40] that fs and sub-fs pulse length can be achieved in an x-ray free-electron laser by selectively spoiling the transverse emittance of the electron bunches. As a result, only a small temporal part of the electron beam lases. The implementation of this technique requires only a thin foil with a slot. Similar to the time-slicing technique described above, an energy chirp is introduced into the beam to obtain an energy-time correlation. When the electron bunch enters a magnetic bunch-compressor chicane, it is tilted relative to the longitudinal t axis, which introduces a space-time bunch tilt in the center of the chicane due to its chromatic dispersion. At the point of maximum tilt, a thin foil with a slot is placed in the beam path. Coulomb scattering of the electrons when passing through the foil increases the horizontal and vertical emittance of the beam except for a very thin unspoiled slice that will lase.

6.2.3
Reducing Pulse Length through Pulse Compression

Time-slicing methods utilize only a fraction of the x-ray pulse to generate short pulses. Another method to reduce the pulse length is pulse compression, which is often preferable since a larger fraction of the total pulse energy is used. Whereas dispersive elements such as gratings work well in the optical and extreme ultraviolet regime, these methods are typically not practical for x rays due to their low efficiencies and the large required geometries. Instead, novel schemes have been proposed, including using strained crystals with a lattice spacing that varies with depth to compress chirped x-ray pulses [41]. Estimates have shown that 230-fs-long x-ray pulses at 8 keV with a 0.5% chirp may be compressed by a factor of ten [41], which is seven times more than what can be achieved with time-slicing. The strained crystal is designed such that the strain varies with depth in a way that different parts of the pulse, corresponding to different wavelengths, will be reflected at different depths, and therefore experience a different time delay. If the strain profile matches the chirp profile of the incoming pulse, that is the leading part of the pulse is reflected deep inside the crystal, the bandwidth of the crystal matches the chirp bandwidth, and the depth of the strain matches the x-ray pulse length, then the pulse can be efficiently compressed.

In order to minimize absorption in the crystal, materials with low atomic charge number, such as carbon or silicon, are preferable as pulse compressors. Also, small Bragg angles are desirable since then the diffraction efficiency is higher. Since dif-

ferent wavelengths are reflected at different depths in the crystal, they also emerge from the crystal surface at different positions, thereby exerting a lateral shear to the beam that leads to an increase in the beam diameter.

6.2.4
Generating Ultrashort X-Ray Pulses

Producing ultrashort x-ray pulses with pulse lengths significantly shorter than one femtosecond continuous to be challenging. High-harmonic generation can produce coherent attosecond pulses in the soft-x-ray spectral range. When the atom is ionized by the laser, the photoelectron will collide with the ion a fraction of an optical laser cycle later. As discussed in Section 6.2.1.1, the energy is emitted as a photon and is the sum of the potential and the quiver or ponderomotive energy, which is the kinetic energy averaged over one optical cycle. Since these collisions occur during each half-cycle of the laser field, this effect produces bursts of attosecond pulses that are coherent with respect to each other. Using this technique of high-harmonic generation, femtosecond optical laser radiation has been shown to be the source of attosecond EUV pulses. The pulses are separated by one half-cycle of the laser period, and the train length was 10 fs [42, 43]. Hentschel *et al*. produced a 650-as soft-x-ray pulse using an intense, few-cycle laser pulse with a stabilized carrier envelope phase [44].

A possible source of attosecond x-ray pulses with shorter wavelengths are x-ray free-electron lasers. In the SASE mode of operation, the output radiation is composed of multiple isolated sub-fs spikes with random arrival times, so they are temporally incoherent. Zholents *et al*. [45] proposed a seeded attosecond x-ray radiation process in which electrons are selected by their previous interaction with a few-cycle intense optical laser pulse, leading to the emission of (temporally synchronized) isolated pulses of attosecond duration.

6.3
Characterizing Short X-Ray Pulses

Characterizing the temporal intensity distribution $I(t)$ of x-ray pulses is still very challenging. Typical photodiodes used to measure light intensity have a response time of tens of picoseconds, depending on the photodiode geometry and material, and the x-ray intensity. The only direct measurement devices for $I(t)$ are x-ray streak cameras with a temporal resolution of about 500 fs, so they cannot resolve femtosecond pulses. Instead, indirect measurements are performed to obtain information about $I(t)$. These techniques usually rely on some correlation of the x-ray pulse either with other beams or with itself, termed cross-correlation and auto-correlation techniques, respectively. Methods that operate in the time-frequency domain have turned out to be especially useful. Cross-correlation techniques typically utilize a well-characterized femtosecond optical laser, and require a good synchronization of the optical and x-ray pulses. Whereas this is a reasonable re-

quirement in case the optical laser is involved in the generation of the x-ray pulse, such as for high-harmonic generation, this is much more difficult when the x-ray pulses are generated independently of the optical laser, such as for SASE x-ray free-electron lasers. We will now discuss the principles and advantages of different pulse-length characterization schemes [12].

6.3.1 X-Ray Streak Cameras

X-ray streak cameras are currently the only direct measurement devices that can characterize the intensity of x-ray pulses with a time resolution of several hundred femtoseconds. In an x-ray streak camera, the x-ray pulse irradiates a material, and an electron beam is generated through photo emission. A transverse electric field is ramped up sufficiently fast so that the electrons in the beam that have been generated at different times impinge on an area detector, such as a photo plate or a charge-coupled device (CCD), at different positions. This streak then contains temporal information about the x-ray pulse intensity. This technique requires a fast electric field ramp and a means to trigger this ramp with the advent of the x-ray pulse. For high x-ray intensities, x-ray streak cameras are limited by space charge effects that lead to temporal broadening. Electrons generated through the Auger effect broaden the signal further. One axis of the area detector is used to sample the temporal shape of the pulse. The second axis perpendicular to the streak axis may be used to measure spatial or spectral information of the x-ray pulse.

6.3.2 Correlation Methods

Cross-correlation techniques characterize short photon pulses by probing the temporal pulse shape with a second, preferably shorter, reference pulse. If a shorter pulse is not available, *auto-correlation techniques* may be used in which the original pulse is split and used as a reference. If the reference is known, one can perform spectral interferometry, which is similar to a double-slit experiment in k space, except that the fringed interference pattern is measured in the frequency domain as a function of the time delay. If the reference is unknown, nonlinear mixing can be utilized to shift spectral regions in frequency. For example, one can measure the auto-correlation of a signal by recording the intensity of light produced by second-harmonic generation in a nonlinear crystal as a function of the time delay, which contains information about the temporal pulse structure. The complete pulse information can be obtained from frequency-resolved optical gating (FROG) [46]. Here the spectrum of the light obtained from second-harmonic generation is measured. To obtain phase information, a technique called spectral interferometry for direct electric-field reconstruction (SPIDER) is used [47]. The FROG technique with a known reference beam in the cross-correlation configuration is called X-FROG. X-FROG has been demonstrated in the VUV regime.

In the x-ray regime, auto-correlation techniques are difficult to realize since nonlinear optical effects are weak. For example, high intensities are needed because two-photon interaction cross sections at shorter wavelength are very small. This has limited this technique to free-electron-laser pulses and pulses generated through high-harmonic generation in the EUV regime. Usually, techniques rely on the cross correlation of an x-ray pulse with an even shorter femtosecond optical laser pulse as a reference beam, using a nonlinear optical process. High-intensity optical lasers are needed since the nonlinear properties, such as nonlinear polarizability, are usually weak in the x-ray regime. Synchronization of the x-ray pulse and the optical laser pulse is often difficult. If the exact temporal pulse shape of the reference is known, one can measure the fringed interference pattern in the frequency domain, which is the spectrum, of two copropagating pulses with a small temporal offset.

6.3.3 Examples

Ponderomotive Shift One of the main challenges of characterizing an x-ray pulse is the relatively weak interaction of x-ray light with materials. This limitation can be circumvented by using an intense optical laser, given the temporal jitter between the optical and the x-ray pulse is small. We assume we have a material with an ionization potential I_p that is smaller than the x-ray energy $\hbar\omega_{x\text{-}ray}$ but that is much larger than the laser photon energy $\hbar\omega_{laser}$. By measuring the spectrum E_p of the photoelectrons we can derive information about the x-ray pulse length indirectly. Without the high-intensity laser light, the energy of the photoelectrons is given by $E_p = \hbar\omega_{x\text{-}ray} - I_p$. When the high-intensity laser is turned on, the laser-assisted photoeffect can be described by the Volkov-state formalism [48], and it can be shown that

$$E_n = \hbar\omega_{x\text{-}ray} + n\hbar\omega_{laser} \tag{6.14}$$

with $n = \ldots, -2, -1, 0, 1, 2, \ldots$ representing the sidebands of order n in the electron spectrum. There are two effects that can be used to characterize the x-ray pulse. First, the energy difference between the highest order sideband and the zero-th order sideband scales linearly with the ponderomotive potential U_p. Second, the high-intensity laser creates an AC stark shift or a ponderomotive shift of the ionization potential on the order of U_p, which shifts the electron energy of the directly photoionized ($n = 0$) peaks. Either of these effects can be used to measure the pulse length by varying the delay between the optical and the x-ray pulse. The spectral positions of the sidebands can also be used to derive information about the chirp rate of the x-ray pulse.

Ponderomotive Streaking In high-harmonic generation, soft-x-ray pulse lengths of a few hundred attoseconds have been achieved. Since the optical laser is directly involved in the pulse generation, it is perfectly locked to the soft-x-ray pulse. The

soft-x-ray pulse duration can be determined by measuring the spectrum of the photoelectrons when the soft-x-ray pulse interacts with matter in the presence of the high-intensity optical laser field. The photoelectrons will be significantly accelerated or decelerated, depending on the phase of the optical laser pulse. By scanning the delay, characteristic modulations of the electron energy are observed in the energy spectrum of the electron, and comparisons to simulated spectra will determine the pulse length.

Laser-Induced Absorption Gating Finally, ultrafast changes of the absorption properties of a crystal may be used to measure pulse duration. In a perfect crystal, x rays can be transmitted through material thicknesses that are much greater than the absorption length. This is an outcome of the dynamic diffraction theory where it is shown that a propagating x-ray wave in a perfect crystal consists of an alpha and a beta mode, where the stationary alpha mode is a standing wave with zero intensity at the positions of the atoms, so that absorption of this mode is very weak. At the exit of the crystal, the alpha and beta solutions are then coherently projected onto the free-space solution. By using a femtosecond optical laser pulse, we can repopulate the extinguished beta solution close to the exit surface, and thereby control the intensity of the forward and Bragg-scattered x-ray light. This technique may provide a femtosecond time scale x-ray shutter when an optical femtosecond laser is used to excite optical phonons.

6.4 Characteristic Time Scales in Matter

Even events that appear to proceed slowly on a macroscopic scale, such as chemical reactions and phase changes, actually often evolve within femtoseconds, the time scale of fundamental microscopic processes. For example, gross atomic motion of clusters and groups of atoms occurs within 100 fs, and can be probed with short-pulse optical light. Electronic motion, on the other hand, occurs on the time scale of atto- and femtoseconds, and short x-ray pulses are needed to probe these processes.

When a particle is in a superposition of two states, the transition time between these states is closely related to their energy difference. Consider a particle in the superposition of the ground state of energy E_0 and the first excited state of energy E_1. The wavepacket that is the solution to the Schrödinger equation undergoes an oscillatory motion with the period

$$T_{osc} = \frac{2\pi\hbar}{\Delta E} , \tag{6.15}$$

with $\Delta E = E_1 - E_0$. A large value for ΔE corresponds to fast particle motions in the superposition state. Taking molecular vibration as an example, ΔE is on the order of meV, so that the oscillation time is 10–100 fs.

Figure 6.6 shows typical time scales of processes in materials, calculated from representative transition energies using (6.15). In the picture of a semiclassical

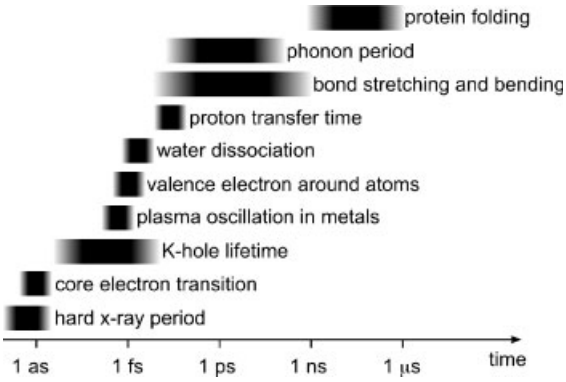

Figure 6.6 Characteristic time scales in matter.

wavepacket, the time scale for the motion of core electrons is between 1 and 10 as, and 20–1000 as for valence electrons. For electrons in the conduction band, the motion occurs on a time scale of 2–10 fs and longer. The plasma oscillation period in a metal is less than a femtosecond. For example, the oscillation in Cu is 0.4 fs. A typical phonon oscillation period is 25–150 fs. The dissociation time of water is 1.8 fs, but large conformational changes in chemical reactions take one nanosecond to a microsecond.

In organic chemistry, the time constant for bond stretching and bending is 10–50 fs. Hydrogen bonds determine the structure of many molecular systems. Of particular importance is the transfer of H along pre-existing hydrogen bonds. Whereas the structure of hydrogen bonds is pretty well understood, the functioning is still an active area of research. It has been shown that the transfer of protons or hydrogen ranges from 10 fs to several picoseconds and even nanoseconds.

For comparison, the oscillation time of 1 to 40-keV x rays is between 4 and 0.1 as, which is well suited to the study of all these phenomena associated with electron motion. For example, the lifetime of K holes in atoms ranges between 5 as and 15 fs. On the other hand, even bandwidth-limited x-ray pulses are not sufficiently short to resolve motion within nuclei that occurs even faster on the time scale of zeptoseconds, which is 10^{-21} s.

6.5
Short-Pulse X-Ray–Matter Interaction Processes

We will now discuss the processes that occur when a short x-ray pulse irradiates a solid material. There are similarities to continuous-wave (CW) interactions, but the time scales are very different so that different processes dominate at different times. In this chapter, we focus on the order in which these processes occur. As a specific example, we consider the case of a 10-keV free-electron-laser pulse with a pulse length of 100 fs irradiating a solid. Figure 1.9 shows the characteristic time

and energy regimes for the case of a low-Z material. High-Z materials behave similarly except that fluorescence dominates over Auger decay processes, as discussed in Section 2.2.2.

When a 10 keV photon is absorbed in the material, an electron with a kinetic energy of several keV is ejected. In subsequent processes, this electron slows down and thermalizes with its surroundings. The absorbed energy disperses into the system, first on an atomic level, and then on increasingly larger length scales. As shown in Figure 1.9, a longer length scale is typically associated with a longer time scale.

In this chapter we focus on the processes occurring on relatively short time scales, approximately up to ten picoseconds. An understanding of these processes is derived by combining atomic physics processes with results that have been obtained from optical-laser–matter interaction studies. Macroscopic processes such as thermal melting, spallation, and thermal fracture are described in Chapter 8.

6.5.1 Atomic Processes

As described in the Section 1.5.1, the dominant x-ray absorption process for moderate x-ray energies is photoionization, primarily of the inner atomic shells. This process proceeds for the duration of the x-ray pulse, given that the pulse fluence is sufficiently low so that at least some electrons remain on the ions and are available for absorption. Compared to the x-ray pulse length, photoionization events occur quasi-instantaneously.

Hollow atoms relax on the time scale of a few fs for low-Z atoms, primarily through Auger decay, and on a time scale ranging from a few attoseconds to a femtosecond for high-Z atoms, primarily through fluorescence, see Figures 2.3–2.5. During an Auger decay event, an electron is ejected. The kinetic energy of the Auger electron depends on the atomic configuration. For example, the kinetic energy of an Auger electron of a carbon atom with a single core hole is approximately 240 eV.

Both the photo- and Auger electron propagate through the solid while being elastically and inelastically scattered. As discussed in Chapter 5, the primary energy dissipation mechanisms for fast electrons are electron impact ionization and excitation. For example, an electron with a kinetic energy of 10 keV transfers its energy in the course of multiple scattering events on the time scale of 10 fs in carbon [49].

At the end of these processes, we obtain a warm or hot electron gas in the solid; the details of the coupling of this electron gas to the ions are not very well understood.

6.5.2 Fast Structural Changes

Structural material changes induced by short-pulse irradiation have been studied for decades [50]. Of particular interest are ultrafast disordering, including melt-

ing, and the study of light-induced phase transformations that potentially led to the discovery of novel ordered structures [51–53]. Studies of fast structural changes usually involve a pump-probe scheme. Most work so far has been performed with an optical pump beam since x-ray sources have been too weak to induce substantial structural changes in materials. Subpicosecond probing of excited materials can be performed through time-resolved reflectivity measurements and second-harmonic generation using optical laser pulses. Longer time scales can be probed using electron and x-ray diffraction, for example to study thermally induced melting, shock propagation, strain distribution, heat diffusion, crystal regrowth, and annealing.

Very important is the subpicosecond time scale corresponding to the motion of atoms on the length scale of the typical molecular bond length. As a specific example, it has been shown that an optical excitation of more than 10% of the valence electrons in a crystal with a diamond or zincblende structure results in structural instabilities, that, in turn, give rise to fast disordering on a time scale that is shorter than the electron–phonon relaxation time. This process can be viewed as an electronically induced solid-to-liquid transition and is also called *nonthermal melting*. In this process, a dense electron-hole plasma with a density on the order of 10^{22} cm^{-3} is formed that leads to ultrafast disordering and the formation of a hot liquid at high pressure. It is possible that in certain cases the instabilities could result in transient, ordered phases. The high-pressure liquid will then evolve on the time scale of several picoseconds as density perturbations propagate away from the molten layer, and macroscopic amounts of material are ablated at higher laser fluences.

The structural changes induced by x-ray radiation are much less understood since powerful x-ray sources are just starting to become available; x-ray free-electron lasers are expected to advance the field substantially. Whereas there are expected to be a number of similarities between the interaction of short x-ray and optical photon pulses with matter, important novel effects are expected to occur in the x-ray regime. This includes the electron cascade process in which one absorbed x-ray photon leads to many ionization events. For example, in carbon it has been estimated [49] that one 10-keV photon leads to 30–50 ionization events. On the other hand, the absorption process itself may be simpler in the x-ray case since high-density effects, including inverse Bremsstrahlung absorption, can often be neglected.

Up to now, x rays have usually been used as a powerful probe instead of a pump. For example, time-resolved x-ray diffraction has been used to study lattice dynamics and ultrafast disordering. Major findings include that ultrafast melting occurs homogeneously over macroscopic volumes of materials and on a subpicosecond time scale. X rays have also enabled the direct observation of large amplitude lattice compression and rarefaction waves, enabled to a large extent by their large penetration depth. This may change significantly with the introduction of x-ray free-electron lasers which will place more emphasis on using x-rays as a pump.

6.6 Single-Pulse X-Ray Optics

X-ray free-electron lasers provide x-ray pulses of unprecedented peak brightness and with full transverse coherence, which will open many unique opportunities in x-ray science. In order to shape and guide the x-ray beam, a variety of optical components such as monochromators, mirrors, and focusing optics are required. A significant challenge is the radiation damage associated with the high output fluence and the short pulse duration. It is usually required that the optics stay intact after x-ray exposure. For very short pulses, it is anticipated that primarily the x-ray fluence, given in units of energy per unit area, determines the onset of damage. We call the critical fluence above which permanent damage is inflicted upon a material the *conventional damage threshold*. At the very least, the x-ray fluence needs to be sufficiently low so that the exposed material does not melt since melting and resolidification may, among other things, alter the microstructure of the material and increase surface roughness. Often, more stringent conditions for the damage threshold are a consequence of chemical reactions, phase transformation, and imperfect vacuum in which the optics are operated. It is expected that the damage threshold for multiple-pulse exposures is even lower due to cumulative effects, including fatigue due to thermo-mechanical stresses [54, 55]. An example of an optical element designed for high radiation load are silicon zone plates with low x-ray absorption cross section, good thermal conductivity, high melting point, and no material interfaces [56].

It has been suggested that the conventional damage threshold may be overcome by taking advantage of the extremely short pulse duration of free-electron lasers since during the pulse, only a limited amount of damage takes place, and the optic could still function. Only after the pulse is the optic destroyed. This concept of *disposable single-pulse optics* has been demonstrated at the FLASH free-electron-laser facility in the wavelength range from 32 to 6 nm for multilayer mirrors [57], apertures [58], and nanolenses. It was found that the optics stay intact during the exposure to a soft x-ray pulse of 25-fs duration, even at fluences that are 50 times larger than the melting threshold.

Figure 6.7 shows the reflectivity of a Si/C multilayer mirror for different photon fluences at a wavelength of 32 nm as a function of the angle of incidence. The curve labeled low-fluence was measured at a synchrotron light source at fluences significantly below the damage threshold so that the multilayer stayed intact. The other data points were measured at fluences that greatly exceeded the single-pulse damage threshold. A typical postexposure site is shown in the optical microscope picture in Figure 6.8. This experiment clearly shows that the multilayer still functions during the pulse, but it is completely destroyed afterwards.

The smallest focal spot produced to date at a photon energy of 19.5 keV is 30 nm [59]. This small focal diameter was achieved using a thick multilayer structure in the Laue geometry. It has been speculated that these multilayer Laue lenses may be capable of producing x-ray spot sizes of less than 5 nm, which, given typical x-ray free-electron-laser output parameters, could lead to fluxes in excess of

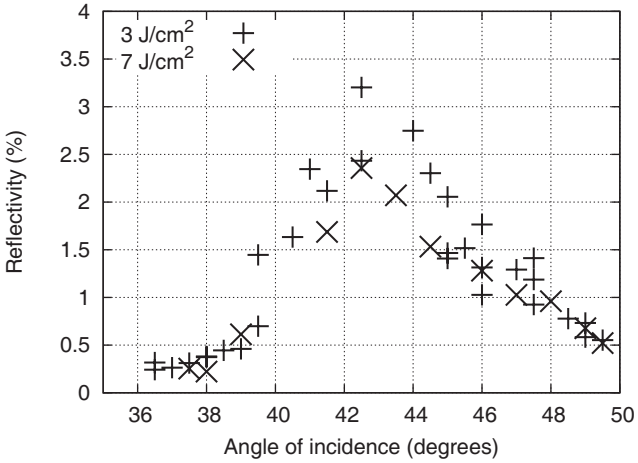

Figure 6.7 Reflectivity as a function of the off-normal angle of incidence θ for different fluences [57]. Reprinted figure with permission from [57]. Copyright (2007) by the American Physical Society.

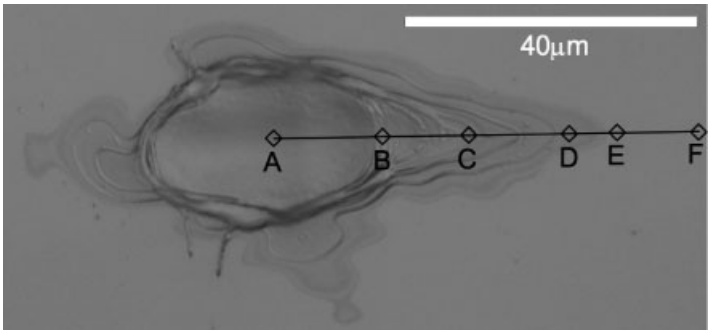

Figure 6.8 Nomarski differential interference contrast micrograph of the damaged multilayer surface [57]. Reprinted figure with permission from [57]. Copyright (2007) by the American Physical Society.

$3 \times 10^{22}\,\mathrm{W/cm^2}$. These Laue lenses are only several 100 μm in diameter so that they will be exposed to a large power density, which could lead to postexposure damage, but they may still function during the pulse.

Single-shot zone plates should be technically feasible but would require some concept of mass production, since the costs of fabrication of zone plates through conventional means, such as electron beam lithography, are very high. Mass production of zone plates is very challenging since zone plates require cutting-edge lithography, and good yield is difficult to achieve. Even if one could fabricate multiple zone plates, a very precise *delivery system* is required to ensure the zone plates are in the right position in the beam.

References

1 Kryukov, P.G. (2001) Ultrashort-pulse lasers. *Quantum Electron.*, **31**, 95.

2 Ding, Y., Brachmann, A., Decker, F.-J., Dowell, D., Emma, P., Frisch, J., Gilevich, S., Hays, G., Hering, P., Huang, Z., Iverson, R., Loos, H., Miahnahri, A., Nuhn, H.-D., Ratner, D., Turner, J., Welch, J., White, W., and Wu, J. (2009) Measurements and simulations of ultralow emittance and ultrashort electron beams in the linac coherent light source. *Phys. Rev. Lett.*, **102**, 254801.

3 Loudon, R. (2000) *The Quantum Theory of Light*. Oxford University Press, Oxford.

4 Mandel, L. and Wolf, E. (1995) *Optical Coherence and Quantum Optics*, Cambridge University Press, Cambridge.

5 Glauber, R.J. (1963) Coherent and incoherent states of the radiation field. *Phys. Rev.*, **131**, 2766–2788.

6 Walls, D.F. (1983) Squeezed states of light. *Nature*, **306**, 141–146.

7 Moffat, K. (2002) The frontiers of time-resolved macromolecular crystallography: Movies and chirped x-ray pulses. *Faraday Discuss.*, **122**, 65–77.

8 Schneidmiller, E.A., Saldin, E.L., and Yurkov, M.V. (2010) Statistical and coherence properties of radiation from x-ray free-electron lasers. *New J. Phys*, **12**, 035010.

9 Li, Y., Krinsky, S., Lewellen, J.W., Kim, K.-J., Sajaev, V., and Milton, S.V. (2003) Characterization of a chaotic optical field using a high-gain, self-amplified free-electron laser. *Phys. Rev. Lett.*, **91**, 243602.

10 Li, Y., Krinsky, S., Lewellen, J., and Sajaev, V. (2005) Frequency-domain statistics of the chaotic optical field of a high-gain, self-amplified free-electron laser and its correlation to the time-domain statistics. *Appl. Phys. B*, **80**, 31–34.

11 Krinsky, S. and Gluckstern, R.L. (2003) Analysis of statistical correlations and intensity spiking in the self-amplified spontaneous-emission free-electron laser. *Phys. Rev. ST Accel. Beams*, **6**, 050701.

12 Pfeifer, T., Spielmann, C., and Gerber, G. (2006) Femtosecond x-ray science. *Rep. Prog. Phys.*, **69**, 443–505.

13 Corkum, P.B. (1993) Plasma perspective on strong field multiphoton ionization. *Phys. Rev. Lett.*, **71**, 1994–1997.

14 Kulander, K.C., Schafer, K.J., and Krause, J.L. (2003) Dynamics of short-pulse excitation, ionization and harmonic conversion. In *Proc. Super-Intense Laser Atom Physics* (eds B. Piraux, A. L'Huillier, and R. Rzazewski), NATO ASI Series, Plenum, New York, pp. 95–110.

15 Seres, E., Seres, J., Krausz, F., and Spielmann, C. (2004) Generation of coherent soft-x-ray radiation extending far beyond the titanium L-edge. *Phys. Rev. Lett.*, **92**, 163002.

16 Seres, J., Seres, E., Verhoef, A.J., Tempea, G., Streli, C., Wobrauschek, P., Yakovlev, V., Scrinzi, A., Spielmann, C., and Krausz, F. (2005) Laser technology: Source of coherent kiloelectronvolt x-rays. *Nature*, **433**, 596.

17 Leemans, W.P., Schoenlein, R.W., Volfbeyn, P., Chin, A.H., Glover, T.E., Balling, P., Zolotorev, M., Kim, K.-J., Chattopadhyay, S., and Shank, C.V. (1997) Interaction of relativistic electrons with ultrashort laser pulses: Generation of femtosecond x-ray pulses and microprobing of electron beams. *IEEE J. Quantum Electron.*, **QE-33**, 1925–1934.

18 Schoenlein, R.W., Leemans, W.P., Chin, A.H., Volfbeyn, P., Glover, T.E., Balling, P., Zolotorev, M., Kim, K.-J., Chattopadhyay, S., and Shank, C.V. (1996) Femtosecond x-ray pulses at 0.4 Angstrom generated by 90° Thomson scattering: A tool for probing the structural dynamics of materials. *Science*, **274**, 236–238.

19 Hinze, U., Egbert, A., Chichkov, B.B., and Eidmann, K. (2004) Generation of picosecond hard-x-ray pulses in a femtosecond-laser-driven x-ray diode. *Opt. Lett.*, **29**, 2079–2081.

20 Oulianov, D.A., Tornov, I.V., Dvornikov, A.S., and Rentzepis, P.M. (2002) Structures of bromoalkanes' photodissociation in solution by means of ultrafast

extended x-ray absorption fine-structure spectroscopy. *Proc. Natl. Acad. Sci. USA*, **99**, 12556–12561.

21 Tomov, I.V. and Rentzepis, P.M. (2004) Ultrafast x-ray determination of transient structures in solids and liquids. *Chem. Phys.*, **299**, 203–213.

22 Murnane, M.M., Kapteyn, H.C., Rosen, M.D., and Falcone, R.W. (1991) Ultrafast x-ray pulses from laser-produced plasmas. *Science*, **251**, 531–536.

23 Winick, H. (1995) *Synchrotron Radiation Sources: A Primer*, World Scientific, Singapore.

24 Chong, H.W., Glover, T.E., Heimann, P.A., Shank, C.V., Zholents, A.A., and Zolotorev, M.S. (2000) Generation of femtosecond pulses of synchrotron radiation. *Science*, **287**, 2237–2240.

25 Treacy, E. (1969) Optical pulse compression with diffraction gratings. *IEEE J. Quantum Electron.*, **QE-5**, 454–458.

26 Bentson, L., Bolton, P., Bong, E., Emma, P., Galayda, J., Hastings, J., Krejcik, P., Rago, C., Rifkin, J., and Spencer, C.M. (2003) Fel research and development at the SLAC sub-picosecond photon source, SPPS. *Nucl. Instrum. Methods Phys. Res. A*, **507**, 205.

27 Andruszkow, J., Aune, B., Ayvazyan, V., Baboi, N., Bakker, R., Balakin, V., Barni, D., Bazhan, A., Bernard, M., Bosotti, A., Bourdon, J.C., Brefeld, W., Brinkmann, R., Buhler, S., Carneiro, J.-P., Castellano, M., Castro, P., Catani, L., Chel, S., Cho, Y., Choroba, S., Colby, E.R., Decking, W., DenHartog, P., Desmons, M., Dohlus, M., Edwards, D., Edwards, H.T., Faatz, B., Feldhaus, J., Ferrario, M., Fitch, M.J., Flöttmann, K., Fouaidy, K., Gamp, A., Garvey, T., Gerth, C., Geitz, M., Gluskin, E., Gretchko, V., Hahn, U., Hartung, W.H., Hubert, D., Hüning, M., Ischebek, R., Jablonka, M., Joly, J.M., Juillard, M., Junquera, T., Jurkiewicz, P., Kabel, A., Kahl, J., Kaiser, H., Kamps, T., Katelev, V.V., Kirchgessner, J.L., Körfer, M., Kravchuk, L., Kreps, G., Krzywinski, J., Lokajczyk, T., Lange, R., Leblond, B., Leenen, M., Lesrel, J., Liepe, M., Liero, A., Limberg, T., Lorenz, R., Hua, L.H., Hai, L.F., Magne, C., Maslov, M., Materlik, G., Matheisen, A., Menzel, J., Michelato, P., Möller, W.-D., Mosnier, A., Müller, U.-C., Napoly, O., Novokhatski, A., Omeich, M., Padamsee, H.S., Pagani, C., Peters, F., Petersen, B., Pierini, P., Pflüger, J., Piot, P., Phung Ngoc, B., Plucinski, L., Proch, D., Rehlich, K., Reiche, S., Reschke, D., Reyzl, I., Rosenzweig, J., Rossbach, J., Roth, S., Saldin, E.L., Sandner, W., Sanok, Z., Schlarb, H., Schmidt, G., Schmüser, P., Schneider, J.R., Schneidmiller, E., Schreiber, H.-J., Schreiber, S., Schütt, P., Sekutowicz, J., Serafini, L., Sertore, D., Setzer, S., Simrock, S., Sonntag, B., Sparr, B., Stephan, F., Sytchev, V.A., Tazzari, S., Tazzioli, F., Tigner, M., Timm, M., Tonutti, M., Trakhtenberg, E., Treusch, R., Trines, D., Verzilov, V., Vielitz, T., Vogel, V., v. Walter, G., Wanzenberg, R., Weiland, T., Weise, H., Weisend, J., Wendt, M., Werner, M., White, M.M., Will, I., Wolff, S., Yurkov, M.V., Zapfe, K., Zhogolev, P., and Zhou, F. (2000) First observation of self-amplified spontaneous emission in a free-electron laser at 109 nm wavelength. *Phys. Rev. Lett.*, **85**, 3825.

28 Yu, L.-H., Babzien, M., Ben-Zvi, I., DiMauro, L.F., Doyuran, A., Graves, W., Johnson, E., Krinsky, S., Malone, R., Pogorelsky, I., Skaritka, J., Rakowsky, G., Solomon, L., Wang, X.J., Woodle, M., Yakimenko, V., Biedron, S.G., Galayda, J.N., Gluskin, E., Jagger, J., Sajaev, V., and Vasserman, I. (2000) High-gain harmonic-generation free-electron laser. *Science*, **289**, 932–934.

29 Yu, L.H., DiMauro, L., Doyuran, A., Graves, W.S., Johnson, E.D., Heese, R., Krinsky, S., Loos, H., Murphy, J.B., Rakowsky, G., Rose, J., Shaftan, T., Sheehy, B., Skaritka, J., Wang, X.J., and Wu, Z. (2003) First ultraviolet high-gain harmonic-generation free-electron laser. *Phys. Rev. Lett.*, **91**, 074801.

30 Materlik, G. and Tschentscher, T. (2001) *TESLA Tech. Design Rep. Part V, The X-Ray Free Electron Laser*, DESY, Hamburg.

31 Milton, S.V., Gluskin, E., Arnold, N.D., Benson, C., Berg, W., Biedron, S.G., Borland, M., Chae, Y.-C., Dejus, J.R., Den Hartog, P.K., Deriy, B.B, Erdmann, M., Eidelman, Y.I., Hahne, M.W., Huang, Z.,

Kim, K.-J., Lewellen, J.W., Li, Y., Lumpkin, A.H., Makarov, O., Moog, E.R., Nassiri, A., Sajaev, V., Soliday, R., Tieman, B.J., Trakhtenberg, E.M., Travish, G., Vasserman, I.B., Vinokurov, N.A., Wang, X.J., Wiemerslage, G., and Yang, B.X. (2001) Exponential gain and saturation of a self-amplified spontaneous emission free-electron laser. *Science*, **292**, 2037–2041.

32 Tiedtke, K., Azima, A., von Bargen, N., Bittner, L., Bonfigt, S., Düsterer, S., Faatz, B., Frühling, U., Gensch, M., Gerth, C., Guerassimova, N., Hahn, U., Hans, T., Hesse, M., Honkavaar, K., Jastrow, U., Juranic, P., Kapitzki, S., Keitel, B., Kracht, T., Kuhlmann, M., Li, W.B., Martins, M., Nuñez, T., Plönjes, E., Redlin, H., Saldin, E.L., Schneidmiller, E.A., Schneider, J.R., Schreiber, S., Stojanovic, N., Tavella, F., Toleikis, S., Treusch, R., Weigelt, H., Wellhöfer, M., Wabnitz, H., Yurkov, M.V., and Feldhaus, J. (2009) The soft x-ray free-electron laser FLASH at DESY: Beamlines, diagnostics and end-stations. *New. J. Phys.*, **11**, 023029.

33 Arthur, J., Bane, K., Bharadwaj, V., Bowden, G., Boyce, R., Carr, R., Clendenin, J., Corbett, W., Cornacchia, M., Cremer, T., Emma, P., Fasso, A., Field, C., Fisher, A., Gould, R., Hettel, R., Humphrey, J., Ko, K., Kotseroglou, T., Li, Z., Martin, D., McSwain, B., Miller, R., Ng, C., Nuhn, H.D., Palmer, D., Pietryka, M., Rokni, S., Ruland, R., Schmerge, J., Sheppard, J., Tatchyn, R., Vylet, V., Walz, D., Warnock, R., Winick, H., Woodley, M., Yeremian, A., Yotam, R., Zimmermann, F., Pellegrini, C., Rosenzweig, J., Bertolini, L., van Bibber, K., Griffith, L., Libkind, M., Moore, R., Scharlemann, E.T., Schriber, S., Sheffield, R., Fawley, W., Halbach, K., Humphries, D., Kim, K.-J., Lidia, S., Schlueter, R., Xie, M., Freund, A., Meyerhofer, D., Serafini, L., and Limberg, T. (1998) Linac coherent light source (LCLS) design study report. *Tech. Rep. SLAC-R-521*, National Technical Information Services, Springfield, Virginia.

34 R&D Group SCSS XFEL (2005) SCSS X-FEL conceptual design report. *Tech. Rep. RIKEN Harima Institute, SPring-8, 1-1-1, Kouto, Mikazuki, Sayo, Hyogo JAPAN 679-5148.*

35 Emma, P. and Nuhn, H.-D. (2000) Quadrupole magnet error sensitivities for FODO-cell and triplet lattices in the LCLS undulator, *LCLS Technical Note LCLS-TN-00-6.*

36 Tatchyn, R. and Bionta, R.M. (2001) Performance studies of a multilayer-based radiation pulse slicer for linac coherent light source (LCLS) applications. *Proc. SPIE*, **4143**, 89–97.

37 Bionta, R. (2000) A transmissive optics approach for time-slicing the LCLS x-ray pulse, *LCLS Technical Note LCLS-TN-00-7.*

38 DeCamp, M.F., Reis, D.A., Bucksbaum, P.H., Adams, B., Caraher, J.M., Clarke, R., Conover, C.W.S., Dufresne, E.M., Merlin, R., Stoica, V., and Wahlstrand, J.K. (2001) Coherent control of pulsed x-ray beams. *Nature*, **413**, 825–828.

39 Emma, P., Bane, K., Cornacchia, M., Huang, Z., Schlarb, H., Stupakov, G., and Walz, D. (2004) Femtosecond and subfemtosecond x-ray pulses from a self-amplified spontaneous-emission-based free-electron laser. *Phys. Rev. Lett.*, **92**, 074801.

40 Frisch, J., Akre, R., Arthur, J., Bionta, R., Bostedt, C., Bozek, J., Brachmann, A., Bucksbaum, P., Coffee, R., Decker, F.-J., Ding, Y., Dowell, D., Edstrom, S., Emma, P., Fisher, A., Gilevich, S., Hastings, J., Hays, G., Hering, P., Huang, Z., Iverson, R., Loos, H., Messerschmidt, M., Miahnahri, A., Möller, S., Nuhn, H.-D., Pile, G., Ratner, D., Rzepiela, J., Schultz, D., Smith, T., Tompkins, H., Turner, J., Welch, J., White, W., Wu, J., Yocky, G., and Galayda, J. (2010) Operation and upgrades of the LCLS. In *Proc. XXV Linear Accelerator Conference*, JACoW. http://epaper.kek.jp. Last access: 25 May 2011.

41 Chapman, H.N. and Nugent, K.A. (2002) X-ray pulse compression using strained crystals. *Opt. Commun.*, **205**(4–6), 351–359.

42 Papadogiannis, N.A., Witzel, B., Kalpouzos, C., and Charalambidis, D. (1999) Observation of attosecond light

localization in higher order harmonic generation. *Phys. Rev. Lett.*, **83**, 4289–4292.

43 Paul, P.M., Toma, E.S., Breger, P., Mullot, G., Auge, F., Balcou, P., Muller, H.G., and Agostini, P. (2001) Observation of a train of attosecond pulses from high harmonic generation. *Science*, **292**, 1689–1692.

44 Hentschel, M., Kienberger, R., Spielmann, C., Reider, G.A., Milosevic, N., Brabec, T., Corkum, P., Heinzmann, U., Drescher, M., and Krausz, F. (2001) Attosecond metrology. *Nature*, **414**, 509–513.

45 Zholents, A.A. and Fawley, W.M. (2004) Proposal for intense attosecond radiation from an x-ray free electron laser. *Phys. Rev. Lett.*, **92**, 224801.

46 Trebino, R. (2002) *Frequency-Resolved Optical Gating: The Measurement of Ultrashort Laser Pulses*, Springer.

47 Iaconis, C. and Walmsley, I.A. (1998) Spectral phase interferometry for direct electric-field reconstruction of ultrashort optical pulses. *Opt. Lett.*, **23**, 792–794.

48 Glover, T.E., Schoenlein, R.W., Chin, A.H., and Shank, C.V. (1996) Observation of laser assisted photoelectric effect and femtosecond high order harmonic radiation. *Phys. Rev. Lett.*, **76**, 2468–2471.

49 Ziaja, B., London, R.A., and Hajdu, J. (2005) Unified model of secondary electron cascades in diamond. *J. Appl. Phys.*, **97**, 64905.

50 Van Vechten, J.A., Tsu, R., Saris, F.W., and Hoonhout, D. (1979) Reasons to believe pulsed laser annealing of Si does not involve simple thermal melting. *Phys. Lett. A*, **74**, 417–421.

51 Larsson, J., Heimann, P.A., Lindenberg, A.M., Schuck, P.J., Bucksbaum, P.H., Lee, R.W., Padmore, H.A., and Falcone, R.W. (1998) Ultrafast structural changes measured by time-resolved x-ray diffraction. *Appl. Phys. A*, **66**, 587–591.

52 Rousse, A., Rischel, C., Fourmaux, S., Uschmann, I., Sebban, S., Grillon, G., Balcou, P., Förster, E., Geindre, J.P., Audebert, P., Gauthier, J.C., and Hulin, D. (2001) Non-thermal melting in semiconductors measured at femtosecond resolution. *Nature*, **410**, 65–68.

53 Sokolowski-Tinten, K., Blome, C., Dietrich, C., Tarasevitch, A., von Hoegen, M.H., von der Linde, D., Cavalleri, A., Squier, J., and Kammler, M. (2001) Femtosecond x-ray measurement of ultrafast melting and large acoustic transients. *Phys. Rev. Lett.*, **87**, 225701.

54 Ryutov, D. (2003) Thermal stresses in the reflective x-ray optics for the linac coherent light source. *Rev. Sci. Instrum.*, **74**, 3722–3725.

55 Ryutov, D. (2004) Erratum: Thermal stresses in the reflective x-ray optics for the linac coherent light source. *Rev. Sci. Instrum.*, **75**, 5059.

56 Vila-Comamala, J., Jefimovs, K., Raabe, J., Kaulich, B., and David, C. (2008) Silicon fresnel zone plates for high heat load x-ray microscopy. *Microelectron. Eng.*, **85**, 1241–1244.

57 Hau-Riege, S.P., Chapman, H.N., Krzywinski, J., Sobierajski, R., Bajt, S., London, R.A., Bergh, M., Caleman, C., Nietubyc, R., Juha, L., Kuba, J., Spiller, E., Baker, S., Bionta, R., Sokolowski-Tinten, K., Stojanovic, N., Kjornrattanawanich, B., Gullikson, E., Plönjes, E., Toleikis, S., and Tschentscher, R. (2007) Subnanometer-scale measurements of the interaction of ultrafast soft x-ray free-electron-laser pulses with matter. *Phys. Rev. Lett.*, **98**, 145502.

58 Chapman, H.N., Barty, A., Bogan, M.J., Boutet, S., Frank, M., Hau-Riege, S.P., Marchesini, S., Woods, B., Bajt, S., Benner, W.H., London, R.A., Plönjes, E., Kuhlmann, M., Treusch, R., Düsterer, S., Tschentscher, T., Schneider, J.R., Spiller, E., Möller, T., Bostedt, C., Hoener, M., Shapiro, D.A., Hodgson, K.O., van der Spoel, D., Burmeister, F., Bergh, M., Caleman, C., Huldt, G., Seibert, M.M., Maia, F.R.N.C., Lee, R.W., Szoeke, A., Timneanu, N., and Hajdu, J. (2006) Femtosecond diffractive imaging with a soft-x-ray free-electron laser. *Nat. Phys.*, **2**, 839–843.

59 Kang, H.C., Maser, J., Stephenson, G.B., Liu, C., Conley, R., Macrander, A.T., and Vogt, S. (2006) Nanometer linear focusing of hard x rays by a multilayer Laue lens. *Phys. Rev. Lett.*, **96**, 127401.

7
High-Intensity Effects in the X-Ray Regime

Most x-ray–matter interaction phenomena observed with today's x-ray sources are linear in intensity and can be described perturbatively. X-ray radiation is most efficient at ionizing dense materials through multiple (sequential) inner-shell ionization events, coupled with Auger- and fluorescence decay steps that replenish the inner shells. Usually, single-photon ionization is the dominant absorption process.

With the advent of high-intensity x-ray sources such as x-ray free-electron lasers, the question arises if there are situations in which nonperturbative or nonlinear electron–photon interactions become important. In the longer wavelength regime between 100 nm and 10 μm and intensities up to 10^{20} W/cm^2, a large variety of surprising effects have been discovered, where in some cases, perturbation theory breaks down. Noticeable examples include multiphoton absorption, above-threshold ionization, high-harmonic generation, resonant AC Stark enhancement, and stabilization. Since experimental data are only starting to become available in the x-ray regime [1], we will now describe how some of the effects that are known in the optical regime are expected to extrapolate to much shorter wavelengths. A more detailed discussion of certain aspects of this topic can be found in [2]. It is likely that detailed experimental studies will lead to the observation of additional effects.

X rays differ from optical light in several key aspects, including that x-ray photons are much more energetic so that they can reach the inner core of atoms and ions and ionize them with a single photon. Optical photons, on the other hand, interact primarily with the outer valence electrons. Further, the wavelength of x rays is on the order of 1 Å and is much shorter than for optical light, so that the amplitude of free-electron oscillations in an x-ray field and the associated quiver energy (ponderomotive potential) are significantly smaller.

After discussing typical x-ray pulse intensities and electric field strengths that will be achievable with x-ray sources now or in the near future, we discuss high-intensity effects in single atoms and in plasmas. We will then discuss the foundations for nonlinear optics and some aspects of fundamental physics that can be investigated with high-intensity x rays.

High-Intensity X-rays – Interaction with Matter, First Edition. Stefan P. Hau-Riege.

7.1 Intensity and Electric Field of Intense X-Ray Sources

The rate of instantaneous energy transport of an electromagnetic wave per unit area is given by the magnitude of the Poynting vector,

$$S(t) = c^2 \epsilon_0 E(t) B(t) , \tag{7.1}$$

where $E(t)$ and $B(t)$ are the magnitudes of the electric and magnetic fields, respectively, c is the speed of light, and $\epsilon_0 \approx 8.85 \times 10^{-12}$ F/m is the permittivity of free space. For a monochromatic plane wave, the time-averaged intensity calculated from the Poynting vector in (7.1) is

$$I = \langle S \rangle_t = \frac{c\epsilon_0}{2} E^2 , \tag{7.2}$$

where E is the amplitude of the electric field. Note that (7.2) does not hold for arbitrary electric fields: For example, an evanescent wave does not transmit any power even though E is final.

For an x-ray free-electron laser with a photon output energy of 2.3 mJ and a pulse length of 100 fs, the light intensities and the corresponding electric fields are listed in Table 7.1 for different focal diameters. Chen and Pellegrini suggested that power densities of 10^{24}–10^{28} W/cm^2 are theoretically possible using tapered undulators and diffraction-limited x-ray focusing [3], but these values are significantly larger than what can be achieved today.

These intensity and field strength values should be compared with the characteristic atomic electric field strength

$$E_{at} = \frac{1}{4\pi\epsilon_0} \frac{e}{a_0^2} \approx 5.14 \times 10^9 \frac{\text{V}}{\text{cm}} , \tag{7.3}$$

above which nonlinear effects may become appreciable. Here $-e$ is the charge of an electron, and a_0 is the Bohr radius of the hydrogen atom given by (2.32). The intensity corresponding to the atomic electric field strength is $I_\gamma \approx 3.51 \times 10^{16}$ W/cm^2. The atomic unit of intensity is defined as $I_{at} \equiv 8\pi\alpha I_\gamma \approx 6.43 \times 10^{15}$ W/cm^2, where $\alpha \approx 1/137.036$ is the fine-structure constant.

Table 7.1 Intensities, electric field strengths, and ponderomotive energies produced by a typical x-ray free-electron laser with an output energy of 2.3 mJ, a pulse length of 100 fs, and x-ray energies of 0.8 and 8 keV.

Focal diameter	Intensity I (W/cm^2)	Electric field E (V/cm)	Ponderomotive energy at 0.8 keV (eV)	Ponderomotive energy at 8 keV (eV)
10 µm	2.93×10^{16}	3.32×10^9	6.57×10^{-3}	6.57×10^{-5}
1 µm	2.93×10^{18}	3.32×10^{10}	6.57×10^{-1}	6.57×10^{-3}
100 nm	2.93×10^{20}	3.32×10^{11}	6.57×10^{1}	6.57×10^{-1}
10 nm	2.93×10^{22}	3.32×10^{12}	6.57×10^{3}	6.57×10^{1}

7.2
High-X-Ray-Intensity Effects in Atoms

When atoms are exposed to high-intensity radiation, they may absorb multiple photons, emit multiple electrons, and emit photons. In optical spectroscopic studies, this leads to very rich effects since transitions are not limited by single-photon selection rules anymore. In strong oscillating fields, the energy of the excited states are shifted, which is termed *dynamic* or *AC Stark shift*. Electrons in highly excited states behave similar to free electrons and perform an oscillating quiver motion as a response to the applied wave field. The cycle-averaged kinetic energy of a free electron in the wave field is given by

$$U_p = \frac{(1+\epsilon)\, I e^2}{2\epsilon_0 c m \omega^2} \tag{7.4}$$

and is called the *ponderomotive* or *quiver energy* of the electron. Here I is the electric field intensity, $\hbar\omega$ the photon energy, and $\epsilon = 0$ for linearly polarized light, and $\epsilon = 1$ for circularly polarized light. The ponderomotive energy is the shift of the atomic energy with respect to the continuum, so that the ionization potential is given by $I_p + U_p$ instead of I_p. This shift can lead to intensity-induced absorption resonances.

Table 7.1 shows ponderomotive energies that can be achieved with x-ray free-electron-laser technology. For photon energies of 0.8 keV, appreciable ponderomotive energies can be achieved only with light that is focused to less than 100 nm. Since $U_p \propto \omega^{-2}$, the ponderomotive energies for the 8-keV case are even smaller by two orders of magnitude. Therefore, ponderomotive effects with x rays are expected to be much less significant for atomic processes than in the optical regime, and are relevant only under extreme focusing conditions not realizable today.

For optical high-power pulsed lasers, the ponderomotive energy can generate a significant driving force for free electrons to leave the high-intensity region, leading to a laser-pulse-shape dependence of the kinetic energy of the ejected electrons. In the x-ray case, also this effect is small.

Multiphoton ionization is the simultaneous absorption of multiple photons to promote bound electrons into the continuum. This effect is common for optical high-intensity radiation for which the photon energy is often less than the ionization energy. Since the final state of the liberated electron is free, the frequency of the incoming light can vary continuously. If this frequency is tuned so that there is an intermediate state that lies at an integral multiple of the photon energy above the initial state, then a strongly peaked resonance in the absorption spectrum occurs, and the process is called *resonance multiphoton absorption*. Simultaneous absorption of multiple photons does occur at sufficiently large x-ray intensities, as we will discuss next, but this effect is still dwarfed by single-photon interaction events. However, a strong nonlinear dependence of x-ray absorption on x-ray intensity occurs due to competing timescales of multiple *sequential* single-photon atomic processes, since the energy of one x-ray photon is sufficient for one-photon ionization events. For example, it has been recently demonstrated [1] that multiple inner-shell single-

photon absorption events compete with Auger relaxation in x-ray-irradiated neon at high intensities.

7.2.1 Multiphoton Absorption

X-ray photon energies are often much larger than the electron binding energy, and absorption due to one-photon ionization events of single bound electrons tends to dominate. At larger x-ray intensities, multiple single-photon ionization events occur sequentially, which is called *sequential multiphoton ionization*. Simultaneous multiphoton absorption, however, does occur in the x-ray regime, albeit this effect tends to be relatively small.

Since in the x-ray regime the photon energy is typically sufficiently large, all intermediate states lie in the continuum. In this case, a multiphoton ionization event involves the excitation of an electron into the continuum and free–free photon absorption events. Such processes are called *above-threshold ionizations*.

7.2.1.1 Multiphoton Absorption Cross Section

The rate of the simultaneous absorption of K photons by an atom is given by

$$P_K = C\sigma^{(K)}F_0^K\,, \tag{7.5}$$

where F_0 is the incoming photon flux in units of number of photons per unit area and unit time, and $\sigma^{(K)}$ is the cross section for K-photon ionization in units of unit area to the power K and unit time to the power $K-1$. C is a constant that depends on the coherence properties of the incoming radiation [4].

In the lowest nonvanishing order of perturbation theory, $\sigma^{(K)}$ can be inferred by summing and integrating the transition rate (2.102) over all final states. The interaction Hamiltonian H_{int} in (2.96) relates the initial, intermediate, and final states. H_{int} consists of two terms: $\boldsymbol{p}\cdot\boldsymbol{A}$ is first order in $\boldsymbol{A}$ and therefore describes single-photon processes, whereas $\boldsymbol{A}^2$ describes two-photon processes. If we include only the first-order H_{int} term in the transition rate (2.102), then $\boldsymbol{p}\cdot\boldsymbol{A}$ describes single-photon absorption (and emission) events, and $\boldsymbol{A}^2$ describes one-photon scattering and two-photon absorption. Taking the transition rate in the second order of H_{int}, $\boldsymbol{p}\cdot\boldsymbol{A}$ also contributes to one-photon scattering and two-photon absorption [5].

7.2.1.2 Two-Photon Absorption by Hydrogen

As a specific example, we consider two-photon above-threshold ionization in hydrogen. The total cross section for linearly polarized light can be derived from the transition rate (2.102) to be [6]

$$\sigma^{(2)}_{total} = \frac{8\pi^3\alpha^2 Ry^3 a_0^2}{(\hbar\omega)^2}\sum_{l_f,m_f}\left|\sum_a \frac{\langle\Psi_f|p_z e^{i\boldsymbol{k}\cdot\boldsymbol{r}}|\Psi_a\rangle\langle\Psi_a|p_z e^{i\boldsymbol{k}\cdot\boldsymbol{r}}|\Psi_i\rangle}{m\,(E_a-E_i-\hbar\omega-i\eta)}\right.$$
$$\left.-\frac{1}{2}\left\langle\Psi_f|e^{2i\boldsymbol{k}\cdot\boldsymbol{r}}|\Psi_i\right\rangle\right|^2_{E_f=E_i+2\hbar\omega}\,, \tag{7.6}$$

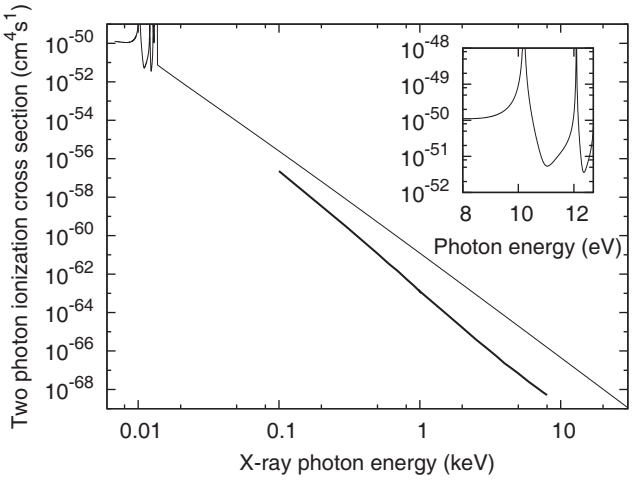

Figure 7.1 The thick line shows the two-photon ionization cross section for hydrogen calculated from (7.6) [6]. Overlaid are calculations based on the method described in [7].

where the polarization vector is taken along the z axis. Ry is the Rydberg energy (2.34), and a_0 is the Bohr radius (2.32) of hydrogen. The first term in (7.6) is the $\boldsymbol{p} \cdot \boldsymbol{A}$ component, and the second term relates to $\boldsymbol{A}^2$. η is an infinitesimally small positive number.

Figure 7.1 shows the two-photon ionization cross section $\sigma^{(2)}_{total}$ of hydrogen as a function of photon energy [6]. We also show the results obtained using a different model based on the dipole approximation that extends to lower energy [7], which highlights the uncertainty of these kinds of calculations. For photon energies below the one-photon ionization threshold of one Ry, the two-photon ionization cross section shows structure associated with resonant absorption, whereas for photon energies above one Ry, the cross section decreases monotonically.

The nondipole contribution to the $\boldsymbol{p} \cdot \boldsymbol{A}$ term in (7.6) is less than 1% even at 8 keV [6]. $\boldsymbol{A}^2$ is a pure nondipole term since for $\boldsymbol{k} = 0$, it is independent of the electrons' degrees of freedom and so does not induce transitions between Eigenstates. For hydrogen, the $\boldsymbol{p} \cdot \boldsymbol{A}$ term is sufficient for calculating $\sigma^{(2)}_{total}$ up to a photon energy of 6.8 keV. Above 6.8 keV, the $\boldsymbol{A}^2$ term dominates [6]. This result stresses the importance of going beyond the dipole approximation in the x-ray regime.

Figure 7.2 shows the flux at which the two-photon ionization rate of hydrogen would equal the single-photon ionization rate. At high photon fluxes, two-photon ionization can be the dominant absorption process, given that the prepulse is sufficiently small so that the hydrogen is not fully ionized through single-photon processes at the beginning of the pulse.

Besides pulse shape, the statistical properties of photon field are also important in determining the ionization process. The rate of two-photon absorption events is given by

$$P^{(2)} = \sigma^{(2)}_{total} \int \left\langle J(t)^2 \right\rangle dt \ , \tag{7.7}$$

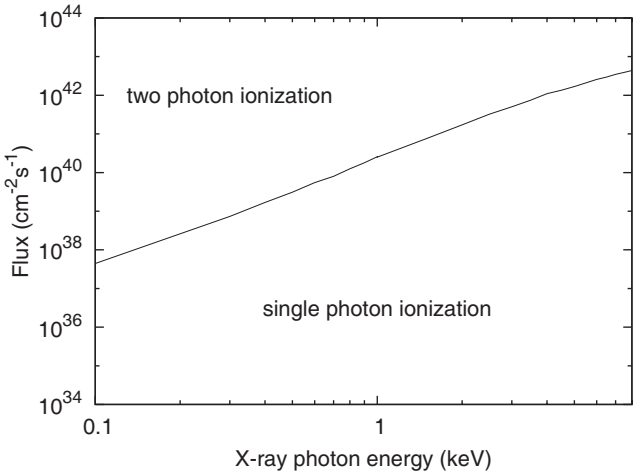

Figure 7.2 Flux for which the two-photon ionization rate is equal to the single-photon ionization rate for hydrogen. For fluxes above this curve, two-photon ionization dominates. The two-photon absorption cross section is taken from [6].

where $\langle J(t)^2 \rangle$ is the ensemble-averaged second moment of the x-ray flux. For example, for an x-ray free-electron laser operated in the SASE mode, $\langle J(t)^2 \rangle = 2\langle J(t) \rangle^2$, so that such a pulse leads to a twice larger transition rate than a constant pulse with the same average flux [4].

7.2.2 Tunneling Ionization

In strong optical laser pulses, a bound electron may respond to an instantaneous laser field by tunneling through the oscillating barrier of the attractive ion force and the electric field of the laser, called *tunneling* or *over-the-barrier* ionization. If the electric field of the laser is very large, the barrier may be so much lowered that tunneling is not necessary and the electron can escape directly from the atom. This effect is called *barrier-suppression ionization*. For tunneling to occur, the tunneling time has to be shorter than the laser cycle duration. The *Keldysh parameter* γ is defined as the ratio of these two times,

$$\gamma = \sqrt{\frac{I_P}{2U_p}}\,, \tag{7.8}$$

where I_p is the ionization potential and U_p the ponderomotive energy. For $\gamma \ll 1$, tunneling dominates. This is achieved most easily for low photon frequencies, large laser intensities, and for weakly bound (valence) electrons. For $\gamma \gg 1$, multiphoton ionization dominates since the electron does not have sufficient time to cross the barrier during one laser cycle. Figure 7.3 shows the fluence required to achieve $\gamma = 1$ for x rays as a function of photon energy. It also shows typical laser intensi-

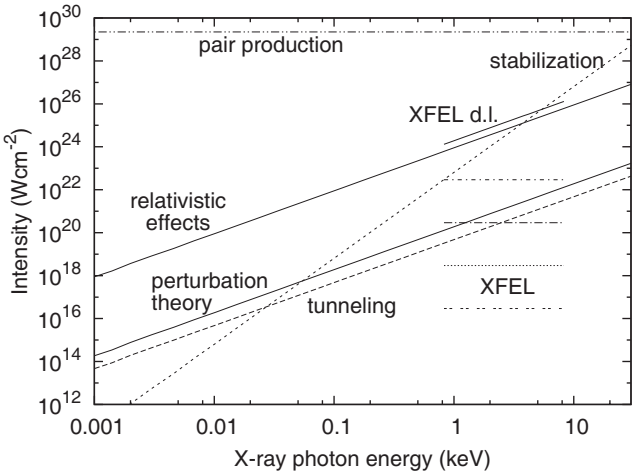

Figure 7.3 Interaction regimes as a function of x-ray intensity and energy. Shown are the intensities required for the onset of Schwinger pair production, relativistic effects, atomic stabilization, breakdown of perturbation theory, and tunneling ionization. The four horizontal lines indicate regimes that may be achieved with an x-ray free-electron laser with focal diameters of 10 and 1 μm and 100 and 10 nm for 100-fs-long pulses of 2.3-mJ energy. "XFEL d.l." indicates diffraction-limited focusing for this kind of x-ray free-electron-laser beam.

ties that can be achieved with x-ray free-electron-laser pulses. As discussed above, single-photon ionization dominates in the x-ray regime. Among the few tunneling and multiphoton absorption events, the latter clearly dominates except for the case of extreme focusing.

7.2.3 Onset of Strong Photon-Field Effects

We now consider the onset of strong photon-field effects in a multiphoton process of order n. Perturbation theory breaks down when the higher-order correction terms become comparable to the nth term. The ratio of a contribution of order $n+2$ to a contribution of order n can be estimated to be [8]

$$R_{n+2,n} \approx \left(\frac{I}{I_\gamma}\right)\left(\frac{Ry}{\hbar\omega}\right)^2, \tag{7.9}$$

where Ry is the Rydberg energy of atomic hydrogen, I is the intensity of the photon field, and $\hbar\omega$ its energy. Figure 7.3 shows the fluence required for the onset of strong photon-field effects in a multiphoton process as a function of the photon energy.

7.2.4 Multiple Ionization and Hollow Atoms

An atom can lose several electrons when irradiated by an x-ray pulse. The electrons depart from the atom either sequentially through a series of single-electron ionization events, or directly all at once. Typically, sequential ionization dominates over direct transitions. At least in the optical regime, there is little evidence for collective excitation of atoms in strong laser fields, and simultaneous ejection of two or more electrons occurs at a rather low rate. Further, the time between sequential ionization events is typically much larger than the electron orbit time so that electrons have time to adjust in between collisions. Therefore, the ionization events can be treated independently, and screening parameters and binding energies are different for each event.

If the x-ray energy is larger than the inner-shell ionization potential, atoms with core holes are formed preferentially since the subshell photoionization cross sections for inner-shell ionization are substantially larger than for the outer shells. At sufficiently large intensities and for atoms with long core hole lifetimes, as shown in Figures 2.3–2.5, multiple inner-shell ionization events can occur before the ion has time to relax toward the ground state through radiative or nonradiative transitions. In this case, *hollow atoms* with multiple inner-shell vacancies can form. Since high-intensity hard x-ray sources are just starting to become available, hollow shells have been observed only in a few elements so far, for example in lithium ($Z = 3$) [9] and, more recently, in neon [1]. The intensity expected at x-ray free-electron lasers is sufficiently large to observe sequential photoionization and multiple core holes. Recent experimental results are discussed in Section 10.1.

The dependence of nonlinear optical processes on the field statistics has been known for several decades. Similar to the simultaneous multiphoton ionization processes discussed in Section 7.2.1.2, the rate of sequential ionization events in the high-intensity x-ray regime is also not determined by the average peak intensity of the radiation field. Instead, sequential processes are correlated and are governed by higher-order coherence properties of the radiation field [4]. It has been proposed that chaotic photon statistics enhances double-core-hole formation via x-ray two-photon absorption. For example, for neon irradiated by an x-ray free-electron-laser SASE pulse as delivered by the LCLS with a 2.6-fs coherence time, there is a 30% enhancement at 10^{16} W/cm^2 [4]. The enhancement increases with the ratio of the x-ray free-electron-laser coherence time and the Auger lifetime. Understanding these enhancement effects is important, for example, to correctly interpret experiments to determine fundamental cross sections of nonlinear processes.

7.2.5 Stabilization of Atoms

Within the perturbation regime, the ionization rate for simultaneous K-photon absorption is proportional to I^K in intense laser beams, see (7.5). At very high laser intensities and high frequencies, it has been proposed that atoms can undergo

stabilization, and the photoionization rate actually decreases with increasing field intensity [10–17]. In a strong laser field, atoms are distorted, or dressed, which means that their wavefunctions are changed and their atomic energies are shifted, because they are increasingly determined by the laser field rather than by the atomic potential. Since the overlap of these dressed states with the field-free initial state is very small, fewer transitions occur. The question if strong-field stabilization actually occurs even in the optical regime is under debate [10] since it requires the field to turn on nearly instantaneously; no experimental data for this effect is currently available in the x-ray regime. It has been estimated that for hydrogen and an x-ray energy of 1 keV, a flux of 10^{20} W/cm^2 is required to observe this effect. For more loosely bound electrons, the required intensity is somewhat lower.

Several mechanisms have been proposed to explain the effect of stabilization. For a review, see [10]. As an example, we will now discuss adiabatic or Kramers–Henneberger stabilization, which is associated with a significant reconstruction of the eigenstates of the atom in the presence of the laser field in the high-frequency limit. In this model, we perform a gauge transformation of the time-dependent Schrödinger equation (2.3) to the Kramers–Henneberger frame, which is the noninertial oscillating frame of reference that follows the motion of a free electron in the laser field. We replace $\boldsymbol{r}$ with $\boldsymbol{r} + \boldsymbol{\alpha}(t)$, where for the linearly polarized monochromatic laser field $\boldsymbol{\alpha}(t) = \alpha_0 \cos(\omega t - \phi)\boldsymbol{x}$ with $\alpha_0 = e|\boldsymbol{E}|/m\omega^2$ which is the excursion amplitude of a free electron, and $\boldsymbol{x}$ is the excursion direction. In the Kramers–Henneberger frame, (2.3) becomes

$$i\hbar \frac{\partial \Psi(\boldsymbol{r}, t)}{\partial t} = \left\{ -\frac{\hbar^2 \nabla^2}{2m} + V\left[\boldsymbol{r} + \boldsymbol{\alpha}(t)\right] \right\} \Psi(\boldsymbol{r}, t) \,, \tag{7.10}$$

which describes the motion of an electron in an oscillatory potential. In the high frequency limit, we can approximate the potential $V[\boldsymbol{r} + \boldsymbol{\alpha}(t)]$ by its time average,

$$V(\boldsymbol{r}) \approx \frac{\omega}{2\pi} \int_0^{2\pi/\omega} V\left[\boldsymbol{r} + \boldsymbol{\alpha}(t)\right] \,, \tag{7.11}$$

and treat the remaining Fourier components of $V[\boldsymbol{r} + \boldsymbol{\alpha}(t)]$ as a perturbation. When α_0 is large, the effective potential has two minima close to $\boldsymbol{r} = \pm \boldsymbol{x}\alpha_0$, called the Kramers–Henneberger bound states. The corresponding wavefunctions of the bound states are centered near these minima, thus exhibiting a dichotomy. Higher-order Fourier components of $V[\boldsymbol{r}+\boldsymbol{\alpha}(t)]$ induce ionization from these bound states. For large α_0, the rates decrease if either the laser intensity increases or ω decreases. This effect has a semiclassical analog: A free electron cannot absorb photons in the monochromatic laser field due to energy and momentum conservation constraints. Absorption is only possible with a potential gradient, for example near a nucleus. If α_0 is larger than the Bohr radius at high intensity, the electron spends most of the time away from the nucleus and therefore does not absorb energy from the laser beam, which means it is stabilized. Stabilization occurs more easily for electrons with an initially large angular momentum and for highly excited states since in both cases the electron is at a far distance from the nucleus already.

7.3 Nonlinear Optics

Until a few decades ago, it was assumed that materials have linear optical properties, that the principle of superposition of light in matter is always a valid concept, and that the frequency of light in materials does not change. Only the advent of the laser in 1960 enabled experiments that showed that these assumptions are not necessarily true at high light intensities [18]. In general, nonlinear optics is concerned with the modification of the optical properties of materials by the presence of light. Whereas in most parts of this book discuss changes only to the opacity of materials, see for example Section 8.2, other optical properties of materials are affected, as well.

7.3.1 Nonlinear Optics in the Visible Regime

In the visible and longer wavelength regime, the theoretical framework for nonlinear optics is often based on the dependence of the polarization $\tilde{P}(t)$, which is the electric dipole moment per unit volume, in a material on the amplitude $\tilde{E}(t)$ of the applied electric field [19, 20]. This dependency describes the properties of a dielectric medium. For a linear medium, this relationship can be written as

$$\tilde{P}(t) = \epsilon_0 \chi^{(1)} \tilde{E}(t) \,, \tag{7.12}$$

where $\chi^{(1)}$ is the linear susceptibility. For nonlinear material, such a simple relationship does not hold, and, instead, the optical response can be written more generally in a series expansion as

$$\tilde{P}(t) = \epsilon_0 \left[\chi^{(1)} \tilde{E}(t) + \chi^{(2)} \tilde{E}^2(t) + \chi^{(3)} \tilde{E}^3(t) + \cdots \right] \tag{7.13}$$

$$\equiv \tilde{P}^{(1)}(t) + \tilde{P}^{(2)}(t) + \tilde{P}^{(3)}(t) + \cdots \,, \tag{7.14}$$

where $\chi^{(2)}$ and $\chi^{(3)}$ are the second- and third-order nonlinear susceptibilities, respectively. Note that this formalism can easily be expanded to anisotropic materials, in which case $\tilde{P}$ and $\tilde{E}$ are vector quantities and $\chi^{(n)}$ are tensors of rank $n + 1$.

Equation 7.13 gives rise to various nonlinear processes [20]. One of the conceptually simplest process is *harmonic generation* when laser light irradiates a crystal. Writing the applied electric field as

$$\tilde{E}(t) = E e^{-i\omega t} + E^* e^{i\omega t} \,, \tag{7.15}$$

then

$$\tilde{P}^{(2)}(t) = 2\epsilon_0 \chi^{(2)} E E^* + \epsilon_0 \chi^{(2)} \left(E^2 e^{-i2\omega t} + E^{*2} e^{i2\omega t} \right). \tag{7.16}$$

Therefore, there is a zero-frequency contribution, which is a static electric field across the crystal, and a contribution at frequency 2ω, the higher harmonic. Numerous other complex nonlinear processes have been observed, usually involving higher-order susceptibilities or more complex forms of the applied electric field

$\tilde{E}(t)$. For example, when the applied electric field $\tilde{E}(t)$ originates from the overlap of lasers with different frequencies, referred to as N-wave mixing, various sum and difference frequencies are observed, as is the case in parametric down conversion.

Physically, nonlinear processes originate from nonlinear scattering processes. Electromagnetic radiation is scattered by inducing oscillatory motion of charges in materials, which lead to re-emission of electromagnetic radiation. If the incoming radiation is sufficiently weak, the emitted radiation depends on the incoming radiation in a linear way. For high-intensity radiation, this relationship becomes nonlinear since the restoring force for large amplitude oscillation does not necessarily depend linearly on the displacement. This model of an anharmonic oscillator is sufficient to explain a large number of nonlinear optical processes.

7.3.2 Nonlinear Optics in the X-Ray Regime

Currently, it is not well understood if and to what extent the nonlinear processes, that have been observed in the visible regime, will occur with x-ray radiation. With the recent advent of x-ray free-electron lasers, we are just starting to explore the regime of nonlinear hard x-ray processes. A few pioneering experiments have been performed to demonstrate nonlinear x-ray optical processes. For example, based on calculations by Freund *et al.* [21], Eisenberger *et al.* demonstrated parametric conversion of x rays [22]. More recently, parametric down conversion was demonstrated indirectly through quantum-mechanical interference known as the Fano effect [23]. Mukamel *et al.* have developed a description for nonlinear x-ray spectroscopy in terms of nonlinear response functions and nonlinear susceptibilities, their analogs in the frequency domain [24].

For visible-light photons, nonlinear phenomena in crystals depend even on macroscopic material properties, such as crystallographic attributes. On the other hand, for sufficiently large x-ray energies beyond bound-electron resonances, nonlinear effects in the x-ray regime depend primarily on *free* electron properties, and macroscopic material parameters such as electron densities or absorption constants tends to determine only the magnitude of the nonlinearity [22]. Only closer to atomic resonances and for tightly bound electrons, do we need to consider the details of the bonding of the electrons, similar to the visual regime. A general formalism to treat nonlinear x-ray optics has been proposed in [2]. We will focus on the simpler case of quasi-free electrons, relevant for large x-ray energies and low-Z materials.

7.3.2.1 Nonlinear Optics with Quasi-Free Electrons

We use the Hamilton–Jacobi formalism to describe the relativistic motion of electrons in a planar electromagnetic field. Nonlinear scattering is the re-emission of radiation from accelerated charges undergoing anharmonic motion. The force on an electron is described by the Lorentz equation (1.18),

$$\boldsymbol{F} = q\left[-\nabla\Phi - \dot{\boldsymbol{A}} + \boldsymbol{v}\times(\nabla\times\boldsymbol{A})\right] . \tag{7.17}$$

In the radiation gauge, see (1.21) and (1.22), Φ is associated with the static charge distribution and $\boldsymbol{A}$ represents the incoming electromagnetic wave. Without an electromagnetic field, the electron simply sits at the potential minimum at $\boldsymbol{r}_0$ with $\boldsymbol{v} = 0$. If the electromagnetic field is weak, corresponding to a small magnitude of $\boldsymbol{A}$, the electron executes a harmonic oscillation around $\boldsymbol{r}_0$. For a strong electromagnetic field, the electron executes an anharmonic oscillation due to anharmonicities in the potential Φ and due to the last term in Lorentz force (7.17). The latter leads to a longitudinal component to the electron motion, which results in a trajectory that resembles a figure eight. The electron will then emit radiation while being accelerated. This description of the nonlinear optical behavior of free electrons is a good model for electromagnetic radiation interacting with weakly bound electrons. The magnetic field contribution complicates the motion of electrons in such a field substantially. We will now discuss how this problem can be solved analytically.

A plane-wave traveling in the positive z direction can be described by

$$\boldsymbol{A} = \left[A_x(\tau), A_y(\tau), 0\right] \tag{7.18}$$

with $\tau = t - z/c$. We assume that the electron rests at the origin initially. It can then be shown that, neglecting radiation reaction, the solution of the force equation (7.17) can be written as [25]

$$p_x = eA_x(\tau)\,, \tag{7.19}$$

$$p_y = eA_y(\tau)\,, \quad \text{and} \tag{7.20}$$

$$p_z = \frac{e^2\left[A_x(\tau)^2 + A_y(\tau)^2\right]}{2mc}\,, \tag{7.21}$$

with $A_x(0) = 0$ and $A_y(0) = 0$. Notice that $p_z > 0$ while the pulse is on, so that the electron is translated into the propagation direction of the electric field. For a linearly polarized plane wave of frequency ω we may write

$$A_x(\tau) = A_0 \sin(\omega\tau)\left[1 - \exp(-\gamma\tau)\right], \quad \text{and} \tag{7.22}$$

$$A_y(\tau) = 0\,. \tag{7.23}$$

Integrating (7.19) to (7.21), we obtain for the electron trajectory after the transient motion

$$x = \frac{1}{k}\left[-2Q\left(\cos\omega\tau' - 1\right) + \text{const}\right], \tag{7.24}$$

$$y = 0\,, \quad \text{and} \tag{7.25}$$

$$z = \frac{1}{k}\left[Q^2\left(\omega\tau' - \frac{1}{2}\sin 2\omega\tau'\right) + \text{const}\right], \tag{7.26}$$

with

$$Q = \frac{eA_0}{2mc} \tag{7.27}$$

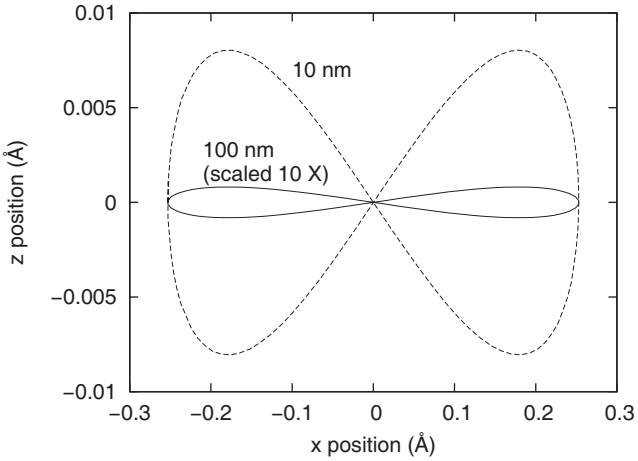

Figure 7.4 Trajectory of a free electron in a 1-keV x-ray pulse with 100-fs duration and 2.3-mJ pulse energy as can be provided by the x-ray free-electron-laser LCLS.

and $k = 2\pi/\lambda$. Here we renormalized τ to $\tau' = t' - z'/c$ after the initial transient motion.

To visualize the path of the electron, we transform these solutions into an average rest frame in which the drift velocity in z, see (7.21), vanishes, by rewriting τ' as

$$\tau' = \frac{1}{\sqrt{1+2Q^2}}\left(t' - \frac{z'}{c}\right), \tag{7.28}$$

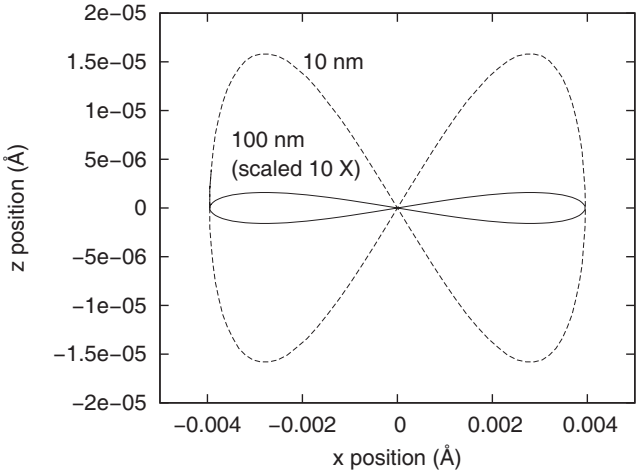

Figure 7.5 Trajectory of a free electron in an 8-keV x-ray pulse with 100-fs duration and 2.3-mJ pulse energy as can be provided by the x-ray free-electron-laser LCLS.

so that

$$z' = \frac{1}{k}\left(-\frac{Q^2}{\sqrt{1+2Q^2}}\frac{1}{2}\sin 2\omega\tau' + \text{const}\right). \tag{7.29}$$

This shows that the trajectory in the x–z plane resembles a figure eight. For small amplitude waves, corresponding to small values of A_0, the trajectory is close to a straight line since Q is small, and therefore $|x| \gg |z|$. The longitudinal motion in z has twice the frequency than the transverse motion in x. Figures 7.4 and 7.5 show the free-electron path for typical x-ray free-electron-laser fluences at 1 and 8 keV, respectively. The oscillation amplitude in this regime is rather small, even if we assume a focal diameter of 10 nm.

7.3.2.2 Magnitude of Nonlinear Effects in the X-Ray Regime

Nonlinear optical effects in the x-ray regime are much weaker than for visible light since x rays induce much more rapid oscillations, so that the oscillation amplitude and velocity are smaller. Therefore, for a given light intensity, the electrons are exposed to a smaller part of the anharmonic potential, and the effect of the Lorentz force is smaller. Since nonlinear optics exhibit a very strong resonance enhancement effect, it is anticipated that nonlinear effects are easier to observe near an atomic resonance.

7.4 High-Intensity Effects in Plasmas

In the optical regime, remarkable new laser–plasma interaction phenomena occur when the laser intensity approaches the relativistic regime at intensities around 10^{18} W/cm^2. Simple scaling suggests that for x rays, the corresponding intensity would be 10^{24} W/cm^2, which is much higher than what can be achieved today (see Table 7.1). Currently, the peak intensity of x-ray free-electron lasers is limited primarily by the performance of the focusing optics which has the potential to be significantly improved.

Ångstrom-size focusing is technically very challenging, and considerable improvements in free-electron laser and optical focusing technologies will be required. Extending Table 7.1 for the intensities of x-ray free-electron-laser radiation, a focal diameter of 1 nm results in a fluence of 3×10^{24} W/cm^2, and a focal diameter of 1 Å leads to 3×10^{26} W/cm^2. The associated electric fields are 3.34×10^{13} and 3.34×10^{14} V/cm, respectively. The accelerations of electrons of mass m_e due to these electric fields,

$$a = \frac{eE}{m_e}, \tag{7.30}$$

are 5.84×10^{26} and 5.84×10^{27} cm/s^2, respectively.

Chen and Pellegrini suggested that the extraction efficiency of an x-ray free-electron laser, which is the efficiency for the energy transfer of the electron beam to

the x-ray photons, can possibly be improved by adding a tapered undulator section or running it as a regenerative amplifier [26]. Tapered undulators are designed to compensate for the energy loss of the radiating electron beam during lasing. With these techniques, two to three orders of magnitude increases in the peak power are conceivable.

Technical immaturity has not stopped numerous researchers to speculate about what *would* happen if we reached such intensities. Many of the proposed effects rely on an extrapolation from the visible into the x-ray high-intensity regime. Whereas it is likely that our understanding of laser–plasma interaction will substantially improve and change as we approach such high x-ray intensities, these investigations may guide and motivate research in this field, and this is one of the main reasons why we chose to discuss some of the proposed phenomena.

7.4.1
Plasma Wakefield Accelerators

High-intensity x-ray pulses can penetrate solid-density plasmas. The electromagnetic pulse causes the electrons to oscillate in the transverse direction. At the same time, the electrons pick up the linear momentum of the x-rays and are displaced in the propagation direction of the x-ray pulse, see (7.24)–(7.26). Once the x-ray pulse has passed, the electrons are pulled back by space-charge effects, and a wake-plasma oscillation is created. This oscillation can trap electrons, and these electrons execute trapping oscillations, during which they can gain a large amount of energy [27].

The wake-field strength can be estimated to be [28]

$$E\left[\frac{\mathrm{GeV}}{\mathrm{cm}}\right] = \left(n\,[10^{18}\,\mathrm{cm}^{-3}]\right)^{0.5} a_0^2\,, \tag{7.31}$$

where $a_0 = eE_0/m\omega_0 c$ is the normalized vector potential, E_0 is the electric field, and ω_0 is the angular frequency of the x-ray pulse. When a_0 approaches unity, the quiver velocity of a free electron is on the order of the speed of light, and the process becomes relativistic. Relativistic nonlinearities lead to a new class of effects in addition to the nonrelativistic phenomena such as multiphoton processes. Figure 7.3 shows that the intensity associated with the electric field necessary to reach $a_0 = 1$ can be achieved with planned x-ray free-electron lasers, assuming diffraction-limited focusing is available. In this case, the field strength is on the order of a TeV/cm according to (7.31), enabling the creation of ultrafast electrons.

7.4.2
Plasma Instabilities at High Intensities

When high-intensity linearly polarized x-ray pulses irradiate a plasma, photoelectrons are ejected primarily in the direction of the electric field vector of the incoming light, see Section 5.2, generating a highly anisotropic electron distribution. This plasma with an anisotropic electron temperature will last until collisions relax the

system to an isotropic state. It has been suggested that such a plasma exhibits two different kinds of instabilities [29], depending on the propagation direction of the plasma wave.

A Weibel-like electromagnetic instability develops in the case where the plasma wave propagates transverse to the polarization direction of the x-ray pulse [30]. Taking the polarization direction as the z axis, we consider a fluctuation of the magnetic field in a plasma such that $B = B_{\gamma\gamma} \cos kx$. Then the electrons moving in the $+z$ direction will move toward a different location than the ones moving in the $-z$ direction. The resulting electron currents generate a magnetic field that *enhances* the original field fluctuation, leading to a growth of the perturbation. This quasi-static magnetic field is excited on a time scale much larger than the electron plasma wave period. The second instability is the photoionization two-stream instability. When electrons are emitted in two different directions, the plasma can be viewed as having two counterpropagating beams of equal density. In this plasma, a strong two-stream instability along the direction of the polarization vector develops, giving rise to plasma turbulences.

At this point it is not clear if these instabilities really will have a significant effect on the interaction of high-intensity x-ray pulses with plasmas. As has been pointed out in [31], collisions in the plasma could well lead to an isotropic electron distribution on a rather fast time scale. In addition, in [32] it was suggested that the Weibel instability may be much weaker than first anticipated since, at least for larger wavelengths, the absorption mechanism is coupled to the development of the instability, which stabilizes the system.

7.5 High-Field Physics

The large-amplitude electric field of x-ray free-electron-laser radiation can potentially be used to study nonlinear high-field physics phenomena predicted by quantum electrodynamics (QED), including nonlinear Compton scattering and pair production, and quantum field theory (QFT), such as Hawking–Unruh radiation. The observable effects are generally relatively weak, so that small spot sizes, large laser pulse energies, and long pulse durations are required to generate observable signals. Since the power of an x-ray free-electron laser is limited by the current laser technology, the most promising approach to achieve high intensities is reducing the focal diameter of the photon beam. Because of the large transverse coherence of free-electron-laser radiation, the focal spot size is in principle diffraction-limited to the order of the x-ray wavelength, and x-ray beam areas can theoretically be 10^8 times smaller than for visible light. Such focused light would produce sufficiently high field strengths for nonlinear effects to occur that allow testing of fundamental physics effects that have not been accessible before [28]. We will now discuss some high-intensity QED effects and elements of observable quantum field theory in more detail.

7.5.1 High-Intensity QED Effects: Pair Production

As discussed in Section 2.1.3.3, the time-independent Dirac equations (2.44) and (2.45) for free electrons admit solutions with positive and negative energies. Dirac suggested [33] that in vacuum, all states with negative energy are occupied with electrons, and that this vacuum state is the energetically lowest state. Understanding the physical nature of the quantum vacuum is extremely important for high-energy physics and cosmology. Various fundamental physical processes are directly related to it, including the Unruh radiation, the Casimir force, and the cosmological constant. So far, QED is in excellent agreement with experiments involving low-intensity electromagnetic fields.

Because of exchange interaction of the electrons with negative energy, virtual electron–positron pairs are continuously created and destroyed in vacuum. At extremely high electromagnetic fields, these virtual electron–positron pairs may be polarized, giving rise to a variety of exciting phenomena, including scattering of light by light, production of electron–positron pairs in vacuum, photon decay, and nonlinear dispersive properties of the vacuum such as field-dependent refractive indices, birefringence, and dichroism. High-intensity laser light is very well suited for demonstrating these effects [34].

Under certain conditions, an electron may be excited from a negative energy state across the bandgap of $2mc^2$ into a positive energy state, leaving behind a hole in the electron sea. This hole behaves like a particle of charge $+e$ and is termed a positron. This concept is the basis for QED. Spontaneous positron–electron pair creation in vacuum can be induced by an external field [35, 36]. This effect is a nonlinear phenomenon that cannot be described perturbatively. It can be shown that pair production is forbidden in the field of a plane monochromatic wave without the presence of a third body, such as a nucleus, that creates a Coulomb field [36]. Alternatively, it was suggested to use multiple overlapping laser beams to enable pair production [37], for example two or more coherent laser beams that form a standing wave at their intersection spot.

Electron–positron pair creation is also called *boiling the vacuum* and can potentially be observed with x-ray free-electron lasers [38, 39]. When the electric field is close to or exceeds a critical field strength, the *Schwinger electric field* E_c, pair production in vacuum can occur through tunneling. The uncertainty principle in the relativistic case states that uncertainty in position, Δx, must be greater than the Compton wavelength, $\lambda_c = \hbar/mc$ [40]. If the energy gain of an electron moving in an intense electric field over this distance approaches the rest mass energy, $eE_c\lambda_c = mc^2$, a virtual electron and positron pair could become real. The critical field strength of an electron is $E_c \approx 1.3 \times 10^{18}$ V/cm, corresponding to a critical intensity of $I_c = c\epsilon_0|E_c|^2 \approx 4.7 \times 10^{29}$ W/cm^2. Since the probability for pair production is proportional to $\exp(E_{laser}/E_c)$, this intensity requirement is exceedingly large for present technology, see Figure 7.3, even when we assume diffraction-limited focusing using current x-ray free-electron-laser facilities. However, if the x-

ray free-electron-laser technology is significantly improved and reaches the terawatt regime, electron–positron creation may be observed this way with future lasers.

It has also been proposed that the electric-field requirement can be significantly relaxed when the nucleus, that is required to ensure momentum conservation in the pair-creation process, is ultrarelativistic. If the nucleus propagates with a very large velocity in the opposite direction of the laser beam, the laser field strength and frequency, as seen in the rest frame of the nucleus, are enhanced by the relativistic Doppler shift. For sufficiently large Doppler shifts the photon energy becomes on the order of the electron rest energy mc^2, and multiple photons can be absorbed simultaneously to create an electron–positron pair [41].

Corresponding experiments have been proposed to observe the creation of muon–antimuon pairs, which are unstable subatomic particles that are similar to electrons and protons but about 200 times heavier. Creation of muon–antimuon pairs through tunneling (as for the electron–positron creation) is difficult since the required electric field strength scales with the mass ratio squared. Instead, a two-step technique has been proposed by first creating an electron–positron pair through tunneling, and then using the laser field to create a muon–antimuon pair by having the electron–positron pair re-collide and annihilate [42]. Alternatively, similar to the electron–positron case, it has been suggested to create muon–antimuon pairs through collision of ultrarelativistic nuclei and high-intensity x-ray beams [43]. A slight complication is that the muon's Compton radius is smaller than the size of a nucleus, so that the reduction of the reaction rate due to the finite extent of nucleus needs to be taken into account.

7.5.2 Experimental Verification of Quantum Field Theory

Chen and Tajima suggested that ultraintense laser radiation can be used to test fundamental aspects of quantum field theory by studying the fundamental interaction of strong electric fields with electrons [38]. When charged particles are accelerated, they emit electromagnetic radiation [44], called Larmor radiation, which can be calculated in a classical framework. For very strong or *violent* accelerations, this radiation pattern is modified, which is related to the *Unruh effect*: A uniformly accelerated particle sees the fluctuations of the quantum vacuum as a radiating heat bath with the characteristic temperature [45, 46]

$$T_{Unruh} = \frac{\hbar a}{2\pi c k_B} \,. \tag{7.32}$$

Here a is the particle acceleration, c is the velocity of light, and k_B is the Boltzmann constant. This radiation actually occurs due to distortion of the correlations of zero-point fluctuations of the quantum vacuum when a charged particle is uniformly accelerated. This effect causes additional jitter which then modifies the electron Larmor radiation. For a typical x-ray free-electron-laser parameter and assuming a beam diameter of 1 Å, the Unruh temperature is $T_{Unruh} = 2.4 \times 10^7$ K, which corresponds to a radiation temperature of 2 keV.

The Unruh radiation is only a minor perturbation of the Larmor radiation, which makes its detection very challenging. It has been proposed to take advantage of a blind spot in the Larmor radiation [38, 47]: When a linearly polarized standing wave interacts with an electron, the Larmor radiation vanishes in the direction of the electric field. The Unruh radiation has a characteristic acceleration and angular dependence that is different and may be detectable. Verifying the occurrence of this radiation and its characterization will have an important impact on our understanding of quantum field theory, and will be beneficial for our understanding of Hawking radiation, black hole evaporation processes, and quantum gravity in general.

References

1 Young, L., Kanter, E.P., Krässig, B., Li, Y., March, A.M., Pratt, S.T., Santra, R., Southworth, S.H., Rohringer, N., DiMauro, L.F., Doumy, G., Roedig, C.A., Berrah, N., Fang, L., Hoener, M., Bucksbaum, P.H., Cryan, J.P., Ghimire, S., Glownia, J.M., Reis, D.A., Bozek, J.D., Bostedt, C., and Messerschmidt, M. (2010) Femtosecond electronic response of atoms to ultra-intense x-rays. *Nature*, **466**, 56–61.

2 Zambianchi, P. (2003) Nonlinear response functions for x-ray laser pulses. In *Nonlinear Optics, Quantum Optics, and Ultrafast Phenomena with X-Rays* (ed. B. Adams), Kluwer Academic Publisher, Norwell, MA, Chapt. 11, pp. 287–299.

3 Chen, P. and Pellegrini, C. (1998) Boiling the vacuum with intense electromagnetic fields. Monterey 1998, Quantum aspects of beam physics, 1998. Prepared for 15th Advanced ICFA Beam Dynamics Workshop on Quantum Aspects of Beam Physics, Monterey, California.

4 Rohringer, N. and Santra, R. (2007) X-ray nonlinear optical processes using a self-amplified spontaneous emission free-electron laser. *Phys. Rev. A*, **76**, 033416.

5 Santra, R. (2009) Concepts in x-ray physics. *J. Phys. B.: At. Mol. Opt. Phys.*, **42**, 169801.

6 Varma, H.R., Ciappina, M.F., Rohringer, N., and Santra, R. (2009) Above-threshold ionization in the x-ray regime. *Phys. Rev. A*, **80**, 053242.

7 Radhakrishnan, R. and Thayyullathil, R.B. (2004) Nonresonant multiphoton absorption in atomic hydrogen. *Phys. Rev. A*, **69**, 033407.

8 Drake, G.W.F. (2006) *Springer Handbooks of Atomic, Molecular, and Optical Physics*, Springer, New York.

9 Azuma, Y., Hasegawa, S., Koike, F., Kutluk, G., Nagata, T., Shigemasa, E., Yagishita, A., and Sellin, I.A. (1995) New photon-induced triply excited hollow atom states of lithium. *Phys. Rev. Lett.*, **74**(19), 3768–3771.

10 Volkova, E.A., Popov, A.M., and Tikhonova, O.V. (2003) Strong-field atomic stabilization: numerical simulation and analytical modelling. *J. Phys. B*, **36**, R125–R165.

11 Bestle, J., Akulin, V.M., and Schleich, M.P. (1993) Classical and quantum stabilization of atoms in intense laser fields. *Phys. Rev. A*, **48**, 746–751.

12 Fedorov, M.V. (1997) *Atomic and Free Electrons in a Strong Light Field*, World Scientific, Singapore.

13 Fedorov, M.V. and Movsesian, A.M. (1989) Interference suppression of photoionization of Rydberg atoms in a strong electromagnetic field. *J. Opt. Soc. Am. B*, **6**, 928–936.

14 Henneberger, W.C. (1968) Perturbation method for atoms in intense light beams. *Phys. Rev. Lett.*, **21**, 838–841.

15 Parker, J. and Stroud Jr., C.R. (1990) Population trapping in short-pulse laser ionization. *Phys. Rev. A*, **41**, 1602–1608.

16 Reiss, H. (1997) Physical basis for strong-field stabilization of atoms against ionization. *Laser Phys.*, **7**, 543–550.

17 Reiss, H. (2001) Dependence on frequency of strong-field atomic stabilization. *Opt. Express*, **8**, 99–105.

18 Franken, P.A., Hill, A.E., Peters, C.W., and Weinreich, G. (1961) Generation of optical harmonics. *Phys. Rev. Lett.*, **7**, 118–119.

19 Bloembergen, N. (1996) *Nonlinear Optics*, 4th edn, World Scientific, Singapore.

20 Boyd, R.W. (2008) *Nonlinear Optics*, 3rd edn, Academic Press, Burlington, MA.

21 Freund, I. and Levine, B.F. (1969) Parametric conversion of x rays. *Phys. Rev. Lett.*, **23**, 854–857.

22 Eisenberger, P. and McCall, S.L. (1971) X-ray parametric conversion. *Phys. Rev. Lett.*, **26**, 684–688.

23 Tamasaku, K., Sawada, K., and Ishikawa, T. (2009) Determining x-ray nonlinear susceptibility of diamond by the optical Fano effect. *Phys. Rev. Lett.*, **103**, 254801.

24 Tanaka, S., Chernyak, V., and Mukamel, S. (2001) Time-resolved x-ray spectroscopies: Nonlinear response functions and Liouville-space pathways. *Phys. Rev. A*, **63**, 063405.

25 Hagenbuch, K. (1977) Free electron motion in a plane electromagnetic wave. *Am. J. Phys.*, **45**, 693–696.

26 Chen, P. and Pellegrini, C. (1998) *Quantum aspects of beam physics*. In Proceedings of the 15th Advanced ICFA Beam Dynamics Workshop, Monterey, CA, World Scientific, Singapore, p. 571.

27 Tajima, T. and Dawson, J.M. (1979) Laser electron accelerator. *Phys. Rev. Lett.*, **43**, 267–270.

28 Tajima, T. (2003) Fundamental physics with an x-ray free electron laser. *Plasma Phys. Rep.*, **29**, 231–235.

29 Bychenkov, V.Y., Romanov, D.V., Rozmus, W., Capjack, C.E., and Fedosejevs, R. (2006) Distinctive features of photoionized plasma from short x-ray-pulse interaction with gaseous medium. *Phys. Plasmas*, **13**, 013101.

30 Weibel, W.S. (1959) Spontaneously growing transverse waves in a plasma due to an anisotropic velocity distribution. *Phys. Rev. Lett.*, **2**, 83–84.

31 Andriyash, I.A. and Bychenkov, V.Y. (2007) Photoionization two-stream instability in a collisional plasma. *Plasma Phys. Rep.*, **33**, 974–981.

32 Sangama, A., Morreeuw, J.-P., and Tikhonchuk, V.T. (2007) Anisotropic instability in a laser heated plasma. *Phys. Plasmas*, **14**, 053111.

33 Dirac, P.A.M. (1930) A theory of electrons and protons. *Proc. R. Soc. Lond. A*, **126**, 360–365.

34 Becker, W. (1991) Quantum electrodynamics in intense laser fields. *Laser Part. Beams*, **9**, 603–618.

35 Sauter, F. (1931) Über das Verhalten eines Elektrons im homogenen elektrischen Feld nach der relativistischen Theorie Diracs. *Z. Phys.*, **69**, 742–764.

36 Schwinger, J. (1951) On gauge invariance and vacuum polarization. *Phys. Rev.*, **82**, 664–679.

37 Fried, H.M., Gabellini, Y., McKellar, B.H.J., and Avan, J. (2001) Pair production via crossed lasers. *Phys. Rev. D*, **63**, 125001.

38 Chen, P. and Tajima, T. (1999) Testing Unruh radiation with ultra-intense lasers. *Phys. Rev. Lett.*, **83**, 256–259.

39 Ringwald, A. (2001) Pair production from vacuum at the focus of an x-ray free electron laser. *Phys. Lett.*, **510**, 107–116.

40 Berestetskii, V.B., Lifshitz, E.M., and Pitaevskii, L.P. (1982) *Quantum Electrodynamics*, 2nd edn, Pergamon Press, Oxford.

41 Milstein, A.I., Müller, C., Hatsagortsyan, K.Z., Jentschura, U.D., and Keitel, C.H. (2006) Polarization-operator approach to electron–positron pair production in combined laser and Coulomb fields. *Phys. Rev. A*, **73**, 062106.

42 Kuchiev, M.Y. (2007) Production of high-energy particles in laser and Coulomb fields and the e^+e^- antenna. *Phys. Rev. Lett.*, p. 130404.

43 Müller, C., Deneke, C., and Keitel, C.H. (2008) Muon-pair creation by two x-ray laser photons in the field of an atomic nucleus. *Phys. Rev. Lett.*, **101**, 060402.

44 Larmor, J. (1897) On a dynamical theory of the electric and luminiferous medium. *Philos. Trans. R. Soc.*, **190**, 205–300.

45 Davies, P.C.W. (1975) Scalar production in Schwarzschild and Rindler metrics. *J. Phys. A*, **8**, 609.

46 Unruh, W. (1976) Notes on black-hole evaporation. *Phys. Rev. D*, **14**, 870–892.

47 Rosu, H. (1999) Blind spot may reveal vacuum radiation. *Phys. World*, **(Oct. 1999)**, 21–22.

8
Dynamics of X-Ray-Irradiated Materials

At sufficiently high fluences, x-ray-irradiated materials undergo microscopic and macroscopic changes. The absorbed photon energy is converted into different forms of energy, including thermal electron energy, ionization energy, thermal ionic energy, kinetic energy associated with hydrodynamic motion, magnetostatic energy, and photon energy at a different wavelength through photon emission. In this chapter we discuss the material dynamics in different x-ray fluence regimes, and the associated thresholds for changes to occur. We first describe the time scales for x-ray–matter interaction, followed by a discussion of the x-ray-flux dependence of x-ray absorption. The latter is based primarily on simulations since experimental results are just starting to become available. Subsequently, we discuss the thermodynamics of phase transformations, ablation, the intensity dependence of x-ray–matter interaction, and mechanical damage. Finally, we discuss specific examples of x-ray–matter interaction dynamics, including x-ray damage to semiconductors and damage mechanisms in x-ray imaging. As a specific example, we consider solids exposed to short-duration high-intensity x-ray radiation, as is emitted by free-electron lasers.

8.1
X-Ray–Matter Interaction Time Scales

Various time scales are relevant for the dynamics of x-ray-irradiated materials, including the pulse length, the time constants for the local coupling of different energy degrees of freedom, and the time constants for energy and mass transport. Both short- and long-term changes can occur in the material. Long-term changes are typically irreversible, and examples include phase transformations, such as solid-state phase transitions and melting, spallation, ablation, and plastic deformation. Short-time changes occur during the pulse and may be reversible or irreversible. Nonthermal melting is an example of an irreversible short-term change that occurs on a time scale of around 1 ps or less.

The pulse length defines the duration of the energy deposition process during which x-ray photons couple with the electron system. The absorbed energy is redistributed over various degrees of freedom through the interaction of electrons, ions,

High-Intensity X-rays – Interaction with Matter, First Edition. Stefan P. Hau-Riege.

and phonons. In semiconductors and metals, the time scale for this interaction is around 1–10 ps, as illustrated in Figure 1.9 in Section 1.5.2. The energy is then transported through thermal conduction, which may occur through electrons or atoms and ions, and through macroscopic mass motion (e.g., convection). At very high pulse energies, radiation transport can play a role. In case the lattice structure is still intact, atomic heat conduction takes place through lattice vibration, that is phonons. Typically, mass transport is the slowest process, proceeding through hydrodynamic and acoustic mechanisms. The expansion of a material is limited by its speed of sound and occurs on a time scale of 100 ps or longer for hard x rays.

Ablation is the removal of material from the surface of a solid upon photon irradiation. Usually, the time scale for ablation is much longer than for thermalization, and it is sufficient to consider *thermal* ablation mechanisms. The ablation velocity of a material is the velocity of the hydrodynamic flow into vacuum and is on the order of 1 km/s for silicon. Sometimes mass transport is faster than heat conduction, in which case the process is called quasi-adiabatic.

8.2
The Influence of X-Ray Heating on Absorption

X rays typically penetrate much deeper into materials than optical radiation, so that, correspondingly, a larger volume is heated. At sufficiently large x-ray intensities, the heating of the electron and ion systems affects the way in which x rays are absorbed and transported by the material. In this chapter we discuss the dependence of the absorption mechanism on the x-ray flux.

8.2.1
Temperature-Dependence of X-Ray Absorption

For low x-ray fluences, x-ray absorption occurs primarily through photoionization. Extensive tables of the photoionization cross section of different materials as a function of the x-ray energy exist in the literature [1]. Since x rays interact primarily with the electron in the inner shells of atoms, x-ray absorption (especially for larger x-ray energies) is less sensitive to the chemical environment of the atoms, and isolated-atom photoionization cross sections are often an excellent approximation even in dense materials. Valence electrons and bonding effects are less important. Figure 8.1 shows the atomic photoionization cross sections as a function of the atomic charge number Z and the x-ray energy. The discontinuous structure in the energy dependence of the cross section corresponds to the ionization thresholds of the elements, as discussed in Section 2.2.3.

X rays heat up materials and modify their absorption characteristics. Figure 8.2 shows the spectral dependence of the absorption coefficient of graphite-like carbon as a function of temperature assuming local thermodynamic equilibrium (LTE) conditions. A plasma is in LTE when the electrons and ions are in a kinetic equilibrium, but the radiation field is not. The calculations have been performed using the

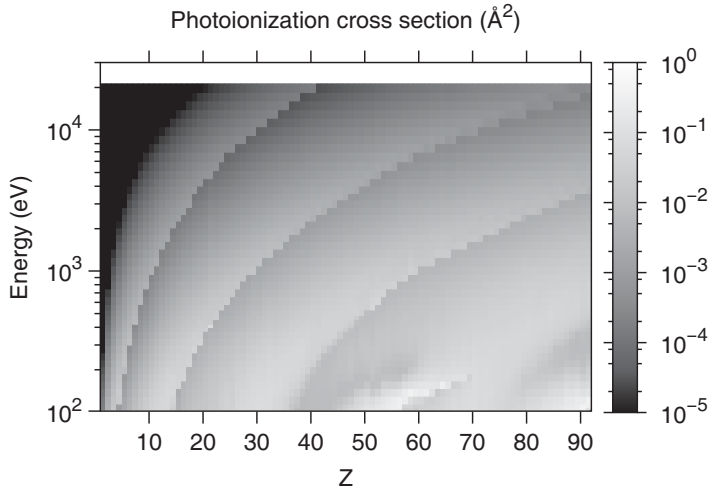

Figure 8.1 X-ray photoionization cross section of the elements as a function of atomic charge number Z [1].

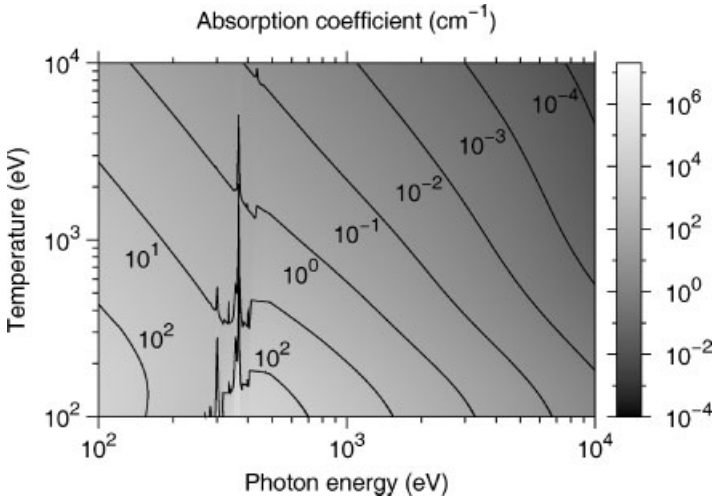

Figure 8.2 Spectral dependence of the total absorption coefficient of carbon with a density of 2.2 g/cm^3 as a function of temperature.

atomic kinetics code Cretin [2]. The absorption coefficient generally decreases with increasing temperature since it is dominated by the excitation of bound electrons into the continuum, which is less efficient when the number of bound electrons decreases at higher temperatures. The bound–free component of the absorption coefficient alone is shown in Figure 8.3. Figure 8.4 shows the free–free component of the absorption coefficient. During free–free (inverse Bremsstrahlung) absorption, free electrons absorb x rays while interacting with an ion. This process is

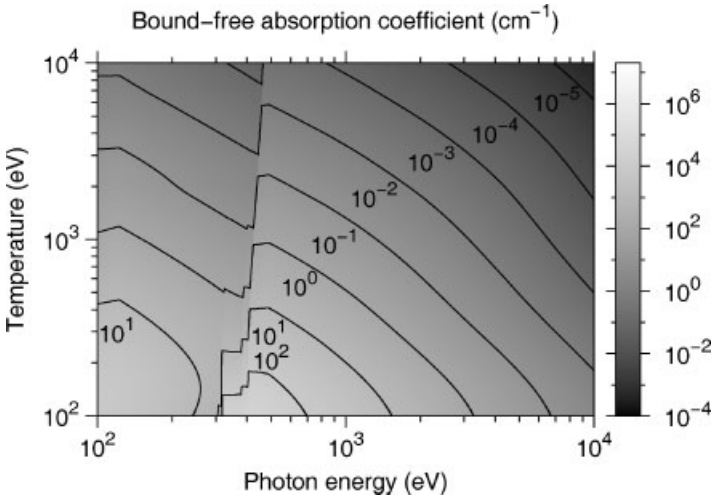

Figure 8.3 Spectral dependence of the bound–free absorption coefficient of carbon with a mass density of 2.2 g/cm^3 as a function of temperature.

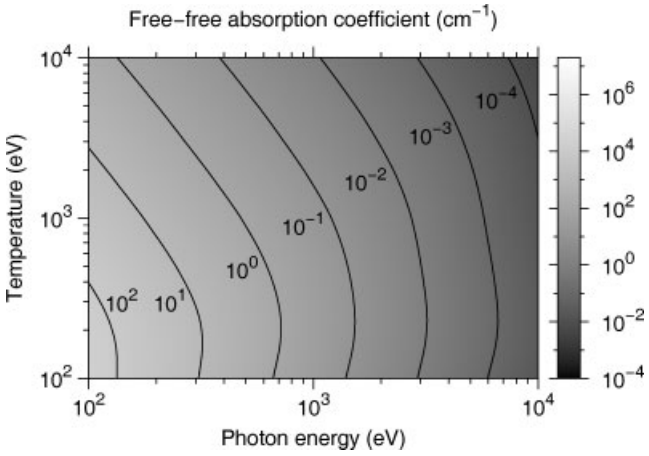

Figure 8.4 Spectral dependence of the free–free absorption coefficient of carbon with a mass density of 2.2 g/cm^3 as a function of temperature.

described in more detail in Section 5.7. Inverse Bremsstrahlung is more effective at lower electron temperatures, large electron densities, and small x-ray energies. The effect of the electron temperature on the free–free absorption coefficient is complicated by changes in the ionization state of the ions and the electron density with temperature. In addition, the electron temperature fundamentally affects the inverse Bremsstrahlung rate as can be seen from (5.48) for the spectral absorption coefficient [3]. Besides bound–free and free–free absorption, the total absorption coefficient in Figure 8.2 also contains bound–bound or line absorption, which is

responsible for most of the structure in the absorption coefficient between 200 and 300 eV.

8.2.2 Time Dependence of X-Ray–Matter Interaction

For the calculation results shown in Figures 8.2–8.4 we assumed that the material is in thermal equilibrium, which is appropriate for systems that have been illuminated by relatively long x-ray pulses. For shorter pulse length around a few hundred fs or less, LTE has not necessarily been achieved, which can have a profound effect on the absorption characteristics: High-intensity x-ray pulses can deplete the inner atomic shells that usually dominate x-ray absorption. Therefore, materials become more transparent with increasing x-ray intensity since fewer bound electrons are available for bound–free absorption. For longer pulses, the inner shells are replenished through Auger or fluorescence relaxation processes, and for very long pulses, recombination occurs. Short and intense x-ray pulses can generate very unusual electron distributions that can be anisotropic, whereas for long pulses, the electrons have time to relax and their velocity distribution becomes thermal.

Figure 8.5 shows the electron temperature of graphite-like carbon illuminated by x rays at 1 and 8 keV for different fluxes, calculated with the time-dependent non-LTE model Cretin. The electron temperature increases with x-ray flux and time and is larger at 1 than at 8 keV due to the difference in absorption coefficient, shown in Figure 8.6. The decrease of the absorption with time during the pulse is corroborated by recent experiments summarized in Section 10.1. Figure 8.7 shows the corresponding average ionization. For longer pulse length and very high fluxes, sample expansion would need to be considered. Since collisional equilibration of electrons and ions is relatively slow, for short pulses the sample is not in lo-

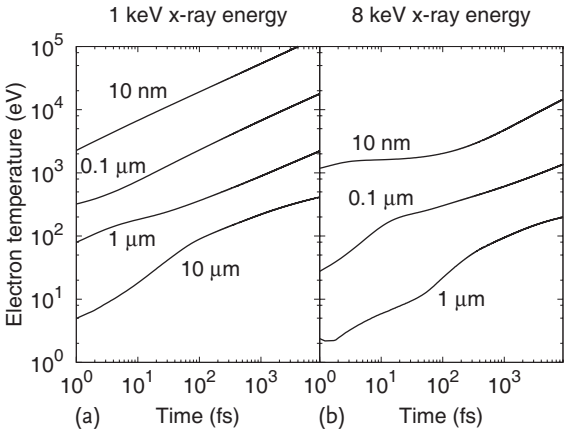

Figure 8.5 Time dependence of the electron temperature of carbon with a mass density of 2.2 g/cm^3, irradiated with a 1-keV (a) and 8-keV (b) x-ray beam with a power of 30 GW for different FWHM beam diameters.

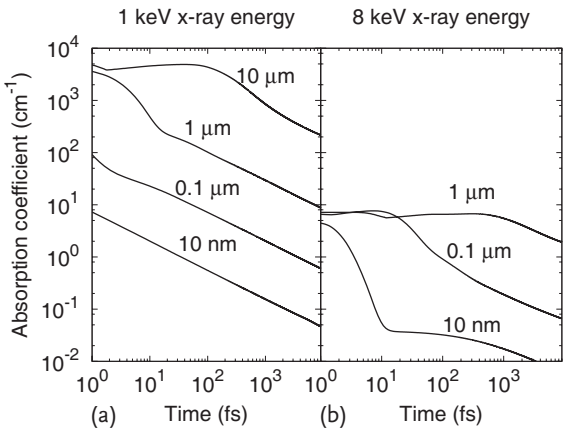

Figure 8.6 Time dependence of the absorption coefficient of carbon with a mass density of 2.2 g/cm^3, irradiated with a 1-keV (a) and 8-keV (b) x-ray beam with a power of 30 GW for different FWHM beam diameters.

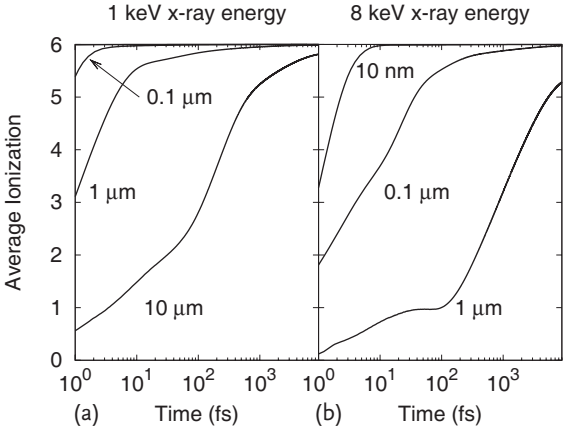

Figure 8.7 Time dependence of the average ionization of carbon with a graphite-like mass density of 2.2 g/cm^3, irradiated with a 1-keV (a) and 8-keV (b) x-ray beam with a power of 30 GW for different FWHM beam diameters.

cal thermodynamic equilibrium: The electron temperature is larger than the ion temperature, and the ionization is less than in equilibrium.

8.2.3 Pulse Length Dependence of X-Ray Absorption

Figure 8.8 shows simulation results of the peak electron temperature of graphite irradiated by 1-keV x-ray radiation, as a function of x-ray pulse length and pulse energy, calculated with the time-dependent non-LTE model Cretin. In these simulations we neglected surface effects, and we assumed that the beam is focused to a full-

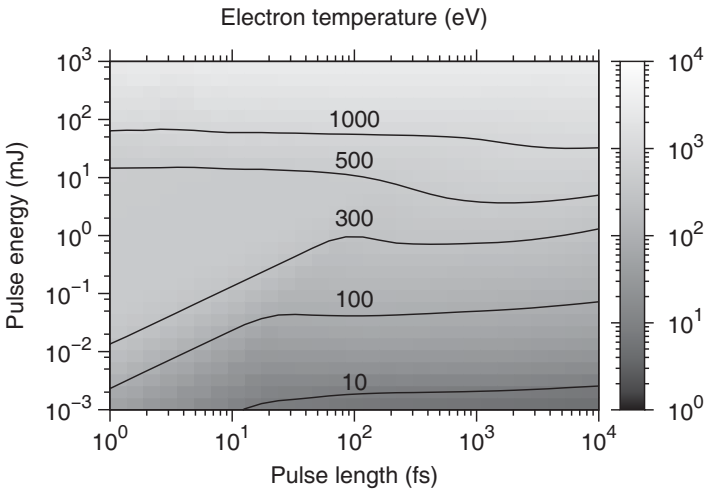

Figure 8.8 Electron temperature as a function of pulse length and pulse energy of carbon with a mass density of 2.2 g/cm^3, irradiated by 1-keV x rays focused to 1 μm FWHM.

width-at-half-maximum (FWHM) width of 1 μm. With x-ray free-electron lasers, the brightest laboratory-scale x-ray sources available today, x-ray pulses shorter than 300 fs and with energies of up to several mJ can be obtained, leading to electron energies of several hundred eV. For pulses longer than 100 fs, the system stays close to LTE, and the pulse length only weakly affects the electron temperature. For shorter pulses, the electron temperature decreases with increasing pulse length for a given pulse energy below about 0.1 mJ since the excited electrons have more opportunity to distribute their kinetic energy through collisions. Above 0.1 mJ, the ions are nearly completely ionized, and the dependence of the electron temperature on the pulse length is much weaker.

Figure 8.9 shows the corresponding average ionization Z at the end of the pulse. For typical free-electron-laser pulse parameters, carbon is nearly completely ionized. This explains that for pulse lengths below 10 fs and energies above about 0.1 mJ, the dependence of the electron temperature on the pulse energy is very weak: The x rays completely deplete the K shell of carbon, and there is not sufficient time for electrons to relax through Auger decay or to refill the K shell through recombination.

For comparison, Figure 8.10 shows the peak electron temperature of graphite irradiated with 8-keV x-ray pulses as a function of pulse energy and pulse length, and Figure 8.11 shows the corresponding average ionization at the end of the pulse. Similar to the 1-keV case, for pulses shorter than approximately 20–100 fs, the electron temperature decreases with increasing pulse length for a given pulse energy. These calculation results illustrate that a very large phase space can be accessed with x-ray heating, depending on the x-ray fluence, pulse length, and x-ray energy. In particular, when solids are illuminated, hot solids, warm dense matter, and hot dense matter can readily be generated.

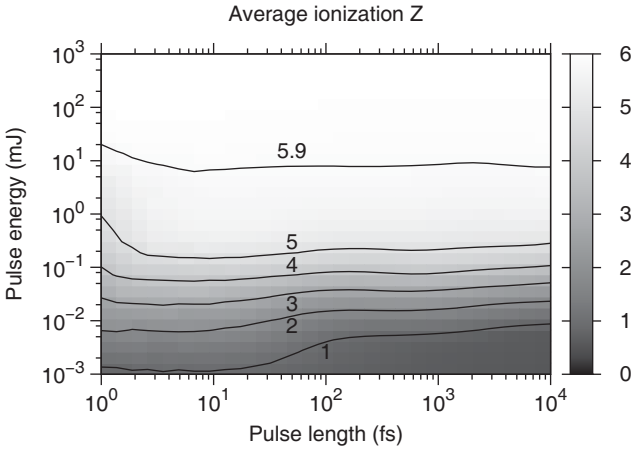

Figure 8.9 Average ionization as a function of pulse length and pulse energy of carbon with a mass density of 2.2 g/cm^3, irradiated by 1-keV x rays focused to 1 μm FWHM.

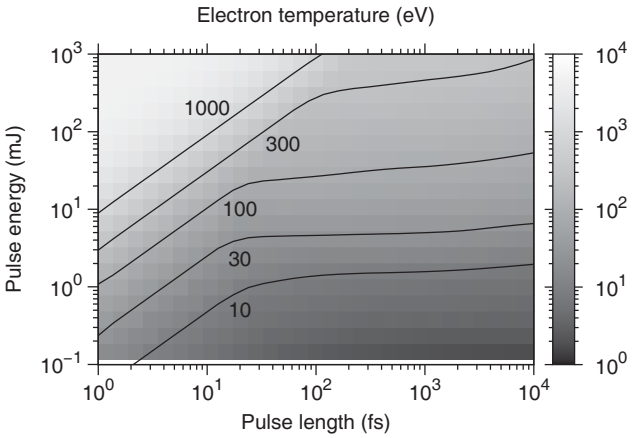

Figure 8.10 Electron temperature as a function of pulse length and pulse energy of carbon with a mass density of 2.2 g/cm^3, irradiated by 8-keV x rays focused to 1 μm FWHM.

Of particular interest is the warm-dense matter (WDM) regime, a unique state of matter than can be accessed using the very short and intense x-ray pulses from x-ray free-electron lasers. With these sources, materials can be heated isochorically, generating well-defined material states. In WDM, the temperature is on the order of the Fermi energy E_{Fermi}, which is the maximum electron energy in cold dense matter. WDM cannot be described by standard condensed matter theory, which is valid only in the limit of small temperatures $T \ll E_{Fermi}$, nor through weakly coupled plasma theory. WDM is strongly coupled, particle correlations are important, ionization levels are depressed, and energy levels are shifted. The electron–ion correlation changes, and the ion–ion correlations show short- and long-range order.

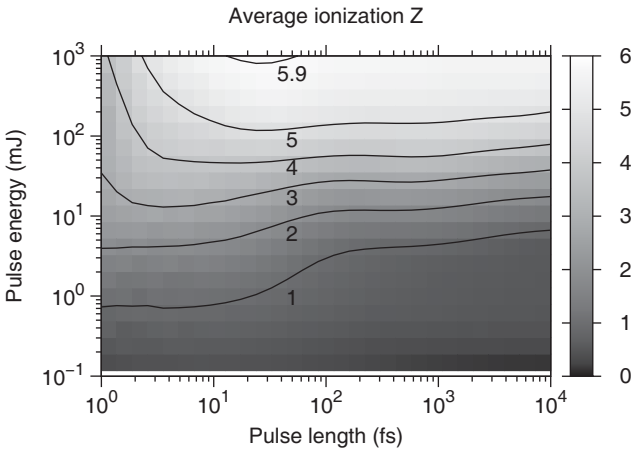

Figure 8.11 Average ionization as a function of pulse length and pulse energy of carbon with a mass density of 2.2 g/cm^3, irradiated by 8-keV x rays focused to 1 μm FWHM.

Therefore, theoretical descriptions of matter in this state are currently not very reliable, and the estimates presented in this chapter in this regime only demonstrate general trends rather than concrete values for measurable quantities such as temperature, ionization, and opacity.

8.3
Thermodynamics of Phase Transformation

X-ray irradiation of materials results in an increase in temperature, pressure, and ionization state, and induces stresses and stress gradients in materials. All these factors can lead to phase transformations. In this section we will discuss the basic thermodynamic concepts of phase diagrams and phase transformations for materials in solid, liquid, and gas phases at moderate temperatures. The associated changes are long time scale transformations. Some ultrafast phase transformations are discussed in Section 8.5.1. An extensive discussion of these concepts can be found in [4, 5]. Understanding the thermodynamic equilibrium of materials is important since this is the state toward which x-ray-excited materials transform. The rate of transformation is described by materials kinetics [6, 7] and is typically much more difficult to understand.

Figure 8.12 shows a generic phase diagram of a material in pressure-temperature space. It gives the phases in which the material exists at thermodynamic equilibrium for certain values of temperature and pressure, and under which conditions two or more phases can coexist. We will now discuss the transition between these phases.

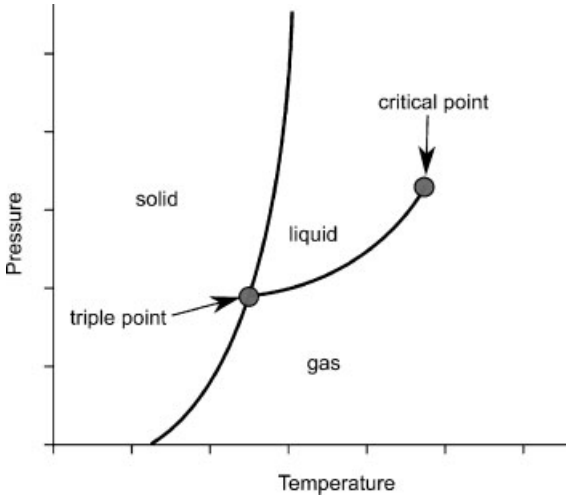

Figure 8.12 Generic phase diagram in pressure–temperature space.

8.3.1 Solid–Liquid Transitions

For pure substances consisting of a single type of atom or molecule, melting takes place at a well-defined temperature T_{melt}. Figure 8.13 shows the melting temperatures of monoatomic solids as a function of the atomic charge number Z. The Lindemann theory of melting relates the amplitude of atomic vibration to the melting temperature. Lindemann hypothesized that melting occurs when the amplitude of atomic vibration reaches a certain fraction f of the interatomic spacing a [8]. Estimates show that $f \approx 5\%$. The melting temperature relates to the bond strength since when the interatomic bonding is strong, more energy is needed to induce vibrations and break the bond. There is also a correlation between the Debye and the melting temperatures. The Debye temperature of a system is the temperature at which the atoms gain access to all their degrees of freedom, and it is the temperature at which the thermal energy of vibration is roughly equal to the energy separation between quantum states of vibration.

Typically, materials expand upon melting, and the melting temperature increases with pressure because the application of pressure to a liquid with available space leads to compression, so that it behaves more like a solid. This stabilization of the solid phase leads to an increase of the melting temperature. Certain materials contract upon melting, including water, silicon, germanium, gallium, and bismuth. Conversely, for these materials, the melting temperature decreases with increasing pressure.

At the melting temperature, the material can coexist in the solid and the liquid phase, and the relative fraction of these two phases depends on the amount of energy that has been added to it in the form of heat. Adding further energy will not change the temperature but increases the liquid fraction of the system. The energy

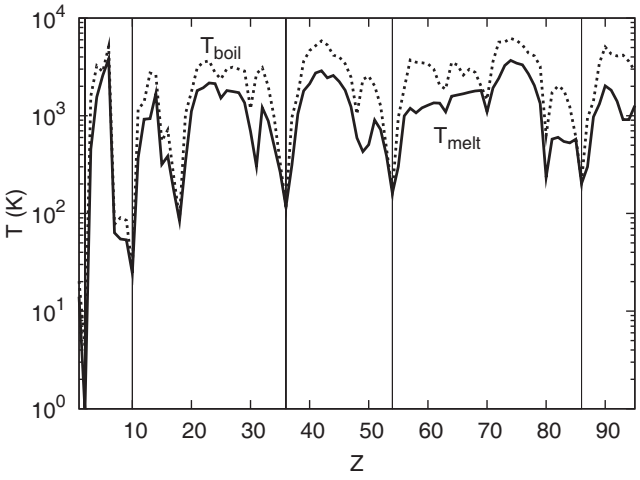

Figure 8.13 Melting and boiling temperatures of solids as a function of the atomic *Z* number. The vertical lines indicate atoms with filled atomic shells.

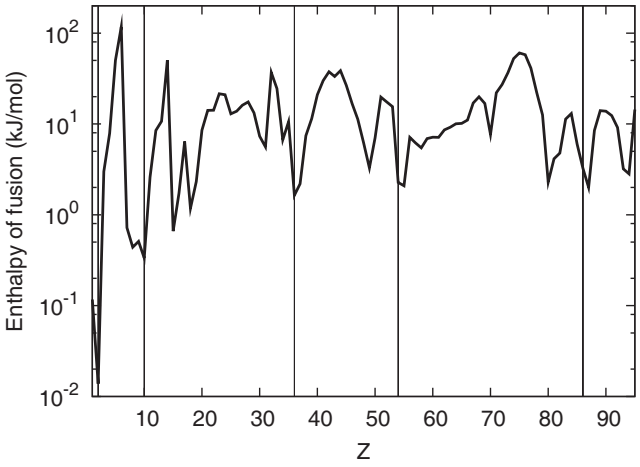

Figure 8.14 Enthalpy of fusion as a function of the atomic *Z* number. The vertical lines indicate atoms with filled atomic shells.

required to transform a solid to a liquid at constant pressures is the enthalpy of fusion. Figure 8.14 shows the enthalpy of fusion of monoatomic solids as a function of the atomic charge number *Z*. The melting temperature is roughly proportional to the enthalpy of fusion, as shown in Figure 8.15: The melting temperature in degrees Kelvin is approximately 1% of the enthalpy of fusion in kJ/mol.

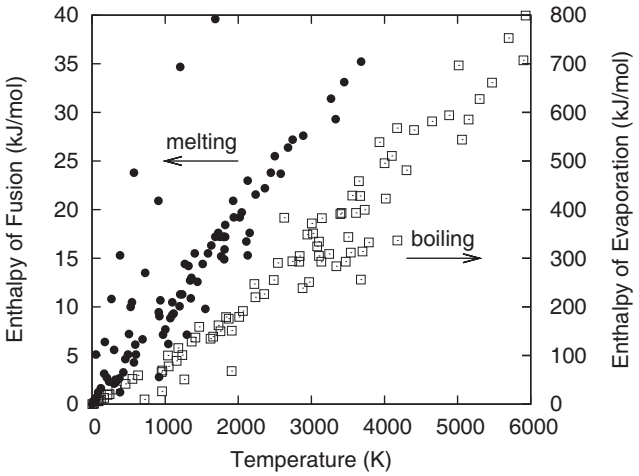

Figure 8.15 Enthalpy of fusion and enthalpy of evaporation as a function of the melting and boiling temperature, respectively. Data taken from [5].

8.3.2
Liquid–Gas Transition

The latent heat of evaporation is the energy required to remove a single molecule from the liquid and add it to the gas phase. Figure 8.15 shows the enthalpy of evaporation as a function of the boiling temperature, which is the temperature at which the vapor pressure of the material is equal to the pressure of the surrounding gas, here taken to be 1 atm. The boiling temperature in degrees Kelvin is about 10% of the enthalpy of evaporation in units of kJ/mol. The melting temperature is roughly 2/3 of the boiling temperature, but there are many exceptions to this rule. The transition temperature is strongly pressure-dependent. The liquid–gas transition is often easier to understand than the solid–liquid transition since the molecules in the gas phase interact only weakly after the transition.

At the critical point shown in Figure 8.12, the gas and liquid phases cannot be distinguished. The surface tension of the liquid disappears, and the material becomes a supercritical fluid. This regime in phase space can be reached without a phase transformation from either the liquid or the gas phase. At the critical point, the densities of the coexisting gas and liquid are equal.

8.3.3
Solid–Gas Transition

Solid–gas transitions are called sublimation. The sublimation temperature is the temperature above which the vapor pressure of a solid reaches 1 atm. Since usually the vapor pressure above solids is rather small, only carbon and arsenic sublime, whereas all other elements will melt before the sublimation temperature is reached.

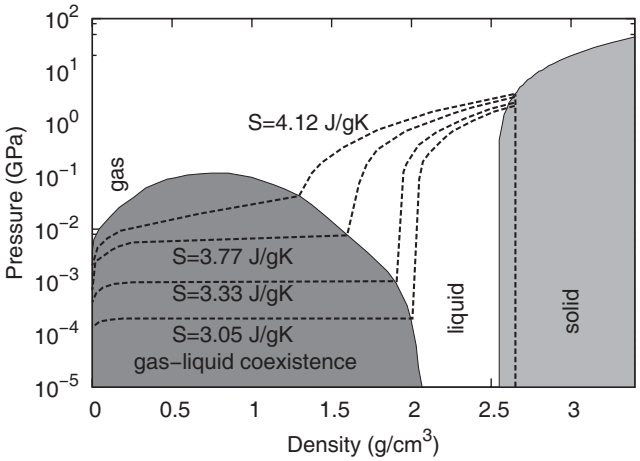

Figure 8.16 Aluminum phase diagram. Reprinted with permission from [9].

8.3.4
Example Phase Diagram

Figure 8.16 shows the phase diagram of aluminum in pressure-density space. For a given pressure, aluminum is in the solid phase at high densities and in the liquid phase at lower densities. At even lower densities, aluminum enters the two-phase regime in which the liquid and gas phases coexist. Also shown in Figure 8.16 are isentropes, which are paths of constant entropy. The boiling temperature is the temperature for which the isentrope crosses the boundary from the one- to the two-phase region. At and above the critical temperature, the isentropes no longer reach the two-phase region. For aluminum, the ratio of the critical to the boiling temperature is 2.4, but this ratio is different for other materials. For example, the ratios are 1.4, 1.35, and 3.3 for silicon, graphite, and gold, respectively.

8.4
Ablation

In this section we will focus on *laser* ablation of materials. Laser ablation (or laser sputtering) is the removal of material from a solid upon laser exposure. The detailed process depends on the thermal and optical materials parameters, and on the laser parameters such as wavelength, intensity, and pulse duration. The minimum energy fluence to achieve material removal is the *ablation threshold*, and the time required to carry away material is the *ablation time*.

In order to remove a macroscopic amount of mass from a surface, the material usually first undergoes transformation into a volatile phase, such as a gas or a plasma. This transformation can occur along different paths in phase space, depending on the experimental conditions. For example, the solid–gas transformation can oc-

cur stepwise by first melting the material, and then transforming the melt into a gas. If the liquid is heated to high temperatures, its vapor pressure exceeds the ambient pressure, and boiling of the melt occurs. When the temperature approaches the critical temperature, the boiling rate becomes very fast, and homogeneous nucleation of the gas phase in the liquid takes place. This phenomenon is called *phase explosion*. The transformation of the material from the solid into the gas phase may

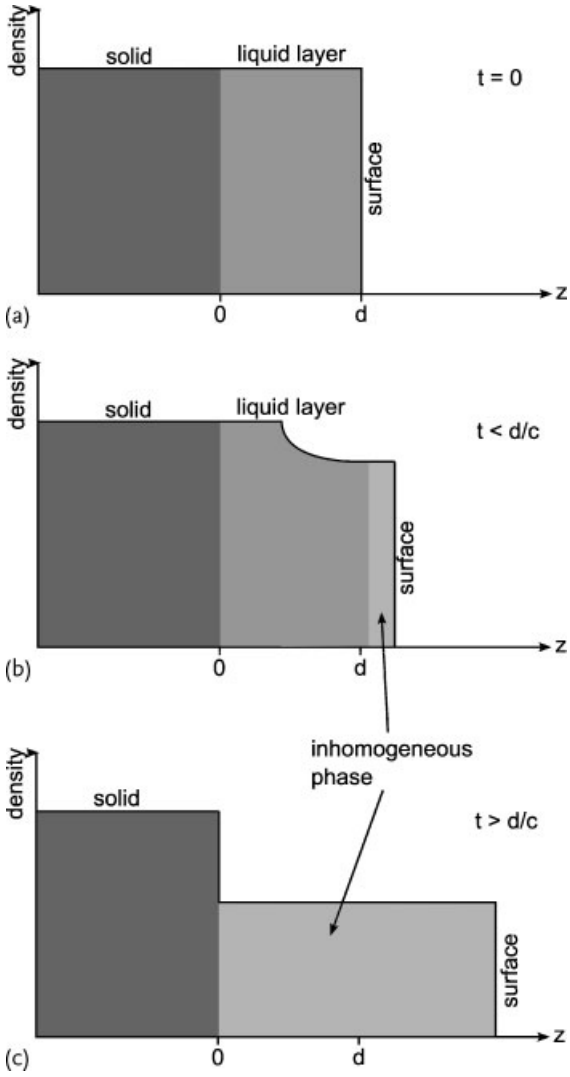

Figure 8.17 Evolution of the ablation layer of a material irradiated by a short-pulse laser. (a) Immediately after excitation, (b) rarefaction wave propagating inward, and (c) after reflection of rarefaction wave from the backside. c is the unperturbed sound velocity in the bulk. Reprinted with permission from [9].

also proceed directly. This process is called *sublimation*. Finally, a material may transform from the solid phase into a plasma when the laser illumination leads to severe ionization of the material.

In short-pulse laser ablation, material expansion during the electron–ion thermalization process is usually negligible, so that the material is heated isochorically. Ablation of materials typically occurs at temperatures of several thousand kelvin, corresponding to pressures of tens of GPa. The heating is followed by an isotropic expansion of the material, during which it can enter the two-phase region, see Figure 8.16, with gas bubbles nucleating in the heterogeneous gas–liquid phase. Figure 8.17 shows density profiles of the ablation layer, demonstrated with optical lasers [9], for different points in time. Right after energy relaxation the top layer is fluid, as shown in Figure 8.17a. Then a rarefaction wave propagates into the material, see Figure 8.17b. The rarefaction wave is reflected at the fluid–solid interface, leading to the density profile shown in Figure 8.17c.

It is anticipated but not yet clear if a similar short-pulse ablation mechanism is going to be observed in the x-ray regime. For optical laser experiments, the interpretation of experimental data is often complicated by the highly nonlinear nature of the deposition of optical energy in the intensity range of interest of more than 10^{12} W/cm^2. The deposition process is generally much easier to understand in the x-ray regime.

8.5
Intensity Dependence of X-Ray–Matter Interaction

The transformation of x-ray-irradiated materials depends on a number of parameters, including the peak x-ray pulse intensity, pulse length, and time-integrated intensity. Because of the large variety of available x-ray sources, each with very different output characteristics as described in Sections 1.3 and 6.2.1, the accessible temperature-density space is relatively large and includes mildly heated materials all the way to materials transformed into a plasma. In addition, the x-ray pulse parameters influence the absorption process of the radiation in the material through the ionization state and electron temperature, which, in turn, determine the x-ray opacity. As was discussed in Section 8.2.1, absorption often decreases with increasing ionization and temperature. This has recently been demonstrated by turning solid aluminum transparent under intense soft x-ray illumination [10]. We will now discuss the transformation mechanisms of materials as a function of the pulse parameters, particularly the x-ray intensity.

It is instructive to distinguish between x-ray–matter interaction processes that depend mainly on the *peak* energy density or electron temperature in the material and processes that depend on the *cumulative* (total) absorbed x-ray dose. An example for the latter type are processes that are based on bond breaking. An example for the former is the onset of a phase transformation, such as melting. The volume fraction of molten or otherwise phase-transformed material also depends on the total absorbed x-ray dose. For sufficiently long pulses or for continuous light sources,

Table 8.1 Intensity dependence of x-ray–matter interaction in tantalum. For simplicity, we assumed cold heat capacities. The phase transformation energy is given for β tantalum films [12].

Intensity	Peak absorbed energy density in eV/atom	Physical mechanism	Reversible?
Very low	$\ll 0.7$	Heating	Yes
		Fatigue through thermal cycling	No
Low	0.1–0.2	Phase transformation	No
	0.7	Thermal melting	No
Medium	≥ 1.3	Ablation	No
	≈ 1.4	Nonthermal melting (short pulses)	No
High	>1.3	Plasma formation	No

the effect of x-ray radiation on materials is somewhat reduced by heat conduction that removes energy from the interaction region, whereas for very short pulses, the peak energy density is given by the absorbed x-ray dose.

If the dominant interaction process depends only on the peak energy density, we can often define a threshold for the onset of that process. As an example, Table 8.1 shows the threshold peak energy densities for various x-ray–matter interaction processes in tantalum irradiated by x rays. Most of the processes we listed are triggered by single x-ray pulses, except for thermal fatigue for which both a threshold x-ray dose as well as a certain number of pulses have to be exceeded, as discussed in more detail in Section 8.6.

The different damage thresholds in Table 8.1 motivates assigning different intensity regimes to x-ray damage, which we will simply call very low, low, medium, and high intensities. At very low intensities, the temperature of the material increases only slightly. If temperature gradients are present, differences in the thermal expansion coefficient can lead to stress gradients and, in the case of multiple exposures, failure due to thermal fatigue. Even at very low intensities, x rays can break chemical bonds in the irradiated material. This effect may be difficult to detect for single x-ray pulses. However, it has been found that certain materials can be ablated when being exposed to multiple x-ray pulses, even though single x-ray pulses have a negligible effect [11].

At somewhat larger intensities, the material is heated to sufficiently high temperatures for phase transformations to occur. For bulk materials, the equilibrium crystal structures as a function of temperature and pressure have been cataloged, as for example in [13]. For thin films, predicting the behavior is complicated by their typical nonequilibrium state. These metastable films transform even under moderate temperature increases, see for example [12] for tantalum. For sufficiently high fluences, the materials eventually melt. The melting transition has gained special significance in the development of x-ray optics since it is the ultimate limit beyond which the optics will fail. The actual damage threshold may be lower than this.

At even higher intensities, material is removed from the surface, which is also called ablation. This process was described in Section 8.4. At these intensities and higher, the x-ray irradiation leads to strong ionization effects, and the irradiated material turns into a plasma.

8.5.1
Interaction of Short X-Ray Pulses with Crystals

In conventional photon-induced melting processes of crystals, electrons transfer the absorbed photon energy to the ions in the lattice, so that electrons and ions stay close to equilibrium until the material reaches the melting temperature and melts. This process has been studied extensively in the visible light regime. The time scale for this process is several picoseconds. It has also been found that thermal processes and equilibrium thermodynamics do not explain some experimental data for intense *short-pulse* laser irradiation with sub-ps pulse duration [14]. Melting in this case occurs much faster, since for light with sufficiently high intensity, the electrons are so far removed from thermodynamic equilibrium that the covalent bonds are weakened, leading to lattice disorder much faster then thermal melting. This photo-induced phase transformation is often called nonthermal melting and has been observed in many semiconductor materials. In metals, the lattice stability does not seem to be affected by electron excitation.

X-ray-induced melting is much less explored. The x-ray photons still couple with the electrons in the system, but they do not only drastically increase the kinetic energy of the electron system but they also cause inner-shell atomic ionization. We therefore have localized charges in the system both due to fast electrons with a small de-Broglie wavelength and due to ions with core holes, so that Coulomb interactions are becoming more important. In order to understand the behavior of the system, atomic physics processes in this dense plasma system and electron cascade processes, by which quasi-free electrons slow down and excite other atoms, are important. Further research in this area is needed.

8.6
X-Ray-Induced Mechanical Damage

When x-ray-irradiated materials have sufficient time to equilibrate microscopically, meaning that the electrons are in equilibrium both among themselves and with the ions, then the behavior of the material is in large part determined by thermal and mechanical dynamics. This can be the case for x-ray pulses that are at least several picoseconds in duration, or for shorter x-ray pulses that do not induce changes *during* the pulse. We will first analyze the time scale associated with thermal and with mechanical phenomena, and then discuss possible failure modes.

The time scale τ_s for mechanical disturbances to propagate through a material is given by the product of the speed of sound v_s and a characteristic distance d, $\tau_s = v_s d$. For example, the speed of sound v_s in aluminum is approximately 4900 km/s.

Taking the distance d as the x-ray attenuation length in solids, typically ranging from 1 to 100 μm, we obtain time scales ranging from 0.2 to 20 ns.

Since heat conduction is a diffusional process, its time scale τ_h can be estimated as

$$\tau_h = \frac{d^2}{2D_h} , \tag{8.1}$$

where the thermal diffusivity D_h is given by

$$D_h = \frac{k}{C_p \rho} . \tag{8.2}$$

k is the thermal conductivity, C_p is the heat capacity, and ρ is the mass density. For aluminum, typical values are $k = 250\,\mathrm{W/(m\,K)}$, $C_p = 910\,\mathrm{J/(kg\,K)}$, and $\rho = 2700\,\mathrm{kg/m^3}$, so that $D_h \approx 10^{-4}\,\mathrm{m^2/s}$. According to (8.1), the time scale τ_h ranges between 10 ns and 100 μs, which is much longer than the times associated with the propagation of mechanical disturbances τ_s. Therefore, mechanical and thermal processes are usually decoupled and can be treated separately.

Solids irradiated with such x-ray pulses typically try to expand, but they are confined by their inertia and the surrounding material, so that compressive stresses develop. Since heat conduction is much slower than the mechanical response, this evolution is nearly perfectly adiabatic [15]. Mechanical disturbances then propagate in the material to reach equilibrium. When compressive waves are reflected from free surfaces, the boundary conditions require that the compressive pulse is replaced by a tensile pulse. This is discussed in more detail in Section 9.4.2, refer to Figure 9.5. If the tensile stresses associated with this pulse reach the ultimate tensile strength, defined as the maximum stress a material can withstand before deforming significantly, spallation of the material occurs. Spallation is the internal rupture of a solid through nucleation, growth, and coalescence of tensile-stress-induced defects, such as microcracks, leading to the ejection of material [16].

Even when the mechanical stresses are sufficiently small so that the material does not fracture, plastic mechanical deformation may still occur, such as macroscopic or micro yielding. Repetitive application of these pulses can then lead to thermal fatigue and fracture, as discussed in more detail in [17, 18].

8.7 X-Ray Damage in Inertial Confinement Fusion

Targets that are laser-irradiated in laser-confinement fusion applications emit x-ray bursts with a few ns duration. These bursts deposit their energy into the walls of the target chamber. The thermal diffusion time is much longer than nanoseconds, and ablation occurs. The pressure in the vaporized material is tens to hundreds of kbar, which can launch a shock in the unvaporized material that can lead to further changes or damage, such as delamination or crater formation [19].

8.8
X-Ray Damage in Semiconductors

Ionizing radiation can lead to malfunction and even damage of electronic systems. Ionizing radiation encompasses both particle radiation and high-energy electromagnetic radiation, and is typically encountered in space applications, high-altitude flight, and during nuclear incidents or warfare. Semiconductors are particularly sensitive to radiation damage. We will now give a brief overview about how x-ray damage can occur during the fabrication of semiconductor circuits, and how semiconductor devices can be made more resistant to ionizing radiation.

8.8.1
X-Ray Damage in Semiconductor Processing

Photolithography is a microfabrication process in which films are patterned by selectively removing or adding material. A photosensitive film is deposited onto the structure that is to be patterned, and it is selectively exposed to radiation by use of a photolithography mask. This leaves a shadow image on the photosensitive film. After developing this film, the mask has been imprinted, and can then be used to selectively add or remove material.

X-ray lithography has been a very promising technology for deep submicron patterning that originated in 1969 [20] and is still used today, albeit not in the volume production mode envisioned originally. It typically operates in the wavelength regime between 1.0–0.1 nm. At these short wavelengths, diffraction effects in lithographic applications are very weak, so that very high patterning resolutions can be achieved.

It has been found that high doses of x-ray radiation as part of the lithography process can lead to radiation damage in semiconductors. The gate oxide in transistors, which is used as an insulator in semiconductor circuits, is most sensitive to damage. Radiation damage includes the creation of oxide charges, interface states, and electron traps [21], all of which alter the transistor performance [22]. It has been found that the effect of radiation damage can be reduced somewhat by annealing [23]. It has also been shown that an x-ray stopping layer made of high-Z materials reduces the number of x-ray photons reaching the oxide gate layer, thus reducing the amount of damage [24].

8.8.2
X-Ray-Damage-Resistant Semiconductors

Radiation hardening methods are techniques for making electronic systems more resistant to ionizing-radiation-induced malfunction or damage. X rays can have a variety of effects on semiconductors. They can induce the creation of electron–hole pairs, which can lead to photo currents. Since these currents are leakage currents in diodes and transistors, they degrade their performance. This effect is often only transient [25, 26]. During nuclear explosions, short-time high-intensity radiation

pulses are generated that induce photo currents in semiconductors, which can lead to opening and closing of transistors at random. X rays can also induce holes in the gate oxide layer, and, similar to hot-carrier degradation in high-speed electronics, this can lead to permanent performance degradation.

Radiation hardening methods need to address both the improvement of total-dose response and the response to single radiation events. The latter is typically much more difficult to achieve [25, 27]. To reduce the chance of charge buildup, which can lead to shifts in the operating threshold of transistors, thinner oxide layers can be used, which simply reduces the amount of volume available for damage. Transistor-to-transistor leakage can be reduced by introducing guard-bands around each individual or groups of transistors [28].

8.9 Damage to Biomolecules in X-Ray Imaging

In the life sciences, the spatial resolution in x-ray imaging is limited primarily by radiation damage to the biological samples. For low fluxes it has been shown that the accumulated absorbed x-ray dose determines the degree of damage, and with that the image resolution [29]. The x-ray dose is measured in units of Gray (Gy = J/kg). For reference, the life dose is around 60 MGy. Figure 8.18 shows the resolution to which objects can be imaged as a function of the x-ray dose. In the resolution range of 0.1–10 nm, the resolution depends linearly on the dose approximately as [30]

$$\text{dose (Gy)} \approx 10^8 \,\text{resolution (nm)} \,. \tag{8.3}$$

We will now focus on the role of damage in x-ray protein crystallography, which is the workhorse technique in structural biology. In Section 10.3 we discuss the new method of single-particle diffractive imaging. X-ray damage of protein crystals is a two-step process [31]. The first step, the primary damage process, is initiated by photoelectric absorption and Compton scattering of the x-ray radiation, leading to atomic excitation and possible breakage of chemical bonds. The excited ion can then release part of its excess potential energy through fluorescence and Auger decay [32]. These processes can lead to multiply charged ions and extensive free-charge buildup in the vicinity of the ion. Figures 8.19 and 8.20 show the energy regime in which photoionization and inelastic scattering processes dominate. Ionization cascades occur along the path of the primary electron through the material, leading to further nonuniform charge buildup in the sample. High-Z atoms in proteins can lead to a substantial increase in the local dose, and metal centers are especially susceptible to this kind of damage. Each 8-keV electron disrupts bonding in about 70 molecules and leads to disorder in at least 90 [33]. These processes happen within a few femtoseconds. After about a picosecond, breakage of S–H, O–H, N–C, and C–H bonds occurs, inducing the creation of reactive species, including electrons and hydroxyl (OH^-) and hydrogen radicals. The radicals may be directly generated in the molecule or indirectly in the surrounding solution.

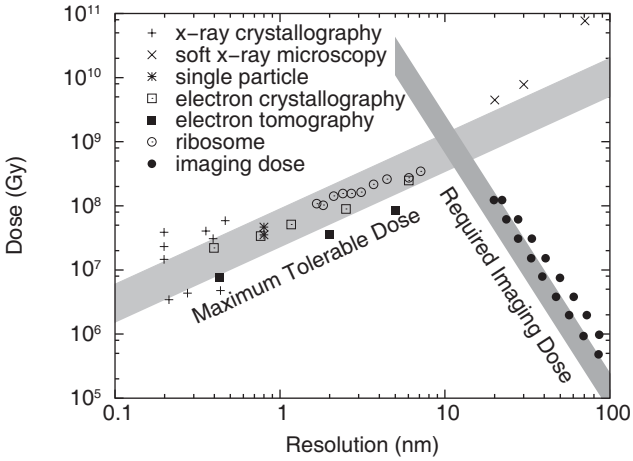

Figure 8.18 Dose required for imaging and maximum tolerable dose of a protein with stoichiometry $H_{50}C_{30}N_9O_{10}S_1$ and mass density 1.35 g/cm^3 against a background of water for 10-keV x rays. Reprinted from [30], with permission from Elsevier.

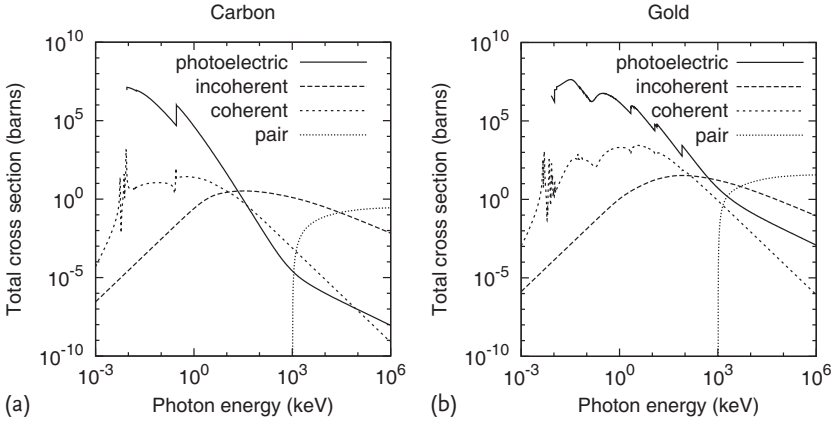

Figure 8.19 Total interaction cross sections for carbon (a) ($Z = 6$) and gold (b) ($Z = 79$) [34].

The second step, also called the secondary damage process, takes micro- to milliseconds and involves the diffusion of these reactive species through the protein crystal, resulting in additional bond breakage and further generation of radicals. The second step is responsible for an increase in the degree of damage in protein crystals *after* exposure, so there is a time dependence to the degree of radiation damage. Secondary processes are assisted by the abundant presence of water in the protein crystal. Since this step is diffusion-limited and therefore strongly temperature-dependent, the effect of radiation damage on protein crystal damage can be reduced by cooling the sample. Besides reducing diffusion, cooling improves the lifetime of protein crystals by mechanically stabilizing the frozen matrix,

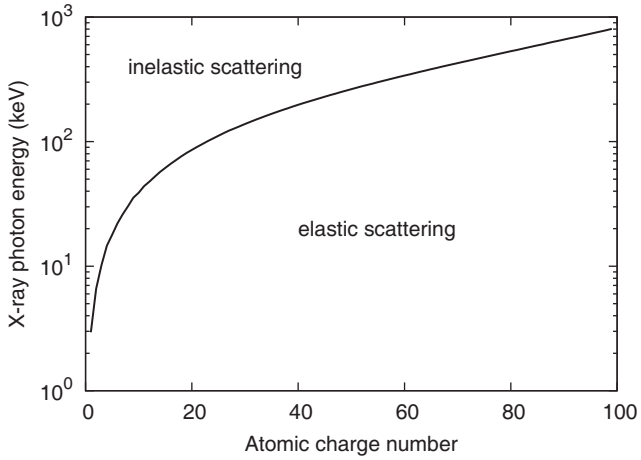

Figure 8.20 Dominant x-ray scattering processes by atoms as a function of atomic charge state and photon energy [34].

and it improves the quality of diffraction patterns by reducing atomic vibrations. Primary damage processes, however, still occur.

In x-ray crystallography, radiation damage leads to changes in the intensity of the diffraction spots. A systematic analysis of this effect is complicated by the wide variation of the mechanical, physical, and chemical properties of protein crystals. Typically, high-resolution data is compromised first, which leads to decreased diffraction power (*spot fading*) of large-scattering-angle diffraction spots [30]. In case x-ray damage leads to the mechanical destabilization of the whole crystal, which can sometimes happen due to solvent loss, the entire diffraction pattern is compromised.

Another manifestation of radiation damage are changes in the unit cell dimensions, [31] which, like the spot fading, is not very reproducible and varies even for crystals of the same protein [35]. Even a rather modest change in all the cell dimensions of 0.5% can lead to a 15% change in the general reflection intensities [36].

References

1 Henke, B.L., Gullikson, E.M., and Davis, J.C. (1993) X-ray interactions: Photoabsorption, scattering, transmission, and reflection at $E = 50-30\,000$ eV, $Z = 1-92$. *Atom. Data Nucl. Data Tables*, **54**, 181–342.

2 Scott, H.A. (2001) Cretin – a radiative transfer capability for laboratory plasma. *J. Quant. Spectrosc. Radiat. Trans.*, **71**, 689–701.

3 Zel'dovich, Y.B. and Raizer, Y.P. (1966) *Physics of Shock Waves and High-Temperature Hydrodynamic Phenomena*, Academic Press, New York.

4 Lupis, C.H.P. (1983) *Chemical Thermodynamics of Materials*, Prentice Hall, New York.

5 De Podesta, M. (2002) *Understanding the Properties of Matter*, 2nd edn, CRC Press, Boca Raton, Florida.

6 Balluffi, R.W., Allen, S.M., and Carter, W.C. (2005) *Kinetics of Materials*, John Wiley & Sons, New York.

7 Porter, D.A. and Easterling, K.E. (2001) *Phase Transformations in Metals and Alloys*, 2nd edn, Nelson Thornes, Cheltenham.

8 Lindemann, F.A. (1910) The calculation of molecular natural frequencies. *Phys. Z.*, **11**, 609–612.

9 von der Linde, D. and Sokolowski-Tinten, K. (1998) Physical mechanisms of short pulse laser ablation. *Proc. SPIE*, **3734**, 2–9.

10 Nagler, B., Zastrau, U., Fäustlin, R.R., Vinko, S.M., Whitcher, T., Nelson, A.J., Sobierajski, R., Krzywinski, J., Chalupsky, J., Abreu, E., Bajt, S., Bornath, T., Burian, T., Chapman, H., Cihelka, J., Döppner, T., Düsterer, S., Dzelzainis, T., Fajardo, M., Förster, E., Fortmann, C., Galtier, E., Glenzer, S.H., Göde, S., Gregori, G., Hajkova, V., Heimann, P., Juha, L., Jurek, M., Khattak, F.Y., Khorsand, A.R., Klinger, D., Kozlova, M., Laarmann, T., Lee, H.J., Lee, R.W., Meiwes-Broer, K.-H., Mercere, P., Murphy, W.J., Przystawik, A., Redmer, R., Reinholz, H., Riley, D., Röpke, G., Rosmej, F., Saksl, K., Schott, R., Thiele, R., Tiggesbäumker, J., Toleikis, S., Tschentscher, T., Uschmann, I., Vollmer, H.J., and Wark, J.S. (2009) Turning solid aluminium transparent by intense soft x-ray photoionization. *Nat. Phys.*, **5**, 693–696.

11 Juha, L., Hajkova, V., Chalupsky, J., Vorlicek, V., Ritucci, A., Reale, A., Zuppella, P., and Stoermer, M. (2009) Radiation damage to amorphous carbon thin films irradiated by multiple 46.9 nm laser shots below the single-shot damage treshold. *J. Appl. Phys.*, **105**, 093117.

12 Lee, S.L., Doxbeck, M., Mueller, J., Cipollo, M., and Cote, P. (2004) Texture, structure and phase transformation in sputter beta tantalum coating. *Surf. Coat. Technol.*, **177/178**, 44–51.

13 Young, D.A. (1991) *Phase Diagrams of the Elements*, University of California Press, Berkeley, CA.

14 Sundaram, S.K. and Mazur, E. (2002) Inducing and probing non-thermal transitions in semiconductors using femtosecond laser pulses. *Nat. Mater.*, **1**, 217–224.

15 Molitvin, A.M. (2003) Strength and specific fracture energy of metals subjected to a thermal shock. *J. Appl. Mech. Tech. Phys.*, **44**, 135–140.

16 Moshe, E., Eliezer, S., Henis, Z., Werdiger, M., Dekel, E., Horovitz, Y., Maman, S., Goldberg, I.B., and Eliezer, D. (2000) Experimental measurements of the strength of metals approaching the theoretical limit predicted by the equation of state. *Appl. Phys. Lett.*, **76**, 1555–1557.

17 de Castro, A.R.B., Vasconcellos, A.R., and Luzzi, R. (2010) Thermoelastic analysis of a silicon surface under x-ray free-electron-laser irradiation. *Rev. Sci. Instrum.*, **81**, 073102.

18 Ryutov, D.D. (2003) Thermal stresses in the reflective x-ray optics for the linac coherent light source. *Rev. Sci. Instrum.*, **74**, 3722–3725.

19 Peterson, R.R. (1989) Experiments to simulate x-ray damage to the first wall of the inertial confinement fusion microfusion facility. In *13th Symp. Fusion Eng.*, Knoxville, TN.

20 Spiller, E. (1993) Early history of x-ray lithography at IBM. *IBM J. Res. Dev.*, **37**, 291–297.

21 Reisman, A., Merz, C.J., Maldonado, J.R., and Molzen Jr., W.W. (1984) Low energy x-ray and electron damage to IGFET gate insulators. *J. Electrochem. Soc.*, **131**, 1404–1409.

22 Hsia, L.C. and Christensen, T. (1992) Radiation damage effects on bipolar and mos devices in x-ray lithography. *J. Electron. Mater.*, 21.

23 Maldonado, J.R., Reisman, A., Lezec, H., Williams, C.K., and Iyer, S.S. (1986) X-ray damage considerations in MOSFET devices. *J. Electrochem. Soc.*, **133**, 628–631.

24 Maldonado, J.R., Reisman, A., Lezec, H., Bumble, B., Williams, C.K., and Iyer, S.S. (1987) Thin film structure to reduce radiation damage in x-ray lithography. *J. Vac. Sci. Technol. B*, **5**, 248–252.

25 Alexander, D.R., Mavis, D.G., Brothers, C.P., and Chavez, J.R. (1996) Design issues for radiation tolerant microcircuits in space. In *1996 IEEE Nuclear*

and Space Radiation Effects Conference (NSREC) Short Course, vol. V-1.

26 Calin, T., Nicolaidis, M., and Valazco, R. (1996) Upset hardened memory design for submicron cmos technology. *IEEE Trans. Nucl. Sci.*, **43**, 2874–2878.

27 Anelli, G., Campbell, M., Delmastro, M., Faccio, F., Florian, S., Giraldo, A., Heijne, E., Jarron, P., Kloukinas, K., Marchioro, A., Moreira, P., and Snoeys, W. (1999) Radiation tolerant VLSI circuits in standard deep submicron CMOS technologies for the LHC experiments: Practical design aspects. *IEEE Trans. Nucl. Sci.*, **56**, 1690–1696.

28 Lacoe, R.C., Osborn, J.V., Koga, R., Brown, S., and Mayer, D.C. (2000) Application of hardness-by-design methodology to radiation-tolerant ASIC technologies. *IEEE Trans. Nucl. Sci.*, **47**, 2334–2341.

29 Blake, C.F.F. and Phillips, D.C. (1962) Effects of x-ray radiation on single crystals of myoglobin. In *Symposium on the biological effects of ionizing radiation on the molecular level*, Vienna, Int. At. Energy Agency, pp. 183–191.

30 Howells, M.R., Beetz, T., Chapman, H.N., Cui, C., Holton, J.M., Jacobsen, C.J., Kirz, J., Lima, E., Marchesini, S., Miao, H., Sayre, D., Shapiro, D.A., and Spence, J.C.H. (2009) An assessment of the resolution limitation due to radiation-damage in x-ray diffraction microscopy. *J. Electron Spectr. Relat. Phenom.*, **170**, 4–12.

31 Ravelli, R.B.G. and McSweeney, S.M. (2000) The 'fingerprint' that x-rays can leave on structures. *Structure*, **8**, 315–328.

32 Nave, C. (1995) Radiation damage in protein crystallography. *Radiat. Phys. Chem.*, **45**, 483–490.

33 Laubinis, P.E., Graham, R.L., Biebuyck, H.A., and Whitesides, G.M. (1991) X-ray damage to CF_3CO_2-terminated organic monolayers on Si/Au: Principal effect of electrons. *Science*, **254**, 981–983.

34 Cullen, D.E., Hubbell, J.H., and Kissel, L. (1997) EPDL97: The evaluated photon data library '97 version. *EPDL Tech. Rep. UCRL-50400*.

35 Murray, J. and Garman, E. (2002) Investigation of possible free-radical scavengers and metrics for radiation damage in protein cryocrystallography. *J. Synchrotron. Radiat.*, **9**, 347–354.

36 Magdoff, B.S. and Crick, F.H.C. (1955) Ribonuclease II. Accuracy of measurement and shrinkage. *Acta Cryst.*, **8**, 461–468.

9
Simulation of X-Ray–Matter Interaction

Intense x-ray pulses can turn condensed matter into plasmas. The description of the involved processes is an inherent many-body problem. Simple analytical models are often inadequate since they require too severe approximations, so computational models are used instead. In many cases, models and tools developed in the fields of plasma physics and continuum mechanics provide useful starting points to describe x-ray–matter interaction. The goal of this chapter is to familiarize the reader with different simulation techniques and to give pointers to the relevant literature for details.

9.1
Models for Different Time- and Length Scales

In general, x-ray–matter interaction can span a vast range of time and length scales, and different models are appropriate for the different regimes. Figure 9.1 shows some of the techniques used today, along with the regimes in which they are typically applied. Most models provide either an atomistic or a continuous description of matter. Examples of the latter are transport or hydrodynamic models. Molecular dynamics and Monte Carlo methods are popular atomistic models. They are typically used to describe small subsets of large systems, smaller samples, and more complex geometries since they naturally allow treatment of full three-dimensional structures. Quantum molecular dynamics, which in essence involves solving the time-dependent Schrödinger equation, is only feasible for very small systems with a few hundred atoms. It allows one to treat degenerate systems for which quantum mechanical effects are important. If larger systems need to be simulated, semiclassical models have to be used. These methods work for nondegenerate, dense and dilute plasmas with more than 10^5 atoms. Nowadays, the state of the art is simulating plasmas including all the electron degrees of freedom with 10^7–10^8 particles [1]. The simulation length in this case is typically limited to a picosecond or less since plasma molecular dynamics simulations are only straight-forward to parallelize in space but not in time. Coincidentally, this time scale is well matched with the temporal length of photon pulses produced by x-ray free-electron lasers. Since the simulation time step is limited by the electron dynamics, integrating out the electron

High-Intensity X-rays – Interaction with Matter, First Edition. Stefan P. Hau-Riege.

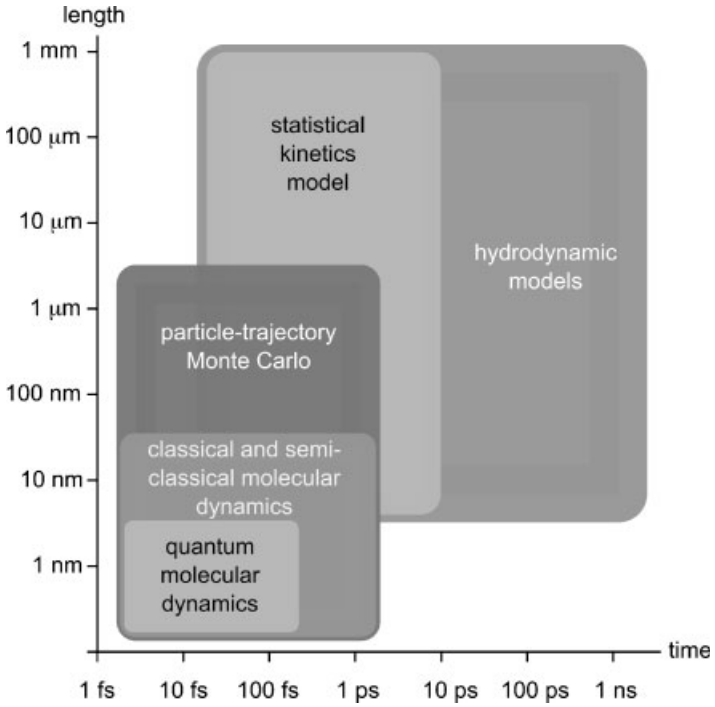

Figure 9.1 Some common modeling methods and typical length- and time scales.

motion allows increasing the time step and therefore enables longer simulation times, at the expense of losing information about detailed electron properties.

Transport and hydrodynamic methods have been applied traditionally to larger systems, preferentially to ones with regular structures to simplify the computational requirements. Recently, these methods have been applied to very small samples, as well, such as nanoclusters and single molecules [2, 3]. Transport methods are very well suited to simulation of the semiequilibrium long-term evolution of plasma systems. We will now discuss some of these models in more detail.

9.2 Atomistic Models

Solving the time-dependent Schrödinger equation for large many-body systems is beyond the capabilities of today's computers. In some cases, the picture of single electrons moving in an effective potential has proven to be sufficient. Unlike conventional atomistic dense-plasma simulations that simply assume an average ionization $\langle Z \rangle$, in the x-ray case, atomic processes need to be included. Ideally, the atomic physics treatment is based on the consideration of the microfields in the plasma [4, 5]. Time-dependent density functional theory [6] has been used

in the past to describe the response of clusters to intense laser pulses. In a one-dimensional model described in [7], the ion positions were assumed to be frozen, and correlation effects were neglected, so this model is a numerical solution of the time-dependent Kohn–Sham equations to describe the electron dynamics in a cluster [8]. In order to extend this model to x rays, single-photon ionization processes would have to be considered.

Since a full quantum-mechanical treatment is usually too involved, classical or semiclassical approaches are often preferable. In these models, nuclei and unbound electrons are treated as classical particles obeying Newton's equation of motion. Such atomistic simulations usually fall into the general groups of either Monte Carlo or molecular dynamics simulations and particle-in-cell (PIC) methods, which we will discuss now in more detail.

9.2.1 Molecular Dynamics and Particle-in-Cell Models

9.2.1.1 Molecular Dynamics Models

Molecular dynamics methods track the position of individual atoms (and possibly electrons) and are preferred when an explicit treatment of the electron interaction is needed, when the detailed atomic structure of the materials needs to be determined, and when the excitation and ionization states of ions are important. For example, crystal diffraction requires detailed information about the position and motion of ions. Classical molecular dynamics models are very useful for describing time-dependent x-ray–matter interaction problems in nondegenerate matter. Recent examples of classical molecular dynamics modeling of the interaction of high-intensity x-ray pulses with matter are given in [9–12].

In the case of the interaction of short x-ray pulses with matter, it is often important to calculate the ion motion on the time-scale of the pulse duration, which is caused both by thermal interaction through electron–ion coupling on the time scale of several picoseconds, and by nonthermal interaction when the ionization fraction is sufficiently large. The latter effect requires a quantum-mechanical treatment of the dynamics. Quantum molecular dynamics has been very successful for describing such dynamics for optical laser–matter interaction [13–16]. We will now discuss classical molecular dynamics and comment on quantum treatments in Section 9.2.1.4.

In classical molecular dynamics simulations it is assumed that the force at any point in space and time can be calculated from the pairwise interaction of particles: When a pair potential is given, the force acting on each particle due to all other particles can be computed by summing up all pairwise interactions. The equation of motion of a particle p is given by

$$m_p \frac{d^2 \boldsymbol{r}_p}{dt^2} = -q_p \nabla \Phi(\boldsymbol{r}_p) \,, \tag{9.1}$$

where m_p is mass of particle p, q_p is its charge, $\boldsymbol{r}_p$ is its position, and $\Phi(\boldsymbol{r})$ is the sum of all pairwise potentials. Typically, a type of Verlet integrator is used to

evaluate (9.1), and in some cases periodic boundary conditions are enforced [17]. A Verlet algorithm is numerically more stable than simple Euler integration, which is the straight-forward numerical integration of the equation of motion. In the simplest form of the Verlet algorithm, the position at the next time step is calculated from the position at the previous and the current time step, using only the forces and not the velocities.

Since the interaction of intense x-ray radiation with matter is a plasma problem, Coulomb-like potentials have to be evaluated which decrease only slowly with distance. Therefore, to calculate the potential at a certain point in space requires the consideration of all particles in a system, and the CPU time requirements scale as $O(N^2)$ for the simplest algorithms, which means that the leading term in the CPU time requirements is proportional to N^2 for an N-particle system.

9.2.1.2 Particle-in-Cell Method

Various methods have been proposed to reduce the computational complexity of the N-body problem that scale better than $O(N^2)$ and therefore allow a more rapid evaluation of the particle interactions. In plasma physics, *particle-in-cell* methods have been very successful. In these methods, a mesh is laid out over the computational domain. During each time step, the following computational steps are performed:

1. Interpolate the charge density to the mesh points, which usually is a Cartesian grid, so that
$$\rho(i, j, k) = \sum_p q_p S\left[\boldsymbol{r}_{i,j,k} - \boldsymbol{x}_p(t)\right], \tag{9.2}$$
where i, j, k are the three-dimensional grid indices, q_p is charge on particle number p, $\boldsymbol{r}_{i,j,k}$ is the position of grid point i, j, k, and S is a shape function.
2. Use a fast Poisson solver to obtain the electric potential values on the mesh [18].
3. Compute the forces from the potential on the mesh, and interpolate to the particle positions, for example using a leap-frog integrator. At this point, periodic boundary conditions can be enforced.

The PIC method was designed for weakly coupled plasmas with many particles in each cell. The application to strongly coupled plasmas requires one to resolve for the space between particles, so that less than one particle resides in each cell on average. The complexity of the PIC method scales as $O(N + M \log M)$, where M is the number of mesh points. Usually, $N \propto M$. Note that the mesh provides only limited resolution, and the performance is poor for highly nonuniform charge distributions. Further, the force calculations are numerically difficult. For more details, see [19].

9.2.1.3 Hybrid Methods

The PIC approach is sometimes considered distinct instead of an implementation of molecular dynamics. This point of view is of little practical value since the

boundaries are becoming blurred. The accuracy of PIC methods can be improved by considering short-range interactions directly, and treating only far-field interaction with a mesh (particle–particle/particle–mesh (P^3M) methods). This approach is most efficient and accurate for reasonably uniform charge distributions. The reader is referred to [20] for more details.

Another form of molecular dynamics implementation are *tree* methods [21], where forces over large distances are computed in the center-of-mass approximation by clustering particles using a tree-like data structure. The algorithm scales as $O(N \log N)$. Tree algorithms are particularly useful for nonuniform charge distributions. The precision can be improved by extending the method from monopole (center-of-mass) expansions to multipoles [22].

9.2.1.4 Quantum Molecular Dynamics Models

In classical molecular dynamics, the interaction potentials of the particles are determined in advance. This approach works well for classical systems, but when quantum-mechanical effects need to be taken into account, modified or new potentials need to be developed for each new problem. Quantum (*ab initio*) molecular dynamics circumvents this limitation by combining traditional molecular dynamics with electronic structure methods to calculate the interparticle forces during the simulation. Various different quantum molecular dynamics methods have been proposed [23]. Specifically, the Car–Parrinello approach is widely used [24]. It is based on the Born–Oppenheimer approximation, in which the electronic and nuclear motion are decoupled. Density functional theory is used to approximately solve the N-body Schrödinger equation, and then the atomic nuclei are advanced. Since regular density functional theory calculates the electronic ground state, improved methods have been devised to perform quantum molecular dynamics at finite temperature based on a finite-temperature functional as suggested by Mermin [25].

9.2.2 Monte Carlo Models

Monte Carlo methods have traditionally been used to study time-independent equilibrium configurations, but they can also be applied to time-dependent problems. Different types of stochastic models are often lumped together and are called Monte Carlo models. For example, in the well-known Metropolis Monte Carlo method [26], the phase space of an N-body system is strategically sampled by setting up a certain chain of phase-space points for most efficient sampling. Other methods sample multiple single particle trajectories stochastically by determining single particle trajectories. The behavior of a large number of electrons is deduced from a few trajectories, as pointed out by Kahn in one of the earliest papers on Monte Carlo methods [27, 28]. These methods can be easily linked to a time evolution, and are often used for electron and x-ray transport. This is described in more detail in [29].

9.2.2.1 Monte Carlo Methods to Sample Phase Space

A typical example for the application of Monte Carlo methods is the estimation of the expectation value of an operator by stochastic sampling. This is especially useful for evaluating quantities in thermodynamic equilibrium, which requires us to evaluate

$$\langle A \rangle = \frac{\int A\,(\boldsymbol{r}_N, \boldsymbol{v}_N) \exp(-\beta H) d^N \boldsymbol{r} d^N \boldsymbol{v}}{\int \exp\,(-\beta H)\; d^N \boldsymbol{r} d^N \boldsymbol{v}}\,. \tag{9.3}$$

Here H is the Hamiltonian for N particles, $\beta = 1/kT$, and T is the temperature. Completely random sampling in this case would not be very efficient since the statistical weight $\exp(-\beta H)$ is very nonlinear. Instead, *importance sampling* is applied in which the small portion of phase space that actually contributes significantly to the average is sampled preferentially. In the Metropolis method [26], a Markov chain of states in phase space is used that migrates toward states of higher probability [30]. For degenerate plasmas, quantum Monte Carlo methods are available. Numerous quantum Monte Carlo methods have been developed, see for example [31, 32].

9.2.2.2 Monte Carlo Methods to Sample Particle Trajectories

In another type of Monte-Carlo method, single-particle interactions are sampled stochastically. We will consider the case of a monochromatic x-ray beam irradiating a material. The heating process by the x rays consists of two parts: (i) x-ray absorption by the electrons, and (ii) the subsequent electron dynamics [33–35]. We will discuss x-ray absorption first.

Photon Absorption If the complex index of refraction $n = 1 - \delta + i\beta$ is known, we can use Maxwell equations (1.23) to (1.26) to calculate the electric field and the intensity distribution I in units of energy per unit area and unit time in the material. For short pulses, this intensity distribution is strongly time-dependent. The imaginary part β of the index of refraction n relates to the linear absorption coefficient through

$$\alpha = \frac{4\pi\beta}{\lambda}\,, \tag{9.4}$$

where λ is the wavelength. The absorbed power density is then given by αI in units of energy per unit volume per unit time, and

$$\rho(\boldsymbol{r}, t) dV dt = \frac{\alpha(\boldsymbol{r}, t) I(\boldsymbol{r}, t) dV dt}{E_\gamma} \tag{9.5}$$

is the number of absorbed photons in the volume element dV during the time dt. The total number of absorbed photons N_γ can be obtained by integrating ρ in (9.5) over space and time. Equation 9.5 gives fractional numbers and has to be interpreted as an average over a large number of realizations of a specific system of interest. Of course, in each realization, only an integer number of photons can be absorbed.

In the Monte Carlo technique, we generate realizations of these systems by interpreting

$$p(\boldsymbol{r}, t)\,dV\,dt = \frac{\rho(\boldsymbol{r}, t)\,dV\,dt}{N_\gamma} \tag{9.6}$$

as the probability of absorbing a photon in the volume element dV in the time interval dt. dV and dt have to be chosen sufficiently small so that this number is much less than one. In the computer simulation, we generate a random number *rnd* between 0 and 1 for each volume element dV and time interval dt. If $p(\boldsymbol{r}, t)\,dV\,dt > rnd$, then a photon is absorbed. By repeating this step N_γ times, we obtain a realization of the system. Since N_γ is typically very large, we reduce the problem by following the interaction of a large but finite number of photons N that are considered representative for all the photons in the system. In order to obtain the correct amount of absorbed energy, the effect of each electron is escalated (scaled) accordingly by N_γ / N.

If instead of the index of refraction n only the absorption cross sections σ for a group of atoms is known, we can use σ to calculate the flux distribution $F(\boldsymbol{r}, t)$ inside the sample, and then the probability that a photon is absorbed by an atom within the time interval dt is given by

$$p(\boldsymbol{r}, t)\,dt = \sigma F(\boldsymbol{r}, t)\,dt\ . \tag{9.7}$$

In this case refractive effects are neglected.

Electron Trajectories X rays are absorbed primarily by bound electrons through photoionization, leading to the emission of photoelectrons. These energetic primary electrons propagate through the sample and excite secondary electrons as described in Chapter 5 on electron dynamics in x-ray-irradiated samples. For example, photons with an energy of 12 keV, corresponding to a wavelength of 1 Å, lead to the emission of photoelectrons with a velocity of around 650 Å/fs in low-Z materials. Subsequently, the atoms emit Auger electrons with a velocity of about 100 Å/fs. Each photo- and Auger electron initiates a cascade of secondary electrons through impact ionization. Both the evolution of the energetic photoelectron as well as the cascade of secondary electrons can be treated with Monte Carlo techniques. This approach has been very successful in the field of electron microscopy in the past, see for example [29].

High-energy electrons can be described as a well-localized wavepacket, whereas at lower energies, the de-Broglie wavelengths become larger than the interatomic spacing, and the single-particle interaction picture is less useful. The electron is performing a random walk, continually undergoing elastic and inelastic scattering events. When calculating a large number of trajectories, a statistically significant number of scattering events is sampled, and the composite result will be a sensible approximation to reality. In electron microscopy, this approach has been shown to give excellent agreement with experiments. We will now describe an algorithm for calculating these electron trajectories through a material. The mean free path $\lambda(E)$

of an electron with kinetic energy E is the distance that it travels between successive interaction events, such as elastic and inelastic scattering. It is given by

$$\lambda(E) = \left[\frac{1}{\lambda_{el}(E)} + \frac{1}{\lambda_{inel}(E)}\right]^{-1}. \tag{9.8}$$

Here λ_{el} and λ_{inel} are the elastic and inelastic mean free paths, respectively. The probability that an electron travels a distance x is

$$p(x) = \exp\left(-\frac{x}{\lambda}\right). \tag{9.9}$$

We use successive Monte Carlo steps to determine the actual distances x that an electron travels between interactions by solving

$$rnd = \frac{\int_0^x \exp\left(-\frac{x'}{\lambda}\right) dx'}{\int_0^\infty \exp\left(-\frac{x'}{\lambda}\right) dx'} \tag{9.10}$$

for x. Here, rnd is a random number between 0 and 1, so that

$$x = -\lambda \ln(rnd). \tag{9.11}$$

In this approach, the average distance $\langle x \rangle$ of successive scattering events will be λ (Figure 9.2 shows an example of the path of an electron calculated using a Monte Carlo model). After a Monte Carlo step to determine the travel distance x between two interactions, we determine the kind of interaction through another Monte Carlo step: The probability for an elastic collision is approximately $p_{el} = \sigma_{el}/(\sigma_{el} + \sigma_{inel})$, and the probability for an inelastic collision is approximately

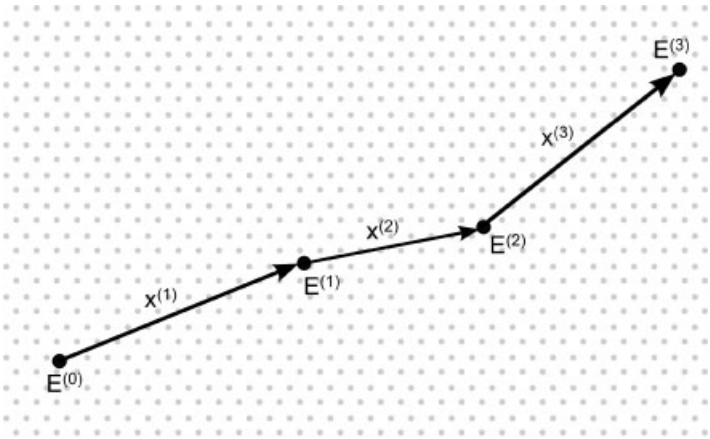

Figure 9.2 Example of the path of an electron calculated using a Monte Carlo model. The gray circles represent the atoms, and the black circle represents the electron at different times. $x^{(n)}$ are the path lengths between consecutive interaction events calculated using (9.11), and $E^{(n)}$ is the energy at the point of the interaction event.

$1 - p_{el} = \sigma_{inel}/(\sigma_{el} + \sigma_{inel})$. Finally, we perform another set of Monte Carlo steps to determine the scattering direction after the interaction by considering the differential scattering cross sections, and, in case of an inelastic scattering event, the energy loss. The simulation code can keep track of the effect of the energy loss mechanisms, which may include heating of the material or the emission of secondary electrons. In an iterative fashion, the path of the secondary electrons can be tracked to simulate an electron cascade. In order to optimize the code's efficiency, often only the high-energy secondary electrons are tracked, whereas the effect of lower-energy electrons is only estimated.

Joy describes a simplified algorithm that is computationally very efficient [29]. In that approach, only elastic scattering events change the path of an electron, whereas inelastic scattering events are assumed to change only the kinetic energy but not the direction of an electron. It is further assumed that the electron loses energy continuously during its passage through the material, which can be described by an electron stopping power. Various expressions for the stopping power have been suggested, see for example [36, 37]. In reality, only a subset of the energy loss mechanisms are continuous, and many lead to a discontinuous energy loss. Therefore, the stopping power approach needs to be seen as an averaging technique. Figure 9.3 shows the traces of multiple photoelectrons created by an unpolarized x-ray beam of small diameter at 8 keV irradiating a semi-infinite silicon sample ($z > 0$) from vacuum ($z < 0$) at normal incidence. The electron trajectories were calculated using the simplified method proposed by Joy [29]. The x-ray penetration depth in this case is 70 μm, and we show only the top 20 μm of the silicon. It can be seen that photoelectrons are emitted preferentially normal to the propagation direction of the x rays, and that most energy is deposited into a radius of less than

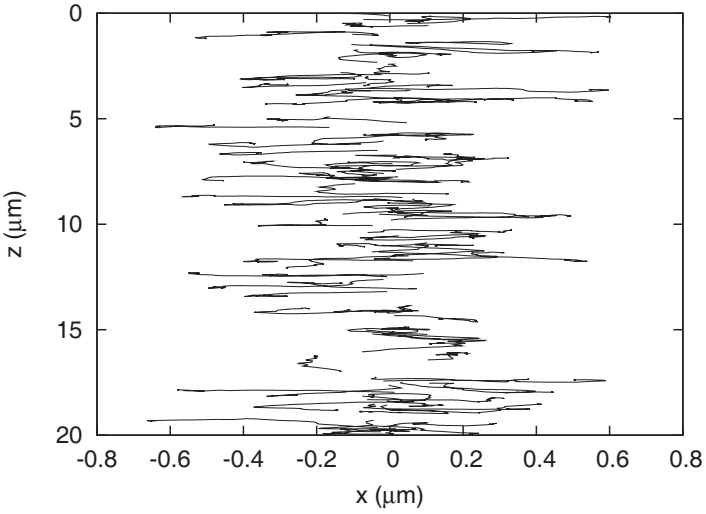

Figure 9.3 Trajectories of photoelectrons of a semi-infinite silicon slab ($z < 0$) irradiated with 8-keV x rays, calculated using the Monte Carlo technique [29].

1 μm. Since we assumed unpolarized light, the energy deposition is circularly symmetric around the z axis. For polarized light, we would need to take into account the preferred ejection of the photoelectrons in the direction of the electric field vector.

The trajectory Monte Carlo approach allows one to include a time description of the particle evolution since in between each interaction, the path length and the particle energy are known. Using this information, we can compute the travel time of the particles. External fields can naturally be accounted for by replacing the straight line segments between interactions with curved paths, as would be the case, for instance, for an applied external magnetic field. Internal fields, for example due to Coulomb charging, can be treated by calculating the particle trajectories simultaneously instead of sequentially, and keeping track of the charge distribution. Using this trajectory Monte Carlo technique, we obtain a quantitative description of the particle distribution and ultimately a space- and time-dependent distribution of the dose. Often it is assumed that the x-ray and electron cross sections are constant during the pulse, which is justifiable when only a small fraction of the core electrons are ionized. The electron energy decreases slowly during its path through the material, and the electron is more or less localized until its energy approaches 100–200 eV. In this energy range, the interaction cross sections are large.

9.3 Statistical Kinetics Models

For larger samples or long interaction times, computational resources are usually not sufficient to follow individual atoms and electrons, and statistical macroscopic methods, described through kinetics equations, are more appropriate. Examples for using this approach to describe x-ray–matter interaction processes are given in [2, 38, 39]. We first summarize the standard treatments used in statistical plasma physics, and how they can be expanded to include ionization dynamics. We then discuss how these approaches can be used to describe x-ray–matter interaction.

9.3.1 Kinetics Equations

In the following, we will only outline the principles of applying kinetics equations to plasma physics. A more detailed treatment can be found in [40]. In order to simplify the notation, we restrict ourselves to one kind of particle. It is relatively straight-forward to extend this treatment to multiple species, such as electrons and ions.

9.3.1.1 Klimontovich Distribution

In the kinetic theory of classical plasmas, a Klimontovich system is given by N identical particles in a box of volume V. Each particle has a position $\boldsymbol{r}$ and a velocity

$\boldsymbol{v}$, so that the trajectory of the ith particle can be described as $\boldsymbol{x}_i(t) = [\boldsymbol{r}_i(t), \boldsymbol{v}_i(t)]$. The *Klimontovich distribution function* is defined as

$$N(\boldsymbol{x}, t) = \sum_i \delta\left[\boldsymbol{x} - \boldsymbol{x}_i(t)\right], \tag{9.12}$$

where $\boldsymbol{x} = [\boldsymbol{r}, \boldsymbol{v}]$, so that $N(\boldsymbol{x}, t)$ is a $6 + 1$-dimensional function. The continuity equation in phase space [41] is given by

$$\frac{dN}{dt} = \frac{\delta N}{\delta t} + \dot{\boldsymbol{x}} \cdot \frac{\delta N}{\delta \boldsymbol{x}} = 0\,. \tag{9.13}$$

9.3.1.2 Liouville Distribution

To connect the microscopic Klimontovich distribution function to coarse-grained, macroscopic quantities, we introduce the phase space distribution function or *Liouville distribution function* $\rho_N(\boldsymbol{X}_N, t)$ which is a $6N+1$-dimensional function. With $\boldsymbol{X}_N = [\boldsymbol{x}_1, \boldsymbol{x}_2, \ldots, \boldsymbol{x}_N]$, $\rho_N(\boldsymbol{X}, t) d^{6N}\boldsymbol{X}_N$ denotes the probability of finding the system in the infinitesimal phase space volume $d^{6N}\boldsymbol{X}_N$. The *Liouville equation* is the continuity equation [41]

$$\frac{\partial \rho_N}{\partial t} + \boldsymbol{X}_N \cdot \nabla_{\boldsymbol{X}_N} \rho_N = 0 \tag{9.14}$$

which in the nonrelativistic case in Euclidean space can be rewritten as

$$\frac{\partial \rho_N}{\partial t} + \boldsymbol{V}_N \cdot \nabla_{\boldsymbol{R}_N} \rho_N + \frac{\boldsymbol{F}_N}{m} \cdot \nabla_{V_N} \rho_N = 0\,. \tag{9.15}$$

Here, $\boldsymbol{R}_N = [\boldsymbol{r}_1, \boldsymbol{r}_2, \ldots, \boldsymbol{r}_N]$, $\boldsymbol{V}_N = [\boldsymbol{v}_1, \boldsymbol{v}_2, \ldots, \boldsymbol{v}_N]$, and

$$\boldsymbol{F}_N = -\nabla_{\boldsymbol{R}_N} \left\{ \sum_{i=1}^{N} \left[\Phi_{ext}(\boldsymbol{r}_i) + \sum_{j=1}^{N} \Phi_{i,j}(\boldsymbol{r}_i, \boldsymbol{r}_j) \right] \right\}. \tag{9.16}$$

Φ_{ext} is the external field potential, and $\Phi_{i,j}(\boldsymbol{r}_i, \boldsymbol{r}_j)$ is the pair potential for interparticle interaction. In quantum mechanics, an analogous Liouville equation exists for the time evolution of mixed states[1)] described by the density matrix ρ [42],

$$\frac{\delta}{\delta t}\rho = \frac{1}{i\hbar}[H, \rho] = \frac{1}{i\hbar}(H\rho - \rho H)\,, \tag{9.17}$$

where $[,]$ are the Poisson brackets.

9.3.1.3 BBGKY Hierarchy

Integrating the Liouville equation (9.15) over part of the variables leads to a chain of equations. The first equation connects the one-particle density probability function with the two-particle density probability function, the second equation connects

1) A *mixed state* can be prepared by statistically combining multiple different pure quantum states.

the two-particle density probability function with the three-particle density probability function, and, generally, the sth equations connects the s-particle density probability function $\rho_s(\boldsymbol{x}_1, \boldsymbol{x}_2, \ldots, \boldsymbol{x}_s, t)$ with the $(s+1)$-particle density probability function [43]:

$$\frac{\partial \rho_s}{\partial t} + \sum_{i=1}^{s} \boldsymbol{v}_i \cdot \nabla_{\boldsymbol{r}_i} \rho_s - \frac{1}{m} \sum_{i=1}^{s} \nabla_{\boldsymbol{r}_i} \left[\Phi_{ext}(\boldsymbol{r}_i) + \sum_{j=1}^{s} \Phi_{i,j}(\boldsymbol{r}_i, \boldsymbol{r}_j) \right] \cdot \nabla_{\boldsymbol{v}_i} \rho_s$$
$$= \frac{1}{m} \sum_{i}^{s+1} \int \nabla_{\boldsymbol{v}_i} \rho_{s+1} \cdot \nabla_{\boldsymbol{r}_i} \Phi_{i,s+1} d^6 \boldsymbol{x}_{s+1} \, . \tag{9.18}$$

This set of equations is called the BBGKY hierarchy, named after Bogoliubov–Born–Green–Kirkwood–Yvon [44–46]. The BBGKY hierarchy in itself is just a formal reformulation of the Liouville equations and requires further information or approximations in order to be solved.

9.3.1.4 Boltzmann and Vlasov Equation

The BBGKY chain can be approximately solved by truncating the chain of equations, so that only a finite system of equations needs to be considered. For $s = 1$, (9.18) can be rewritten as

$$\frac{\partial \rho_1(\boldsymbol{x}_1)}{\partial t} + \boldsymbol{v}_1 \cdot \nabla_{\boldsymbol{r}_1} \rho_1(\boldsymbol{x}_1) - \frac{1}{m} \nabla_{\boldsymbol{r}_1} \Phi_{ext}(\boldsymbol{r}_1) \cdot \nabla_{\boldsymbol{v}_1} \rho_1(\boldsymbol{x}_1)$$
$$= \frac{1}{m} \int \nabla_{\boldsymbol{v}_1} \rho_2(\boldsymbol{x}_1, \boldsymbol{x}_2) \cdot \nabla_{\boldsymbol{r}_1} \Phi_{1,2}(\boldsymbol{r}_1, \boldsymbol{r}_2) d^6 \boldsymbol{x}_2 \, . \tag{9.19}$$

We set $\rho_2(\boldsymbol{x}_1, \boldsymbol{x}_2) = \rho_1(\boldsymbol{x}_1)\rho_1(\boldsymbol{x}_2) + g(\boldsymbol{x}_1, \boldsymbol{x}_2)$, where g is the pair correlation function. Then (9.19) can be rewritten as the *collisional Boltzmann equation* [43],

$$\frac{\partial \rho_1}{\partial t} + \boldsymbol{v}_1 \cdot \nabla_{\boldsymbol{r}_1} \rho_1 + \frac{\boldsymbol{F}}{m} \cdot \nabla_{\boldsymbol{v}_1} \rho_1 = \left(\frac{\partial \rho_1}{\partial t} \right)_c \, , \tag{9.20}$$

where $\boldsymbol{F}$ is the force experienced by one electron due to all the other electrons plus the force due to the applied electric field, and

$$\left(\frac{\partial \rho_1}{\partial t} \right)_c = \frac{1}{m} \int \nabla_{\boldsymbol{r}_1} \Phi_{1,2}(\boldsymbol{r}_1, \boldsymbol{r}_2) \cdot \nabla_{\boldsymbol{v}_1} g(\boldsymbol{x}_1, \boldsymbol{x}_2) d^6 \boldsymbol{x}_2 \tag{9.21}$$

is the *collision term* or *collision integral*. These equations as such are of little practical use since the collision integral is unspecified. Various approximations for this term have been suggested. For example, Boltzmann suggested to include solely two-body collisions, and assumed that colliding particles are uncorrelated before collisions. In this *molecular chaos assumption*, the collision integral can be written as an integral over products of one-particle distribution functions.

For uncorrelated particles, the pair correlation function vanishes, that is $g = 0$. In this case, $(\partial \rho_1 / \partial t)_c = 0$, and (9.21) simplifies to the *Vlasov equation* (*collisionless*

Boltzmann equation),

$$\frac{\partial \rho_1}{\partial t} + \boldsymbol{v}_1 \cdot \nabla_{r_1} \rho_1 + \frac{\boldsymbol{F}}{m} \cdot \nabla_{x_1} \rho_1 = 0 \,. \tag{9.22}$$

9.3.1.5 Fokker–Planck Equation

In the case of an ideal plasma with a large number of particles in the Debye sphere, small-angle scattering collisions dominate. The evolution of such a system can be described using the *Fokker–Planck equation*. The Fokker–Planck equation resembles a Taylor expansion of a continuity equation for small-deflection collisions in velocity space. It is a limiting form of the Liouville equation for long-range (Coulomb) forces [40]. The Fokker–Planck equation solves the many-body problem of elastic Coulomb collisions of electron and ion gases. Because of long-range interaction of $1/r$ potentials, more distant particles have to be considered in collisions, and each electron is always interacting with multiple electrons and ions simultaneously. Therefore, frequent distant collisions with small deflections dominate over single encounters with large deflections. In this regime, the usual assumptions made in solving the Boltzmann equation are invalid, and the Fokker–Planck equation should be used instead.

We closely follow the derivation given by Max Planck [47]. We consider a system of particles with velocity vectors $\boldsymbol{v}$. Assuming there exists a process leading to small changes $\Delta\boldsymbol{v}$, we can introduce a transition probability $\Psi(\boldsymbol{v}, \Delta\boldsymbol{v})$ as the probability of changing particle position from $\boldsymbol{v}$ to $\boldsymbol{v} + \Delta\boldsymbol{v}$. Ψ is not explicitly time-dependent but may depend on the instantaneous particle distribution. Let $f(\boldsymbol{v})$ be the velocity distribution function so that $f(\boldsymbol{v})d^3\boldsymbol{v}$ is the probability of finding a particle with a velocity within the volume element $d^3\boldsymbol{v}$ around $\boldsymbol{v}$. It then follows that

$$f(\boldsymbol{v}, t) = \int f(\boldsymbol{v} - \Delta\boldsymbol{v}, t - \Delta t)\Psi(\boldsymbol{v} - \Delta\boldsymbol{v}, \Delta\boldsymbol{v})d^3\Delta\boldsymbol{v} \,. \tag{9.23}$$

The Fokker–Planck equation then describes the evolution of f due to changes described by Ψ, assuming that $\Delta\boldsymbol{v}$ is small, so that

$$\Delta\boldsymbol{v} \cdot \frac{1}{f}\frac{\partial f}{\partial \boldsymbol{v}} \ll 1 \quad \text{and} \tag{9.24}$$

$$\Delta\boldsymbol{v} \cdot \frac{1}{\Psi}\frac{\partial \Psi}{\partial \boldsymbol{v}} \ll 1 \,, \tag{9.25}$$

given that the time interval for these changes Δt is short, that is

$$\Delta t \cdot \frac{1}{f}\frac{\partial f}{\partial t} \ll 1 \,. \tag{9.26}$$

Using a Taylor expansion of f and Ψ, (9.23) can be rewritten as the *Fokker–Planck equation*,

$$\frac{\partial f}{\partial t} = -\frac{\partial}{\partial \boldsymbol{v}} \cdot \left[\langle \Delta\boldsymbol{v} \rangle \, f\right] + \frac{1}{2}\frac{\partial^2}{\partial \boldsymbol{v}\boldsymbol{v}} : \left[\langle \Delta\boldsymbol{v}\Delta\boldsymbol{v} \rangle \, f\right] \tag{9.27}$$

$$= -\sum_i \frac{\partial}{\partial v_i} \langle \Delta v_i \rangle \, f + \frac{1}{2} \sum_{i,j} \frac{\partial^2}{\partial v_i \partial v_j} \langle \Delta v_i v_j \rangle \, f \, , \tag{9.28}$$

with

$$\langle \Delta \boldsymbol{v} \rangle = \frac{1}{\Delta t} \int \Delta \boldsymbol{v} \, \Psi(\boldsymbol{v}, \Delta \boldsymbol{v}) d^3 \Delta \boldsymbol{v} \, , \tag{9.29}$$

$$\langle \Delta v_i \rangle = \frac{1}{\Delta t} \int \Delta v_i \, \Psi(\boldsymbol{v}, \Delta \boldsymbol{v}) d^3 \Delta \boldsymbol{v} \, , \tag{9.30}$$

$$\langle \Delta \boldsymbol{v} \Delta \boldsymbol{v} \rangle = \frac{1}{\Delta t} \int \Delta \boldsymbol{v} \Delta \boldsymbol{v} \, \Psi(\boldsymbol{v}, \Delta \boldsymbol{v}) d^3 \Delta \boldsymbol{v} \, , \quad \text{and} \tag{9.31}$$

$$\langle \Delta v_i \Delta v_j \rangle = \frac{1}{\Delta t} \int \Delta v_i \Delta v_j \, \Psi(\boldsymbol{v}, \Delta \boldsymbol{v}) d^3 \Delta \boldsymbol{v} \, . \tag{9.32}$$

The colon in (9.27) refers to a double contraction with the diffusion tensor. Equation 9.27 describes the evolution of the distribution function f under the action of a process described by the function Ψ in the form of a convection, the first term in (9.27), and a dispersion, the second term in (9.27), in the vector $\boldsymbol{v}$.

In order to solve (9.27), a physical model for the microscopic processes needs to be constructed. Making some assumptions about the distributions over all initial conditions, since the exact initial status is unknown, a transition probability Ψ is calculated. Then, it is straight-forward to solve the Fokker–Planck equation. For plasmas with a large number of particles in a Debye sphere, small-angle collisions dominate. A collision operator for this case has been derived by Landau [48]. More detailed information on the Fokker–Planck equation can be found in [40].

9.3.2
Atomic Kinetics

When describing the evolution of x-ray-irradiated materials, the above treatments need to be extended to deal with the time dependence of the populations of electrons and ions in their different ionization states. In principle, this extension to multicomponent plasmas is straight-forward. Atomic kinetics is implemented by calculating the transition rates and the evolution of the atomic populations through atomic rate equations. For example, these rates may be included in the two-body collision terms in (9.20) and (9.21). Often, forward rates such as excitation and ionization are calculated from atomic models, and the rates for the inverse processes are obtained from detailed balance relations.

9.3.3
Using Statistical Kinetics Models to Describe X-Ray–Matter Interaction

Ziaja *et al.* [3] suggested a model to describe short-pulse x-ray radiation damage in spherical particles by using the Boltzmann equation. A typical application for this

model is the evolution of clusters irradiated by x-ray free-electron-laser light. X-ray free-electron lasers generate relatively cold, strongly coupled electron plasmas, for which plasma screening is important since it lowers ionization potentials and leads to modifications of the interaction cross sections, as discussed in Section 2.3. Since full *ab initio* calculations in strongly coupled plasmas are not available yet [49], various approximate theoretical models have been proposed instead [38, 39]. The estimates of plasma effects in these models vary significantly [39].

Ziaja's model is computationally efficient and also applies to large nonuniform samples. It uses the Boltzmann equation with the Boltzmann two-body collision term, and so it is limited to systems that fulfill the molecular-chaos and two-body-collision assumptions. It only deals with the single-particle density function. Extending the model to include three-body or higher correlations will require using the more fundamental Liouville equation. The model works well in the classical weak-coupling limit. For computational reasons, the long-term evolution of the sample is modeled by taking the hydrodynamic semiequilibrium limit discussed in Section 9.4.

Using Debye cutoffs in the Rutherford cross sections, long-range interaction of electrons and ions can be correctly described with the two-body Boltzmann collision terms. Electron–electron interactions are not described [40] but may be included using the Fokker–Planck equation [39].

The model uses the collision term also as a source/sink operator, so it describes change in charge density due to interparticle collisions or other short-range processes. It does not consider the photon gas but only a photoionization source term. Other source terms that are included are (i) the creation of secondary electrons and highly charged ions via photo- and collisional ionizations of atoms and ions, (ii) elastic and inelastic collisions of electrons and ions, (iii) the inverse bremsstrahlung process, that is absorptions and emissions of photons by electrons during the elastic electron–ion collisions, (iv) recombination processes, (v) three-body recombination processes, and (vi) short-range electron–electron interactions. The number of short-range processes effectively involved in the sample dynamics depends on the wavelength of the laser radiation.

9.4
Hydrodynamic Models

9.4.1
Fluid Models

Fluid models are generally useful for studying longer time scales and larger systems, when the velocity distributions for each species are close to Maxwellian. The moments of the kinetic equations lead to a hierarchy of equations for mass, momentum, and energy conservation. These moments are obtained by multiplying the Boltzmann equation (9.21) by polynomials in $\boldsymbol{v}_1$ and integrating over $\boldsymbol{v}_1$. We extend the treatment now to multiple atomic species α, for example electrons and

ions. ρ_α is the one-particle distribution function of species α. It can be shown that collisional-conservation equations hold [43],

$$\int \left(\frac{\partial \rho_\alpha}{\partial t}\right)_c d^3\boldsymbol{v} = 0 \tag{9.33}$$

$$\sum_\alpha m_\alpha \int \boldsymbol{v} \left(\frac{\partial \rho_\alpha}{\partial t}\right)_c d^3\boldsymbol{v} = 0 \tag{9.34}$$

$$\sum_\alpha \frac{m_\alpha}{2} \int \boldsymbol{v}\cdot\boldsymbol{v} \left(\frac{\partial \rho_\alpha}{\partial t}\right)_c d^3\boldsymbol{v} = 0. \tag{9.35}$$

We define the number density n_α as

$$n_\alpha(\boldsymbol{r}, t) = \int \rho_\alpha(\boldsymbol{r}, \boldsymbol{v}, t) d^3\boldsymbol{v} \tag{9.36}$$

and the flow velocity $\boldsymbol{u}_\alpha(\boldsymbol{r}, t) = (u_\alpha^{(1)}, u_\alpha^{(2)}, u_\alpha^{(3)})$ as

$$u_\alpha(\boldsymbol{r}, t) = \frac{1}{n_\alpha(\boldsymbol{r}, t)} \int \boldsymbol{v}\rho_\alpha(\boldsymbol{r}, \boldsymbol{v}, t) d^3\boldsymbol{v} \ . \tag{9.37}$$

Then we can derive continuity equations from the conservation (9.33) to (9.35) [43],

$$0 = \frac{\partial n_\alpha}{\partial t} + \nabla\cdot(n_\alpha \boldsymbol{u}_\alpha) \tag{9.38}$$

$$R_\alpha^{(i)} = \frac{\partial n_\alpha m_\alpha u_\alpha^{(i)}}{\partial t} + \frac{\partial}{\partial r_j}\left[m_\alpha n_\alpha u_\alpha^{(i)} u_\alpha^{(j)} + n_\alpha T_\alpha \delta_{i,j} + \Pi_\alpha^{(i,j)}\right] - e_\alpha n_\alpha E^{(i)} \tag{9.39}$$

$$\frac{2}{3} Q_\alpha = n_\alpha \frac{\partial T_\alpha}{\partial t} + n_\alpha \boldsymbol{u}_\alpha\cdot\nabla T_\alpha + \frac{2}{3} n_\alpha T_\alpha \nabla\cdot\boldsymbol{u}_\alpha + \frac{2}{3}\Pi_\alpha^{(i,j)} \frac{\partial u_\alpha^{(i)}}{\partial r_j} + \frac{2}{3}\nabla\cdot\boldsymbol{q}_\alpha \ , \tag{9.40}$$

where T_α is the particle temperature, $\boldsymbol{E} = [E^{(1)}, E^{(2)}, E^{(3)}]$ is the local electric field, and e_α is the charge of species α. The rate of momentum transfer from other species to species α is

$$\boldsymbol{R}_\alpha = m_\alpha \int \boldsymbol{v} \left(\frac{\partial \rho_\alpha}{\partial t}\right)_c d^3\boldsymbol{v} \ , \tag{9.41}$$

and the rate of transfer of thermal energy is

$$Q_\alpha = \frac{m_\alpha}{2} \int |\boldsymbol{v} - \boldsymbol{u}_\alpha|^2 \left(\frac{\partial \rho_\alpha}{\partial t}\right)_c d^3\boldsymbol{v} \ . \tag{9.42}$$

The thermal energy flux vector is given by

$$\boldsymbol{q}_\alpha(\boldsymbol{r}, t) = \frac{m_\alpha}{2} \int |\boldsymbol{c}_\alpha|^2 \boldsymbol{c}_\alpha \rho_\alpha(\boldsymbol{r}, \boldsymbol{v}, t) d\boldsymbol{v} \ , \tag{9.43}$$

with the thermal velocity

$$\boldsymbol{c}_\alpha = \left[c_\alpha^{(1)}, c_\alpha^{(2)}, c_\alpha^{(3)}\right] = \boldsymbol{v} - \boldsymbol{u}_\alpha \ . \tag{9.44}$$

Finally,

$$\Pi_\alpha^{(i,j)} = m_\alpha \int \left[c_\alpha^{(i)} c_\alpha^{(j)} - \frac{1}{3}|\boldsymbol{c}_\alpha|^2 \delta_{i,j}\right] \rho_\alpha d\boldsymbol{v} \tag{9.45}$$

is the pressure tensor.

In the fluid-dynamics description of a plasma, the evolution of the system is described by the hydrodynamic equations, which govern the conservation of particles, momentum, and energy [50, 51] and are given by

$$\frac{D n_\alpha}{D t} = 0 \ , \tag{9.46}$$

$$m_\alpha n_\alpha \frac{D \boldsymbol{u}}{D t} = -\nabla P_\alpha + e_\alpha n_\alpha \boldsymbol{E} + \boldsymbol{R}_\alpha \ , \quad \text{and} \tag{9.47}$$

$$n_\alpha \frac{D E_\alpha}{d t} = -P(\nabla \cdot \boldsymbol{u}) - \nabla \cdot \boldsymbol{q} + Q_0 \ , \tag{9.48}$$

where

$$\frac{D}{d t} = \frac{\partial}{\partial t} + \boldsymbol{u} \cdot \nabla \tag{9.49}$$

is the *material derivative* which is the derivative taken along the path of a fluid element moving with velocity $\boldsymbol{u}$. The meaning of the material derivative can most easily be explained in the integral form. Consider the integral of a quantity $A(\boldsymbol{r}, t)$ over a fluid element of volume V,

$$I = \int_V A(\boldsymbol{r}, t) d^3\boldsymbol{r} \ . \tag{9.50}$$

We can calculate the change in value of I for an observer moving with the fluid element as

$$\frac{D I}{D t} = \lim_{\Delta t \to 0} \frac{1}{\Delta t} \left[\int_{V'} A(\boldsymbol{r}', t + d t) d^3\boldsymbol{r}' - \int_V A(\boldsymbol{r}, t) d^3\boldsymbol{r}\right] \ . \tag{9.51}$$

As sketched in Figure 9.4, there are two contributions to (9.51): One stems from the region V_0 that V and V' have in common, given by

$$\int_{V_0} \frac{\partial A}{\partial t} d^3\boldsymbol{r} \ , \tag{9.52}$$

and the other stems from the surface S of V that sweeps over a volume V_1, which using Gauss' law can be written as

$$\int_{V_0} \nabla(A\boldsymbol{v}) d^3\boldsymbol{r} \ , \tag{9.53}$$

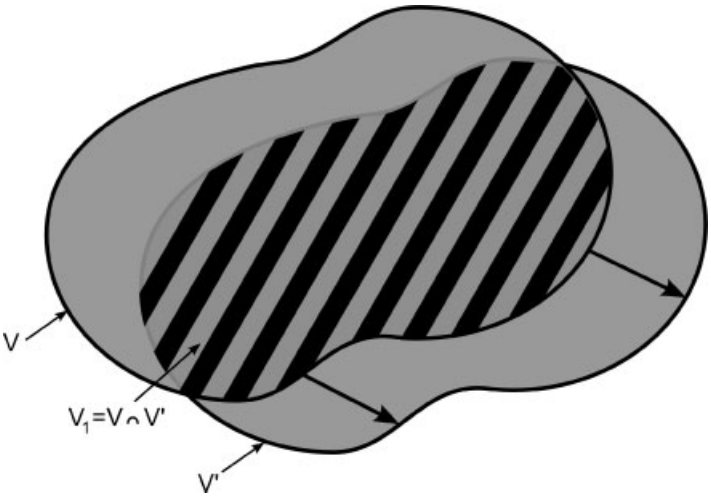

Figure 9.4 Change of a region V during the motion of a fluid element.

so that we can rewrite (9.51) as

$$\frac{D}{Dt}\int_V A(\boldsymbol{r},t)\,d^3\boldsymbol{r} = \int_V \left[\frac{\partial A}{\partial t} + \nabla(\boldsymbol{v}A)\right] d^3\boldsymbol{r}\,. \tag{9.54}$$

Considering an infinitesimal V we obtain

$$\frac{D}{Dt}A(\boldsymbol{r},t) = \left[\frac{\partial A}{\partial t} + \nabla(\boldsymbol{v}A)\right] \tag{9.55}$$

for the material derivative of A.

In (9.48), P_α is the partial pressure of species α, $\boldsymbol{E}$ is the electric field, E_α is the total energy of species α. Equations 9.46–9.48 are related to (9.38) to (9.40), with the simplifying assumptions that the effects of viscosity and surface tension are negligible. For a partially ionized plasma, the species α can be electrons and the ions in their different ionization states. In this case additional source/sink terms can be added to (9.46) to (9.48) to describe atomic ionization and recombination processes.

Solving (9.46) to (9.48) requires an equation of state (EOS) that relates the energy E_α, the pressure P_α, the particle density n_α, and the temperature T_α, which enters through the expressions of the heat conduction $\boldsymbol{q}_\alpha$ and the terms Q_α that describe the e^-/ion and ion/ion interaction. Besides the EOS, we also need models for $\boldsymbol{q}_\alpha$ and Q_α that are consistent with the EOS. Since often a large range of density and temperatures and different phases are encountered, global EOS are usually formed by combining different theoretical models valid in different regimes, with ad-hoc interpolation in-between. Nowadays, EOS are often given in the form of lookup tables, for example SESAME EOS [52], and usually also provide consistent opacity and conductivity data.

9.4.2
Using Hydrodynamic Models to Describe X-Ray–Matter Interaction

Hydrodynamic models have been useful to describe the long-term evolution of x-ray-irradiated materials. Such continuum dynamics (or hydrodynamic) methods are applicable once the electrons are thermalized. By including material strength that allows for tensile stresses in the materials, which is usually done via the EOS, continuum models can also be used to describe stress waves and the resultant processes such as melting, shear, spallation fracture, and cracking, see for example [53, 54].

As a specific example, we now consider the long-term evolution of an x-ray-irradiated semi-infinite aluminum solid. The x-ray energy is 2 keV. We assume that the x-ray beam diameter is much larger than the x-ray penetration depth, so that a one-dimensional treatment is sufficient. We further assume that the pulse duration is much shorter than hydrodynamic time scales which are on the order of picoseconds. Our treatment is similar to the one presented by London *et al*. [55] for Si mirrors exposed to x-ray free-electron-laser radiation. The deposition of the radiation energy leads to heating of the material. The heated material tries to expand, but is confined by its inertia and the surrounding material, leading to a high pressure state. This high pressure region launches stress waves that are directed into the material and toward the front surface. The wave directed toward the front surface is reflected with a reversal in the sign of the pressure, leading to the bipolar wave as shown in Figure 9.5. The stress wave then propagates into the material, leaving behind a long-lasting thermal expansion at the surface. Within tens of nanoseconds, heat conduction leads to a relaxation of the temperature and pressure. The tensile component of the stress wave can lead to spallation of the material if the magnitude of the stress is greater than the spall strength, which is about 80 kbar in Al for short pulses [56]. Note that the temperature may be larger than the melting temperature which could lead to surface ripples upon refreezing. This effect is not included in our simulations. Also, at even higher fluences, gas phase ablation would occur, see Section 8.4.

Numerous simulation codes have been proposed to model x-ray-induced evaporation. As an example, we will discuss the ABLATOR model [57–59] which has been applied successfully to inertial confinement fusion and ablation applications. For computational purposes, the material is divided up into zones. The energy deposition of the x rays occurs within a thin surface layer. The energy is deposited into separate electron energy bins within each zone. A transient thermal conduction model is required to describe the evolution of strongly heated surface layers. The internal energy in each zone is tracked. The temperature of each zone depends on the phase (solid, liquid, or vapor), and is a function of the enthalpy. For the heat conduction, a simple Fourier model is used with a temperature-dependent thermal conductivity. Thermal expansion leads to a hydrodynamic motion of the zone. Using the zone energy, its density, and the EOS, the pressure and stress in each zone is calculated. In ABLATOR, a simple Mie–Gruneisen EOS is used for the solid and liquid phase [60], and an ideal gas EOS for the vapor. The zones are moved

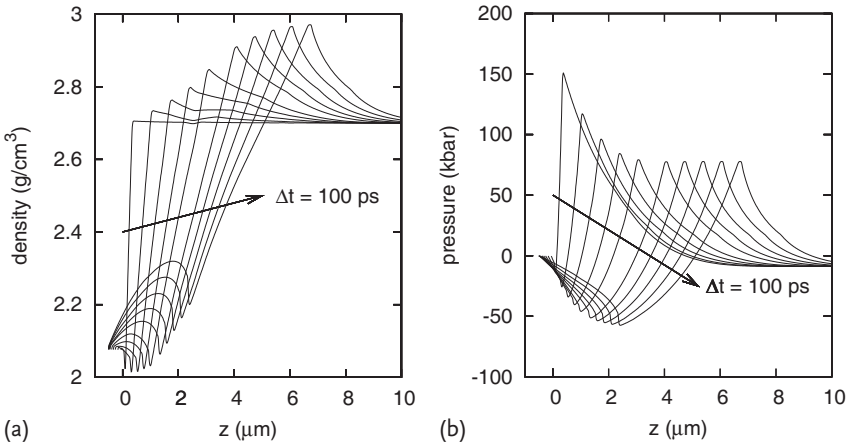

Figure 9.5 (a,b) Response of an aluminum solid to a 2-keV x-ray pulse with 2 J/cm^2. At $t = 0$, there is vacuum for $z < 0$ and aluminum at $z \geq 0$.

according to the total forces. The removal of evaporated material is modeled using kinetically limited surface vaporization. The evaporation rate is governed by the maximum flux of atoms per unit area that would occur under equilibrium between the vapor and the liquid, given by the *Langmuir free evaporation equation* [61]

$$flux = P_{sat} \frac{1}{\sqrt{2\pi m k T}} \,. \tag{9.56}$$

The flux increases exponentially with the surface temperature since it depends on the saturated vapor pressure P_{sat}. Unlike other models that are based on instantaneous energy deposition and instantaneous vaporization, no single boiling temperature is used. In this model, recondensation is neglected, which is usually a reasonable assumption in vacuum.

As an exception to the general trend of applying hydrodynamic models to specifically larger systems and for problems with longer time scales, a hydrodynamic model has been proposed recently to predict the interaction of short x-ray pulses with biological molecules [2]. In this two-fluid electron–ion model, the fluids interact through Coulomb forces, and the electrons are assumed to have equilibrated among themselves. The model does not assume local charge neutrality, and electrons can be found in three different states, bound, quasi-free, and free. This model can be applied to describe the evolution of nanoparticles exposed to x-ray free-electron-laser radiation, see Section 10.3.

References

1 Glosli, J.N., Graziani, F.R., More, R.M., Murillo, M.S., Streitz, F.H., Surh, M.P., Benedict, L.X., Hau-Riege, S., Langdon, A.B., and London, R.A. (2008) Molecular dynamics simulations of temperature equilibration in dense hydrogen. *Phys. Rev. E*, **78**, 025401.

2 Hau-Riege, S.P., London, R.A., and Szoke, A. (2004) Dynamics of biological molecules irradiated by short x-ray pulses. *Phys. Rev. E*, **69**, 051906.

3 Ziaja, B., de Castro, A.R.B., Weckert, E., and Möller, T. (2006) Modelling dynamics of samples exposed to free-electron-laser radiation with Boltzmann equations. *Eur. Phys. J. D*, **40**, 465–480.

4 Ingles, D.R. and Teller, E. (1939) Ionic depression of series limits in one-electron spectra. *Astrophys. J.*, **90**, 439–448.

5 Romanovsky, M.Y. and Ebeling, W. (2006) Elementary many-particle processes in plasma microfields. *Contrib. Plasma Phys.*, **46**, 195–260.

6 Runge, E. and Gross, E.K.U. (1984) Density-functional theory for time-dependent systems. *Phys. Rev. Lett.*, **52**, 997–1000.

7 Rusek, M., Lagadec, H., and Blenski, T. (2001) Cluster explosion in an intense laser pulse: Thomas–Fermi model. *Phys. Rev. A*, **63**, 013203.

8 Gross, E.K.U. and Kohn, W. (1990) Time-dependent density functional theory. In *Advances in Quantum Chemistry*, **21**, 255.

9 Bergh, M., Timneanu, N., and van der Spoel, D. (2004) Model for the dynamics of a water cluster in an x-ray free electron laser beam. *Phys. Rev. E*, **70**, 051904.

10 Gnodtke, C., Saalmann, U., and Rost, J.M. (2009) Ionization and charge migration through strong internal fields in clusters exposed to intense x-ray pulses. *Phys. Rev. A*, **79**, 041201(R).

11 Jurek, Z., Faigel, G., and Tegze, M. Dynamics in a cluster under the influence of intense femtosecond hard x-ray pulses. *Eur. Phys. J. D*, **29**, 217–229.

12 Neutze, R., Wouts, R., van der Spoel, D., Weckert, E., and Hajdu, J. (2000) Potential for biomolecular imaging with femtosecond x-ray pulses. *Nature*, **406**, 752–757.

13 Allen, R.E., Dumitrica, T., and Torralva, B. (2001) *Electronic and Structural Response of Materials to Fast Intense Laser Pulses*, Academic Press, New York.

14 Gambirasio, A., Bernasconi, M., and Colombo, L. (2000) Laser-induced melting of silicon: A tight-binding molecular dynamics simulation. *Phys. Rev. B*, **61**, 8233–8237.

15 Jeschke, H.O., Garcia, M.E., and Benneman, K.H. (1999) Theory for laser-induced ultrafast phase transitions in carbon. *Appl. Phys. A*, **69**, S49–S53.

16 Silvestrelli, P.L., Alavi, A., Parrinello, M., and Frenkel, D. (1997) Structural, dynamical and bonding properties of laser-heated silicon: An ab-initio molecular-dynamics study. *Phys. Rev. B*, **56**, 3806–3812.

17 Verlet, L. (1967) Computer "experiments" on classical fluids. I. Thermodynamical properties of Lennard-Jones molecules. *Phys. Rev.*, **159**(1), 98–103.

18 Krishnagopal, S. (1996) Luminosity-limiting coherent phenomena in electron-positron colliders. *Phys. Rev. Lett.*, **76**(2), 235–238.

19 Hockney, R.W. and Eastwood, J.W. (1981) *Computer Simulation Using Particles*, McGraw-Hill, New York.

20 Birdsall, C.K. and Langdon, A.B. (1991) *Plasma physics via computer simulation*. Series on Plasma Physics, Institute of Physics Publishing, Bristol, UK.

21 Appel, A.W. (1985) An efficient program for many-body simulations. *SIAM J. Sci. Stat. Comput.*, **6**, 85–103.

22 Greengard, L. and Rokhlin, V. (1997) A fast algorithm for particle simulations. *J. Comput. Phys.*, **135**, 280–292.

23 Marx, D. and Hutter, J. (2009) *Ab Initio Molecular Dynamics: Basic Theory and Advanced Methods*. Cambridge University Press, Cambridge.

24 Car, R. and Parrinello, M. (1985) Unified approach for molecular dynamics and density-functional theory. *Phys. Rev. Lett.*, **55**, 2471–2474.

25 Alavi, A., Kohanoff, J., Parrinello, M., and Frenkel, D. (1994) Ab initio molecular dynamics with excited electrons. *Phys. Rev. Lett.*, **73**, 2599–2602.

26 Metropolis, N., Rosenbluth, A.W., Rosenbluth, M.N., Teller, A.H., and Teller, E. (1953) Equation of state calculations by fast computing machines. *J. Chem. Phys.*, **21**, 1087–1092.

27 Kahn, H. (1950) Random sampling (Monte Carlo) techniques in neutron attenuation problems–I. *Nucleonics*, **6**, 27–33.

28 Kahn, H. (1950) Random sampling (Monte Carlo) techniques in neutron attenuation problems–II. *Nucleonics*, **6**, 60–65.

29 Joy, D.C. (1995) *Monte Carlo Modeling for Electron Microscopy and Microanalysis*, Oxford University Press, New York.

30 Frenkel, D. and Smit, B. (1996) *Understanding Molecular Simulation, From Algorithms to Applications*. Academic Press, San Diego.

31 Ceperley, D. and Alder, B. (1986) Quantum Monte Carlo. *Science*, **231**, 555–560.

32 Thijssen, J.M. (1999) *Computational Physics*, Cambridge University Press, New York.

33 Battistoni, G., Muraro, S., Sala, P.R., Cerutti, F., Ferrari, A., Roesler, S., Fasso, A., Ranft, J (2007) The FLUKA Code: Description and Benchmarking. *Proceedings of the Hadronic Shower Simulation Workshop 2006, Fermilab 6–8 September 2006* (eds M. Albrow and R. Raja), *AIP Conf. Proc.*, **896**, 31–49.

34 Salvat, F., Fernandez-Varea, J.M., Baro, J., and Sempau, J. (1996) Penelope, an algorithm and computer code for Monte Carlo simulation of electron–photon showers. *Inf. Tec. CIEMAT no. 799* (Madrid: CIEMAT).

35 Sempau, J., Acosta, E., Baro, J., Fernandez-Varea, J.M., and Salvat, F. (1997) An algorithm for Monte Carlo transport. *Nucl. Instrum. Methods B*, **132**, 377–390.

36 Bethe, H. (1930) Zur Theorie des Durchgangs schneller Korpuskularstrahlen durch Materie. *Ann. Phys.*, **397**, 325–400.

37 Joy, D.C. and Luo, S. (1989) An empirical stopping power relationship for low-energy electrons. *Scanning*, **11**, 176–180.

38 Schlanges, M. and Bornath, T. (1993) Ionization and recombination coefficients for a dense nonideal hydrogen plasma: effects of screening and degeneracy. *Physica A*, **192**, 262–279.

39 Weisheit, J.C. and Murillo, M.S. (1998) Dense plasmas, screened interactions, and atomic ionization. *Phys. Rep.*, **302**, 1–65.

40 Sharkofsky, I.P., Johnston, T.W., and Bachynski, M.P. (1966) *The Particle Kinetics of Plasmas*, Addison Wesley Publishing Company, Inc., Reading, MA

41 Ishimaru, S. (2004) *Statistical Plasma Physics, Volume I: Basic Principles*, Westview Press, Boulder, CO.

42 Greiner, W. (2001) *Quantum Mechanics – Special Chapters*, Springer, Berlin.

43 Boyd, T.J.M and Sanderson, J.J. (2003) *Phys. Plasmas*. Cambridge University Press, Cambridge, UK.

44 Bogoliubov, N.N. (1946) Kinetic equations. *J. Exp. Theor. Phys.*, **16**, 691–702.

45 Bogoliubov, N.N. (1946) Kinetic equations. *J. Phys. USSR*, **10**, 265–274.

46 Bogoliubov, N.N. and Gurov, K.P. (1947) Kinetic equations in quantum mechanics. *J. Exp. Theor. Phys.*, **17**, 614–628.

47 Planck, M. (1917) Über einen Satz der statistischen Dynamik und seine Erweiterung in der Quanthentheorie. *Sitzungsberichte der Preussischen Akademie der Wissenschaften*, pp. 324–341.

48 Landau, L.D. (1936) Kinetic equation for the Coulomb effect. *Phys. Z. Sowjetunion*, **10**, 154–341.

49 Kremp, D., Bornath, T., Bonitz, M., Kraeft, W.D., and Schlanges, M. (2000) Quantum kinetic equations for nonideal plasmas: Bound states and ionization kinetics. *Phys. Plasmas*, **7**, 59–67.

50 Zel'dovich, Y.B. and Raizer, Y.P. (1966) *Physics of Shock Waves and High-Temperature Hydrodynamic Phenomena*, Academic Press, New York.

51 Zimmerman, G.B. (1973) Numerical simulation of the high-density approach to laser fusion. *Tech. Rep. UCRL-74811*.

52 Los Alamos National Laboratory (1992) *SESAME: The Los Alamos National Laboratory Equation of State Database*. http://t1web.lanl.gov/newweb_dir/t1sesame.html. Last access: 30 May 2011.

53 Marinak, M.M., Haan, S.W., Dittrich, T.R., Tipton, R.E., and Zimmerman, G.B. (1998) A comparison of three-dimensional multimode hydrodynamic instability growth on various National Ignition Facility capsule designs with HYDRA simulations. *Phys. Plasmas*, **5**, 1125–1132.

54 Zimmerman, G.B. and Kruer, W.L. (1975) Numerical simulation of laser-initiated fusion. *Comments Plasma Phys. Control. Fusion*, **2**, 51–61.

55 London, R.A., Bionta, R.M., Tatchyn, R.O., and Roesler, S. (2001) Computational simulations of high-intensity x-ray matter interaction. In *Proc. SPIE*, **4500**, 51–62.

56 Moshe, E., Eliezer, S., Henis, Z., Werdiger, M., Dekel, E., Horovitz, Y., Maman, S., Goldberg, I.B., and Eliezer, D. (2000) Experimental measurements of the strength of metals approaching the theoretical limit predicted by the equation of state. *Appl. Phys. Lett.*, **76**, 1555–1557.

57 Anderson, A.T. (1996) X-Ray Ablation Measurements and Modeling for ICF Applications. PhD thesis, University of California at Berkeley.

58 Anderson, A.T., Burnham, A.K., Tobin, M.T., and Peterson, P.F. (1996) Modeling and experiments of x-ray ablation of national ignition facility first wall materials. *Fusion Technol.*, **30**, 757–763.

59 Anderson, A.T. and Peterson, P.F. (1997) Experimental methods for measuring x-ray ablation response of surfaces. *Exp. Heat Transf.*, **10**, 51–65.

60 McQuarrie, D.A. (1976) *Statistical Mechanics*, Harper and Row, New York.

61 The Nobel Foundation (2011) *The Nobel Prize in Chemistry 1932*. http://nobelprize.org/nobel_prizes/chemistry/laureates/1932/langmuir-lecture.html Last access: 30 May 2011.

10
Examples of X-Ray–Matter Interaction

In this chapter we describe some recent examples for x-ray–matter interaction, drawing primarily on recent experimental results obtained at x-ray free-electron-laser facilities. We discuss experimental progress in the field of high-intensity interaction of x rays with atoms, molecules, and clusters. We then discuss short-pulse x-ray imaging in structural biology, which is a new technique that goes beyond protein crystallography described in Section 8.9. Finally, we describe the use of x-ray scattering as a plasma diagnostic, a technique that is especially important for high-density plasmas.

10.1
Interaction of Intense X-Ray Radiation with Atoms and Molecules

In the optical regime, a large variety of interaction processes of photons with atoms and molecules have been observed [1]. Below photon intensities of 10^{12} W/cm^2, the strength of photon–matter interaction is relatively weak, and atoms and molecules absorb single or multiple photons. Close to 10^{12} W/cm^2, molecules can be aligned along the laser polarization direction. Between 10^{14} W/cm^2 and 10^{15} W/cm^2, structural deformation of molecules occurs, and beyond this intensity Coulomb explosions of molecules are observed. Up to 10^{18} W/cm^2, molecules turn into plasmas, and beyond this intensity wakefield effects lead to x-ray emission from molecules.

An in-depth knowledge of the basic atomic physics is required to understand the interaction of *x rays* with matter. Recent high-intensity x-ray sources, such as x-ray free-electron lasers, may enable just that. Ultimately, they will provide the short and energetic x-ray pulses required to enable imaging of the internal dynamics of excited atoms and molecules with high spatial resolution. Early experiments at the LCLS x-ray free-electron laser have been focused on validating basic x-ray–matter interaction models for single atoms and simple molecules. An example is the phenomenon of frustrated absorption: The atomic subshell photoionization cross section is generally largest for inner-shell atomic resonances just below the x-ray photon energy. The subshell ionization cross section of the next atomic shell out is much lower, see Section 2.2.3. If the x-ray intensity is sufficiently large that the atomic inner shell is depleted, the x-ray absorption rate will suddenly drop signif-

High-Intensity X-rays – Interaction with Matter, First Edition. Stefan P. Hau-Riege.

icantly. This phenomenon of frustrated absorption has been demonstrated at the LCLS in puffs of N_2 gas, irradiated with 1100-eV x-ray pulses with pulse lengths between 4 and 300 fs. This x-ray energy is sufficiently large to ionize the *K* shell of nitrogen. For longer pulses, all electrons were stripped from the N_2 since the *K*-shell is replenished with electrons from the *L* shell by Auger decay events, whereas for pulses shorter than the Auger decay time of 6.4 fs (refer to Figure 2.3) electrons remain in the *L* shell [2].

Double core hole production in N_2 was observed through photoelectron spectroscopy and Auger electron spectroscopy [3] at 1.0 and 1.1 keV. Besides shake-up and shake-off Auger signals, Auger hypersatellites [4] were observed, as well [5], and their angular distribution was studied. Double-core holes are rare in single-photon absorption processes [4].

In a similar experiment, the competition between photoionization and Auger decay in Ne has been studied at the LCLS for energies ranging from 0.8 to 2 keV [6]. Depending on the photon energy and the pulse length, the *K* shell of Ne can be singly or doubly ionized. It was found that the time to refill the *K* shell increases with x-ray energy, which may be due to the ejection of *L*-shell electrons during complex shake-off and double Auger processes [6–8].

10.2
Interaction of Intense X-Ray Pulses with Atomic Clusters

Atomic clusters are groups of atoms that are bound together by interatomic forces, including van de Waals forces, metallic bonds, and covalent bonds. Atomic clusters can be created by expanding a noble[1)] or other gases adiabatically [9]. It has been found that for each atomic element, clusters with a certain number of atoms are particularly stable. These numbers of atoms are referred to as the cluster magic numbers, and relate directly to the electronic and ionic structure of the cluster [10]. Atomic clusters are distinct from single atoms and the solid state, and exhibit special chemical and physical properties [11, 12].

Clusters present a very useful model system to study x-ray–matter interaction since they have bulk densities, which makes them relevant to understanding solid behavior, and energy does not dissipate, thereby simplifying the interpretation of experimental results. Particularly interesting aspects of clusters include the interplay of inter- and intra-atomic effects, the details of photon absorption and atomic ionization, the onset of nonlinear and multiphoton processes, and the time scales relevant for electron emission and atomic motion.

Even though the details of the photon–cluster interaction processes depend on the wavelength of the incident light, some general statements about their behavior can be made. When an intense light source, such as a free-electron laser, irradiates atomic clusters, the atoms in the clusters are ionized, and the cluster is in a highly nonequilibrium state. Multiple ionizations can lead to very highly charged ions. At

1) Noble gases are helium, neon, argon, krypton, xenon, and radon.

the same time, electrons can escape the cluster, thereby charging it up, which eventually leads to sample expansion due to repulsive Coulomb forces. The electrons in the plasma first equilibrate among themselves, followed by a thermalization of the electrons and ions.

Most experiments on high-intensity laser–cluster interactions at short wavelengths have been performed using free-electron-laser radiation in the VUV (vacuum ultraviolet) to soft x-ray regime. Only recently has the interaction of high-intensity hard x-ray radiation with clusters been studied. We will now review and contrast the key experiments in the different wavelength regimes, and discuss the relevant interaction mechanisms.

10.2.1
Interaction of Clusters with High-Intensity 12.7-eV Radiation

The first high-intensity photon–cluster interaction experiment below a wavelength of 100 nm was performed by Wabnitz *et al*. [13–15]. They exposed xenon clusters to 50-fs-long free-electron-laser pulses at 12.7 eV, corresponding to a wavelength of 98 nm, and a power density of up to 10^{14} W/cm^2. It was found that in large clusters, each atom absorbs up to 30 photons, corresponding to an energy of 400 eV. When the electrons have acquired sufficient kinetic energy, they are ejected from the cluster, and, eventually, the cluster undergoes a Coulomb explosion.

It is expected that the 12.7-eV photons interact primarily with the valence electrons of xenon. Even though 12.7 eV is only slightly larger than the 12.1 eV ionization potential, multiply charged xenon ions with energies in the keV range were detected. Also, the absorbed photon energy is nearly one order of magnitude larger than what was predicted by conventional, classical models. On the other hand, single, isolated atoms were only singly ionized by the 12.7-eV photon beam, as expected.

Multiple models have been proposed to explain these at first surprising results. In [16] it was proposed that the 12.7-eV photons ionize the valence electron of xenon, so that a plasma is formed. This plasma leads to a suppression of the interatomic potential barriers in the cluster, and charge-enhanced ionization takes place. In [17] it was proposed that the cluster plasma is heated through inverse Bremsstrahlung absorption, and that the inverses Bremsstrahlung absorption rates are enhanced due to the close proximity of the electrons to the nuclei. In [17] this is treated with effective atomic potentials. The high charge states are then produced by collisional ionization. Finally, in [18] it was proposed that the quasi-free electrons are heated through many-body recombination, and that high-charged states are then produced during collisional ionization.

Ziaja *et al*. [19] combined these models into a single continuum model, which is described in Section 9.3.3. They found that the highly charged ions originate from the outer cluster shell, and that the ions within the cluster predominantly recombine with the plasma electrons. The concept of intense heating of the quasi-free electrons agrees with the measured electron emission spectra [20].

10.2.2
Interaction of Clusters with High-Intensity 40- to 100-eV Radiation

Whereas at 12.7-eV photon energy the electron and photons interact only with the valence electrons, at 40 eV and higher both valence and inner-shell electrons contribute to the cluster dynamics. Because of the larger photon energy, radiation absorption occurs through sequential photoionization steps, whereas plasma heating through inverse Bremsstrahlung as well as thermionic electron emission is negligible [20, 21].

At 100 eV, energy absorption occurs mainly through atomic inner-shell photoionization. This has been demonstrated in [22] for flux densities of 10^{14} W/cm^2. The photoelectrons are trapped by the Coulomb potential of the cluster, and highly nonequilibrium plasmas are created.

Surface doping of clusters is possible by having a cluster jet cross an atomic beam. By co-expanding gas mixtures of various concentrations into vacuum, volume-doped clusters can be created [23]. For an argon gas with a 1–5% xenon concentration, xenon nucleates inside argon clusters, forming core-shell systems,

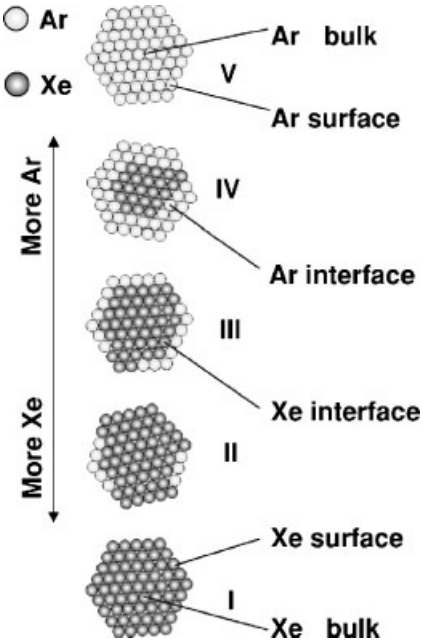

Figure 10.1 A schematic illustration of the structural development of the Ar/Xe clusters, from pure Xe (I) to pure Ar (V). In cases II and III, there are, in addition to the Xe surface and bulk atoms, Ar atoms sitting on the surface coordinated with Xe and Xe atoms sitting in the bulk coordinated to the surface Ar atoms, forming an interface layer. In case IV, with more Ar, there will in addition be Ar surface atoms coordinated to Ar, as in a pure Ar cluster. Reprinted figure with permission from [24]. Copyright (2004) by the American Physical Society.

since argon and xenon phase-separate due to different cohesive energies and melting points [24]. A schematic of the dependence of the cluster formation on the xenon concentration is shown in Figure 10.1. These core-shell systems exhibit efficient charge redistribution, leading to a Coulomb explosion of the outer part of the cluster, whereas the inner part of the cluster tends to be neutral and less ionized due to recombination processes. Therefore, the core expands hydrodynamically, that is on a longer time scale. Since charge trapping is involved, these processes show a strong cluster size effect [25], as discussed in Section 5.8.1.

Even though direct multiphoton processes have a very small cross section in the 100-eV photon regime, and sequential ionization dominates, it was observed that relatively fast electrons are emitted from xenon clusters [26]. This is consistent with an electron-equilibration process through multiple energy-exchanging collisions that produces electrons with kinetic energies well beyond the dominant photo electron energy for atomic xenon. These fast electrons then leave the cluster. This phenomenon is expected to be rather general and occurs whenever a large number of photons are absorbed. In the case reported in [26], xenon has unusually large photo cross sections associated with the electrons in the 4d shell, leading to a large density of quasi-free electrons.

10.2.3
Interaction of Clusters with High-Intensity Hard X-Ray Radiation

Experimental observations of the interaction of high-intensity photon radiation with clusters in the 0.2- to 12-keV hard x-ray regime are just starting to become available. Both intra- and interatomic processes are expected to be of relevance. The intra-atomic processes are local interactions such as inner-shell photoionization and Auger decay of excited atoms. The effect of the cluster environment on these processes is not very well understood yet. In a theoretical study it has been suggested that the delocalization of valence states in a plasma, as for example for argon clusters irradiated by 350-eV x rays, affects photoionization and Auger decay processes since the electron–hole overlap is reduced [27]. The interatomic processes are strongly effected by the cluster environment and include secondary ionization processes such as electron impact ionization and field ionization, as well as plasma dynamics such as electron–electron and electron–ion equilibration processes, charge screening, and charge emission.

The dynamic of hard-x-ray-irradiated clusters is strongly affected by the escape of high-energy photo and Auger electrons. As discussed in Section 5.8.1, electrons with large kinetic energy can escape the cluster until the electrostatic field associated with the positive charge that is left behind is sufficiently large to hold the electrons back. Figure 10.2 shows the average number of electrons per ion that have to escape from the cluster in order for 12-keV and 250-eV electrons to be trapped. These kinetic energies correspond to typical kinetic energies of photo and Auger electrons, respectively, in low-Z clusters irradiated by hard x-ray free-electron-laser radiation. As pointed out in [28], the quasi-static electric fields in these clusters are so large that the ionization barriers in the atoms are suppressed and over-the-

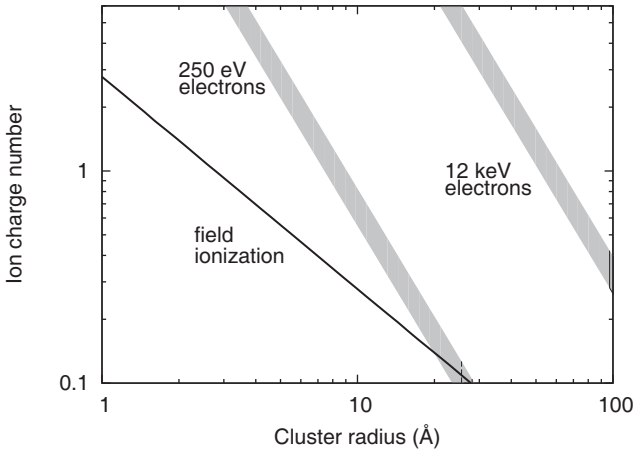

Figure 10.2 Average number of electrons per ion that have to escape from a cluster in order for 12-keV and 250-eV electrons to be trapped. In these estimates we assumed a carbon cluster with a density of 1.3 g/cm^3. Also shown in this figure is the average number of escaped electrons per ion that is required for field-ionization of a neutral carbon ion to occur at the cluster surface. This figure is based on [28].

barrier ionization occurs. In the simple model of an electron in an effective potential created by the Coulomb field of the atom core and the external electric field, the field strength for this field ionization can be estimated using Bethe's rule

$$E_{crit} = \frac{\pi\epsilon_0 I_B^2}{Ze^3} , \tag{10.1}$$

where I_B is the ionization potential for an ion with charge $Z-1$ [29]. The field at the surface of a homogeneously charged sphere can be derived from (5.50) as

$$E(r_0) = -\frac{\rho_c}{3\epsilon_0} r_0 , \tag{10.2}$$

were ρ_c is the charge density and r_0 is the cluster radius. The degree of ionization required for field ionization to occur is relatively low, as shown in Figure 10.2 for a carbon cluster. Field ionization due to the strong internal electric fields leads to charging of the surface layer and screening of the atoms in the center of the cluster.

Considering the effect of field ionization, the high-intensity hard x-ray interaction process with clusters will probably occur in the following manner [28]: First, the inner shells of atoms are photoionized, and the photoelectrons will escape. The ion charge that is left behind creates a large electric field, especially at the cluster surface, that leads to field ionization. The electrons that are released are of relatively low kinetic energy and are trapped, so that a plasma is created. For sufficiently large clusters, Auger and photoelectrons are trapped, as well. The electrons shield the core of the cluster, and the highly charged outer shell Coulomb explodes.

10.3 Biological Imaging

Light imaging has proven to be essential for centuries and is still one of the most powerful experimental tools in biology today. For example, in the nineteenth century, visible light provided a morphological description of the complex response of living systems to real-time perturbations. In the twentieth century, genome sequencing had a major impact, but it has lacked three-dimensional spatial and time resolution. It is anticipated that the challenge for the twenty-first century is the development of an understanding of the structure and the dynamics of biochemical molecules, signals, and processes, which requires an atomic-resolution time-resolved imaging technique. Candidates include electron tomography, which has a somewhat limited temporal resolution, and coherent x-ray diffractive imaging that potentially offers atomic-resolution imaging with fs time resolution.

X-ray crystallography is the workhorse in structural biology. Currently, 80% of the biological structures have been determined using this technique. Most of the remaining structures have been determined by nuclear magnetic resonance (NMR), which is limited to relatively small molecules. Cryogenic electron microscopy is rapidly developing, and recently 7-Å resolution has been achieved in a virus particle [30].

In conventional x-ray crystallography, the resolution of biological macromolecules such as proteins and viruses is limited only by the x-ray wavelength and the quality of the crystal. Often, biological macromolecules are difficult to crystallize, so that large systematic gaps exist in the database of protein structures. For example, membrane proteins, a class of molecules important in many areas of life sciences including drug development, are strongly under-represented. The hope is that the enormous peak brightness of x-ray free-electron lasers may enable imaging of single particles, such as biological macromolecules, at atomic resolution and with unprecedented time resolution without the need for crystallization, since x-ray free-electron lasers make it possible to obtain a reasonably strong scattering signal even from weak scatterers.

10.3.1 Image Formation

In the simplest scenario, a plane wave of x rays illuminates an object, and the intensity distribution of the scattered light is measured in the far-field, that is at distances where the angular intensity distribution is independent of the distance from the object. The elastically scattered light signal is used to reconstruct the electron density in the sample, whereas inelastic scattering contributes to noise and damage in the sample. It has been suggested that 8- to 12-keV x-ray photons are especially suitable since the wavelength around 1 Å is short enough for atomic-resolution imaging, they penetrate objects easily, and the detrimental effect of Compton scattering is still not too big, see Figure 8.19 in Section 8.9. Also, the x-ray energies are much larger than atomic resonances in biological materials, so that the electric

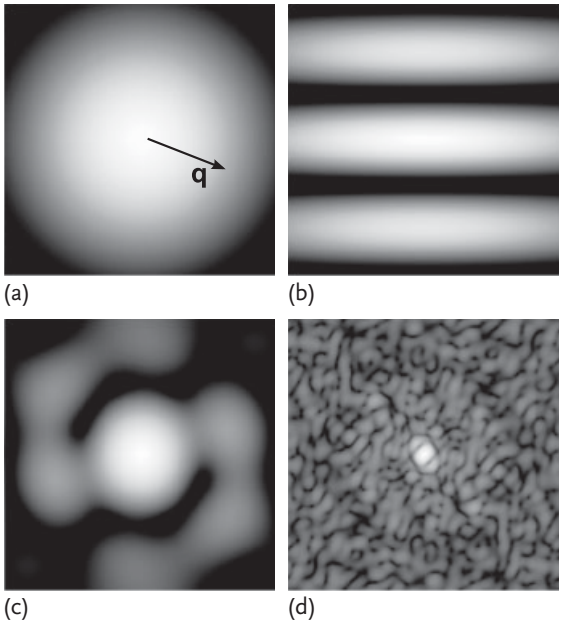

Figure 10.3 Diffraction patterns of (a) a single atom, (b) two atoms, (c) ten atoms, and (d) a protein molecule on a logarithmic intensity scale. The intensity scale is different for each case.

field at the detector simply is proportional to the Fourier transform of the electron density. However, as we will discuss in Section 10.3.2, the detector only measures the amplitude of the electric field and not the phase, so that part of the information is lost.

Figure 10.3 shows the diffraction pattern of a single atom, of a pair of atoms, of a small cluster of atoms, and a full protein molecule. Considering that the plots use a logarithmic intensity scale, it can be seen that the intensity of the diffraction pattern at large scattering angles (large momentum transfer vectors $\boldsymbol{q}$), which encode the high-resolution information, is very weak. A few years ago, it was recognized that x-ray-induced damage prevents conventional imaging of single molecules, so that crystals of molecules were used instead, giving rise to x-ray crystallography. In this case, the radiation dose is spread out over many (on the order of $N \approx 10^{10}$) molecules. Instead of measuring the full diffraction pattern as in Figure 10.3d, in a crystal we only measure the intensity of this pattern in the direction of the Bragg peaks, see (3.94).

10.3.2
Protein X-Ray Crystallography

Protein crystallography takes advantage of the high intensity of the Bragg reflections. As discussed in Section 3.5.1.1 a perfect crystal made up of N unit cells,

the peak intensities of the Bragg reflections are proportional to N^2 and the widths are proportional to $1/N$, so that the integrated intensities are proportional to N. Therefore, for reasonably large crystals, strong signals are observed. However, the information in between the Bragg peaks is lost.

According to the sampling theory, which is based on Shannon's information theorem [31], the accurate reconstruction of a continuous function from a sampled set of discrete data points requires sampling at a frequency that is larger than the Nyquist frequency f_{Nyq}, which is given by the inverse of the sample size. If we sample below the Nyquist frequency, we undersample, information is lost, and errors in the reconstruction occur. The sampling theorem assumes that both the amplitude and the phase are sampled, whereas in x-ray imaging, we usually can measure only the amplitude, corresponding to the intensity, of the diffracted light. In x-ray crystallography, the Bragg peaks are positioned such that we always sample just at the Nyquist frequency [32], so that we do not have sufficient information to reconstruct the electron density. This is the *fundamental phase problem* in crystallography. We can overcome this problem only by making further assumptions about the electron density.

Protein crystallography is typically performed at synchrotron light sources using relatively low fluences, and damage in this case is a cumulative process, as discussed in Section 8.9. Each photoelectron with an energy of about 8 keV disrupts about 70 bonds in a biological crystal on average [33]. It has been found that above a fluence of 160 photons/A^2, permanent damage [34] is observed. In addition, any temperature rise has to be avoided since cells and protein crystals do not tolerate heat. Since in protein crystallography the x-ray dose is shared over all the molecules in the crystal, large crystals allow spreading the x-ray dose over many unit cells.

10.3.3 Coherent Diffractive Imaging

Coherent diffractive imaging can be used to image single particles, for example, single clusters or macromolecules, instead of large periodic arrays, such as crystals. In the simplest scenario, a plan wave irradiates the particles, and the intensity of the scattered light is measured up to an angle θ_{max}, which is related to the image resolution d by

$$d = \frac{\lambda}{\sin(\theta_{max})}, \tag{10.3}$$

where λ is the wavelength of the light. The experimental setup is sketched in Figure 10.4. Since in coherent diffractive imaging we measure the full continuous diffraction pattern and not just at the Bragg peaks, we can sample at frequencies much larger than f_{Nyq}, which helps in compensating for the missing phase information. This concept is called oversampling. Typically, the diffraction pattern is sampled at more than twice the Nyquist frequency [35]. Since we record much finer features of the diffraction pattern, better coherence of the incoming beam is required than for crystallography.

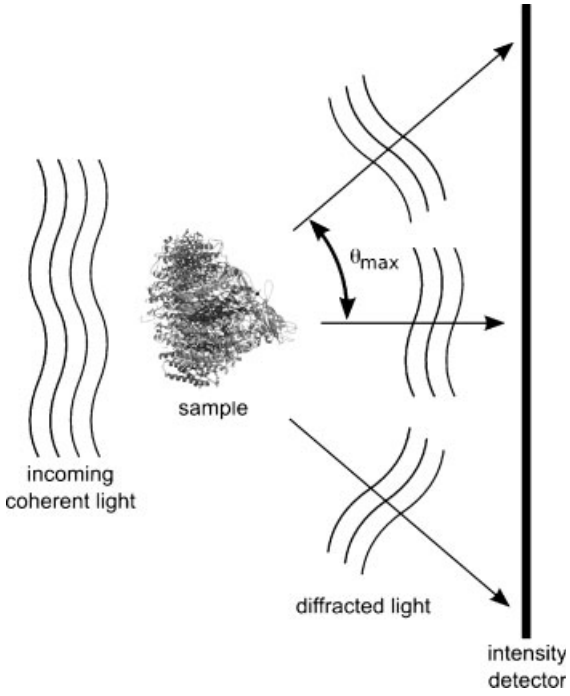

Figure 10.4 Sketch of a typical coherent diffractive imaging setup.

In optical microscopy, a lens is placed behind the sample to recombine the scattered radiation and to form an image on the intensity detector. Since the index of refraction for x rays tends to be very small, appropriate lenses are not available, and we need to use computational phasing algorithms instead to reconstruct the phases. Gerchberg proposed such an algorithm [36], and Fienup extended it to objects of finite size [37], called the hybrid input–output (HIO) algorithm. In these algorithms, a Fourier transform is used to iterate between a representation of the sample's electron density in real and in reciprocal space. Before the transformation, we apply appropriate constraints to the data, for example the measured diffraction intensity in reciprocal space, or certain assumptions about the electron density in real space, such as positivity or a finite volume, sometimes also called support. The HIO algorithm is surprisingly stable and tolerates missing diffraction data very well. Numerous other phasing algorithms have been proposed, including the charge flipping algorithm [38], other iterative phase retrieval algorithms as described in [39], direct methods [40], real-space conjugate-gradient minimization [41], and a shrink-wrap algorithm that adjusts the support dynamically [42, 43].

Since coherent diffractive imaging cannot take advantage of intense Bragg peaks, the signal is significantly lower, and very bright x-ray sources are required to overcome the noise problem. X-ray damage then limits the achievable resolution. For example, the resolution limit for coherent diffraction on biological objects

is around 10 nm at synchrotrons, as has been shown for living cells, even when the sample is chemically fixated or cooled with liquid nitrogen to avoid diffusion and mass loss. This conventional, static damage limit at synchrotrons of about 160 photons/A^2 can be overcome by imaging with x-ray free-electron lasers, instead. This new approach has been enabled by two significant advances: (i) The development of algorithms to reconstruct a real-space image from x-ray diffraction data of noncrystalline objects without prior knowledge [32], and (ii) the advent of femtosecond x-ray free-electron-laser pulses that allows the collection of usable diffraction data beyond the static damage limit [44]. In this case, the image resolution depends on the radiation intensity, the pulse duration, the wavelength, and the degree of sample damage through atomic ionization and atomic motion.

10.3.3.1 Dynamic Damage Limits

Many x-ray damage mechanisms require a finite time to manifest themselves. Therefore, if the pulse duration is sufficiently short, certain damage processes are not relevant for x-ray imaging. As a general trend, the shorter the x-ray pulses, the larger is the damage threshold. This concept led Solem and Baldwin to the idea of x-ray-laser flash-imaging microscopy, which goes beyond the static (cumulative) damage limit by using short pulses to obtain structural information before the radiation destroys the sample [45]. About a decade later, single-shot x-ray laser microscopy was demonstrated [46]. Neutze *et al.* [44] extended this idea to image single biological macromolecules beyond the static damage limit at x-ray free-electron lasers.

As discussed in Section 8.9, the dominant damage mechanisms in conventional x-ray diffractive imaging of biomolecules through crystallography behave cumulatively. An example is continuous mass loss. For very short and intense x-ray pulses, on the other hand, ionization and Coulomb-force-driven atomic motion dominate. When a 12-keV x-ray pulse irradiates a biological molecule, for which the dominant species by mass is carbon, 90% of the radiation is absorbed through photoionization, associated with the emission of photoelectrons with a kinetic energy of slightly less than 12 keV. Within 11 fs, atoms with a core hole relax through Auger decay, leading to the emission 250-eV electrons. These electrons interact with the electrons in the molecule further through electron impact ionization, causing the emission of secondary electrons with a kinetic energy of a few electron volts. Only 7 to 10% of the radiation is elastically scattered, leading to the formation of the signal in the diffraction pattern, and about 3% is inelastically scattered. The high-energy electrons initially escape the molecule, leaving a positive charge behind. When this charge is sufficiently large, electrons become electrostatically trapped (described in more detail in Section 5.8), which can lead to increased ionization at first, and eventually to recombination. Charging of the molecule leads to a Coulomb explosion due to the repulsive nature of the forces. On a little longer time scale, the molecule will expand due to hydrodynamic forces associated with the trapped hot electrons. Multiple models have been proposed to describe this behavior, see for example [44, 47–49].

10.3.3.2 Coherent Diffractive Imaging at X-Ray Free-Electron Lasers

For single-particle imaging, it is preferable to avoid any kind of device to hold the particles in the interaction region since such a holder will inadvertently scatter, and that scattering signal is potentially much stronger than scattering from the particle itself. Therefore, a holder-less scheme in which the particle is injected into the beam is preferable. Ideally, the particle is sufficiently hydrated to ensure that it stays in its native conformation, which is its structural arrangement, during the injection process. It has been shown that a hydration fraction of 20% is necessary to preserve biological activity [50, 51]. It is also necessary to characterize and select the injected particles. Several techniques have been proposed, including electrospray [52, 53], aerodynamic lens stacks [54], and Rayleigh droplet sources [55].

In most cases, the particles are injected in a random orientation, and a major issue is determining their orientation from the noisy diffraction pattern. It has been suggested initially to classify the collected diffraction patterns first into groups of similar orientation, and then orient the class averages [56]. Since each diffraction pattern is a sample of the Ewald sphere, the curvature of the Ewald sphere can be used to simplify the orientation process. Since the scattering strength of single macromolecules is small, the signal-to-noise ratio of each diffraction pattern is rather weak, with only single photons in the higher resolution part of the pattern. Classifying these patterns is very challenging and other more efficient approaches have been proposed, see for example [57, 58]. In general, classification is expected to be easier at larger fluences and for larger particles since the scattering signal in these cases is stronger. Different experimental methods have been proposed to ease the classification and orientation process, such as using ejected ion fragments or marker atoms to determine the particle orientation. Once the diffraction patterns have been categorized, class averages can be formed that have an improved signal-to-noise ratio. Then a three-dimensional diffraction pattern can be assembled, and phasing algorithms are used to calculate the electron density.

Radiation damage in the form of atomic motion and ionization modifies the diffraction pattern, but the effect has not been studied in much detail yet. Different methods have been proposed to reduce the required x-ray fluence, including prealignment of the molecules or using nanocrystals [59]. Molecules can be aligned using lasers [60, 61], and specifically elliptically polarized light holds the potential for full three-dimensional alignment. Note that alignment errors lead to a reduction of the image resolution. It has also been proposed to use a molecular tamper [62], such as water or liquid He, with water having the additional advantage that it keeps proteins in their native conformation. However, the tamper affects the diffraction pattern of the sample, which may lead to loss of structural information.

10.3.4 Outlook

By using high-intensity short x-ray pulses we will be able to image particles with atomic resolution and femtosecond time resolution. This technique holds the promise of not only imaging macromolecules but also determining the dynamics

and function. Improved beam coherence will enable holographic studies, as well. Combined with spectroscopy, imaging of chemical reactions may be possible. Several aspects of this technique need further development, including the injection and control of single molecules, and image reconstruction techniques that take advantage of the specific symmetry of single particles.

Recently it has been demonstrated that crystallography can be performed on nanocrystals with only a few unit cells at x-ray free-electron lasers [59]. The Bragg peaks in this case can be used to determine the orientation of the nanocrystal.

10.4
X-Ray Scattering Diagnostics of Dense Plasmas

Time-dependent inelastic x-ray scattering can be used to characterize dense matter, including solid-density plasmas. With this technique, information about basic electronic properties, such as temperature and density, and ionic structure can be obtained [63–65]. Light can propagate in plasmas only if the free-electron density is smaller than the critical electron density n_c, which depends on the photon energy E_γ. For small photon energies, the photon frequency is smaller than the plasma frequency, and inverse Bremsstrahlung absorption becomes very efficient, preventing the penetration of the photons. The dependence of n_c on E_γ is given by [66]

$$n_c = \frac{\epsilon_0 m_e E_\gamma^2}{e^2 \hbar^2} \,. \tag{10.4}$$

As can be seen in Figure 10.5, high-density plasmas are opaque to visible radiation, whereas x-ray radiation is able to penetrate solid- and higher-density materials.

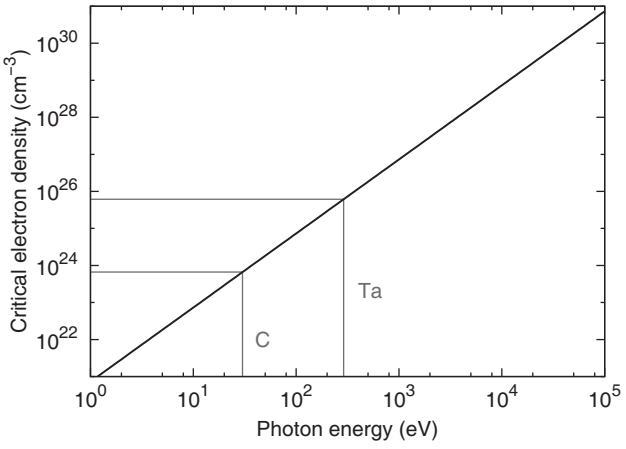

Figure 10.5 Critical electron density n_c as a function of the photon energy E_γ, given by (10.4). Also shown is the photon energy needed to penetrate a fully ionized solid-density graphite and tantalum plasma.

10.4.1 Experimental Setups

In order to utilize inelastic x-ray scattering as a high-fidelity plasma diagnostic, high-intensity x-ray pulses with short pulse durations and high spectral purity are required. The first experiments of this kind [63, 67] used the high-intensity helium-alpha (He_α) and Lyman-alpha (Ly_α) spectral lines of solid titanium irradiated by high-power lasers, a method introduced in Section 1.3.2. The Ly_α lines are the spectral lines of an ion with a single electron that transitions from the $n = 2$ to the $n = 1$ orbital. The He_α lines are the spectral lines of a two-electron ion associated with the transition from 1s2p to $1s^2$. For titanium, these lines lie between 4.7–4.75 keV. More recently, x-ray free-electron lasers have been used as sources for inelastic x-ray scattering [68, 69].

A typical setup for an x-ray-scattering diagnostic experiment is shown in Figure 10.6. A monochromatic x-ray beam irradiates a plasma and the spectrum of the scattered radiation is measured in different directions. We assume that the x-ray source and the detector are located at distances large in comparison to the extent of the plasma. The incoming wave vector is $\boldsymbol{k}_0$, and the scattered wave vector is $\boldsymbol{k}_1$. The angle between $\boldsymbol{k}_0$ and $\boldsymbol{k}_1$ is the scattering angle θ. The energy of the incoming photon is $\hbar\omega_0 = c\hbar k_0$, and the energy of the scattered photon is $\hbar\omega_1 = c\hbar k_1$. We define the downshift of the energy as $\hbar\omega = \hbar\omega_0 - \hbar\omega_1$, and the momentum transfer as $\hbar\boldsymbol{q} = \hbar\boldsymbol{k}_1 - \hbar\boldsymbol{k}_0$. In the nonrelativistic limit and for small values of q,

$$q \approx 2k_0 \sin\left(\frac{\theta}{2}\right) . \tag{10.5}$$

The measured intensity $I(q, \omega)$ is proportional to the x-ray-scattering cross section, which, in turn, is proportional to the total electron structure factor $S(q, \omega)$,

$$I(q, \omega) \propto \frac{d^2\sigma}{dq\,d\omega} \propto S(q, \omega) . \tag{10.6}$$

$S(q, \omega)$ is the Fourier transform of the electron–electron density fluctuations [70], and it measures the spatial correlations in the plasma. A more detailed discussion can be found in Sections 3.3 and 3.4. An expression for $S(q, \omega)$ was given by Chi-

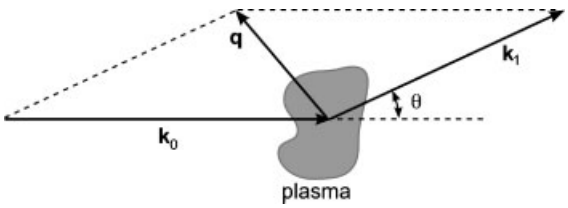

Figure 10.6 Setup to use inelastic x-ray scattering as a plasma diagnostic. The direction and length of $\boldsymbol{k}_1$ are solely given by the scattering geometry and the observed wavelength, respectively.

hara *et al.* [71], see (3.75). This model was further developed by Gregori *et al.* [72–74].

First x-ray-scattering diagnostics experiments did not discriminate the spectral dependence of S and instead focused on the dependence of S on q. By measuring the x-ray-scattering cross section as a function of scattering angle, information about the average short-range structure in a plasma can be obtained. The position and width of the peak in $S(q)$ depend on the plasma density and temperature. In a proof-of-principle experiment, shock-compressed aluminum was probed with He_α line radiation from high-power-laser-irradiated titanium [67]. The coherent part of the scattering radiation $I(q)$ is dominated by $I(q) \propto f(q)^2 S(q)$, where $f(q)$ is the bound electron form factor, $S(q)$ the ion–ion structure factor, and $q = 4\pi/\lambda \sin(\theta/2)$. For an ideal plasma for which the plasma temperature significantly exceeds the average Coulomb interaction energy of its constituents, the position of the peak in $S(q)$ relates to the density and the width to the ion temperature.

Figure 10.7 shows schematic spectra $S(\omega)$ of graphite probed at 8 keV, showing both elastic and inelastic scattering features. Tightly bound electrons with ionization potentials larger than the Compton shift scatter the x-ray radiation elastically, resulting in the ion feature in the spectra. This peak is also called the elastic or Rayleigh peak. Two processes lead to inelastic scattering: First, free electrons scatter x rays inelastically through the Compton effect, which leads to an energy shift of the scattered light due to momentum conservation. The Compton shift increases with scattering angle θ and is more easily accessible in a backward-scattering geometry. In the example spectrum in Figure 10.7, the Compton feature nearly coincides with the ion feature since this spectrum was measured in the forward-scattering geometry, that is for small θ. In nondegenerate plasmas, the Compton

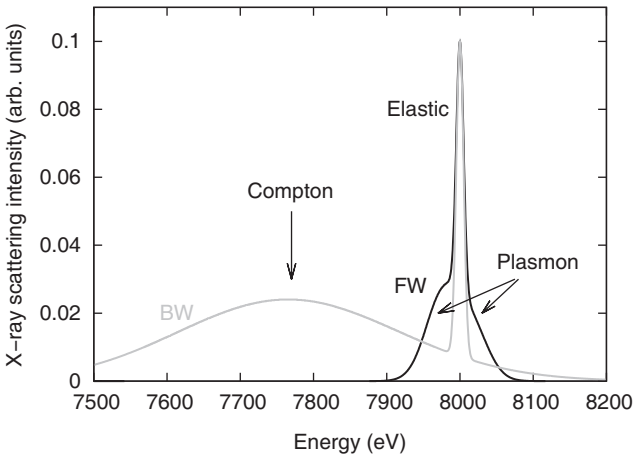

Figure 10.7 Schematic forward (FW) and backward (BW) scattering spectra $I(q, \omega)$ of doubly-ionized graphite with a temperature of 50 eV, probed with 8 keV x rays. Both the inelastic plasmon and Compton and the elastic ion feature are clearly visible.

peak is broadened by the thermal motion of the electrons and is a measure for the electron temperature. The Compton feature was used in one of the first x-ray Thomson scattering experiments to extract the electron density and temperature of heated beryllium [63]. In degenerate plasmas, the width of the Compton peak is related to the Fermi energy $\epsilon_F = \hbar^2(3\pi^2 n)^{2/3}/2m$, from which we can determine the electron density [75]. Finally, x rays may also be scattered by plasma oscillations (plasmons). Plasmon features represent collective plasma effects and are accessible primarily in the forward-scattering geometry [64, 75, 76]. At higher electron temperatures, upshifted plasmon features also become detectable, from which the electron temperature can be extracted directly using the relation of detailed balance, see (3.81) [76].

10.4.2 Collective and Noncollective Scattering

The length scale probed by the x rays is given by $2\pi/q$, which depends primarily on the x-ray wavelength and scattering geometry through (10.5) and only weakly on the frequency shift of the scattered light. For smaller scattering angles (small q), the x rays probe primarily collective effects associated with larger length scales. On the other hand, for larger scattering angles, the x rays probe mostly noncollective effects associated with smaller length scales. The significance of electronic correlation effects can be described by the scattering parameter

$$\alpha = \frac{1}{q\lambda_{sd}}\,, \tag{10.7}$$

where λ_{sd} is the correlation length in the plasma or the screening distance of electrostatic forces, which is determined by the plasma conditions. In nondegenerate plasmas, the correlation length can be taken as the Debye screening length,

$$\lambda_{sd} \approx \lambda_D = \left(\frac{\epsilon_0 k_B T_e}{n_e e^2}\right)^{1/2}, \tag{10.8}$$

whereas for a degenerate plasma, for which the Fermi energy is larger than the thermal energy, a better approximation is

$$\lambda_{sd} \approx \lambda_{TF} = \sqrt{\frac{\pi\epsilon_0\hbar^2}{m_e e^2}\left(\frac{\pi}{3n_e}\right)^{1/3}}\,. \tag{10.9}$$

When the scattering parameter α is larger than one, the scattering is of collective nature, associated with scattering from plasmons and acoustic oscillations. Because of the limited spectral resolution of spectrometers, acoustic oscillations have not been observed yet. The plasmon frequency shift is determined by the plasmon dispersion relation, which is approximately the plasma frequency $\omega_p = (n_e e^2/\epsilon_0 m_e)^{1/2}$, from which the electron density may be determined. Higher-order terms depend on the electron temperature. For small momentum transfer vectors $\boldsymbol{q}$, often a modified analytical Bohm–Gross dispersion relation is used [77], for

which the plasmon frequency is given by

$$\omega_{pl}^2 = \omega_p^2 + 3q^2 v_{th}^2 \left(1 + 0.088 n_e \Lambda^3\right) + \left(\frac{\hbar q^2}{2m_e}\right)^2 . \tag{10.10}$$

$v_{th} = (k_B T_e/m_e)^{1/2}$ is the thermal velocity, and $\Lambda_e = h/\sqrt{2\pi m_e k_B T_e}$ is the thermal de-Broglie wavelength. The first term in (10.10) refers to the electron oscillations, the second term to the effect of thermal pressure, the third term to degeneracy effects from the Fermi pressure, and the last term to the quantum diffraction shift. The width of the plasmons depends on Landau and collisional damping, which is related to the electron temperature.

The scattering parameter α decreases with increasing scattering angle θ. When α is much less than one, the scattered x rays are only sensitive to distances shorter than the screening length λ_{sd}, and the noncollective behavior of the plasma is probed. The Compton downshift of the scattered radiation is given by

$$\frac{1}{\hbar\omega_1} - \frac{1}{\hbar\omega_0} = \frac{1 - \cos\theta}{m_e c^2} , \tag{10.11}$$

which in the nonrelativistic limit, $\hbar\omega \ll \hbar\omega_0$, simplifies to

$$E_C = \hbar\omega = \frac{\hbar^2 q^2}{2m_e} = \hbar\omega_0 - \hbar\omega_s . \tag{10.12}$$

Since the ratio of the integrated Compton feature to the integrated ion feature is sensitive to the ionization state of the plasma, spectrally resolved scattering experiments allow us to probe the atomic physics in a plasma. For a free electron, the energy shift is determined by both the Compton and Doppler effect,

$$\omega = -\frac{\hbar q^2}{2m_e} \pm \boldsymbol{q} \cdot \boldsymbol{v} . \tag{10.13}$$

To calculate the broadening of the Compton peak, (10.13) needs to be integrated over the velocity space, weighted by the electron velocity distribution function. For nondegenerate systems, this provides the opportunity to extract the electron temperature from the shape of the Compton peak by fitting. For degenerate systems, the width of the Compton feature is proportional to $(\epsilon_F)^{1/2} \propto (n_e)^{1/3}$.

10.4.3
Theoretical Description of Inelastic X-Ray Scattering

The dynamic structure factor $S(q, \omega)$ is related to the longitudinal dielectric function $\epsilon(q, \omega)$ of the plasma by the fluctuation–dissipation theorem [70],

$$S(q, \omega) = -\frac{\epsilon_0 \hbar q^2}{\pi e^2 n_e} \frac{1}{1 - \exp\left(-\frac{\hbar\omega}{k_B T_e}\right)} \Im \frac{1}{\epsilon(q, \omega)} . \tag{10.14}$$

The random-phase approximation (RPA) describes the dielectric response of a weakly collisional, ideal plasma. The dielectric function in the RPA approximation is given by

$$\epsilon_{RPA}(q,\omega) = 1 - \frac{e^2}{\epsilon_0 q^2 \Omega_0} \sum_{\boldsymbol{p}} \frac{n_F^{(c)}\left(\boldsymbol{p} + \frac{\hbar \boldsymbol{q}}{2}\right) - n_F^{(c)}\left(\boldsymbol{p} - \frac{\hbar \boldsymbol{q}}{2}\right)}{\hbar \boldsymbol{q} \cdot \frac{\boldsymbol{p}}{m_e} - \hbar(\omega + i\eta)} \,. \tag{10.15}$$

Here, $n_F^{(c)}(p)$ is the Fermi momentum distribution function, and $\eta > 0$ is a small finite frequency to ensure convergence of the sum. Equation 10.15 has been used to derive an analytical model for $S(q,\omega)$ [74].

The RPA approach can be significantly improved by accounting for electron–ion collisions in the plasma, as has been demonstrated with the Born–Mermin approximation [78, 79]. In the Mermin formula for the dielectric function [80], collisions are accounted for in the relaxation-time approximation. Höll *et al.* suggested to treat the effect of collisions on the dielectric function using a frequency-dependent dynamic collision frequency $\nu(\omega)$. $\nu(\omega)$ can be calculated in the Born approximation with statically screened potentials [78]. This approach can be improved further by considering dynamical screening and strong collisions [79]. The Born–Mermin approximation is in agreement with current experimental findings [72–74, 77–79]. Models for the elastic scattering features are still being developed. Some models are based on the hyper-netted-chain approximation with quantum potentials or density functional theory [81–83]. A model for the electron in screening cloud in fully- and partially ionized plasmas, described by $d(\boldsymbol{q})$, is given in [84].

References

1 Yamanouchi, K. (2002) Laser chemistry and physics: The next frontier. *Science*, **295**, 1659–1660.

2 Hener, M., Fang, L., Kornilov, O., Gessner, O., Pratt, S.T., Gühr, M., Kanter, E.P., Blaga, C., Bostedt, C., Bozek, J.D., Bucksbaum, P.H., Buth, C., Chen, M., Coffee, R., Cryan, J., DiMauro, L., Glownia, M., Hosler, E., Kukk, E., Leone, S.R., McFarland, B., Messerschmidt, M., Murphy, B., Petrovic, V., Rolles, D., and Berrah, N. (2010) Ultraintense x-ray induced ionization, dissociation, and frustrated absorption in molecular nitrogen. *Phys. Rev. Lett.*, **104**, 253002.

3 Fang, L., Hoener, M., Gessner, O., Tarantelli, F., Pratt, S.T., Kornilov, O., Buth, C., Gühr, M., Kanter, E.P., Bostedt, C., Bozek, J.D., Bucksbaum, P.H., Chen, M., Coffee, R., Cryan, J., Glownia, M., Kukk, E., Leone, S.R., and Berrah, N. (2010) Double core-hole production in N_2: Beating the Auger clock. *Phys. Rev. Lett.*, **105**, 083005.

4 Kanter, E.P., Dunford, R.W., Krässig, B., and Southworth, S.H. (1999) Double *K*-vacancy production in molybdenum by x-ray photoionization. *Phys. Rev. Lett.*, **83**, 508–511.

5 Cryan, J.P., Glownia, J.M., Andreasson, J., Belkacem, A., Berrah, N., Blaga, C.I., Bostedt, C., Bozek, J., Buth, C., DiMauro, L.F., Fang, L., Gessner, O., Gühr, M., Hajdu, J., Hertlein, M.P., Hoener, M., Kornilov, O., Marangos, J.P., March, A.M., McFarland, B.K., Merdji, H., Petrovic, V.S., Raman, C., Ray, D., Reis, D., Tarantelli, F., Trigo, M., White, J.L., White, W., Young, L., Bucksbaum, P.H., and Coffee, R.N. (2010) Auger

electron angular distribution of double core-hole states in the molecular reference frame. *Phys. Rev. Lett.*, **105**, 083004.

6 Young, L., Kanter, E.P., Krässig, B., Li, Y., March, A.M., Pratt, S.T., Santra, R., Southworth, S.H., Rohringer, N., DiMauro, L.F., Doumy, G., Roedig, C.A., Berrah, N., Fang, L., Hoener, M., Bucksbaum, P.H., Cryan, J.P., Ghimire, S., Glownia, J.M., Reis, D.A., Bozek, J.D., Bostedt, C., and Messerschmidt, M. (2010) Femtosecond electronic response of atoms to ultra-intense x-rays. *Nature*, **466**, 56–61.

7 Amusia, M.Y., Lee, I.S., and Kilin, V.A. (1992) Double auger decay in atoms: Probability and angular distribution. *Phys. Rev. A*, **45**, 4576–4587.

8 Krause, M.O., Vestal, M.L., Johnston, W.H., and Carlson, T.A. (1964) Readjustment of the neon atom ionized in the *K* shell by x rays. *Phys. Rev.*, **133**, A385–A390.

9 Hagena, O.F. and Obert, W. (1972) Cluster formation in expanding supersonic jets: Effect of pressure, temperature, nozzle size, and test gas. *J. Chem. Phys.*, **56**, 1793–1802.

10 Kiran, B., Jena, P., Li, X., Grubisic, A., Stokes, S.T., Ganteför, G.F., Bowen, K.H., Burgert, R., and Schnöckel, H. (2007) Magic rule for Al_nH_m magic clusters. *Phys. Rev. Lett.*, **98**, 256802.

11 Connerade, J.P., Solov'yov, A.V., and Greiner, W. (2002) The science of clusters: An emerging field. *Europhys. News*, **33**, 200–201.

12 Guet, C., Hobza, P., Spiegelman, F., and David, F. (eds) (2001) *Atomic Clusters and Nanoparticles*. EDP Sciences and Springer Verlag, Berlin, New York, London, Paris, Tokyo.

13 Laarmann, T., de Castro, A.R.B., Gürtler, P., Laasch, W., Schulz, J., Wabnitz, H., and Möller, T. (2004) Interaction of argon clusters with intense VUV-laser radiation: The role of electronic structure in the energy-deposition process. *Phys. Rev. Lett.*, **92**, 143401.

14 Laarmann, T., Rusek, M., Wabnitz, H., Schulz, J., de Castro, A.R.B., Gürtler, P., Laasch, W., and Möller, T. (2005) Emission of thermally activated electrons from rare gas clusters irradiated with intense VUV light pulses from a free electron laser. *Phys. Rev. Lett.*, **95**, 063402.

15 Wabnitz, H., Bittner, L., de Castro, A.R.B., Döhrmann, R., Gürtler, P., Laarmann, T., Laasch, W., Schulz, J., Swiderski, A., von Häften, K., Möller, T., Faatz, B., Fateev, A., Feldhaus, J., Gerth, C., Hahn, U., Saldin, E., Schneidmiller, E., Sytchev, K., Tiedtke, K., Treusch, R., and Yurkov, M. (2002) Multiple ionization of atom clusters by intense soft x-rays from a free-electron laser. *Nature*, **420**, 482–485.

16 Siedschlag, C. and Rost, J.M. (2004) Small rare-gas clusters in soft x-ray pulses. *Phys. Rev. Lett.*, **93**, 43402.

17 Santra, R. and Green, C.H. (2003) Xenon clusters in intense VUV laser fields. *Phys. Rev. Lett.*, **91**, 233401.

18 Jungreuthmayer, C., Ramunno, L., Zanghellini, J., and Brabec, T. (2005) Intense VUV laser cluster interaction in the strong coupling regime. *J. Phys. B*, **38**, 3029.

19 Ziaja, B., Wabnitz, H., Wang, F., Weckert, E., and Möller, T. (2009) Energetics, ionization, and expansion dynamics of atomic clusters irradiated with short intense vacuum-ultraviolet pulses. *Phys. Rev. Lett*, **102**, 205002.

20 Ziaja, B., Laarmann, T., Wabnitz, H., Wang, F., Weckert, E., Bostedt, C., and Möller, T. (2009) Emission of electrons from rare gas clusters after irradiation with intense VUV pulses of wavelength 100 nm and 32 nm. *New J. Phys.*, 11.

21 Bostedt, C., Thomas, H., Hoener, M., Eremina, E., Fennel, T., Meiwes-Broer, K.-H., Wabnitz, H., Kuhlmann, M., Plönjes, E., Tiedtke, K., Treusch, R., Feldhaus, J., de Castro, A.R.B., and Möller, T. (2008) Multistep ionization of argon clusters in intense femtosecond extreme ultraviolet pulses. *Phys. Rev. Lett.*, **100**, 133401.

22 Thomas, H., Bostedt, C., Hoener, M., Eremina, E., Wabnitz, H., Laarmann, T., Plönjes, E., Treusch, R., de Castro, A.R.B., and Möller, T. (2009) Shell explosion and core expansion of xenon

clusters irradiated with intense femtosecond soft x-ray pulses. *J. Phys. B*, **42**, 134018.

23 von Pietrowski, R., Rutzen, M., von Haeften, K., Kakar, S., and Möller, T. (1997) Fluorescence excitation spectroscopy of xenon doped neon clusters: size and site effects, and cluster melting. *Z. Phys. D*, **40**, 22–24.

24 Tchaplyguine, M., Lundwall, M., Gisselbrecht, M., Oehrwall, G., Feifel, R., Sorensen, S., Svensson, S., Martensson, N., and Bjoerneholm, O. (2004) Variable surface composition and radial interface formation in self-assembled free, mixed Ar/Xe clusters. *Phys. Rev. A*, **69**, 031201(R).

25 Hoener, M., Bostedt, C., Thomas, H., Landt, L., Eremina, E., Wabnitz, H., Laarmann, T., Treusch, R., de Castro, A.R.B., and Möller, T. (2008) Charge recombination in soft x-ray laser produced nanoplasmas. *J. Phys. B*, 181001.

26 Bostedt, C., Thomas, H., Hoener, M., Möller, T., Saalmann, U., Georgescu, I., Gnodtke, C., and Rost, J.-M. (2010) Fast electrons from multi-electron dynamics in xenon clusters induced by inner-shell ionization. *New J. Phys.*, **12**, 083004.

27 Saalmann, U. and Rost, J.M. (2002) Ionization of clusters in strong x-ray laser pulses. *Phys. Rev. Lett.*, **89**, 143401.

28 Gnodtke, C., Saalmann, U., and Rost, J.M. (2009) Ionization and charge migration through strong internal fields in clusters exposed to intense x-ray pulses. *Phys. Rev. A*, **79**, 041201(R).

29 Bethe, H. and Salpeter, E.E. (1977) *Quantum Mechanics of One- and Two-Electron Atoms*, 2nd edn, Plenum-Rosetta, New York.

30 Böttcher, B., Wynne, S.A., and Crowther, R.A. (1997) Determination of the fold of the core protein of hepatitis B virus by electron cryomicroscopy. *Nature*, **386**, 88–91.

31 Shannon, C.E. (1948) A mathematical theory of communication. *Bell Syst. Tech. J.*, **27**, 379–423 and 623–656.

32 Sayre, D. (1952) Some implications of a theorem due to Shannon. *Acta Cryst.*, **5**, 843.

33 Blake, C.C.F. and Phillips, D.C. (1962) *Biological Effects of Ionizing Radiation at the Molecular Level*, Int. At. Energy Agency, Vienna, pp. 183–191.

34 Henderson, R. (1990) Cryoprotection of protein crystals against radiation damage in electron and x-ray diffraction. *Proc. R. Soc. Lond. B*, **241**, 6–8.

35 Miao, J., Kirz, J., and Sayre, D. (2000) The oversampling phasing method. *Acta Cryst. D*, **56**, 1312–1315.

36 Gerchberg, R.W. and Saxton, W.O. (1972) A practical algorithm for the determination of phase from image and diffraction plane pictures. *Optik*, **35**, 237–246.

37 Fienup, J.R. (1978) Reconstruction of an object from the modulus of its Fourier transform. *Opt. Lett.*, **3**, 27–29.

38 Oszlanyi, G. and Sueto, A. (2004) Ab initio structure solution by charge flipping. *Acta Cryst.*, **A60**, 134–141.

39 Elser, V. (2003) Phase retrieval by iterated projections. *J. Opt. Soc. Am. A*, **20**, 40–55.

40 Spence, J.C.H., Wu, J.S., Giacovazzo, C., Carrozzini, B., Cascarano, G.L., and Padmore, H.A. (2003) Solving non-periodic structures using direct methods: phasing diffuse scattering. *Acta Cryst. A*, **59**, 255–261.

41 Hau-Riege, S.P., Szoke, H., Chapman, H.N., Szoke, A., Marchesini, S., Noy, A., He, H., Howells, M., Weierstall, U., and Spence, J.C.H. (2004) SPEDEN: reconstructing single particles from their diffraction patterns. *Acta Cryst.*, A**60**, 294–305.

42 Chapman, H.N., Barty, A., Marchesini, S., Noy, A., Hau-Riege, S.P., Cui, C., Howells, M.R., Rosen, R., He, H., Spence, J.C.H., Weierstall, U., Beetz, T., Jacobsen, C., and Shapiro, D. (2006) High-resolution ab initio three-dimensional x-ray diffraction microscopy. *J. Opt. Soc. Am. A*, **23**, 1179–1200.

43 Marchesini, S., He, H., Chapman, H.N., Hau-Riege, S.P., Noy, A., Howells, M.R., Weierstall, U., and Spence, J.C.H. (2003) X-ray image reconstruction from a diffraction pattern alone. *Phys. Rev. B*, **68**, 140101(R).

44 Neutze, R., Wouts, R., van der Spoel, D., Weckert, E., and Hajdu, J. (2000) Potential for biomolecular imaging with femtosecond x-ray pulses. *Nature*, **406**, 752–757.

45 Solem, J. and Baldwin, G.C. (1982) Microholography of living organisms. *Science*, **218**, 229–235.

46 Da Silva, L.B., Trebes, J.E., Balhorn, R., Mrowka, S., Anderson, E., Attwood, D.T., Barbee Jr. T.W., Brase, J., Corzett, M., and Gray, J. (1992) X-ray laser microscopy of rat sperm nuclei. *Science*, **258**, 269–271.

47 Bergh, M., Timneanu, N., and van der Spoel, D. (2004) Model for the dynamics of a water cluster in an x-ray free electron laser beam. *Phys. Rev. E*, **70**, 051904.

48 Hau-Riege, S.P., London, R.A., and Szoke, A. (2004) Dynamics of x-ray irradiated biological molecules. *Phys. Rev. E*, **69**, 051906.

49 Jurek, Z., Faigel, G., and Tegze, M. (2004) Dynamics in a cluster under the influence of intense femtosecond hard x-ray pulses. *Eur. Phys. J. D*, **29**, 217–229.

50 Dunn, R.V. and Daniel, R.M. (2004) The use of gas-phase substrates to study enzyme catalysis at low hydration. *Philos. Trans. R. Soc. Lond. B Biol. Sci.*, **359**, 1309–1320.

51 Kurkal, V., Daniel, R.M., Finney, J.L., Tehei, M., Dunn, R.V., and Smith, J.C. (2005) Enzyme activity and flexibility at very low hydration. *Biophys. J.*, **89**, 1282–1287.

52 Cech, N.B. and Enke, C.G. (2001) Practical implications of some recent studies in electrospray ionization fundamentals. *Mass Spectrom. Rev.*, **20**, 362–87.

53 Fenn, J.B., Mann, M., Meng, C.K., Wong, S.F., and Whitehouse, C.M. (2001) Electrospray ionization for mass spectrometry of large biomolecules. *Science*, **246**, 64–71.

54 Benner, W.H., Bogan, M.J., Rohner, U., Boutet, S., Woods, B., and Frank, M. (2008) Non-destructive characterization and alignment of aerodynamically focused particle beams using single particle charge detection. *J. Aerosol Sci.*, **39**, 917–928.

55 Weierstall, U., Chapman, H., Doak, R., Spence, J., Starodub, D., Shapiro, D., Kennedy, P., Warner, J., Hembree, G., and Fromme, P. (2008) Droplet streams for serial crystallography of proteins. *Exp. Fluids*, **44**, 675–689.

56 Huldt, G., Szoke, A., and Hajdu, J. (2003) Diffraction imaging of single particles and biomolecules. *J. Struct. Biol.*, **144**, 219–227.

57 Fung, R., Shneerson, V.L., Saldin, D.K., and Ourmazd, A. (2009) Structure from fleeting illumination of faint spinning objects in flight. *Nat. Phys.*, **5**, 64–67.

58 Duane Loh, N.-T. and Elser, V. (2009) Reconstruction algorithm for single-particle diffraction imaging experiments. *Phys. Rev. E*, **80**(2), 026705.

59 Chapman, H.N., Fromme, P., Barty, A., White, T., Kirian, R.A., Aquila, A., Hunter, M.S., Schulz, J., DePonte, D.P., Weierstall, U., Doak, R.B., Maia, F.R.N.C., Martin, A., Schlichting, I., Lomb, L., Coppola, N., Shoeman, R.L., Epp, S., Hartmann, R., Rolles, D., Rudenko, A., Foucar, L., Kimmel, N., Weidenspointner, G., Holl, P., Liang, M., Barthelmess, M., Caleman, C., Boutet, S., Bogan, M.J., Krzywinski, J., Bostedt, C., Bajt, S., Gumprecht, L., Rudek, B., Erk, B., Schmidt, C., Hömke, A., Reich, C., Pietschner, D., Strüder, L., Hauser, G., Gorke, H., Ullrich, J., Herrmann, S., Schaller, G., Schopper, F., Soltau, H., Kühnel, K.-U., Messerschmidt, M., Bozek, J.D., Hau-Riege, S.P., Frank, M., Hampton, C.Y., Sierra, R., Starodub, D., Williams, G.J., Hajdu, J., Timneanu, N., Seibert, M.M., Andreasson, J., Rocker, A., Jönsson, O., Stern, S., Nass, K., Andritschke, R., Schröter, C.-D., Krasniqi, F., Bott, M., Schmidt, K.E., Wang, X., Grotjohann, I., Holton, J., Marchesini, S., Schorb, S., Rupp, D., Adolph, M., Gorkhover, T., Svenda, M., Hirsemann, H., Potdevin, G., Graafsma, H., Nilsson, B., and Spence, J.C.H. (2011) *Femtosecond x-ray protein nanocrystallography*, *Nature*, **470**, 7377.

60 Stapelfeldt, H. and Seideman, T. (2003) Colloqium: Aligning molecules with strong laser pulses. *Rev. Mod. Phys.*, **75**, 543–557.

61 Wu, J.S. and Spence, J.C.H. (2005) Phasing diffraction data from a stream of hydrated proteins. *J. Opt. Soc. Am.*, **22**, 1453–1459.

62 Hau-Riege, S.P., London, R.A., Chapman, H.N., Szoke, A., and Timneanu, N. (2007) Encapsulation and diffraction-pattern-correction methods to reduce the effect of damage in x-ray diffraction imaging of single biological molecules. *Phys. Rev. Lett.*, **98**, 198302.

63 Glenzer, S.H., Gregori, G., Lee, R.W., Rogers, F.J., Pollaine, S.W., and Landen, O.L. (2003) Demonstration of spectrally resolved x-ray scattering in dense plasmas. *Phys. Rev. Lett.*, **90**, 175002.

64 Glenzer, S.H., Landen, O.L., Neumayer, P., Lee, R.W., Widmann, K., Pollaine, S.W., Wallace, R.J., and Gregori, G. (2007) Observations of plasmons in warm dense matter. *Phys. Rev. Lett.*, **98**, 065002.

65 Garcia Saiz, E., Gregori, G., Gericke, D.O., Vorberger, J., Barbrel, B., Clarke, R.J., Freeman, R.R., Glenzer, S.H., Khattak, F.Y., Koenig, M., Landen, O.L., Neely, D., Neumayer, P., Notley, M.M., Pelka, A., Price, D., Roth, M., Schollmeier, M., Spindloe, C., Weber, R.L., van Woerkom, L., Wünsch, K., and Riley, D. (2008) Probing warm dense lithium by inelastic x-ray scattering. *Nat. Phys.*, **4**, 940–944.

66 Jackson, J.D. (1975) *Classical Electrodynamics*, 2nd edn, John Wiley & Sons, New York.

67 Riley, D., Woolsey, N.C., McSherry, D., Weaver, I., Djaoui, A., and Nardi, E. (2000) X-ray diffraction from a dense plasma. *Phys. Rev. Lett.*, **84**, 1704–1707.

68 Fäustlin, R.R., Bornath, T., Döppner, T., Düsterer, S., Förster, E., Fortmann, C., Glenzer, S.H., Göde, S., Gregori, G., Irsig, R., Laarmann, T., Lee, H.J., Li, B., Meiwes-Broer, K.-H., Mithen, J., Nagler, B., Przystawik, A., Redlin, H., Redmer, R., Reinholz, H., Röpke, G., Tavella, F., Thiele, R., Tiggesbäumker, J., Toleikis, S., Uschmann, I., Vinko, S.M., Whitcher, T., Zastrau, U., Ziaja, B., and Tschentscher, T. (2010) Observation of ultrafast nonequilibrium collective dynamics in warm dense hydrogen. *Phys. Rev. Lett.*, **104**, 125002.

69 Höll, A., Bornath, T., Cao, L., Döppner, T., Düsterer, S., Förster, E., Fortmann, C., Glenzer, S.H., Gregori, G., Laarmann, T., Meiwes-Broer, K.-H., Przystawik, A., Radcliffe, P., Redmer, R., Reinholz, H., Röpke, G., Thiele, R., Tiggesbäumker, J., Toleikis, S., Truong, N.X., Tschentscher, T., Uschmann, I., and Zastrau, U. (2007) Thomson scattering from near-solid density plasmas using soft x-ray free electron lasers. *High Energy Density Phys.*, **3**, 120–130.

70 Ichimaru, S. (1973) *Basic Principles Of Plasma Physics: A Statistical Approach*, W.A. Benjamin, Reading, MA.

71 Chihara, J. (2000) Interaction of photons with plasmas and liquid metals – photoabsorption and scattering. *J. Phys. Condens. Matter*, **12**, 231–247.

72 Gregori, G., Glenzer, S.H., and Landen, O.L. (2003) Strong coupling corrections in the analysis of x-ray Thomson scattering measurements. *J. Phys. A*, **36**, 5971–5980.

73 Gregori, G., Glenzer, S.H., and Landen, O.L. (2006) Generalized x-ray scattering cross section from nonequilibrium plasmas. *Phys. Rev. E*, **74**, 026402.

74 Gregori, G., Glenzer, S.H., Rozmus, W., Lee, R.W., and Landen, O.L. (2003) Theoretical model of x-ray scattering as a dense matter probe. *Phys. Rev. E*, **67**, 026412.

75 Lee, H.J., Neumayer, P., Castor, J., Döppner, T., Falcone, R.W., Fortmann, C., Hammel, B.A., Kritcher, A.L., Landen, O.L., Lee, R.W., Meyerhofer, D.D., Munro, D.H., Redmer, R., Regan, S.P., Weber, S., and Glenzer, S.H. (2009) X-ray Thomson-scattering measurements of density and temperature in shock-compressed beryllium. *Phys. Rev. Lett.*, **102**, 115001.

76 Neumayer, P., Fortmann, C., Döppner, T., Davis, P., Falcone, R.W., Kritcher, A.L., Landen, O.L., Lee, H.J., Lee, R.W., Niemann, C., Pape, S.L., and Glenzer, S.H. (2010) Plasmons in strongly coupled shock-compressed matter. *Phys. Rev. Lett.*, **105**, 075003.

77 Thiele, R., Bornath, T., Fortmann, C., Höll, A., Redmer, R., Reinholz, H., Röpke, G., Wierling, A., Glenzer, S.H., and Gregori, G. (2008) Plasmon resonance in warm dense matter. *Phys. Rev. E*, **78**, 026411.

78 Höll, A., Redmer, R., Röpke, G., and Reinholz, H. (2004) X-ray Thomson scattering in warm dense matter. *Eur. Phys. J. D*, **29**, 159–162.

79 Redmer, R., Reinholz, H., Röpke, G., Thiele, R., and Höll, A. (2005) Theory of x-ray Thomson scattering in dense plasmas. *IEEE Trans. Plasma Sci.*, **33**, 77.

80 Mermin, N.D. (1970) Lindhard dielectric function in the relaxation time approximation. *Phys. Rev. B*, **1**, 2362–2363.

81 Schwarz, V., Bornath, T., Kraeft, W.-D., Glenzer, S.H., Höll, A., and Redmer, R. (2007) Hypernetted chain calculations for two-component plasmas. *Contrib. Plasma Phys.*, **47**, 324–330.

82 Wünsch, K., Hilse, P., Schlanges, M., and Gericke, D.O. (2008) Structure of strongly coupled multicomponent plasmas. *Phys. Rev. E*, **77**, 056404.

83 Wünsch, K., Vorberger, J., and Gericke, D.O. (2009) Ion structure in warm dense matter: Benchmarking solutions of hypernetted-chain equations by first-principle simulations. *Phys. Rev. E*, **79**, 010201(R).

84 Gericke, D.O., Vorberger, J., Wünsch, K., and Gregori, G. (2010) Screening of ionic cores in partially ionized plasmas within linear response. *Phys. Rev. E*, **81**, 065401(R).

Index

High-Intensity X-rays – Interaction with Matter, First Edition. Stefan P. Hau-Riege.